UNIVERSITY OF CALIFORNIA SAN DIEGO

Exploring and Expanding the Coordination Chemistry of Metal-Binding Pharmacophores for Metalloenzyme Inhibition

A dissertation submitted in partial satisfaction of the requirements
for the degree Doctor of Philosophy

in

Chemistry

by

Benjamin L. Dick

Committee in charge:

Professor Seth M. Cohen, Chair
Professor Faik Akif Tezcan, Co-Chair
Professor Geoffrey Chang
Professor Michael J. Sailor
Professor Andrea R. Tao

2020

The Dissertation of Benjamin L. Dick. is approved, and it is acceptable in quality and form for publication on microfilm and electronically:

_____

_____

_____

_____

Co-Chair

_____

Chair

University of California San Diego

2020

DEDICATION

To my parents, my sister, and the rest of my family and friends who have supported me throughout this journey, I could not have done it without you.

A mi abuelo Benjamín Martínez Moriones, gracias por creer en mí.

TABLE OF CONTENTS

LIST OF FIGURES

LIST OF SCHEMES

LIST OF TABLES

ACKNOWLEDGEMENTS

I would first like to acknowledge Professor Seth M. Cohen for all his support. His mentorship and encouragements were absolutely critical to my development as a scientist. Seth is one of the most capable, organized, and diligent scientists I have known, and I have improved as a scientist these past six years because of his support. I appreciate him never letting me settle for anything less than my best, even when it was hard. I will always be thankful to have been mentored by you, as well as your impeccable taste in television shows.

Thank you to all past and present members of the Cohen lab who have supported me as colleagues and as friends. I want to especially thank Dr. David P. Martin, who got me hooked on protein crystallography. To those who worked on various project and papers with me, Dr. Cy V. Credille, Dr. Christian Perez, Dr. Christine N. Morrison, Dr. Allie Y. Chen, Rebecca N. Adamek, and Ryjul W. Stokes, I could not have done it without you. I want to thank the remaining MBP-subgroup past and present members, Dr. Yao Chen, Dr. Kathleen E. Prosser, and Stephanie Duggan, for their helpful discussions and critical analysis of my work. I also want to acknowledge, Dr. Michael S. Denny, Dr. Jessie Moreton, Dr. Xiao Yu, Dr. Le Wang, Sergio Ayala, Joseph M. Palomba, Kyle S. Barcus, and Mark Kalaj for their help when research got tough and for being great colleagues.

I would like to acknowledge my outside collaborators, particularly Professor J. Andrew McCammon and Dr. Ashay Patel for advancing my understanding of the materials discussed in this work, I am grateful for your help. I would like to thank Professor Arnold L. Rheingold, Dr. Curtis E. Moore, and Dr. Milan Gembicky for teaching me the art of X-ray crystallography and all their help throughout the years .

I would like to thank Professor Kara L. Bren because she gave me my start as a research chemist when I was just an undergraduate student at the University of Rochester. Professor Thomas R. Krugh you helped me find my way during my undergraduate years and ultimately to graduate school at UCSD. I would also like to thank Neal Lambert and Steven K. MacLeod for their exceptional mentorship during my time at Bausch +Lomb.

To all my friends, you have made graduate school so much fun and kept me whole these past years during the good and the bad. To my fellow inhabitants of the Robbin's Residence, Thomas G. Bartholow, Jefferey T. Mindrebo, and Dr. Ryan J. Lumpkin as well as honorary member Dr. Laëtitia Misson, I absolutely could not have done this without your support.

Finally, I want to thank my family for their unconditional love and support throughout this difficult journey. I want to thank my sister, Dr. Michelle H. Dick, for telling it to me straight when I needed it, as well as listening to me and supporting me. I want to give a special thanks to my parents, Claudia M. Dick and David B. Dick. To my mother, you have been the absolute best I could have asked for and have supported me in everything I do, I will always be thankful. To my father, David B. Dick, you have made my life an adventure by making me laugh, showing me how to live and work hard, teaching me what you know, and always being there. Lastly, I would like to thank my extended family who always supported me throughout this journey. Thank you all.

Chapter 2 is a reprint of the material published in the following publication, "Effect of Donor Atom Identity on Metal-Binding Pharmacophore Coordination" Benjamin L. Dick, Ashay Patel, J. Andrew McCammon, and Seth M. Cohen *J. Biol. Inorg. Chem***.** 2017**,** *22*, 605-613. The dissertation author was the primary researcher and author of this publication and gratefully acknowledges the contributions of coauthors Ashay Patel, J. Andrew McCammon, and Seth M. Cohen.

Chapter 3 is a reprint of the material published in the following publication, "Metal-Binding Isosteres as New Scaffolds for Metalloenzyme Inhibitors" Benjamin L. Dick, Seth M. Cohen. *Inorg. Chem.* 2018, *57*, 15, 9538-9543. The dissertation author was the primary author and researcher and gratefully acknowledges the contributions of coauthor Seth M. Cohen.

. Chapter 4 is a reprint of the material published in the following publication, "Effect of Heterocycle Content on Metal-Binding Isostere Coordination" Benjamin L. Dick, Ashay Patel, and Seth M. Cohen. *Chem. Sci*., 2020, *11*, 26, 6907-6914. The dissertation author was the primary author and researcher of this manuscript and gratefully acknowledges the contributions of coauthors Ashay Patel and Seth M. Cohen.

The content and figures in Chapter 5 are in large part adapted from "Structure-Activity Relationships in Metal-Binding Pharmacophores for Influenza Endonuclease" Cy V. Credille, Benjamin L. Dick, Christine N. Morrison, Ryjul W. Stokes, Rebecca N. Adamek, Nicholas C. Wu, Ian A. Wilson, and Seth M. Cohen. *J. Med. Chem.* 2018, *61*, 22, 10206-10217 and "SAR Exploration of Tight-Binding Inhibitors of Influenza Virus PA Endonuclease" Cy V. Credille*, Christine N. Morrison*, Ryjul W. Stokes*, Benjamin L. Dick, Yifan Feng, Jiaxing Sun, Yao Chen, and Seth M. Cohen. *J. Med. Chem.* 2019, *62*, 21, 9438-9449. The dissertation author was the primary researcher for the data presented and gratefully acknowledges the contributions of coauthors Cy V. Credille, Christine N. Morrison, Ryjul W. Stokes, Rebecca N. Adamek, Nicholas C. Wu, Ian A. Wilson, Yifan Feng, Jiaxing Sun, Yao Chen, and Seth M. Cohen.

Select content in Chapters 1 and 5 are adapted from "Targeting Metalloenzymes for Therapeutic Intervention" Allie Y. Chen*, Rebecca N. Adamek*, Benjamin L. Dick, Cy V. Credille, Christine N. Morrison, and Seth M. Cohen. *Chem. Rev.* 2019, *119*, 2, 1323-1455. The dissertation author was a coauthor on this publication and gratefully acknowledges the

contributions of coauthors Allie Y. Chen, Rebecca N. Adamek, Cy V. Credille, Christine N. Morrison, and Seth M. Cohen.

VITA

Education

2013 Bachelor of Science, University of Rochester

2014 Master of Science, University of Rochester

2020 Doctor of Philosophy, University of California San Diego

Honors and Awards

2015-2017 National Institute of Health Molecular Biophysics Training Grant

Publications

Benjamin L. Dick, Ashay Patel, and Seth M. Cohen. “Effect of Heterocycle Content on Metal-Binding Isostere Coordination,” *Chem. Sci.* **2020**, 11, 6907-6914.

Cy V. Credille*, Christine N. Morrison*, Ryjul W. Stokes*, Benjamin L. Dick, Yifan Feng, Jiaxing Sun, Yao Chen, and Seth M. Cohen, "SAR Exploration of Tight-Binding Inhibitors of Influenza Virus PA Endonuclease," *J. Med. Chem.* **2019**, 62, 9438-9449.

Christian L. Perez, Amanda M. Barley-Levenson, Benjamin L. Dick, Peter F. Glatt, Yadira Martinez, Dionicio Siegel, Jeremiah D. Momper, Abraham A. Palmer, and Seth M. Cohen. "A Metal-Binding Pharmacophore Library Yields the Discovery of a Glyoxalase 1 Inhibition," *J. Med. Chem.* **2019**, 62, 1609-1625.

Allie Y. Chen*, Rebecca N. Adamek*, Benjamin L. Dick, Cy V. Credille, Christine N. Morrison, and Seth M. Cohen. "Targeting Metalloenzymes for Therapeutic Intervention" *Chem. Rev.* **2019**, 119, 1323-1455.

Cy V. Credille, Benjamin L. Dick, Ryjul W. Stokes, Rebecca N. Adamek, Nicholas C, Wu, Ian A. Wilson, and Seth M. Cohen. "Structure-Activity Relationships in Metal-Binding Pharmacophores for Influenza Endonuclease," *J. Med. Chem.* **2018**, 61, 10206-10217.

Benjamin L. Dick and Seth M. Cohen. "Metal-Binding Isosteres as New Scaffolds for Metalloenzyme Inhibitors," *Inorg. Chem.* **2018**, 15, 9538-9543.

Rebecca N. Adamek, Cy V. Credille, Benjamin L. Dick, and Seth M. Cohen. "Isosteres of Hydroxypyridinethione as Druglike Pharmacophores for Metalloenzyme Inhibition," *J. Biol. Inorg. Chem.* **2018**, 23, 1129-1138.

Giulia E. M. Schukraft, Sergio Ayala Jr., Benjamin L. Dick, and Seth M. Cohen. “Isoreticular Expansion of polyMOFs Achieves High Surface Area Materials,” *Chem. Commun.* **2017**, 53, 10684-10687.

Benjamin L. Dick, Ashay Patel, J. Andrew McCammon, and Seth M. Cohen. “Effect of Donor Atom Identity on Metal-Binding Pharmacophore Coordination,” *J. Biol. Inorg. Chem*. **2017**, 22, 605-613.

ABSTRACT OF THE DISSERTATION

Exploring and Expanding the Coordination Chemistry of Metal-Binding Pharmacophores for Metalloenzyme Inhibition

by

Benjamin L. Dick

Doctor of Philosophy in Chemistry

University of California San Diego, 2020

Professor Seth M. Cohen, Chair

Professor Faik A. Tezcan, Co-Chair

A major shortcoming to the field of metalloenzyme inhibition has been the application of the same metal-binding pharmacophores (MBPs). Using novel MBPs for metalloenzyme inhibition has become an increasingly important strategy that overcomes the deficits encountered in the development of novel metalloenzyme inhibitors. Unfortunately, some functional groups utilized by MBPs may become problematic for further drug development. To help circumvent this issue and expand the range of chemical matter utilized in MBPs, this dissertation describes efforts

to apply and study bioisostere/isostere replacement to MBPs and create isosteric MBPs with varied physicochemical properties, so-called metal-binding isosteres (MBIs).

Chapter 2 describes the study of the effect of MBP donor atom identity on coordination to metalloenzyme active sites. Utilizing the model protein system human carbonic anhydrase II (hCAII), upon introduction of an active site mutation changes in MBP coordination based on donor atom identity were observed.

The application of isostere replacement to MBPs was evaluated in Chapter 3. The MBP picolinic acid (pyridine-2-carboxylic acid) was studied utilizing a range of carboxylic acid isosteres to develop a series of metal-binding isosteres (MBIs). These novel metal-binding fragments afforded a range of physicochemical properties while retaining metal coordination ability and metalloenzyme inhibitory activity.

In Chapter 4, a broader study of the application of carboxylic acid isostere replacement on MBPs is described. A series of complex nitrogen containing heterocycles with varying heteroatom content and arrangement were evaluated as MBI scaffolds. The success of isostere replacements on the studied scaffolds was manipulated based on specific heteroatoms and their arrangement within the heterocycle.

Chapter 5 describes a structure-based inhibitor development campaign for the influenza polymerase acidic N-terminal endonuclease domain (Endo) of the RNA-dependent RNA polymerase complex. The optimization, using scaffold modification and isostere replacement, of a potent MBP was undertaken based on observed coordination modes from protein crystal structures.

Chapter 1: Metalloenzymes and Coordination Chemistry of their Inhibitors

1.1 Metalloenzymes and Their Inhibitors in Human Health

In all biological systems enzymes are the pathway by which most chemical transformations required to sustain life are accomplished. For a significant portion (~40-50%) of these enzymes to accomplish their specific functions, at least one metal ion is required.[1-4] These metals can provide either a structural, catalytic, electron transfer, or regulatory role. Enzymes that utilize a metal in their active site for which the substrate can bind to and have the metal promote catalysis are termed metalloenzymes. These metal-dependent enzymes can be distinguished from enzymes utilizing metals for structural purposes, by the active site metals possessing open coordination sites. The reactions that metalloenzymes catalyze cover a vast range of biological processes including, but not limited to, maintenance of physiological pH, nitrogen fixation, and respiration.[5-9]

Due to the pervasive roles that metalloenzymes play in necessary biological chemistry, it is not surprising that they are involved in human health. The human disease states or infections that metalloenzymes are implicated in are just as diverse as the reactions they catalyze, such as tumor angiogenesis, neurological conditions, and microbial infections.[10-13] Some metalloenzymes that are the target of approved therapeutics or have garnered interest towards being targeted to treat a clinical condition are summarized below in Table 1.1.[14]

Table 1.1. Examples of metalloenzymes that have been implicated in various disease states/infections. Adapted from Chen et al.[14]

Metalloenzyme	Metal	Disease State/Infection
Angiotensin Converting Enzyme	Zn^{2+}	Hypertension
Arginase	Mn^{2+}	Cancer
Botulinum Neurotoxin	Zn^{2+}	Botulinum infection
Carbonic Anhydrases	Zn^{2+}	Glaucoma / Cancer
Glyoxalase I	Zn^{2+}	Cancer / Depression
Histone Deacetylase	Zn^{2+}	Cancer
Histone Demethylase	Fe^{2+}	Cancer
HIV integrase	Mg^{2+}	HIV/AIDS
Influenza Polymerase	Mn^{2+}	Influenza infection
Insulin degrading enzyme	Zn^{2+}	Diabetes / Alzheimer's
Lipoxygenase	Fe^{2+}	Asthma
LPxC	Zn^{2+}	Bacterial Infection
Matrix Metalloproteases	Zn^{2+}	Cancer
Metallo-β-lactamase	Zn^{2+}	Bacterial Infection
Methionine Aminopeptidase	Mn^{2+}/Fe^{2+}	Cancer/Bacterial Infection
Peptide Deformylase	Fe^{2+}	Bacterial Infection
RPN-11	Zn^{2+}	Cancer
Tyrosinase	Cu^{2+}	Cancer

For treatment of human disease endogenous metalloenzymes are typically targeted to address an overexpression, correct misregulation, or modulate native activity.[3] In cases of infection, the pathogens endogenous metalloenzymes are targeted to prevent further proliferation in the host, allowing clearance of the pathogen.[3] Because the activity of a metalloenzyme is dependent on the ability of the active site metal to interact with a substrate, the activity of the enzyme can be blocked by introducing a metal-binding pharmacophore (MBP), which

competitively binds to the active site metal through coordination chemistry. The MBP can then be derivatized to add interactions with the surrounding active site of the metalloenzyme such as hydrogen bonding, hydrophobic interactions, and electrostatic interactions.[15-16] An example of a United States of America Food and Drug Administration (FDA) approved metalloenzyme inhibitor bound to the active site of its target is shown in Figure 1.1.[17] The inhibitor, suberoylanilide hydroxamic acid (SAHA), utilizes a hydroxamic acid MBP to coordinate to the active site Zn^{2+} of a Histone Deacetylase (HDAC). Additionally, the alkyl portion of the inhibitor sits inside of a hydrophobic channel and the amide capping group makes contacts with the opening to the active site.

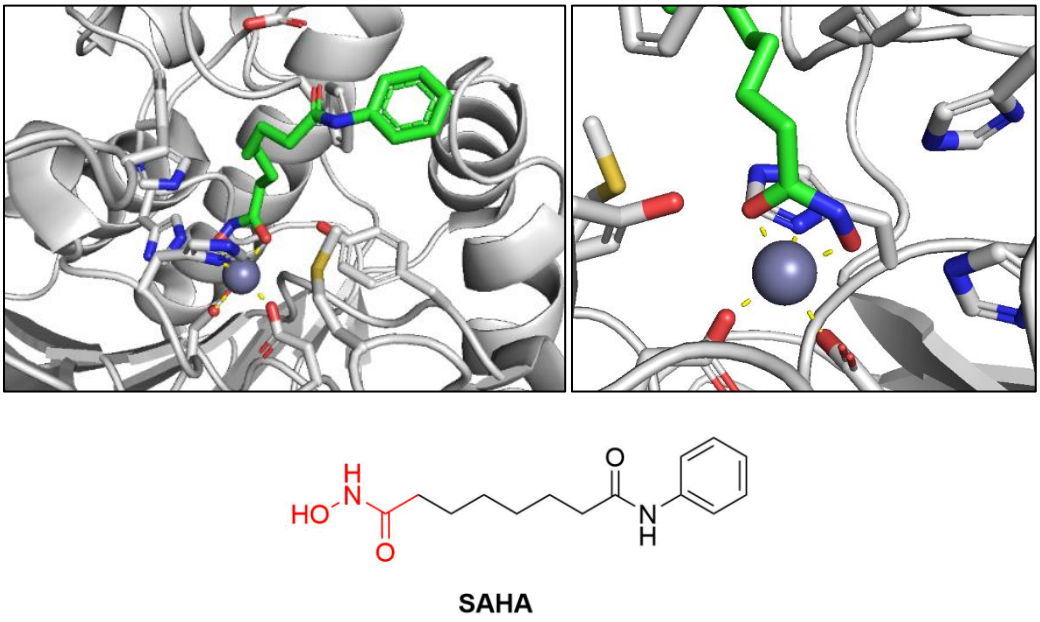

Figure 1.1. Structure of HDAC-8 with the approved inhibitor SAHA bound in the active site (*top*). The chemical structure of SAHA with the MBP highlighted in red (*bottom*). Note: metal coordination bonds are shown in yellow.

One of the more frequently utilized MBPs in metalloenzyme inhibitors is the hydroxamic acid (Figure 1.1.1).[18] Other functional groups that have been commonly used in metalloenzyme inhibitors include carboxylic acids, sulfonamides, phosphinates, 5-membered nitrogen heterocycles, and thiols.[19] More recently there has been a shift towards novel MBPs; however, there is a deficit in the understanding of the coordination chemistry of these moieties in bioinorganic systems.

1.2 FDA-Approved Metalloenzyme Inhibitors

Traditionally, FDA-approved metalloenzyme inhibitors have made use of a limited range of MBPs. Most FDA-approved therapeutics that target metalloenzymes utilize common coordination motifs such as hydroxamic acids, 5-membered heterocycles, carboxylic acids, sulfonamides, phosphinates, and thiols (Figure 1.2).[19] For example, the hydroxamic acid MBP has been widely used to target Zn^{2+}-dependent HDACs.[20] Topical antifungal inhibitors targeting Fe-dependent heme containing metalloenzymes typically utilize a nitrogen containing, 5-membered heterocycle MBP.[21-22] Carboxylic acids, thiols, and phosphinate MBPs have been used against the Zn^{2+}-dependent angiotensin converting enzyme (ACE).[3] Finally, sulfonamides have been the MBP of choice for Zn^{2+}-dependent carbonic anhydrase (CA) inhibitors.[19] Sulfonamides and heterocycles make up the two largest classes of MBPs in FDA-approved metalloenzyme inhibitors, at 30% and 37% respectively.[3] This disproportionate targeting of a select few metalloenzymes with the same MBPs has generally been a consistent phenomenon in metalloenzyme inhibition.

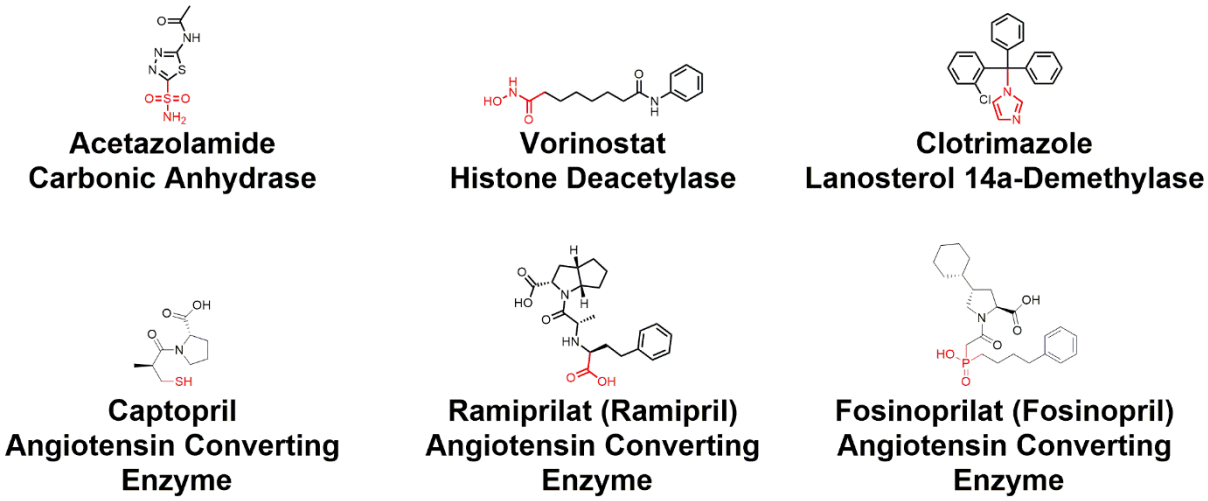

Figure 1.2. Structures of approved metalloenzyme inhibitors with MBPs being highlighted (red). Ramipril and Fosinopril are administered as prodrugs and so their respective active metabolites, ramiprilat and fosinoprilat, are shown instead.

Recently, an analysis of the approved new molecular entities (NMEs) from the FDA from 2013 to 2017 found that out of 137 NMEs approved overall, only 13 target metalloenzymes (~9.5%), of which only 9 are metal binding inhibitors (~6.6%).[3] Some recently approved NMEs that interact with the active site metal target HIV integrase (2), phosphodiesterase (1), HDACs (2), and heme containing enzymes such as lanosterol 14α-demethylase (4) (Figure 1.3).

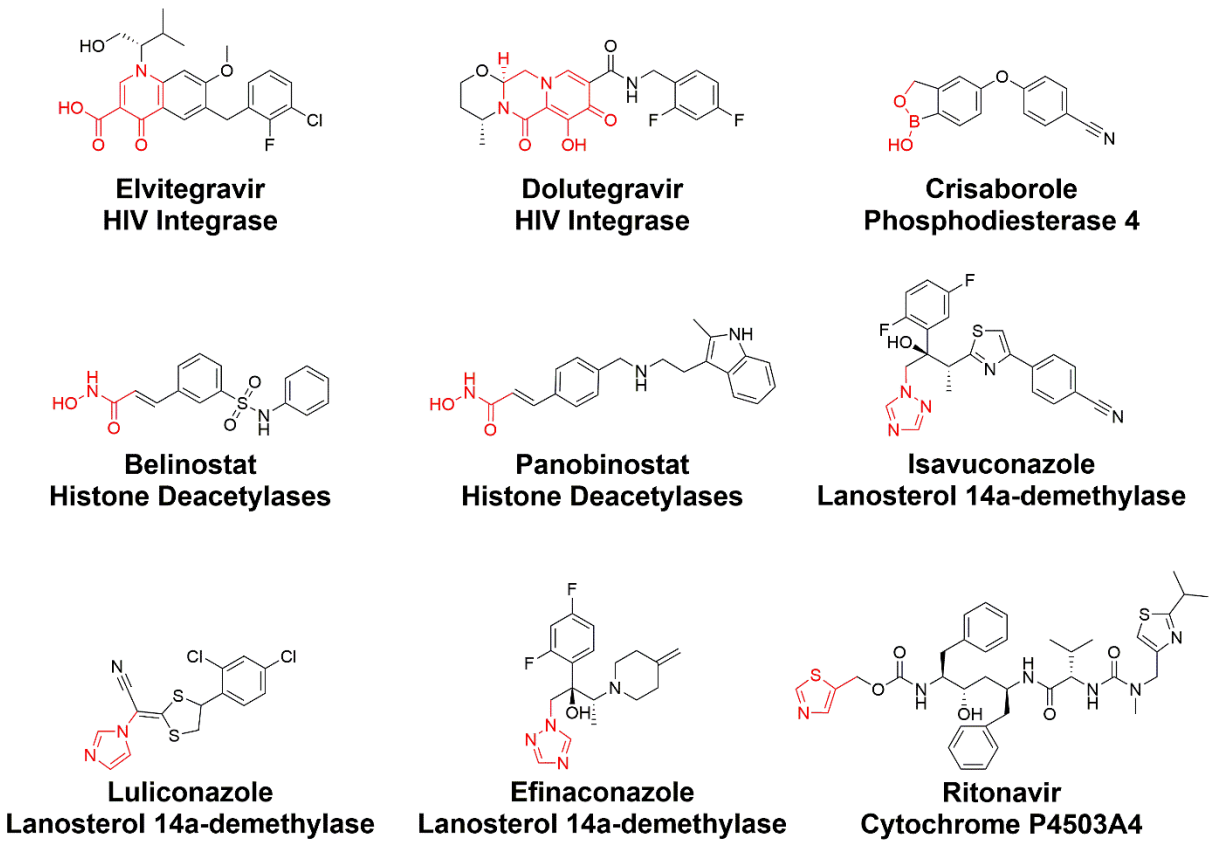

Figure 1.3. Structures of recently approved inhibitors of metalloenzymes that possess MBPs (highlighted in red) which coordinate to the active site metals of their target. These more recently approved metal binding metalloenzyme inhibitors utilize a broader range of MBPs than has been utilized in past approved inhibitors.

These recently approved metal binding metalloenzyme inhibitors have expanded the repertoire of MBPs slightly. Clinically approved metal binding HIV integrase inhibitors utilize ring-fused oxygen donor containing MBPs. This class of MBP has also been utilized by the very recently approved therapeutic, Baloxavir Marboxil, for inhibiting a key influenza enzyme endonuclease domain (see Chapter 5).[23] The recently approved inhibitor, Crisaborole, which targets phosphodiesterase utilizes a boronic acid MBP, is a leading push in the development of this MBP for clinically approved metalloenzyme inhibition.[24] For HDACs the commonly utilized hydroxamic acids are the MBP in each approved metal binding inhibitor.[20] Approved inhibitors

of lanosterol 14α-demethylase and other heme containing metalloenzymes utilize the 5-membered heterocycle MBP class including imidazole, triazole, or thiazole. While there appears to have been a more concerted effort by the medicinal chemistry community to expand the range of targeted metalloenzymes, as well as MBPs for metalloenzyme inhibition, there remains a reliance on the many of the same categories of MBPs. Thus, there is still a need for novel functional groups as MBPs for metalloenzyme inhibition.

1.3 Fragment Based Drug Discovery for Metalloenzyme Inhibitors

In drug development there are several methods for discovering molecules as inhibitors. Fragment-based drug discovery (FBDD) is one such strategy that has proved very useful for the development of biologically active compounds.[25-26] FBDD focusses on screening a library of small molecular fragments, with a molecular weight typically <300 g/mol, against a target of interest.[27] The benefits for doing so are being able to access more diverse chemical space than would be possible with larger compounds and the ability to identify specific and potent enthalpic interactions, because larger molecules may have potency due to an increased number of hydrophobic/entropic interactions which can be nonspecific. Once a fragment with inhibitory activity is identified, this fragment is elaborated synthetically to increase the observed inhibitory activity.[28] In the case of applying FBDD to metalloenzyme inhibitor development, the use of MBPs as privileged fragment scaffolds for metalloenzyme targets has been a novel application of FBDD.[29] In a true FBDD fashion, a library of MBPs (Figure 1.4) was assembled and screened in a high throughput fashion against metalloenzymes of interest. This library of MBPs focuses on enthalpic interactions with metalloenzyme active site metals via dative coordinate covalent bonds.

In addition, in each screen MBPs are organized into families containing core inorganic ligand scaffolds that allow preliminary structure activity relationships (SAR) to be determined.

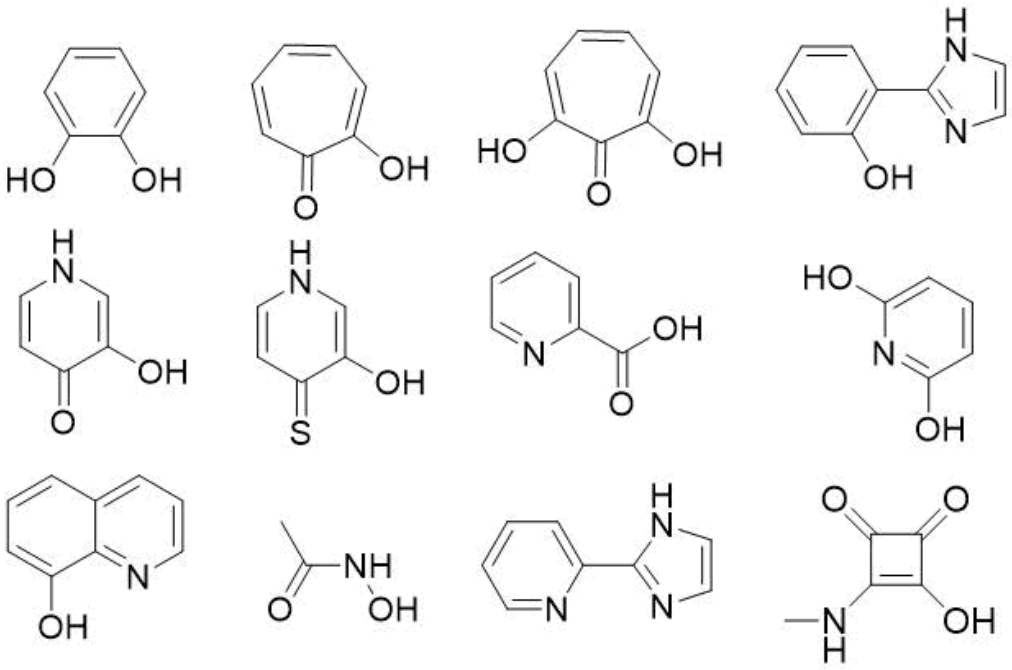

Figure 1.4. Representative showing of MBPs contained within the library, demonstrating the variety of coordination motifs that are included. The library possesses MBPs capable of monodentate and multidentate coordination to active site metal/metals.

Once an MBP with significant inhibitory activity (<100 μM) has been identified, the core scaffold is synthetically elaborated. In elaborating the MBP there are two main goals, the first being to increase potency against the target of interest via conventional ligand-protein interactions and the second being to increase selectivity for the metalloenzyme target of interest.[30-31] Additionally, elaboration of the MBP causes the fragment to favor conventional competitive inhibitory behavior over any potential metal stripping inhibition mechanism.[32] An example case of fragment elaboration of an MBP is exemplified by recent work on inhibitor development against

the influenza polymerase acidic subunit N-terminal endonuclease domain (Endo) of the RNA-dependent RNA polymerase complex.[15] In this study the allomaltol MBP core scaffold (Figure 1.5) was identified as potent fragment, as were hydroxypyridinones. Fragment elaboration strategies were employed on both scaffolds, with both synthetic elaborations vectors being merged, resulting in an inhibitor with an IC_{50} value of 14 nM.

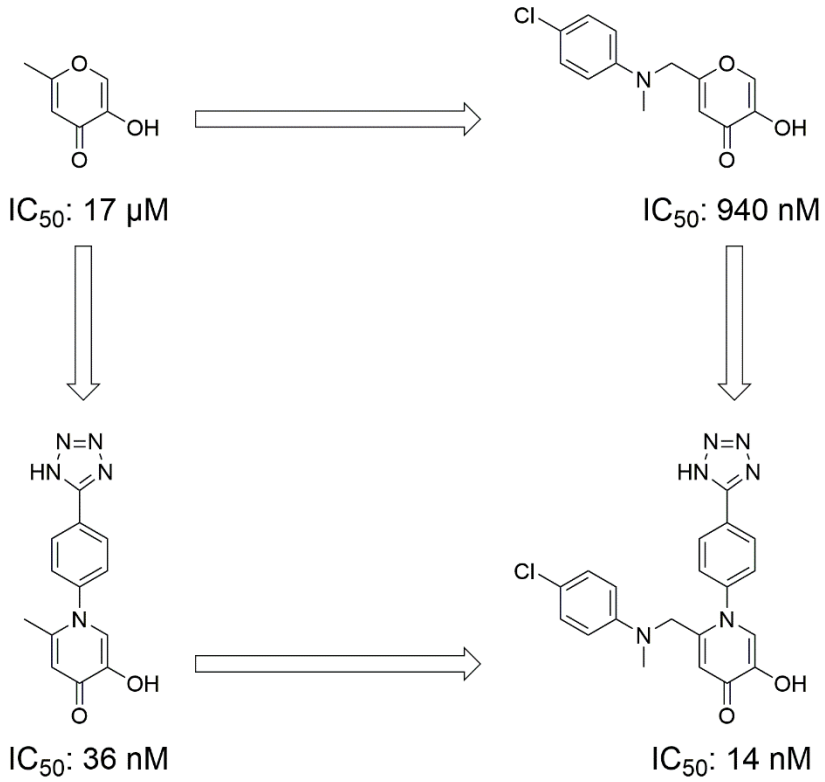

Figure 1.5. FBDD of an Endo inhibitor where two elaboration routes on an MBP (*top left*) were explored. Upon determining the most potent elaborations from each route both were merged together to produce a more active inhibitor (*bottom right*).

Another case where FBDD utilizing an MBP focused approach has been utilized is in the development of inhibitors of the metalloenzyme new delhi-metallo-β-lactamase-1 (NDM-1), a dinuclear Zn^{2+}-dependent metalloenzyme. Screening the library of MBPs resulted in dipiccolinic

acid being discovered as a potent inhibitor (Figure 1.6).[32] It was proposed that both carboxylic acids and the pyridinyl nitrogen of the MBP are all engaging in coordinative interactions with the active site metals. To further increase its inhibitory activity the MBP was elaborated at the top of the pyridine ring to increase binding affinity to the peripheral active site, yielding one of the most potent inhibitors of NDM-1 at the time.

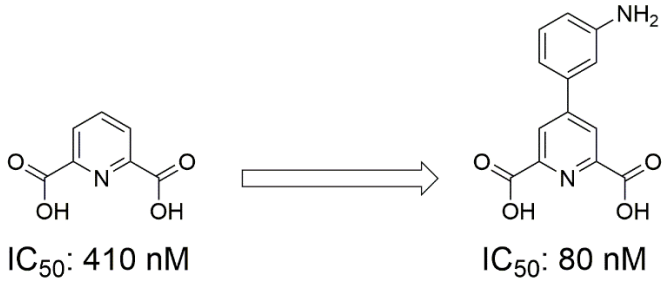

Figure 1.6. FBDD of a novel inhibitor of NDM-1 starting from a potent MBP, dipiccolinic acid (*left*) which can engage in multiple interactions with the active site Zn^{2+} atoms. The addition of an aniline substituent improved inhibitory activity significantly (*right*) and was suspected to be interacting with an active site loop.[32]

Although this leading inhibitor of NDM-1 presents a major advancement in medicinal chemistry space of this target, its activity is predominantly dependent on the carboxylic acid coordinating functional groups. Carboxylic acids, while a widely utilized functional group in the approved drug chemical space, can be problematic for drug development.[33] Another coordinatively strong functional group that has been utilized for metalloenzyme FBDD inhibitor development are thiols/thiones.[34-35] While thiol containing metalloenzyme inhibitors possess strong coordination preferences, they are not without biological liabilities.[36] Both functional groups are useful for metalloenzyme inhibitor development but they can present liabilities for

further drug development.[33, 37] In these cases problematic atoms/groups are either masked via a prodrug moiety or replaced with a similar but different moiety.

1.4 Bioisosteres in Medicinal Chemistry

The concept of replacing an atom or group of atoms for another atom or group with similar properties has been around for over a century.[38] Initially these replacements were defined as being isosteric when the replacements had the same number of electrons. This classification was extended more broadly to refer to the peripheral layer (valence) electrons.[39] Later on this concept was applied to molecules with biological activity leading to the creation of the definition of bioisosteres, molecules that elicit a similar biological effect while fitting the concept of an isostere in the broadest sense.[40] More recently bioisosteres have been expanded to cover "*compounds or groups that possess near-equal molecular shapes and volumes, approximately the same distribution of electrons, and which exhibit similar physical properties*".[41]

In medicinal chemistry, specifically the drug development process, certain moieties present in a potential clinical candidate may be a liability upon introduction into a multicellular organism. Using isosteres (the term "isosteres" is used here-in to include classical isosteres and bioisosteres) to replace functional groups that produce liabilities, is a core concept in modern medicinal chemistry and critical for advancing lead compounds to clinically effective therapeutics.[42] Some issues that isostere replacement can resolve include metabolic instability, poor solubility, low permeability, or even toxicity.[43] A functional group that this technique has been the focus of a significant amount is carboxylic acids.[33] An example where a carboxylic acid has been successfully replaced is in the development of the antihypertensive drug losartan (Figure 1.7).[44]

Initially the carboxylic acid derivative had problems displaying efficacy in in-vivo models but upon replacement of the carboxylic acid for a similarly acidic isosteric tetrazole moiety lead to a significant increase in lipophilicity and in-vivo potency (11 mg/kg to 0.6 mg/kg).

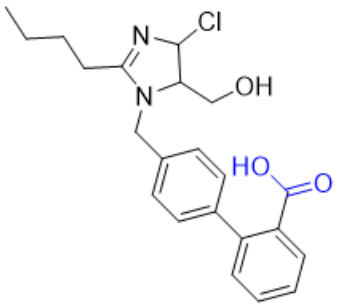

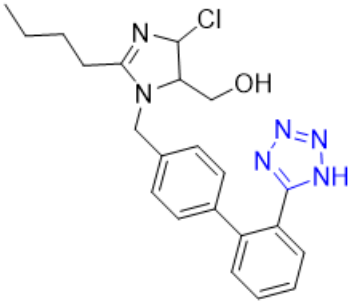

	EXP7711	Losartan
pK_a	4.5	5.0
LogP	1.2	4.5
ED_{30} (mg/kg)	11	0.6

Figure 1.7. In a successful utility of isostere replacement, the clinical candidate EXP7711 upon replacing the carboxylic acid for a tetrazole significantly improved the lipophilicity of the candidate and in-vivo activity, while retaining a similar acidity of the replaced functional group (in blue).

The tetrazole functional group has a long history of being a common carboxylic acid isostere but more recently there has been a significant push to develop a broader repertoire of carboxylic acid isosteric functional groups. A recent review by Ballatore et al. binned carboxylic acid isosteres into two classes, acyclic and cyclic (Figure 1.8).[45] All the presented isosteres in some way mimic the ability of a carboxylic acid to engage in polar interactions such as hydrogen bonding interactions or electrostatic interactions. More recently in an extremely valuable study

Ballatore et al. analyzed the changes of 35 carboxylic acid isostere replacements on the same phenyl propionic scaffold.[46] This study provided an assessment of how a significant number of replacements affect physicochemical relevant properties on the same scaffold.

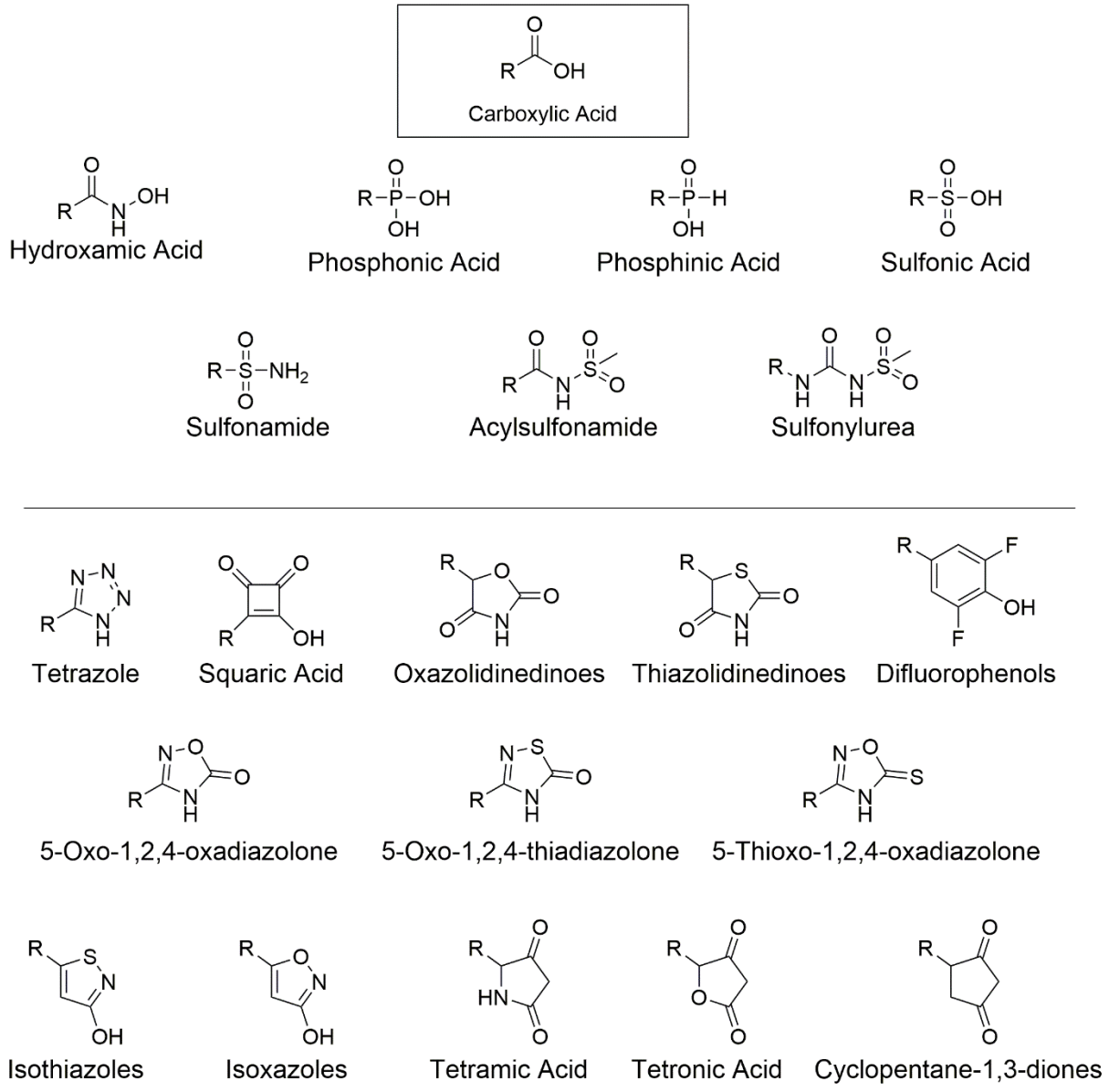

Figure 1.8. Representative examples of acyclic (*top*) and cyclic (*bottom*) carboxylic acid isosteres, adapted from Ballatore et al.[45]

In metalloenzyme inhibitors, carboxylic acids are a common moiety present in MBPs.[3] Additionally, once a coordination motif is identified there is typically significantly less if at all any optimization to the core MBP relative to the synthetic elaborations off the scaffold. As discussed preciously there has not been a widespread usage of alternative coordinating groups, so not too surprisingly carboxylic acid isostere replacement offers many alternative coordinating motifs that could be explored and have been utilized in other areas of medicinal chemistry. However, as with any modification or novel coordinating motif the coordination behavior can change dramatically. The best methods to assess and understand any changes are structural studies allowing direct elucidation of binding modes.

1.5 Model Bioinorganic Systems

As a concept, model compounds can serve as a simplified approximation of a complex biological system. In bioinorganic chemistry, the use of model coordination complexes as an approximate metalloenzyme active site has a long history of being utilized to study diverse metalloenzymes from dioxygen activating to Zn^{2+} dependent metalloenzymes.[47-49] In the case of mononuclear Zn^{2+}-dependent metalloenzymes tetrahedral coordination geometry around the active site metal is more energetically preferred and subsequently the most common.[50] In this geometry three coordination sites are typically occupied by protein residues and the fourth site is occupied by a water molecule. Therefore, model complexes which reproduce this active site tetrahedral geometry have been the focus of study for Zn^{2+}-dependent metalloenzymes, in particular tripodal or scorpionate ligands having been utilized extensively.[48]

In metalloenzyme active sites there are a variety of combinations of coordinating residues that have been observed. Common coordinating residues include neutral ligands such as histidine (imidazole) and anionic residues such as aspartic/glutamic acid (carboxylic acid) and cysteine/serine (thiol/hydroxyl).[4] Tripodal model complexes have tried to reproduce the coordination geometry of various combinations such as tris-histidine as well as other combinations of coordination residue motifs.[48] Additionally the charge state of tripodal ligand scaffold can be different even though they are reproducing the same Zn^{2+} active site binding motif, as is the case with the respective Zn^{2+}(OH) complexes of $Tp^{Ph,Me}$ ($Tp^{Ph,Me}$ = hydrotris(5,3-methylphenylpyrazolyl)borate) and tris(imidazolyl)phosphine ligands which are monoanionic and neutral ligands, respectively.[51-52] One area that model complexes have been used to study metalloenzyme active sites is with metalloenzyme inhibitors.

The $Tp^{Ph,Me}$Zn model system has been utilized as a structural model system to elucidate metalloenzyme active site metal-MBP interactions.[53-54] Because this model system is an approximation of Zn^{2+} tris-histidine active sites it mimics those of human carbonic anhydrase II (hCAII), matrix metalloproteases (MMPs), and others. Additionally, the scaffold readily forms complexes with monoanionic MBPs resulting in an overall neutral complex that is easily crystallized for X-ray diffraction studies. A range of MBPs with different coordinating atom donor sets have been investigated in order to understand their coordination in bioinorganic systems including acetohydroxamic acid, thiomaltol, and picolinic acid (Figure 1.9).[53, 55-56] From the structures of these complexes the coordination behavior of various MBPs can be elucidated in a model environment. Therefore, bioinorganic model systems are a sufficient approximation of the first coordination sphere of bioinorganic systems and exhibit how MBPs may bind in metalloenzyme active sites.

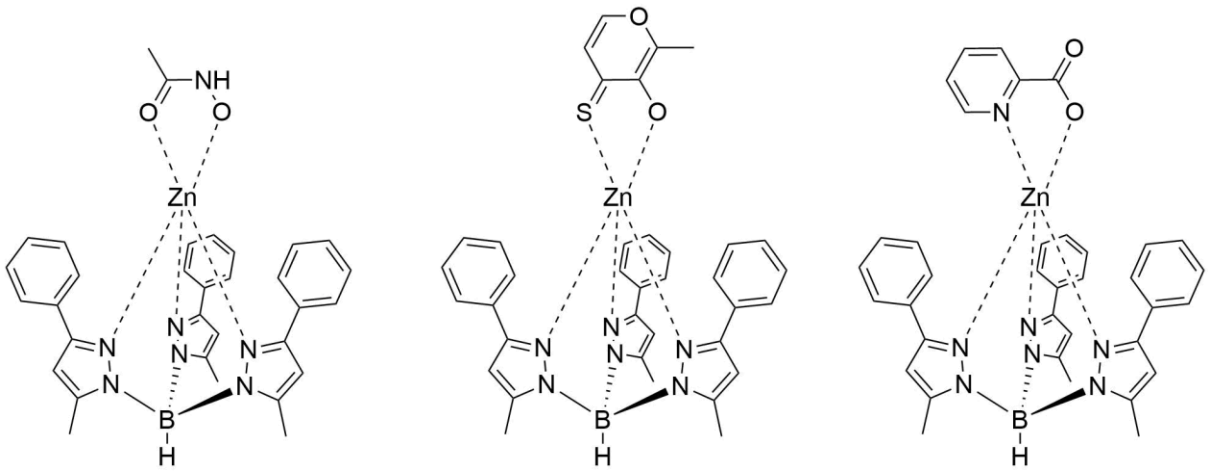

Figure 1.9. Structures of $Tp^{Ph,Me}Zn$(MBP) model complexes acetohydroxamic acid (*left*), thiomaltol (*middle*), and picolinic acid (*right*). Each complexed MBP exhibited bidentate coordination to the Zn^{2+}. Coordination bonds are shown as dashed lines.

While bioinorganic model systems can reproduce the first coordination sphere of metalloenzyme active sites they are still just simplified versions. Specifically, second coordination sphere affects are not as significant or non-existent in model complexes. In a comparison of a bidentate MBP (thiomaltol) binding to the $Tp^{Ph,Me}Zn$ model complex and hCAII, the observed modes of binding to the hCAII active site Zn^{2+} was significantly influenced by the active site architecture (sterics, hydrophobic interactions, and hydrogen bonding).[57] Additionally hCAII has proved a reliable model system in and of itself to study MBP-metalloenzyme interactions such as changing coordinating active site residues as well as MBP substituents on MBP modes of binding.[58-59] While hCAII is a more complicated system to study MBP-metalloenzyme interactions than the $Tp^{Ph,Me}Zn$ model complex, both are still useful models that provide structural and coordination behavior information in the absence of other structural data. Typically, in metalloenzyme inhibition changes to an MBP can lead to changes in coordination mode to the active site metal/metals. Because structural characterization of an inhibitor-enzyme complex may

not be possible, or if there are a significant number of derivatives, model complexes provide a reasonable alternative to provide structural data.

1.6 Scope of this Dissertation

This dissertation will discuss efforts to develop and understand the application of isostere replacement to MBPs. Chapter 2 describes the effect of donor atom identity on MBP coordination to the model system hCAII. Upon introduction of changes to the architecture of the metalloenzyme active site significant deviations in coordinative behavior were observed based on the coordinating atoms.

Chapter 3 describes the application of carboxylic acid isostere replacement to MBPs. By applying isostere replacement to a simple MBP scaffold, picolinic acid (pyridine-2-carboxylic acid), a new series of compounds named metal-binding isosteres (MBIs) of picolinic acid were obtained. These compounds retain the coordinative behavior of the original MBP, change the physicochemical properties, and broadly retain inhibitory activity, thus allowing for a way to tune the properties of MBPs against a target of interest.

Chapter 4 describes the study of MBIs on more complex heterocyclic scaffolds. A series of various carboxylic acid-nitrogen containing heterocycle scaffolds with differing heteroatom content and arrangement were studied. By performing isostere replacement on each MBP and generation of the respective MBIs, changes on coordination behavior were observed that were dependent on the scaffold heteroatom content and arrangement within the heterocycle.

Chapter 5 describes structural biology efforts to understand the optimization of an MBP fragment against Endo. Crystal structures of lead inhibitor candidates provided valuable information that was used to improve an MBP through scaffold modification and isostere

replacement. Changes in activity were rationalized through changes in coordination and electronics.

1.7 Acknowledgements

Select content in Chapter 1 is adapted from "Targeting Metalloenzymes for Therapeutic Intervention" Allie Y. Chen*, Rebecca N. Adamek*, Benjamin L. Dick, Cy V. Credille, Christine N. Morrison, and Seth M. Cohen. *Chem. Rev.* 2019, *119*, 2, 1323-1455. The dissertation author was an author of this paper and gratefully acknowledges the contributions of coauthors Allie Y. Chen, Rebecca N. Adamek, Cy V. Credille, Christine N. Morrison, and Seth M. Cohen. The permission to reproduce this paper was granted by the American Chemical Society. Copyright 2019, American Chemical Society.

1.8 References

1. Andreini, C.; Bertini, I.; Cavallaro, G.; Holliday, G. L.; Thornton, J. M., Metal ions in biological catalysis: from enzyme databases to general principles. *J. Biol. Inorg. Chem.* **2008,** *13* (8), 1205-18.

2. Waldron, K. J.; Rutherford, J. C.; Ford, D.; Robinson, N. J., Metalloproteins and metal sensing. *Nature* **2009,** *460* (7257), 823-30.

3. Chen, A. Y.; Adamek, R. N.; Dick, B. L.; Credille, C. V.; Morrison, C. N.; Cohen, S. M., Targeting Metalloenzymes for Therapeutic Intervention. *Chem. Rev.* **2019,** *119* (2), 1323-1455.

4. Holm, R. H.; Kennepohl, P.; Solomon, E. I., Structural and Functional Aspects of Metal Sites in Biology. *Chem. Rev.* **1996,** *96* (7), 2239-2314.

5. Fernandes, H. S.; Teixeira, C. S. S.; Sousa, S. F.; Cerqueira, N. M. F. S. A., Formation of Unstable and very Reactive Chemical Species Catalyzed by Metalloenzymes: A Mechanistic Overview. *Molecules* **2019,** *24* (13).

6. Malmstrom, B. G.; Neilands, J. B., Metalloproteins. *Annu. Rev. Biochem.* **1964,** *33*, 331-54.

7. Solomon, E. I.; Augustine, A. J.; Yoon, J., O2 reduction to H2O by the multicopper oxidases. *Dalton Trans.* **2008,** (30), 3921-32.

8. Al-Attar, S.; de Vries, S., Energy transduction by respiratory metallo-enzymes: From molecular mechanism to cell physiology. *Coord. Chem. Rev.* **2013,** *257* (1), 64-80.

9. Rees, D. C.; Akif Tezcan, F.; Haynes, C. A.; Walton, M. Y.; Andrade, S.; Einsle, O.; Howard, J. B., Structural basis of biological nitrogen fixation. *Philos. Trans. R. Soc., A* **2005,** *363* (1829), 971-84; discussion 1035-40.

10. Sin, N.; Meng, L.; Wang, M. Q.; Wen, J. J.; Bornmann, W. G.; Crews, C. M., The anti-angiogenic agent fumagillin covalently binds and inhibits the methionine aminopeptidase, MetAP-2. *Proc. Natl. Acad. Sci. U. S. A.* **1997,** *94* (12), 6099-103.

11. Williams, R. t.; Lim, J. E.; Harr, B.; Wing, C.; Walters, R.; Distler, M. G.; Teschke, M.; Wu, C.; Wiltshire, T.; Su, A. I.; Sokoloff, G.; Tarantino, L. M.; Borevitz, J. O.; Palmer, A. A., A common and unstable copy number variant is associated with differences in Glo1 expression and anxiety-like behavior. *PLoS One* **2009,** *4* (3), e4649.

12. Hovatta, I.; Tennant, R. S.; Helton, R.; Marr, R. A.; Singer, O.; Redwine, J. M.; Ellison, J. A.; Schadt, E. E.; Verma, I. M.; Lockhart, D. J.; Barlow, C., Glyoxalase 1 and glutathione reductase 1 regulate anxiety in mice. *Nature* **2005,** *438* (7068), 662-6.

13. Dias, A.; Bouvier, D.; Crepin, T.; McCarthy, A. A.; Hart, D. J.; Baudin, F.; Cusack, S.; Ruigrok, R. W., The cap-snatching endonuclease of influenza virus polymerase resides in the PA subunit. *Nature* **2009,** *458* (7240), 914-8.

14. Metalloprotein Inhibitors. In *Ligand Design in Medicinal Inorganic Chemistry*, pp 375-403.

15. Credille, C. V.; Chen, Y.; Cohen, S. M., Fragment-Based Identification of Influenza Endonuclease Inhibitors. *J. Med. Chem.* **2016,** *59* (13), 6444-54.

16. Nunez, S.; Venhorst, J.; Kruse, C. G., Target-drug interactions: first principles and their application to drug discovery. *Drug Discov. Today* **2012,** *17* (1-2), 10-22.

17. Somoza, J. R.; Skene, R. J.; Katz, B. A.; Mol, C.; Ho, J. D.; Jennings, A. J.; Luong, C.; Arvai, A.; Buggy, J. J.; Chi, E.; Tang, J.; Sang, B. C.; Verner, E.; Wynands, R.; Leahy, E. M.; Dougan, D. R.; Snell, G.; Navre, M.; Knuth, M. W.; Swanson, R. V.; McRee, D. E.; Tari, L. W., Structural snapshots of human HDAC8 provide insights into the class I histone deacetylases. *Structure* **2004,** *12* (7), 1325-1334.

18. Cohen, S. M., A Bioinorganic Approach to Fragment-Based Drug Discovery Targeting Metalloenzymes. *Acc. Chem. Res.* **2017,** *50* (8), 2007-2016.

19. Yang, Y.; Hu, X. Q.; Li, Q. S.; Zhang, X. X.; Ruan, B. F.; Xu, J.; Liao, C., Metalloprotein Inhibitors for the Treatment of Human Diseases. *Curr. Top. Med. Chem.* **2016,** *16* (4), 384-96.

20. Yoon, S.; Eom, G. H., HDAC and HDAC Inhibitor: From Cancer to Cardiovascular Diseases. *Chonnam Med. J.* **2016,** *52* (1), 1-11.

21. Allen, D.; Wilson, D.; Drew, R.; Perfect, J., Azole antifungals: 35 years of invasive fungal infection management. *Expert Rev. Anti-Infect. Ther.* **2015,** *13* (6), 787-98.

22. Ngo, H. X.; Garneau-Tsodikova, S.; Green, K. D., A complex game of hide and seek: the search for new antifungals. *MedChemComm* **2016,** *7* (7), 1285-1306.

23. Hayden, F. G.; Sugaya, N.; Hirotsu, N.; Lee, N.; de Jong, M. D.; Hurt, A. C.; Ishida, T.; Sekino, H.; Yamada, K.; Portsmouth, S.; Kawaguchi, K.; Shishido, T.; Arai, M.; Tsuchiya, K.; Uehara, T.; Watanabe, A.; Baloxavir Marboxil Investigators, G., Baloxavir Marboxil for Uncomplicated Influenza in Adults and Adolescents. *N. Engl. J. Med.* **2018,** *379* (10), 913-923.

24. Akama, T.; Baker, S. J.; Zhang, Y. K.; Hernandez, V.; Zhou, H. C.; Sanders, V.; Freund, Y.; Kimura, R.; Maples, K. R.; Plattner, J. J., Discovery and structure-activity study of a novel benzoxaborole anti-inflammatory agent (AN2728) for the potential topical treatment of psoriasis and atopic dermatitis. *Bioorg. Med. Chem. Lett.* **2009,** *19* (8), 2129-2132.

25. Erlanson, D. A.; Fesik, S. W.; Hubbard, R. E.; Jahnke, W.; Jhoti, H., Twenty years on: the impact of fragments on drug discovery. *Nat Rev Drug Discov* **2016,** *15* (9), 605-19.

26. Shuker, S. B.; Hajduk, P. J.; Meadows, R. P.; Fesik, S. W., Discovering high-affinity ligands for proteins: SAR by NMR. *Science* **1996,** *274* (5292), 1531-4.

27. Congreve, M.; Carr, R.; Murray, C.; Jhoti, H., A 'rule of three' for fragment-based lead discovery? *Drug Discov. Today* **2003,** *8* (19), 876-7.

28. Scott, D. E.; Coyne, A. G.; Hudson, S. A.; Abell, C., Fragment-based approaches in drug discovery and chemical biology. *Biochemistry* **2012,** *51* (25), 4990-5003.

29. Jacobsen, J. A.; Fullagar, J. L.; Miller, M. T.; Cohen, S. M., Identifying Chelators for Metalloprotein Inhibitors Using a Fragment-Based Approach. *J. Med. Chem.* **2011,** *54* (2), 591-602.

30. Garner, A. L.; Struss, A. K.; Fullagar, J. L.; Agrawal, A.; Moreno, A. Y.; Cohen, S. M.; Janda, K. D., 3-Hydroxy-1-alkyl-2-methylpyridine-4(1H)-thiones: Inhibition of the Pseudomonas aeruginosa Virulence Factor LasB. *ACS Med. Chem. Lett.* **2012,** *3* (8), 668-672.

31. Garner, A. L.; Fullagar, J. L.; Day, J. A.; Cohen, S. M.; Janda, K. D., Development of a High-Throughput Screen and Its Use in the Discovery of Streptococcus pneumoniae Immunoglobulin A1 Protease Inhibitors. *J. Am. Chem. Soc.* **2013,** *135* (27), 10014-10017.

32. Chen, A. Y.; Thomas, P. W.; Stewart, A. C.; Bergstrom, A.; Cheng, Z.; Miller, C.; Bethel, C. R.; Marshall, S. H.; Credille, C. V.; Riley, C. L.; Page, R. C.; Bonomo, R. A.; Crowder, M. W.; Tierney, D. L.; Fast, W.; Cohen, S. M., Dipicolinic Acid Derivatives as Inhibitors of New Delhi Metallo-beta-lactamase-1. *J. Med. Chem.* **2017,** *60* (17), 7267-7283.

33. Kalgutkar, A. S.; Scott Daniels, J., Chapter 3 Carboxylic Acids and their Bioisosteres. In *Metabolism, Pharmacokinetics and Toxicity of Functional Groups: Impact of Chemical Building Blocks on ADMET*, The Royal Society of Chemistry: 2010; pp 99-167.

34. Perez, C.; Li, J.; Parlati, F.; Rouffet, M.; Ma, Y.; Mackinnon, A. L.; Chou, T. F.; Deshaies, R. J.; Cohen, S. M., Discovery of an Inhibitor of the Proteasome Subunit Rpn11. *J. Med. Chem.* **2017,** *60* (4), 1343-1361.

35. Agrawal, A.; de Oliveira, C. A.; Cheng, Y.; Jacobsen, J. A.; McCammon, J. A.; Cohen, S. M., Thioamide hydroxypyrothiones supersede amide hydroxypyrothiones in potency against anthrax lethal factor. *J. Med. Chem.* **2009,** *52* (4), 1063-74.

36. Gavras, H.; Gavras, I., Angiotensin Converting Enzyme-Inhibitors - Properties and Side-Effects. *Hypertension* **1988,** *11* (3), S37-S41.

37. Lin, J. H.; Lu, A. Y., Role of pharmacokinetics and metabolism in drug discovery and development. *Pharmacol. Rev.* **1997,** *49* (4), 403-49.

38. Langmuir, I., ISOMORPHISM, ISOSTERISM AND COVALENCE. *J. Am. Chem. Soc.* **1919,** *41* (10), 1543-1559.

39. Erlenmeyer, H.; Leo, M., Über Pseudoatome. *Helv. Chim. Acta* **1932,** *15* (1), 1171-1186.

40. Friedman, H. L., Influence of Isosteric Replacements Upon Biological Activity. *Natl. Acad. Sci.* **1951,** *206*, 295-362.

41. Burger, A., Isosterism and bioisosterism in drug design. *Prog. Drug Res.* **1991,** *37*, 287-371.

42. Meanwell, N. A., Synopsis of Some Recent Tactical Application of Bioisosteres in Drug Design. *J. Med. Chem.* **2011,** *54* (8), 2529-2591.

43. Patani, G. A.; LaVoie, E. J., Bioisosterism: A Rational Approach in Drug Design. *Chem. Rev.* **1996,** *96* (8), 3147-3176.

44. Carini, D. J.; Duncia, J. V.; Aldrich, P. E.; Chiu, A. T.; Johnson, A. L.; Pierce, M. E.; Price, W. A.; Santella, J. B., 3rd; Wells, G. J.; Wexler, R. R.; et al., Nonpeptide angiotensin II receptor antagonists: the discovery of a series of N-(biphenylylmethyl)imidazoles as potent, orally active antihypertensives. *J. Med. Chem.* **1991,** *34* (8), 2525-47.

45. Ballatore, C.; Huryn, D. M.; Smith, A. B., 3rd, Carboxylic acid (bio)isosteres in drug design. *ChemMedChem* **2013,** *8* (3), 385-95.

46. Lassalas, P.; Gay, B.; Lasfargeas, C.; James, M. J.; Tran, V.; Vijayendran, K. G.; Brunden, K. R.; Kozlowski, M. C.; Thomas, C. J.; Smith, A. B.; Huryn, D. M.; Ballatore, C., Structure Property Relationships of Carboxylic Acid Isosteres. *J. Med. Chem.* **2016,** *59* (7), 3183-3203.

47. Vahrenkamp, H., Transitions, transition states, transition state analogues: Zinc pyrazolylborate chemistry related to zinc enzymes. *Acc. Chem. Res.* **1999,** *32* (7), 589-596.

48. Parkin, G., The bioinorganic chemistry of zinc: synthetic analogues of zinc enzymes that feature tripodal ligands. *Chem. Commun.* **2000,** (20), 1971-1985.

49. Liang, H. C.; Dahan, M.; Karlin, K. D., Dioxygen-activating bio-inorganic model complexes. *Curr. Opin. Chem. Biol.* **1999,** *3* (2), 168-175.

50. Dudev, T.; Lim, C., Tetrahedral vs octahedral zinc complexes with ligands of biological interest: A DFT/CDM study. *J. Am. Chem. Soc.* **2000,** *122* (45), 11146-11153.

51. Kimblin, C.; Parkin, G., Comparison of Zinc and Cadmium Coordination Environments in Synthetic Analogues of Carbonic Anhydrase: Synthesis and Structure of {[Pim(Pr)()i(,Bu)()t]Cd(OH(2))(OClO(3))}(ClO(4)). *Inorg. Chem.* **1996,** *35* (24), 6912-6913.

52. Puerta, D. T.; Cohen, S. M., [(TpMe,Ph)2Zn2(H3O2)]ClO4: a new H3O2 species relevant to zinc proteinases. *Inorg. Chim. Acta* **2002,** *337*, 459-462.

53. Puerta, D. T.; Cohen, S. M., Elucidating drug-metalloprotein interactions with tris(pyrazolyl)borate model complexes. *Inorg. Chem.* **2002,** *41* (20), 5075-82.

54. Puerta, D. T.; Cohen, S. M., Examination of novel zinc-binding groups for use in matrix metalloproteinase inhibitors. *Inorg. Chem.* **2003,** *42* (11), 3423-30.

55. Jacobsen, F. E.; Lewis, J. A.; Cohen, S. M., A New Role for Old Ligands: Discerning Chelators for Zinc Metalloproteinases. *J. Am. Chem. Soc.* **2006,** *128* (10), 3156-3157.

56. Puerta, D. T.; Lewis, J. A.; Cohen, S. M., New beginnings for matrix metalloproteinase inhibitors: identification of high-affinity zinc-binding groups. *J. Am. Chem. Soc.* **2004,** *126* (27), 8388-9.

57. Martin, D. P.; Blachly, P. G.; Marts, A. R.; Woodruff, T. M.; de Oliveira, C. A.; McCammon, J. A.; Tierney, D. L.; Cohen, S. M., 'Unconventional' coordination chemistry by metal chelating fragments in a metalloprotein active site. *J. Am. Chem. Soc.* **2014,** *136* (14), 5400-6.

58. Martin, D. P.; Blachly, P. G.; McCammon, J. A.; Cohen, S. M., Exploring the influence of the protein environment on metal-binding pharmacophores. *J. Med. Chem.* **2014,** *57* (16), 7126-35.

59. Martin, D. P.; Hann, Z. S.; Cohen, S. M., Metalloprotein-inhibitor binding: human carbonic anhydrase II as a model for probing metal-ligand interactions in a metalloprotein active site. *Inorg. Chem.* **2013,** *52* (21), 12207-15.

Chapter 2: Effect of Donor Atom Identity on Metal-Binding Pharmacophore Coordination

2.1 Introduction

As discussed in Chapter 1, model complexes have often been used to interrogate the influence of the active site environment on MBP coordination.[1-2] Despite major advances in their development in mimicking the coordinating residues and the first coordination sphere of an active site, model complexes still struggle to mimic the nuanced details of the second coordination sphere of a metalloenzyme active site.[3] These key second coordination sphere interactions can have a significant impact on MBP/inhibitor binding. Important second coordination sphere interactions that control selectivity include sterics, hydrogen bonding, and electrostatics. These interactions may force MBPs to coordinate to the metal center in a non-idealized, distorted geometries relative to model complexes.

Our group previously highlighted the differences between predicted and observed MBP binding based on model complexes and MBP binding in a metalloenzyme active site. This was achieved by comparing the binding of various MBPs to human carbonic anhydrase II (hCAII) and a Zn^{2+} model complex that employed a (hydrotris(5,3-methylphenylpyrazolyl)borate) ligand ($Tp^{Ph,Me}$).[1, 4-5] Although the primary coordination spheres provided by hCAII and $Tp^{Ph,Me}$ are similar, the $Tp^{Ph,Me}$ model lacks the second coordination sphere nuances of hCAII. The influences of the second coordination sphere were made apparent by analyzing the structure of the MBPs 1-hydroxypyridine-2(1*H*)-thione (1,2-HOPTO) and 3-hydroxy-2-methyl-4*H*-pyran-4-thione (thiomaltol) when bound to [($Tp^{Ph,Me}$)Zn(MBP)] versus hCAII-MBP. The [($Tp^{Ph,Me}$)Zn(MBP)] complexes showed bidentate coordination with coordination dihedral angles near 180° (Figure 2.1). In contrast, the complex of 1,2-HOPTO with hCAII showed bidentate binding as well, but with a highly distorted, non-ideal dihedral angle of ~130° (Figure 2.1). The thiomaltol model complex [($Tp^{Ph,Me}$)Zn(thiomaltol)] was similar to that observed with 1,2-HOPTO, but when bound to hCAII,

the thiomaltol complex deviated even more dramatically, displaying monodentate coordination to the Zn^{2+} ion via only the sulfur donor atom, as well as a compressed dihedral angle <180°. From the differences in MBP binding to the $Tp^{Ph,Me}$ complex and hCAII it was determined that the active site pocket and steric influences had a major influence on MBP binding. To understand the observed deviations between the MBP-model complexes and the corresponding hCAII-MBP complexes, density functional theory (DFT) calculations were performed utilizing the [($Tp^{Ph,Me}$)Zn(MBP)] complexes. The DFT calculations demonstrated that MBP coordination with a larger dihedral angle was energetically favorable as was bidentate coordination (as opposed to the monodentate coordination observed with thiomaltol-hCAII). The computational results provided further support for the significant influence the second coordination sphere has on the coordination geometries of MBPs to metalloenzymes.

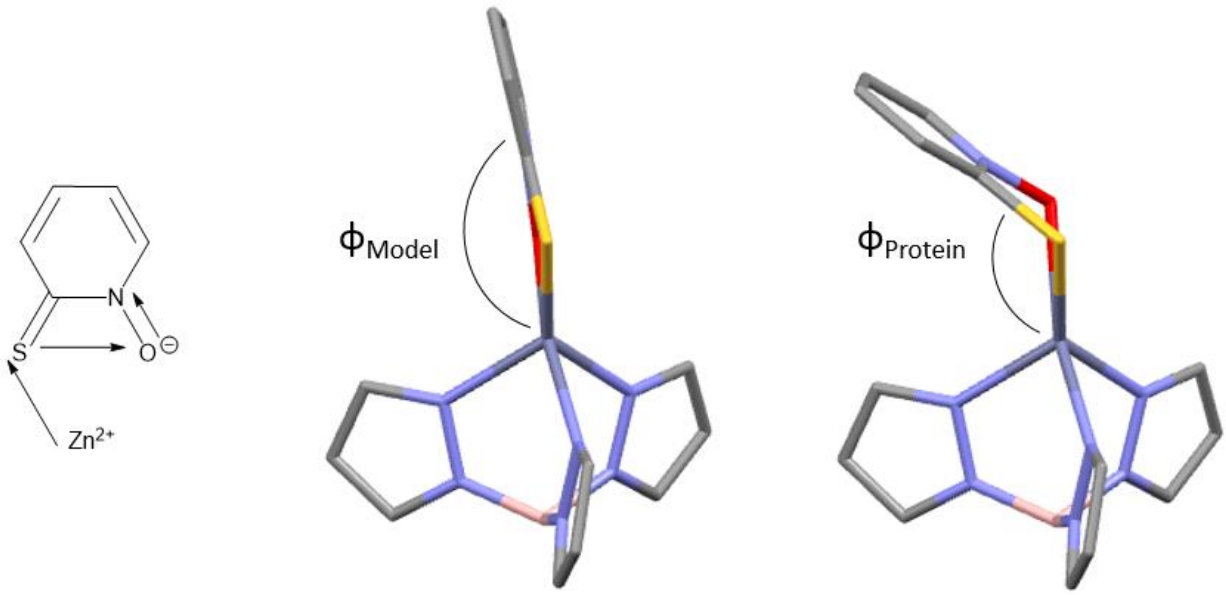

Figure 2.1. The angle φ is illustrated in this image with 1,2-HOPTO binding to Zn^{2+} (*left*), as the Zn^{2+}-S-O-N dihedral angle, which represents the degree of ring canting observed when MBP binds the active site Zn^{2+}. The differences in MBP binding mode between a [($Tp^{Ph,Me}$)Zn(1,2-HOPTO)] model complex (*middle*) and the protein hCAII-1,2-HOPTO (*right*) is apparent for this MBP. Adapted from reference.[5] Color scheme: carbon = gray, sulfur = yellow, oxygen = red, nitrogen = blue, boron = pink, and zinc = teal.

In this chapter, to further probe the influence of protein active sites on observed binding geometry, particularly steric influences, a mutation that decreases the steric influence of the hCAII active site was investigated. A previous study on L198 mutants of hCAII revealed that the polarity of residue 198 modulated the inhibitory activities of the known hCAII inhibitors, acetazolamide and dansylamide.[6] From the results of this study and the location of residue 198 in the active site, it was hypothesized that a L198G mutation would decrease the steric congestion of the active, allowing MBPs to form less distorted complexes with hCAII L198G. Therefore, using the hCAII L198G mutant, we probed the effects of decreased steric pressure on the selectivity and binding mode of several MBPs to hCAII versus hCAII L198G by screening a library of MBP fragments and crystallizing select hCAII-MBP complexes to determine their mode of binding. The results

reveal that the binding of an MBP in a metalloenzyme active site depends on the size and shape of the active site, the active site residues, and on the identity of the donor atoms of the MBP that are coordinated to the active site metal ion. Additionally, DFT calculations were performed in order to estimate the energetic costs for differences in dihedral angle and coordination geometry for the observed complexes.

2.2 hCAII and hCAII L198G Inhibition

To determine inhibition activity of MBPs against hCAII and hCAII L198G, both enzymes were screened against a library of approximately 250 MBP fragments, which was an expansion of a previous compound library.[7] Percent inhibition values from a MBP library screen at fragment concentration of 500 μM revealed that most MBPs exhibited greater activity against the L198G mutant when compared to wild type hCAII. Although the tropolone derivative, *β*-thujaplicin (4-isopropyltropolone) has been previously studied as an inhibitor of hCAII, the unsubstituted tropolone examined here has not been previously described.[8] The MBP tropolone (Table 2.1) exhibited about 3- to 4-fold greater percent inhibition against hCAII L198G compared to hCAII. In contrast, both thiotropolone and 1,2-HOPTO (Table 2.1) did not exhibit significant differences in percent inhibition against hCAII and the hCAII L198G mutant, suggesting that the sulfur heteroatom in both 1,2-HOPTO and thiotropolone might play a role in retaining activity against both forms of the metalloenzyme. To confirm these observations, the inhibitor binding constants (K_i) values for three MBPs were determined against hCAII and hCAII L198G (Table 2.1). The two sulfur-containing ligands, 1,2-HOPTO and thiotropolone, showed small differences (0.4 and 1.6-fold) in activity against the wild type and mutant metalloenzymes. The inhibitory activity of thiotropolone is significantly greater toward either form of the enzyme than that of 1,2-HOPTO (about 6- to 23-fold). Unlike the sulfur-containing ligands, tropolone is less active than either 1,2-

HOPTO or thiotropolone against hCAII and also displays a greater difference in activity (5.5-fold) against hCAII L198G and hCAII. In order to validate that the K_i values are true binding values, isothermal titration calorimetry (ITC) experiments with tropolone and hCAII were performed and yielded a K_d of 1.68 mM (Figure 2.S1), which was close to the determined K_i of 1.35 mM. To further validate the ITC and activity assay results 4-(trifluoromethyl)-benzene sulfonamide was assayed and analyzed by ITC against hCAII. The results showed a close agreement between the determined K_i and K_d (~45 and ~70 nM, respectively, Appendix Fig. 2.S2). The measured values for 4-(trifluoromethyl)-benzene sulfonamide are in close agreement with a report that determined the K_i to be 28.5 nM.[9] The reason for the activity assay data not being in closer agreement is that the K_i is below the limit of quantitation for the assay protocol utilized in our study. When performing dose response analysis, the limit of accurate quantitation in enzyme activity assays is half the total enzyme concentration.[10] In our assay protocol 100 nM hCAII was used, which limits accurate quantitation to K_i values above 50 nM. To better understand the origin of the similarities and differences in these K_i values, crystallographic and computational studies were performed.

Table 2.1. Structure of the MBPs examined in this study and K_i values against hCAII and hCAII L198G, with relative differences in activity against hCAII and hCAII L198G shown.

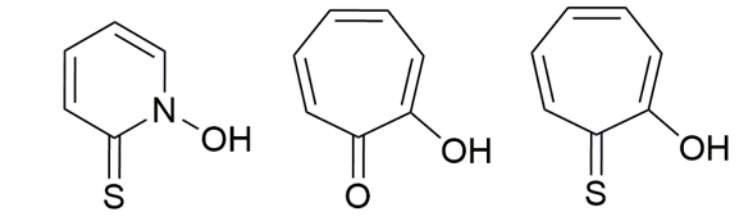

1,2-HOPTO Tropolone Thiotropolone

MBP	K_i hCAII (μM)	K_i hCAII L198G (μM)	Difference in Activity (K_i WT/ K_i L198G)
1,2-HOPTO	567 ± 85	1419 ± 32	0.4- fold
Tropolone	1346 ± 39	245 ± 14	5.5-fold
Thiotropolone	96 ± 13	61 ± 5	1.6-fold

2.3 Crystallography of hCAII and hCAII L198G

The crystal structure of ligand-free hCAII L198G was obtained and compared to hCAII (PDB: 3KS3) (Figure 2.2). The L198G mutation increases the volume of the hydrophobic pocket adjacent to the active site by ~100 $Å^3$ (the approximate volume of a leucine side chain). In the crystal structure of the mutant, this free space is occupied by two water molecules. The larger size of the active site as shown in Figure 2.2 has the potential to decrease the steric congestion exerted by the active site on bound MBPs.

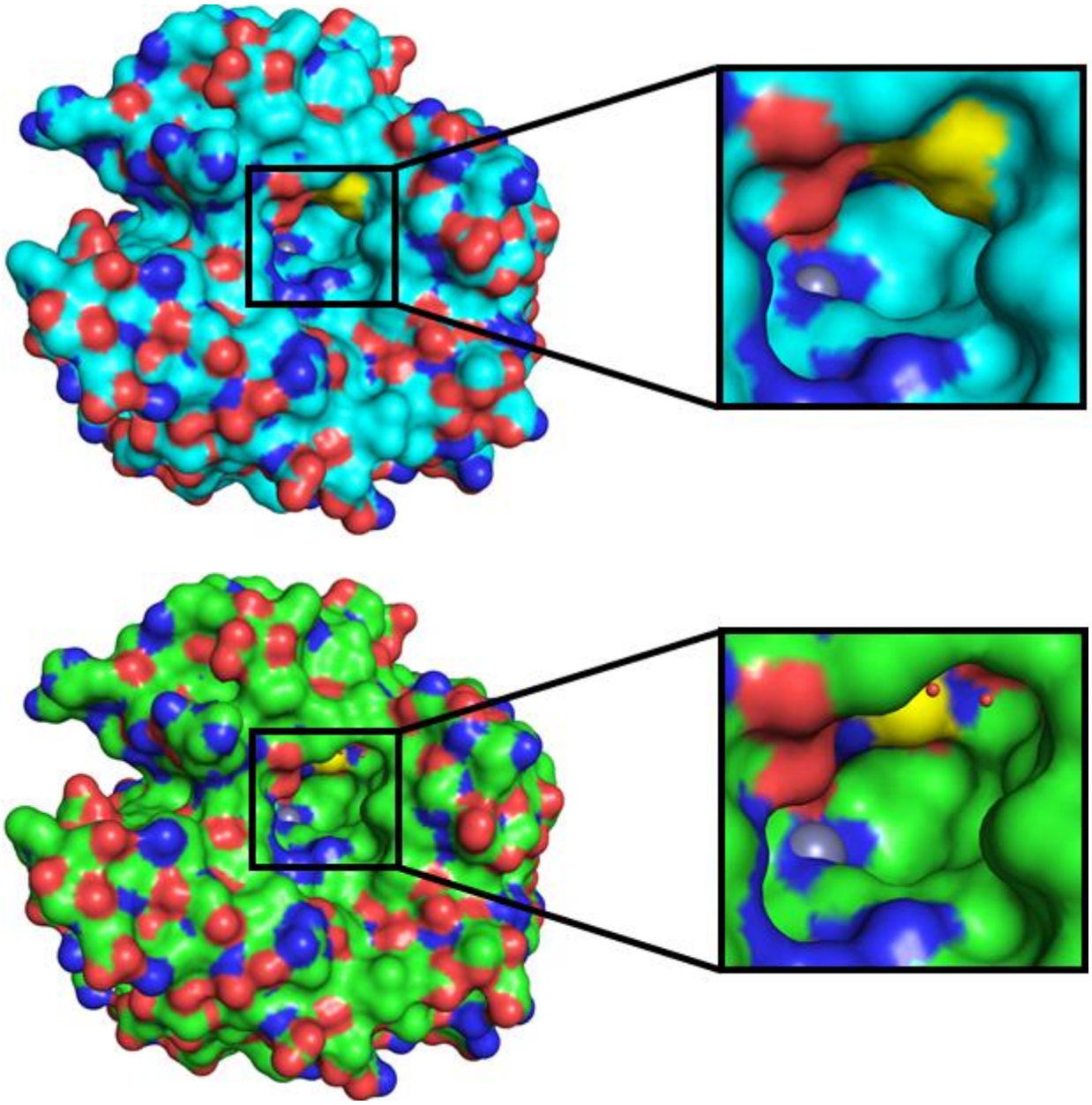

Figure 2.2 Structures of hCAII (*top*, molecular surface rendered with carbon in cyan, oxygen in red, and nitrogen in blue) (PDB: 3KS3) and hCAII L198G (*bottom*, molecular surface rendered with carbon in green, oxygen in red, and nitrogen in blue) with residue 198 highlighted in yellow and the two water molecules that replace L198 side chain shown as small, red spheres.

The crystal structures of both hCAII and hCAII L198G with tropolone bound were obtained by soaking the tropolone MBP into pre-formed crystals. The resolution for both tropolone-bound structures was obtained to 1.5 Å. As seen in Figure 2.3, the binding mode and

coordination geometry of tropolone differs substantially in the two enzymes. In both structures, tropolone displays the expected bidentate coordination to the active site Zn^{2+} ion with Zn-O bond distances ranging from ~1.9 Å to ~2.4 Å (Table 2.S1). However, the coordination geometry of tropolone is much more distorted from its ideal trigonal bipyramidal binding geometry in the wild type enzyme than in the L198G mutant (Figure 2.3). In the structure of tropolone bound to hCAII, the aromatic ring of tropolone makes considerable contacts with the hydrophobic wall of the active site, including residue L198 in the case of tropolone binding to hCAII. As shown in Figure 2.3, the ring of the tropolone when bound to hCAII L198G partially occupies the space vacated by the L198G mutation, while still maintaining considerable contacts with the hydrophobic wall. Two waters (not shown) occupy the residual freed space. Therefore, the measurable difference (~5.5-fold) in K_i values of tropolone toward hCAII versus hCAII L198G (Table 2.1) can be attributed to the difference in binding geometry.

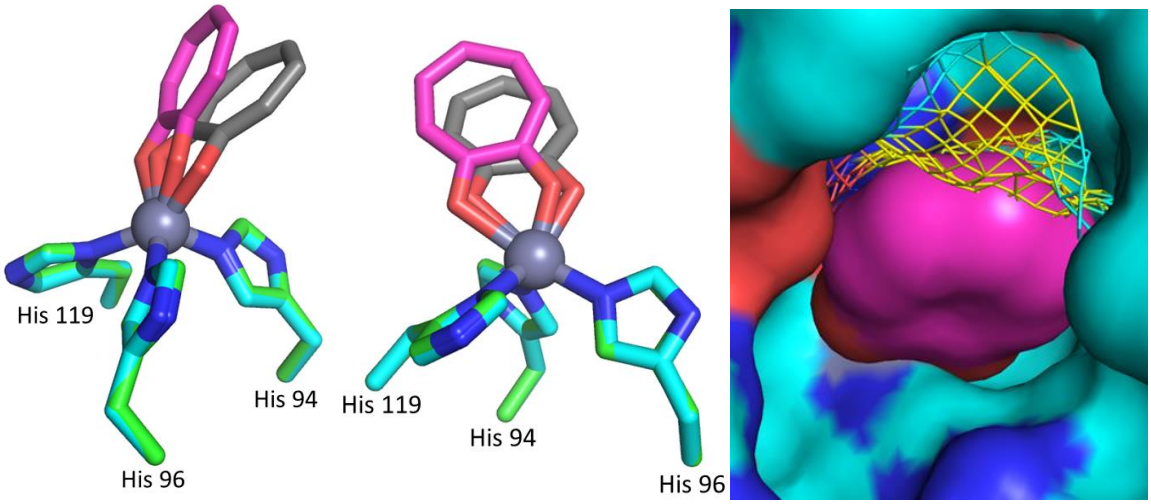

Figure 2.3. The binding mode of tropolone in hCAII (gray) and hCAII L198G (pink), shown in two different orientations (*left* and *middle*). Surface structure of hCAII showing tropolone (pink) occupying significant free space created by mutating the L198 sidechain shown as the yellow mesh (*right*).

Tropolone binding to the L198G active site adopts a binding geometry that is closer to the binding geometry exhibited in the [($Tp^{Ph,Me}$)Zn(tropolone)] model complex.[4] Along with the change in coordination geometry tropolone binds with different dihedral angles φ (Zn^{2+}−O−O−C) of around 152° in hCAII and 161° in hCAII L198G (Table 2.S1). The dihedral angle φ (Figure 2.1) for hCAII L198G is closer to ideal head-on geometry (180°), which has been shown to be energetically favorable.[5] The more favorable coordination geometry in the mutant structure correlates well with the increased inhibitory activity of tropolone against hCAII L198G compared to the wild type hCAII.

The structures of hCAII and hCAII L198G with thiotropolone bound were obtained by soaking the MBP into pre-formed crystals. The structure of hCAII was obtained to a resolution of 1.33 Å and the structure of hCAII L198G was obtained to a resolution of 1.42 Å. The binding of thiotropolone to both enzymes was nearly identical (Figure 2.4) with Zn-S and Zn-O bond distances of ~2.4 Å and ~2.5 Å, respectively. The resulting complexes are 5-coordinate species with almost identical trigonal bipyramidal coordination geometries. The dihedral angles φ (Zn^{2+}−S−O−C) of the complexes are 132° for hCAII and 137° for hCAII L198G, which are much smaller than those exhibited by tropolone. In both structures the aromatic ring makes significant contacts with the hydrophobic wall of the active site, which likely contributes to the high inhibitory activity of thiotropolone. While thiotropolone makes contacts with residue L198, thiotropolone maintains a similar binding affinity the L198G mutant indicating the contacts made with this residue in the wild type are not critical for strong binding. Indeed, the free volume that is created in the L198G mutation is occupied by a dimethyl sulfoxide (DMSO) molecule.

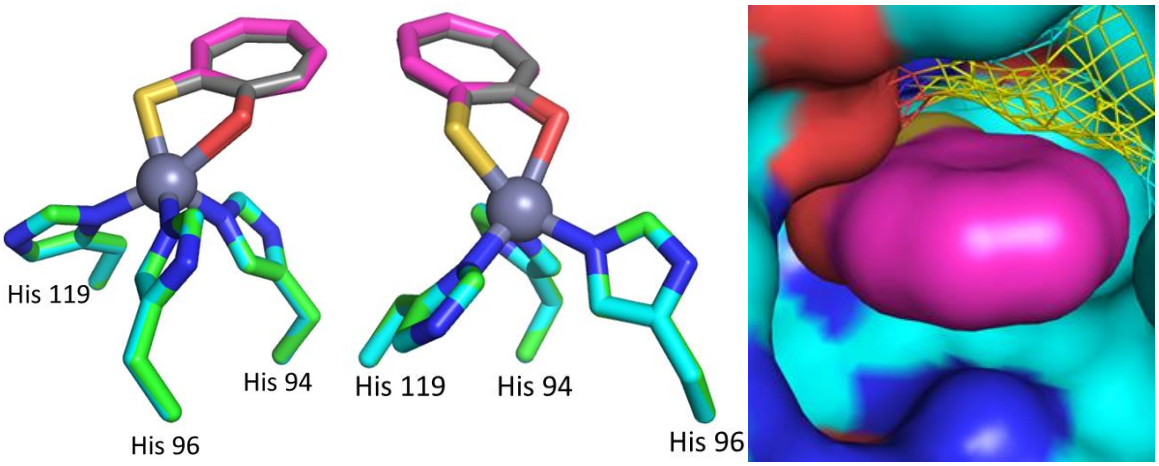

Figure 2.4. The binding mode of thiotropolone in hCAII (gray) and hCAII L198G (pink) shown in two different orientations. Surface structure of hCAII showing thiotropolone (pink) and free space created by mutating the L198 sidechain shown as the yellow mesh (*right*).

To facilitate comparison to our earlier studies, the MBP 1,2-HOPTO was soaked into crystals of the hCAII L198G mutant.[5] The crystal structure of hCAII L198G with 1,2-HOPTO bound (1.42 Å resolution) shows the MBP does not change its binding geometry when compared to the same compound bound in wild type hCAII (Figure 2.5, PDB:3M1K).[11] In both enzymes, 1,2-HOPTO is bound in a bidentate fashion to the Zn^{2+} ion, with Zn-S and Zn-O bond distances of ~2.4 Å to ~2.6 Å creating a 5-coordinate species at the metal center with a trigonal bipyramidal geometry. The dihedral angles observed for this MBP in hCAII and hCAII L198G are almost identical at 128° and 127°, respectively. The ring of 1,2-HOPTO makes some contacts with the hydrophobic wall of hCAII and hCAII L198G, especially residue L198 in hCAII. The small decrease in the K_i of 1,2-HOPTO for hCAII L198G (Table 2.1), while maintaining nearly identical modes of binding to both hCAII and hCAII L198G, is consistent with the contacts between 1,2-HOPTO and residue L198 contributing to the binding of this ligand. In an almost exact fashion as was observed in the thiotropolone-hCAII L198G structure a DMSO molecule occupies the space created by in the L198G.

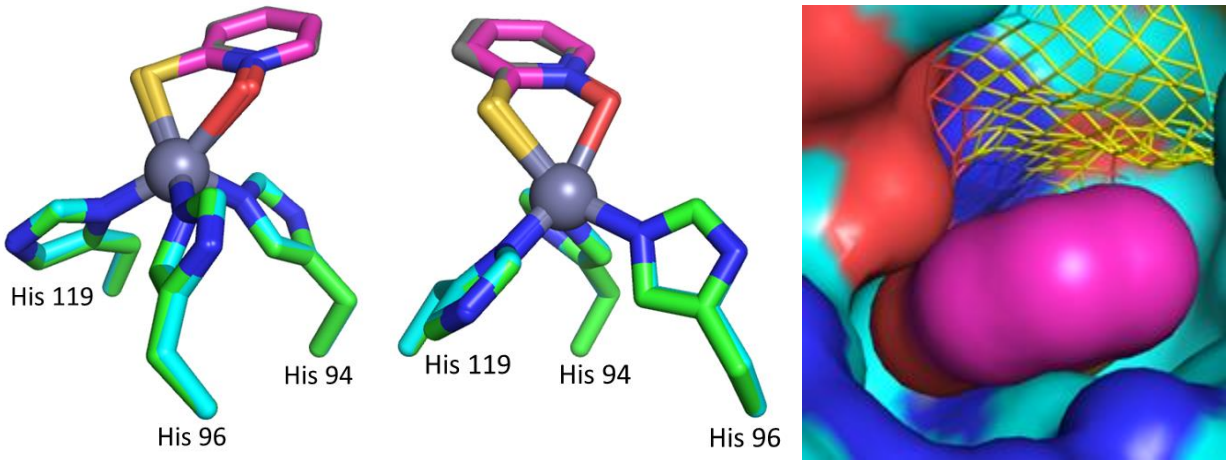

Figure 2.5. The binding mode of 1,2-HOPTO in hCAII (gray) and hCAII L198G (pink) shown in two different orientations (*left* and *middle*). Surface structure of hCAII showing 1,2-HOPTO (pink) and free space created by mutating the L198 sidechain shown as the yellow mesh (*right*).

2.4 [($Tp^{Ph,Me}$)Zn(thiotropolone)] Model Complex

In order to understand the 'ideal' binding of thiotropolone to a tris(histidine) metal active site, a model complex of this active site was synthesized and the structure was determined by X-ray crystallography. The structure of [($Tp^{Ph,Me}$)Zn (thiotropolone)] shows thiotropolone bound in a bidentate fashion resulting in a 5-coordinate complex (Figure 2.6) (Note: Brackets are used when referring to synthesized complexes). The complex exhibits trigonal bipyramidal coordination geometry, with a dihedral angle (Zn^{2+}–S–O–C) of 179° and Zn-S and Zn-O bond distances of ~2.3 Å and ~2.1 Å, respectively. The coordination geometry is generally similar to that found for tropolone in the same model system, except for the Zn-S bond being longer and causing the coordination of thiotropolone to be slightly asymmetric when compared to tropolone, to accommodate the longer bond (Figure 2.6).

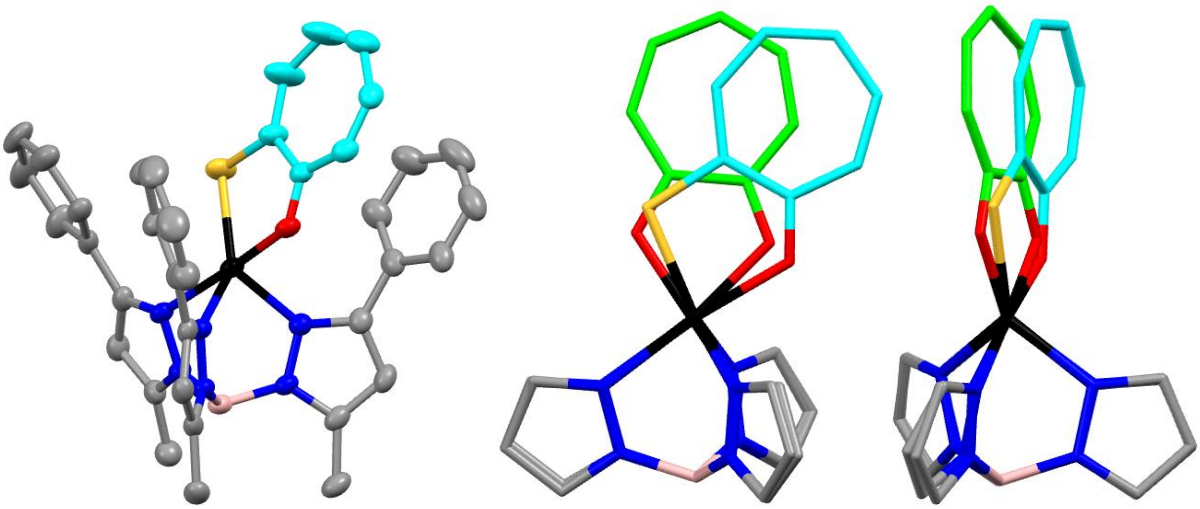

Figure 2.6. Crystal structure of [($Tp^{Ph,Me}$)Zn(thiotropolone)] (*left*) (hydrogen atoms removed for clarity, 50% probability ellipsoids) along with an overlay of [($Tp^{Ph,Me}$)Zn(thiotropolone)] and [($Tp^{Ph,Me}$)Zn(tropolone)] complexes viewed from different orientations *(middle* and *right*) (with hydrogen, phenyl, and methyl groups removed for clarity in overlay). Color scheme: carbon = gray, sulfur = yellow, oxygen = red, nitrogen = blue, boron = pink, thiotropolone carbon = teal, tropolone carbon = green, and zinc = black.

2.5 Density Functional Theory Analysis

To better understand the observed differences in MBP binding in the tropolone and thiotropolone hCAII L198G mutant structures, linear transit computations utilizing DFT were performed on truncated (Tp^{Me})Zn(MBP) model complexes varying φ from 180° to 105°, as defined as the Zn^{2+}-(S/O)-O-N dihedral angle (Figure 2.1). Free geometry optimizations were performed with the truncated model complexes using both tropolone and thiotropolone as the MBP and the resulting structures had no significant deviations from the crystallographically observed structures (Figure 2.5 and Appendix).

According to the linear transition computations, the donor atom bond distances increased slightly as φ decreased from an initial value of 180° until the coordination of both tropolone and thiotropolone "irreversibly" switched from a bidentate to monodentate mode of coordination. This

change in coordination occurred at dihedral angles of φ = 115° and φ = 120° for (Tp^{Me})Zn(tropolone) and (Tp^{Me})Zn(thiotropolone), respectively and was clearly apparent due to a sharp increase in distance between Zn^{2+} ion and the equatorial oxygen donor atom to values >3.3 Å and >3.0 Å for (Tp^{Me})Zn(tropolone) and (Tp^{Me})Zn(thiotropolone), respectively (Figure 2.7).

Both optimized trigonal bipyramidal (Tp^{Me})Zn(tropolone) and (Tp^{Me})Zn(thiotropolone) complexes possessed φ of approximately 180°, permitting ideal head-on binding. Decreasing φ of these complexes caused parabolic increases in their respective energies until a change in coordination occurred. Interestingly, the parabolic increase in energy for tropolone was much greater than that of thiotropolone, with the two complexes differing in energy by approximately 3.5 kcal mol^{-1} at φ = 125°.

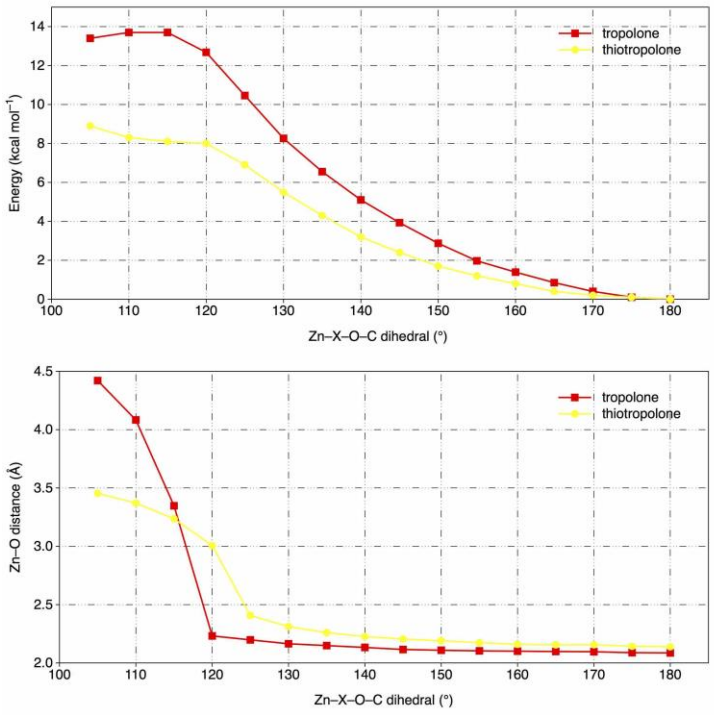

Figure 2.7. Relative binding energies (*top*) and Zn-O bond distances (*bottom*) as a function of the Zn^{2+}-X-O-C dihedral.

2.6 Discussion

Based on X-ray crystallography, thiotropolone binds to hCAII and hCAII L198G in nearly identical trigonal bipyramidal geometries. The [($Tp^{Ph,Me}$)Zn(thiotropolone)] model complex and the enzyme-thiotropolone complexes exhibited a large difference in φ, as was observed previously with 1,2-HOPTO.[5] In contrast, tropolone bound to the enzyme with a φ dihedral angle (ca. 152° and 161° for the wild type hCAII and hCAII L198G, respectively) more in line with that of the model complex, [($Tp^{Ph,Me}$)Zn(tropolone)]. The hCAII L198G mutation cavity allows tropolone to bind to the enzyme with a larger (more ideal) φ, and the change in geometry is quite pronounced in the tropolone-hCAII L198G complex and essentially absent in the thiotropolone-hCAII L198G complex. These observations indicate that steric congestion plays a significant role in the coordination geometry of tropolone to the hCAII active site.

The large dihedral angles observed when tropolone binds to hCAII and hCAII L198G indicates that the head-on binding observed in the [($Tp^{Ph,Me}$)Zn(tropolone)] model complex is important for maintaining strong binding in the tropolone-protein complex. This importance of a large dihedral angle for binding, does not appear to be the same for thiotropolone binding. The far from ideal dihedral angle observed with thiotropolone bound to hCAII and the minimal change in inhibition (Table 2.1), coordination geometry, and dihedral angle in response to the L198G mutation, strongly suggests that the sulfur donor atom enables the MBP to bind with a non-ideal geometry (dihedral angle). The DFT computations demonstrate that distortion of tropolone from head-on binding (i.e., φ = 180°, Figure 2.1) to the metal center is energetically disfavored compared to the corresponding distortion of thiotropolone (Figure 2.7). These results demonstrate sulfur donor atoms can enable MBPs to adopt 'non-ideal' dihedral angles without significant penalties in binding affinity. This is consistent with both 1,2-HOPTO and thiotropolone as they

did not as significantly change coordination geometry or binding affinity between the hCAII and hCAII L198G enzymes.

The lack of change observed in dihedral angle and coordination geometry with thiotropolone and 1,2-HOPTO (*O,S* donor MBPs) when binding to hCAII and hCAII L198G is consistent with previous studies, where changes in coordination geometry and binding mode for 1,2-HOPTO were only observed when unfavorable interactions were introduced by derivatization of the 1,2-HOPTO MBP.[12] On the other hand, MBPs that bind only with *O,O* donor atoms, such as tropolone, are found to be quite sensitive to perturbations from the ideal coordination geometry, as highlighted by changes in the dihedral angle upon binding. This is manifest by tropolone being a significantly more potent inhibitor of hCAII L198G (Figure 2.2), where it exhibits a more idealized coordination geometry and a larger dihedral angle than when it binds hCAII. These difference in *O,S* and *O,O* donor MBPs to changes in protein active site composition will likely have important implications for their development into metalloenzyme inhibitors.

In order to improve the design of metalloenzyme inhibitors, an understanding of how the inhibitors interact with active site metal ions and the active site environment is needed. Sulfur donor atom MBPs often show higher activity against Zn^{2+}-dependent metalloenzymes than their oxygen-containing analogs, due to the thiophilicity of Zn^{2+}.[13] The results here demonstrate that strong coordination by sulfur may permit inhibitors to adopt more distorted dihedral angles while preserving strong bidentate coordination, without a substantial loss in binding affinity for the metal center. This may allow for better predictability in binding mode for these MBPs across different metalloenzymes. In contrast, the affinity of *O,O* donor set MBPs are more sensitive to deviations in coordination dihedral angle, which can cause their mode of binding to be more variable in order to preserve a favorable dihedral angle. This variability, as seen with the MBP tropolone, is

dependent on the protein active site structure and second coordination sphere and may allow for these MBPs to better adapt to mutational changes in the metalloprotein active site.

2.7 Conclusions

The goal of this work was to study the effect that active site architecture has on MBP coordination. This was achieved by screening the MBP library against hCAII and hCAII L198G and studying differences in inhibition by structural studies. From the combined analysis of inhibition and structural data it was determined that donor atom identity influences the response of the ligand to changes in the protein active site environment, as structural modifications of the hCAII active site were shown to have a stronger effect on MBPs with an O,O versus O,S donor set. These findings were corroborated with DFT calculations of model coordination complexes. Overall, the results suggest that the MBP binding geometry is a malleable interaction, particularly for certain ligands, and that the identity of the donor atoms influences the response of the ligand to changes in the protein active site environment. This study highlights that the choice of MBP for metalloenzyme inhibitors merits serious consideration, as donor atom identity can affect the introduction of other protein-inhibitor interactions, constraining the inhibitor to a specific binding geometry, and make the mode of binding more or less predictable and tolerant of active site mutations. Overall, understanding the underlying interactions between an MBP and a metalloenzyme active site may aid in the design and development of potent metalloenzyme inhibitors. While the work presented here highlights the effect donor atom changes has on MBP inhibitory activity and mode of binding, in Chapter 3, changes to the donor groups of the MBPs are explored with the goal of tuning the physiochemical properties of an MBP.

2.8 Experimental

Chemicals. The MBP 2-hydroxycyclohepta-2,4,6-trien-1-one (tropolone) and 1-hydroxypyridine-2(1*H*)-thione (1,2-HOPTO) were purchased from commercial suppliers and were used without further purification. 2-Hydroxycyclohepta-2,4,6-triene-1-thione (thiotropolone) was synthesized as previously reported.[14] The hydrotris(5,3-methylphenylpyrazolyl)borate ($Tp^{Ph,Me}$) ligand was purchased from Strem Chemical and the [($Tp^{Ph,Me}$)Zn(OH)] complex was prepared as previously reported.[15] All other chemicals utilized in buffers or assays were purchased from chemical suppliers and used without further purification or modification.

Synthesis and Crystallization of [($Tp^{Ph,Me}$)Zn(thiotropolone)]. To a round bottom flask, [($Tp^{Ph,Me}$)Zn(OH)] (100 mg, 0.18 mmol) was dissolved in 15 mL of CH_2Cl_2 and the resulting solution was added to a stirring solution of 1.0 equiv (25 mg, 0.18 mmol) of thiotropolone dissolved in 10 mL of methanol (MeOH). The mixture was stirred overnight under nitrogen at room temperature. The reaction mixture was then evaporated to dryness under vacuum resulting in a yellow-white solid. The resulting solid was dissolved in benzene (3 mL) and filtered to remove any insoluble materials. The filtrate solution was directly used for crystallization via vapor diffusion with pentane, resulting in pale yellow blocks suitable for single-crystal X-ray diffraction. Data collection and refinement statistics details for [($Tp^{Ph,Me}$)Zn(thiotropolone)] can be found in the Appendix.

CA Activity Assay. The plasmids encoding hCAII and hCAII L198G with a T7 RNA polymerase promotor and an ampicillin resistance gene (pACA) were generous gifts from Thomas R. Ward

(U. Basel, Switzerland) and Carol A. Fierke (University of Michigan). Both hCAII and hCAII L198G were expressed and purified using previously reported methods.[16] Assays were performed in 50 mM HEPES pH 8.0 containing no more than 5% DMSO. *p*-Nitrophenyl acetate was used as the substrate at a concentration of 1 mM with a final protein concentration of 100 nM. MBP fragments were added to protein solutions in 96-well plates, followed by incubation at room temperature for 15 min before addition of substrate. Absorbance at 405 nm was monitored for 20 min at 1 min intervals over a linear range. Half maximal inhibitory concentration (IC_{50}) values were determined by comparing activity of reaction wells containing fragments to the activity of a control well containing no inhibitor. Inhibitor binding constants (K_i) were derived using the Cheng-Prusoff equation and verified by comparison to isothermal titration calorimetry (ITC) measurements (Appendix).[17] Absorbance data for all assays were performed using a BioTek Synergy HT plate reader.

CA Crystallization. Crystals of hCAII and hCAII L198G were obtained by sitting drop vapor diffusion method. The concentration of the protein solution was 20 mg/mL of hCAII or hCAII L198G with 1 mM *p*-chloromercuri-benzoic acid in 50 mM Tris-SO_4 (pH 8.0). The precipitation solution for hCAII was 2.7-3.0 M $(NH_4)_2SO_4$ in 50 mM Tris-SO_4 (pH 8.15). For hCAII L198G the precipitation solution was 3.0-3.1 M $(NH_4)_2SO_4$ in 50 mM Tris-SO_4 (pH 8.15). For growing hCAII and hCAII L198G crystals, protein and precipitant solution were added in ratios ranging from 0.5:1 to 1:0.5 to sitting drop wells and equilibrated against precipitant solution in a reservoir well. Crystals appeared within 2 weeks with an average size of 0.3×0.3×0.3 mm. MBP fragments were soaked into crystals by placing crystals for 2-3 days in 15-20 μL of a solution containing the

MBP at high concentrations (typically between 1-10 mM), 1.5 M sodium citrate, 5% glycerol, and no more than 5% DMSO in 50 mM HEPES (pH 8.15).

Protein Crystal Structure Determination. X-ray diffraction experiments on protein crystals were performed using a Bruker D8 Smart 6000 CCD detector at 100K utilizing Cu Kα radiation (λ = 1.5478 Å) from a Bruker-Nonius FR-591 rotating anode generator. Collected data was integrated and scaled using the Bruker APEX software suite. All diffracted hCAII and hCAII L198G crystals were in the $P2_1$ space group. The phase problem was solved via molecular replacement using a previously solved hCAII structure (PDB: 3KS3) with Zn occupancy set to 0 and all water molecules deleted.[18] Model refinement was performed by refining with REFMAC5 followed by manual refinement using Coot.[19-20] All ligands and MBP were generated via the PRODRG server.[21] Data collection and refinement statistics (Table 2.S3) details for hCAII and hCAII L198G crystal structures can be found in the Appendix. All figures were made in PyMOL.[22]

Density Functional Theory Calculations. Both linear transit computations and free geometry optimizations were performed using the Gaussian 09 suite of programs.[23] All calculations were performed with Becke's three-parameter hybrid method with the Lee, Yang, and Parr correlation functional (B3LYP) and the 6-311+G(d,p) basis set with conductor-like polarizable continuum model (CPCM) solvation (CH_2Cl_2, ε = 8.93).[24-30] Ligand coordination of models of Zn^{2+} metalloenzyme active sites have successfully been studied using the B3LYP functional previously as well as free energies of water-chloride exchange in zinc chloride complexes.[31-32] Calculations

were performed with the phenyl rings omitted to decrease computational cost; the truncated system is referred to as Zn(Tp^{Me}).

2.9 Appendix: Supporting Information

Structure Determination and Refinement of [($Tp^{Ph,Me}$)Zn(thiotropolone)]. A structure of [($Tp^{Ph,Me}$)Zn(thiotropolone)] was determined at 100 K using a Bruker Kappa diffractometer equipped with a Mo rotating anode radiation source and a Bruker APEX-II detector. Peak integrations were performed with the Siemens SAINT software package. Absorption corrections were performed using SADABS. The structure was solved using direct methods with SHELXT and refined by a full-matrix least squares procedure using SHELXL within the Olex2 small-molecule solution, refinement, and analysis software. A disordered solvent molecule was treated with the SQUEEZE protocol in PLATON to account for electron density. Data collection and refinement statistics can be found in Table 2.S2.

Conversion of IC_{50} values to Inhibitor Binding Constants (K_i). To convert the obtained IC_{50} values to inhibitor binding constant values, the Cheng-Prusoff equation was utilized as follows: $K_i = IC_{50} / (1 + [S]/K_m)$. The concentration of the substrate, *p*-nitrophenyl acetate, used for every IC_{50} measurement was 1 mM. The K_m constants used in the calculations were determined to be 28 mM for hCAII and 11 mM for hCAII L198G. These values were calculated by varying the substrate concentration using the IC_{50} assay conditions and fitting the results to a Lineweaver-Burke Plot. They were determined in duplicate and the average of the two values were used in the calculation.

Validation of K_i Values by Isothermal Titration Calorimetry. To validate that the obtained K_i values are valid binding constants, ITC experiments were performed on hCAII with tropolone and 4-(trifluoromethyl)-benzene sulfonamide. The experiments were performed on a TA Instruments low volume Nano-ITC at 25 °C and 250 rpm. The buffer system for the experiments was 150 mM HEPES and 150 mM NaCl, with 0.1 % DMSO (v/v) included for 4-(trifluoromethyl)-benzene sulfonamide. For tropolone the best data fit was obtained when 47.5 µL of 20 mM tropolone was titrated with 2.5 µL per injection into 300 µL of 1 mM hCAII in the same buffer. For the 4-(trifluoromethyl)-benzene sulfonamide titrations, 50 µM of the ligand was titrated in 8 µM hCAII. Heat of ligand dilution was corrected for by performing a blank titration of both ligands at the same concentration as in the protein titration experiments, into buffer and subtracting the resulting peak areas from the hCAII-ligand titrations. The data was processed with TA instruments Nano Analyze software. The data and resulting fit of tropolone and 4-(trifluoromethyl)-benzene sulfonamide can be seen in Figure 2.S1 and Figure 2.S2 respectively. In the case of a weak interaction being measured (K_d > 100µM), the interaction between the ligand and hCAII was set to 1 (n = 1) to be able to fit the non-sigmoidal data (c-value not between 5 and 500).

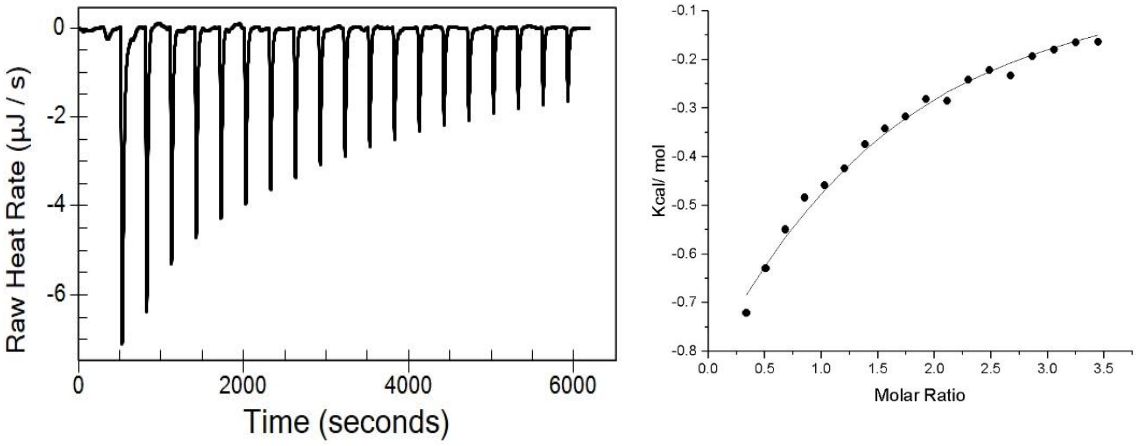

Figure 2.S1. ITC analysis of tropolone binding to hCAII. From the sequential titration binding isotherm (*left*) the tropolone heat of dilution was subtracted. The resulting data was fitted to an independent model (*right*) with the n value fixed to 1 due to the limitations on the hCAII and tropolone concentration generating a low c value of the curve. The resulting K_d was calculated as 1.68 mM, which is close to the determined K_i of tropolone (1.346 mM).

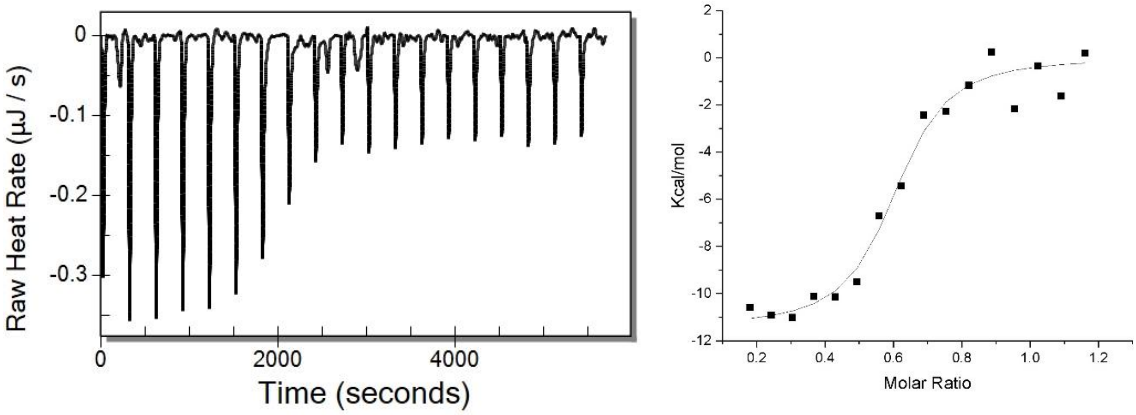

Figure 2.S2. ITC Analysis of 4-(trifluoromethyl)-benzene sulfonamide binding to hCAII. From the sequential titration binding isotherm (*left*) the 4-(trifluoromethyl)-benzene sulfonamide heat of dilution was subtracted. The resulting data was fitted to an independent model (*right*) and the resulting curve yielded a K_d of 72 nM and an approximate n-value of 0.6.

Computational Methods. All computations were performed using Gaussian 09. Linear transit calculations and geometry optimizations were performed using the $CPCM_{DCM}$/B3LYP/6-311+G(d,p) unless otherwise noted. To model the influence of the dielectric environment of the

active on coordination geometries, computations were performed in implicit dichloromethane (DCM, $\varepsilon = 8.93$). using the conductor-like polarizable continuum (solvation) model (CPCM). The B3LYP functional has been demonstrated to reliably compute the structure of zinc coordination complexes and has accurately reproduced the energetics of a number of zinc-mediated transformations. Structures for computations were prepared using Avogadro and Gaussview. Phenyl groups of the crystallized model complex were replaced with hydrogen atoms.

Table 2.S1. MBP- Zn^{2+} bond distances and dihedral angles.

Complex	O-Zn Bond (Å)	O/S-Zn Bond (Å)	Dihedral Angle (°)
hCAII-1,2-HOPTO	2.48	2.45	128
hCAII L198G-1,2-HOPTO	2.44	2.56	127
hCAII-Tropolone	2.27	2.08	152
hCAII L198G-Tropolone	2.37	1.90	161
hCAII-Thiotropolone	2.54	2.35	132
hCAII L198G-Thiotropolone	2.47	2.42	137
[($Tp^{Ph,Me}$)Zn(tropolone)]	2.08	1.99	179
[($Tp^{Ph,Me}$)Zn(thiotropolone)]	2.11	2.3	179

Table 2.S2. Data collection and refinement statistics for the crystal structure of [($Tp^{Ph,Me}$)Zn(thiotropolone)].

Empirical Formula	$C_{37}H_{33}BN_6OSZn$
Formula Weight	685.93
Collection *T* (K)	100(2)
Crystal System	Triclinic
Space Group	P-1
a (Å)	12.0027(6)
b (Å)	17.8661(10)
c (Å)	18.9524(10)
α (deg)	107.824(2)
β (deg)	100.6210(10)
γ (deg)	92.097(2)
V ($Å^3$)	3784.0(3)
Z	4
D_{calcd} (g cm^{-3})	1.204
μ (mm^{-1})	0.739
min/max *T*	0.787/0.809
hkl ranges	-14<*h*<15
	-22<*k*<22
	-23<*l*<23
Total reflections	80430
Unique reflections	15564
R (int)	0.0676
Parameters/restraints	853/0
R_1 (all data)	0.0628
wR_2 (all data)	0.1091
max/min residual ($e^-/Å^3$)	0.49/-0.73
G.O.F.	1.008

Table 2.S3. Crystal and Refinement data for hCAII crystal structures.

Protein-Inhibitor	hCAII L198G 1,2-HOPTO	hCAII Tropolone	hCAII L198G Tropolone	hCAII Thiotropolone	hCAII L198G Thiotropolone
PDB ID	5TH4	5THJ	5THI	5THN	5TI0
a (Å)	42.20	42.28	42.19	41.98	42.12
b (Å)	41.33	41.34	41.37	41.11	41.14
c (Å)	72.16	71.85	71.73	71.67	71.86
α (deg)	90.00	90.00	90.00	90.00	90.00
β (deg)	104.65	104.00	104.2	104.23	104.44
γ (deg)	90.00	90.00	90.00	90.00	90.00
Resolution Range[a] (Å)	40.00-1.47 (1.508-1.47)	40.00-1.50 (1.537-1.498)	40.00-1.50 (1.539-1.50)	40.00-1.33 (1.365-1.33)	40.00-1.42 (1.457-1.42)
Completeness (%)	98.7 (95.40)	99.5 (95.06)	99.45 (95.32)	99.9 (99.63)	99.94 (99.85)
R_{work}	0.180 (0.332)	0.154 (0.25)	0.168 (0.254)	0.177 (0.245)	0.162 (0.255)
R_{free}[b]	0.211 (0.373)	0.189 (0.31)	0.195 (0.326)	0.206 (0.25)	0.195 (0.255)
Bond Length RMS (Å)	0.025	0.022	0.022	0.027	0.024
Bond Angle RMS (deg)	2.432	2.185	2.147	2.457	2.325

[a] Parentheses indicate values for the highest resolution shell. [b] Calculated using 5% of the data excluded from refinement.

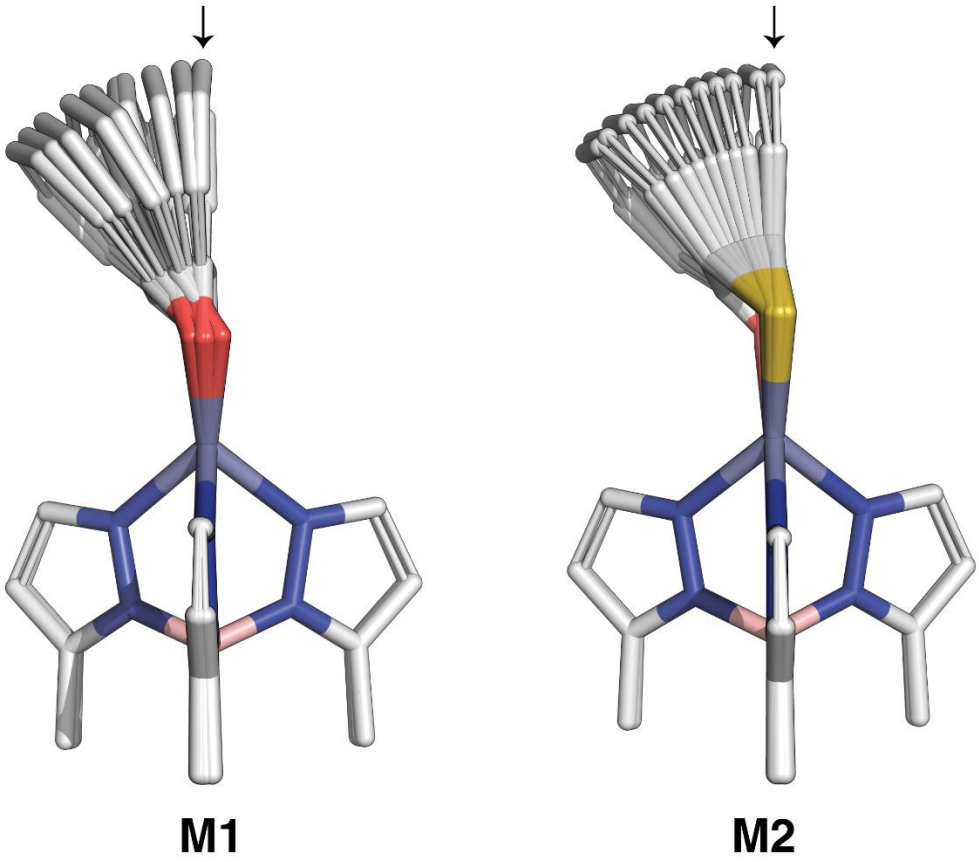

Figure 2.S3. Overlay of the optimized structures for the linear transit along φ. Only geometries bidentate coordination of tropolone or thiotropolone are shown. The minimized trigonal pyramidal geometry is indicated by the black arrows.

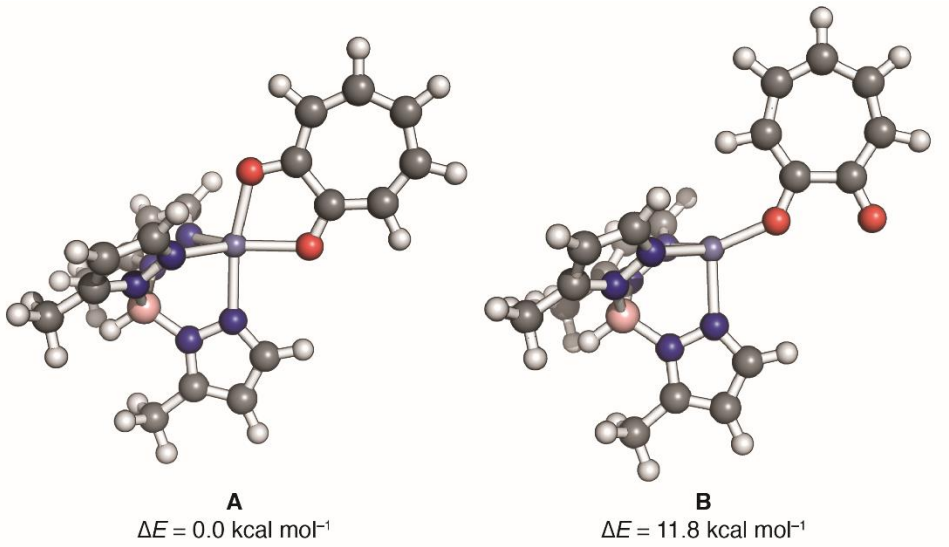

Figure 2.S4. $CPCM_{DCM}$/B3LYP/6-311+G(d,p)-optimized model tetrahedral and trigonal pyramidal coordination complexes of tropolone and their relative energies. **A** and **B** are the computed trigonal pyramidal and tetrahedral complexes of the zinc-tropolone model complex. The tetrahedral complex is significantly less stable (ca. 12 kcal mol^{-1}) than the bidentate trigonal bipyramidal structure **A**.

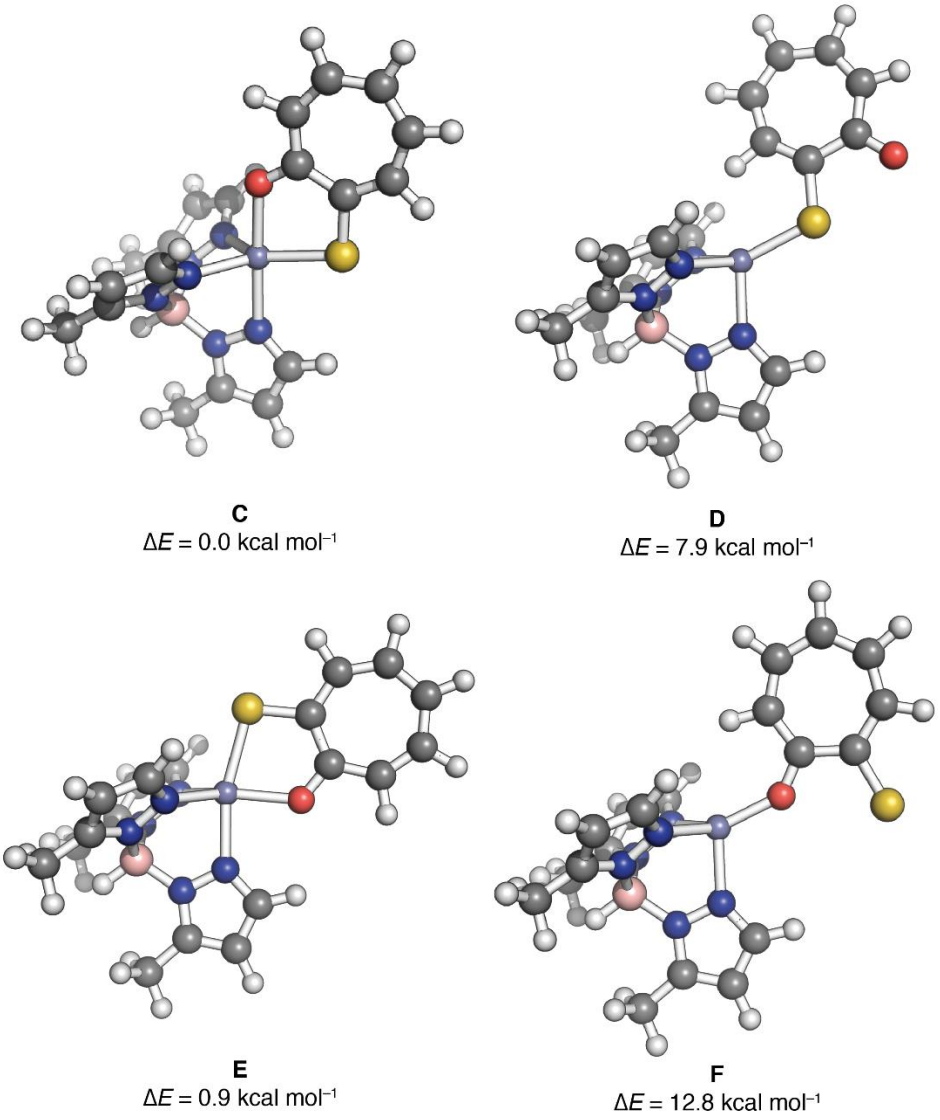

Figure 2.S5. $CPCM_{DCM}$/B3LYP/6-311+G(d,p)-optimized model tetrahedral and trigonal pyramidal coordination complexes of thiotropolone and their relative energies. Four stationary points for the zinc-thiotropolone complex were located computationally. Two 5-coordinate complexes **C** and **E** that feature axial *O*- and *S*-coordination, respectively, were located computationally. **C**, which corresponds to the 5-coordinate complex observed experimentally, is more the stable of the two complexes. Analogously, a pair of tetrahedral complexes **B** and **F** were modeled computationally. Based on the computed energies of these 4-coordinate complexes, *O*-coordination is a much weaker interaction than *S*-coordination. These data are consistent with the conclusions derived from the experiments and linear transit computations described in the main text.

2.10 Acknowledgements

Chapter 2 is a reprint of the material published in the following publication "Effect of Donor Atom Identity on Metal-Binding Pharmacophore Coordination" Benjamin L. Dick, Ashay Patel, J. Andrew McCammon, and Seth M. Cohen *J. Biol. Inorg. Chem*. 2017, *22*, 605-613. The dissertation author was the primary researcher and author of this publication and gratefully acknowledges the contributions of coauthors Ashay Patel, J. Andrew McCammon, and Seth M. Cohen.

2.11 References

1. Puerta, D. T.; Cohen, S. M., Examination of novel zinc-binding groups for use in matrix metalloproteinase inhibitors. *Inorg. Chem.* **2003,** *42*, 3423-30.

2. Puerta, D. T.; Schames, J. R.; Henchman, R. H.; McCammon, J. A.; Cohen, S. M., From model complexes to metalloprotein inhibition: a synergistic approach to structure-based drug discovery. *Angew. Chem., Int. Ed. Engl.* **2003,** *42*, 3772-4.

3. Cook, S. A.; Hill, E. A.; Borovik, A. S., Lessons from Nature: A Bio-Inspired Approach to Molecular Design. *Biochemistry* **2015,** *54*, 4167-80.

4. Jacobsen, F. E.; Lewis, J. A.; Heroux, K. J.; Cohen, S. M., Characterization and evaluation of pyrone and tropolone chelators for use in metalloprotein inhibitors. *Inorg. Chim. Acta* **2007,** *360*, 264-272.

5. Martin, D. P.; Blachly, P. G.; Marts, A. R.; Woodruff, T. M.; de Oliveira, C. A. F.; McCammon, J. A.; Tierney, D. L.; Cohen, S. M., 'Unconventional' Coordination Chemistry by Metal Chelating Fragments in a Metalloprotein Active Site. *J. Am. Chem. Soc.* **2014,** *136*, 5400-5406.

6. Nair, S. K.; Krebs, J. F.; Christianson, D. W.; Fierke, C. A., Structural basis of inhibitor affinity to variants of human carbonic anhydrase II. *Biochemistry* **1995,** *34*, 3981-3989.

7. Jacobsen, J. A.; Fullagar, J. L.; Miller, M. T.; Cohen, S. M., Identifying chelators for metalloprotein inhibitors using a fragment-based approach. *J. Med. Chem.* **2011,** *54*, 591-602.

8. Costa, G.; Gidaro, M. C.; Vullo, D.; Supuran, C. T.; Alcaro, S., Active Components of Essential Oils as Anti-Obesity Potential Drugs Investigated by in Silico Techniques. *J. Agric. Food Chem.* **2016,** *64* (26), 5295-5300.

9. Bereau, T.; Kramer, C.; Monnard, F. W.; Nogueira, E. S.; Ward, T. R.; Meuwly, M., Scoring Multipole Electrostatics in Condensed-Phase Atomistic Simulations. *J. Phys. Chem. B* **2013,** *117* (18), 5460-5471.

10. Brooks, H. B.; Geeganage, S.; Kahl, S. D.; Montrose, C.; Sittampalam, S.; Smith, M. C.; Weidner, J. R., Basics of Enzymatic Assays for HTS. In *Assay Guidance Manual*, Sittampalam, G. S.; Grossman, A.; Brimacombe, K.; Arkin, M.; Auld, D.; Austin, C. P.; Baell, J.; Bejcek, B.; Caaveiro, J. M. M.; Chung, T. D. Y.; Coussens, N. P.; Dahlin, J. L.; Devanaryan, V.; Foley, T. L.; Glicksman, M.; Hall, M. D.; Haas, J. V.; Hoare, S. R. J.; Inglese, J.; Iversen, P. W.; Kahl, S. D.; Kales, S. C.; Kirshner, S.; Lal-Nag, M.; Li, Z.; McGee, J.; McManus, O.; Riss, T.; Saradjian, P.; Trask, O. J., Jr.; Weidner, J. R.; Wildey, M. J.; Xia, M.; Xu, X., Eds. Bethesda (MD), 2004.

11. Schulze Wischeler, J.; Innocenti, A.; Vullo, D.; Agrawal, A.; Cohen, S. M.; Heine, A.; Supuran, C. T.; Klebe, G., Bidentate Zinc chelators for alpha-carbonic anhydrases that produce a trigonal bipyramidal coordination geometry. *ChemMedChem* **2010,** *5*, 1609-1615.

12. Martin, D. P.; Blachly, P. G.; McCammon, J. A.; Cohen, S. M., Exploring the Influence of the Protein Environment on Metal-Binding Pharmacophores. *J. Med. Chem.* **2014,** *57*, 7126-7135.

13. Sigel, H.; McCormick, D. B., Discriminating behavior of metal ions and ligands with regard to their biological significance. *Acc. Chem. Res.* **1970,** *3* (6), 201-208.

14. Machiguchi, T.; Hasegawa, T.; Kano, Y., General Synthesis, Spectroscopic Properties, and Dipole Moments of 2-Substituted Tropothiones. *Bull. Chem. Soc. Jpn.* **1993,** *66*, 3699-3706.

15. Puerta, D. T.; Lewis, J. A.; Cohen, S. M., New beginnings for matrix metalloproteinase inhibitors: identification of high-affinity zinc-binding groups. *J. Am. Chem. Soc.* **2004,** *126*, 8388-9.

16. Monnard, F. W.; Heinisch, T.; Nogueira, E. S.; Schirmer, T.; Ward, T. R., Human carbonic anhydrase II as a host for piano-stool complexes bearing a sulfonamide anchor. *Chem. Commun.* **2011,** *47*, 8238-40.

17. Yung-Chi, C.; Prusoff, W. H., Relationship between the inhibition constant (KI) and the concentration of inhibitor which causes 50 per cent inhibition (I50) of an enzymatic reaction. *Biochem. Pharmacol.* **1973,** *22* (23), 3099-3108.

18. Avvaru, B. S.; Kim, C. U.; Sippel, K. H.; Gruner, S. M.; Agbandje-McKenna, M.; Silverman, D. N.; McKenna, R., A short, strong hydrogen bond in the active site of human carbonic anhydrase II. *Biochemistry* **2010,** *49*, 249-51.

19. Murshudov, G. N.; Vagin, A. A.; Dodson, E. J., Refinement of macromolecular structures by the maximum-likelihood method. *Acta Crystallogr., Sect. D: Biol. Crystallogr.* **1997,** *53*, 240-55.

20. Emsley, P.; Cowtan, K., Coot: model-building tools for molecular graphics. *Acta Crystallogr., Sect. D: Biol. Crystallogr.* **2004,** *60*, 2126-32.

21. Schüttelkopf, A. W.; van Aalten, D. M. F., PRODRG: a tool for high-throughput crystallography of protein-ligand complexes. *Acta Crystallogr., Sect. D: Biol. Crystallogr.* **2004,** *60*, 1355-63.

22. Schrodinger, L. *The PyMOL Molecular Graphics System*, Version 1.8; 2015.

23. Frisch, M. J.; Trucks, G. W.; Schlegel, H. B.; Scuseria, G. E.; Robb, M. A.; Cheeseman, J. R.; Scalmani, G.; Barone, V.; Mennucci, B.; Petersson, G. A.; Nakatsuji, H.; Caricato, M.; Li, X.; Hratchian, H. P.; Izmaylov, A. F.; Bloino, J.; Zheng, G.; Sonnenberg, J. L.; Hada, M.; Ehara, M.; Toyota, K.; Fukuda, R.; Hasegawa, J.; Ishida, M.; Nakajima, T.; Honda, Y.; Kitao, O.; Nakai, H.; Vreven, T.; Montgomery Jr., J. A.; Peralta, J. E.; Ogliaro, F.; Bearpark, M. J.; Heyd, J.; Brothers, E. N.; Kudin, K. N.; Staroverov, V. N.; Kobayashi, R.; Normand, J.; Raghavachari, K.; Rendell, A. P.; Burant, J. C.; Iyengar, S. S.; Tomasi, J.; Cossi, M.; Rega, N.; Millam, N. J.; Klene, M.; Knox, J. E.; Cross, J. B.; Bakken, V.; Adamo, C.; Jaramillo, J.; Gomperts, R.; Stratmann, R. E.; Yazyev, O.; Austin, A. J.; Cammi, R.; Pomelli, C.; Ochterski, J. W.; Martin, R. L.; Morokuma, K.; Zakrzewski, V. G.; Voth, G. A.; Salvador, P.; Dannenberg, J. J.; Dapprich, S.; Daniels, A. D.; Farkas, Ö.; Foresman, J. B.; Ortiz, J. V.; Cioslowski, J.; Fox, D. J., *Gaussian 09*. Gaussian, Inc.: Wallingford, CT, USA, 2009.

24. Barone, V.; Cossi, M., Quantum Calculation of Molecular Energies and Energy Gradients in Solution by a Conductor Solvent Model. *J. Phys. Chem. A* **1998,** *102*, 1995-2001.

25. Cossi, M.; Rega, N.; Scalmani, G.; Barone, V., Energies, structures, and electronic properties of molecules in solution with the C-PCM solvation model. *J. Comput. Chem.* **2003,** *24*, 669-681.

26. Klamt, A.; Schüürmann, G., COSMO: a new approach to dielectric screening in solvents with explicit expressions for the screening energy and its gradient. *J. Chem. Soc., Perkin Trans. 2* **1993,** (5), 799-805.

27. Becke, A. D., Density-functional thermochemistry. III. The role of exact exchange. *J. Chem. Phys.* **1993,** *98*, 5648.

28. Lee, C.; Yang, W.; Parr, R. G., Development of the Colle-Salvetti correlation-energy formula into a functional of the electron density. *Phys. Rev. B* **1988,** *37*, 785-789.

29. Stephens, P. J.; Devlin, F. J.; Chabalowski, C. F.; Frisch, M. J., Ab Initio Calculation of Vibrational Absorption and Circular Dichroism Spectra Using Density Functional Force Fields. *J. Phys. Chem.* **1994,** *98*, 11623-11627.

30. Vosko, S. H.; Wilk, L.; Nusair, M., Accurate spin-dependent electron liquid correlation energies for local spin density calculations: a critical analysis. *Can. J. Phys.* **1980,** *58* (8), 1200-1211.

31. Dudev, T.; Lim, C., Tetrahedral vs Octahedral Zinc Complexes with Ligands of Biological Interest: A DFT/CDM Study. *J. Am. Chem. Soc.* **2000,** *122*, 11146-11153.

32. Ryde, U., Carboxylate Binding Modes in Zinc Proteins: A Theoretical Study. *Biophys. J.* **1999,** *77*, 2777-2787.

Chapter 3: Metal-Binding Isosteres as New Scaffolds for Metalloenzyme Inhibitors

3.1 Introduction

Using isosteres to replace functional groups that possess liabilities, such as metabolic instability, poor solubility, low permeability, or even toxicity is a core concept in modern medicinal chemistry and critical for advancing lead compounds to clinically-effective therapeutics.[1-2] In a more pragmatic, but still important application, isosteres can also be used to help develop new chemical matter. For these and many related reasons, the application of isosteres is an essential tool in modern drug development, particularly for the carboxylic acid functional group. In this chapter, the terms isosteres and bioisosteres will be used interchangeably.

Carboxylic acids are extremely important pharmacophores in bioactive compounds as is evidenced by their use in >450 drugs worldwide.[3] The ability of this functional group to engage in strong hydrogen bonding, electrostatic interactions, and metal coordination are key to its utility in bioactive molecules. Despite its broad use, carboxylic acids are not without liabilities, which can range from poor membrane permeability to idiosyncratic toxicity.[4-5] One solution to this limitation is prodrugging carboxylic acids, often as esters;[6] however, a second solution is the use of isosteres. Recently, Ballatore and co-workers have highlighted the exceptional importance, success, versatility, and vast chemical space of carboxylic acid isosteres.[7] In a valuable study, Ballatore reported on a series of phenylpropionic isosteres and compared these compounds across a range of physicochemical properties such as LogP, log$D_{7.4}$, pK_a, and others.[8] This thorough study demonstrated the broad range of carboxylic acid isosteres available and their physicochemical properties.

As discussed in chapter 1, the use of MBPs as privileged scaffolds for FBDD has been successful against a number of metalloenzyme targets.[9-13] However, several of these MBPs contain carboxylic acids or free thiols which could have pharmokinetic liabilities. Herein, the concepts of

MBPs and isosteres are combined to develop original metal-binding isosteres (MBIs) as a new class of compounds for FBDD. Using picolinic acid (**3.1**, Figure 3.1) as a representative carboxylic acid containing MBP, we report 23 MBIs and explore their metal-binding properties, physicochemical properties, and metalloenzyme inhibitory activity against the influenza polymerase acidic subunit N-terminal endonuclease domain of the RNA-dependent RNA polymerase complex (Endo) and human carbonic anhydrase II (hCAII), both of which are metalloenzymes of clinical relevance. Like other isosteres, MBIs capture the potential to retain key properties of the pharmacophore (e.g., metal binding), while allowing for versatile and flexible modulation of physicochemical properties (e.g., pK_a, LogP). Although a relatively straightforward concept, the intimate and enabling combination of bioinorganic and medicinal chemistry presented in these findings demonstrate that MBIs are a valuable and uncharted part of chemical space for developing innovative new pharmacophores for metalloenzyme inhibition.

3.2 Metal-Binding Isostere Design and Synthesis

Picolinic acid (**3.1**, Figure 3.1) is an MBP that has been found to have activity against several metalloenzymes.[14] Inspired by recent work on the properties of carboxylic acid isosteres,[8] several MBIs of **3.1**, where the pyridinyl nitrogen coordination motif was maintained and the carboxylic acid group was varied, were prepared. A few previous studies utilizing isostere replacement for metalloenzyme inhibition have been reported, but they were limited to a small number of isosteres and provided little characterization beyond target inhibition data.[15-16] In designing MBIs, maintaining chelate ring size was prioritized, as it has a significant impact on the energetics of metal coordination. Therefore, the proposed MBIs (Figure 3.1) are designed such that they retain the ability to form a 5-membered chelate ring with a metal ion as is found for picolinic acid. Similarly, the MBIs were designed to retain the acidic character of the carboxylic acid. Maintaining

chelate ring size and acidic ability were expected to be important in developing MBIs that would possess similar metal coordination and inhibitory activity as **3.1**.

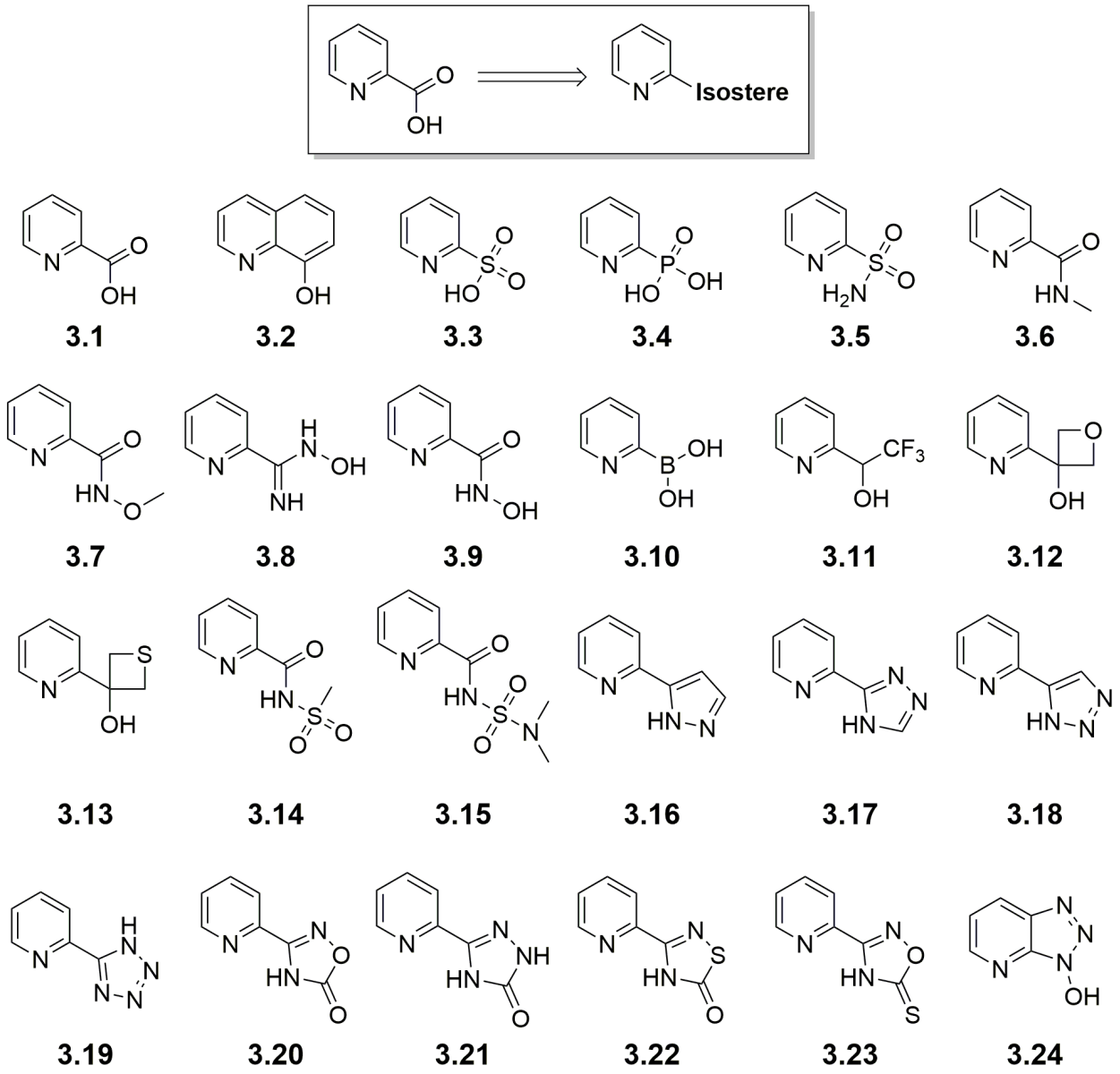

Figure 3.1. Metal-binding isosteres (MBIs) of picolinic acid (**3.1**) synthesized and investigated in this study.

Several of the MBIs were purchased from commercial vendors, including compounds **3.1**, **3.2**, **3.3**, **3.5**, **3.8**, **3.10**, **3.11**, **3.16**, **3.17**, and **3.24** (Figure 3.1). The remaining MBIs were synthesized starting from one of several pyridine precursors, including pyridine 1-oxide (**3.4**), 2-pyridine acid chloride (**3.6**), picolinic acid (**3.7**, **3.14**, **3.15**), methyl picolinate (**3.9**), 2-bromopyridine (**3.12**,

3.13) 2-ethynylpyridine (**3.18**), 2-pyridinecarbonitrile (**3.19**), pyridine-2-carboxamide oxime (**3.20**, **3.23**), methyl picolinimidate (**3.21**), and pyridine-2-carboximidamide (**3.22**). The detailed synthetic procedures used to obtain these compounds and their complete characterization can be found in the Appendix.

3.3 Synthesis and Characterization of Model Complexes

The metal binding mode of each isostere was evaluated utilizing a bioinorganic $Tp^{Ph,Me}Zn$ complex as a model system.[17] As the tridentate pyrazole ligand system closely resembles the co-ordination environment of a tris(histidine) metalloenzyme active site, it is a suitable system for a preliminary assessment of metal binding capability of MBIs. Our lab has previously reported the coordination complexes of compound **3.1**, namely [($Tp^{Ph,Me}$)Zn(**3.1**)] (Figure 3.S1).[18] [($Tp^{Ph,Me}$)Zn(**3.1**)] shows that **3.1** binds in a bidentate fashion with the pyridine ring in an axial position and the carboxylate in an equatorial position, resulting in trigonal bipyramidal geometry. The crystal structure of **3.2** complexed to [($Tp^{Ph,Me}$)Zn] has also been reported,[19] showing the quinoline and hydroxyl group respectively coordinating in the same positions as pyridine and carboxylate groups of **3.1**.

Coordination complexes of [($Tp^{Ph,Me}$)Zn] were successfully obtained with several MBIs including, **3.3**, **3.5**, **3.7**, **3.9**, **3.11**, **3.12**, **3.15**, **3.17**, **3.18**, **3.19**, **3.20**, **3.21**, **3.23**, and **3.24**. In all obtained complexes, bidentate coordination to the Zn^{2+} ion was observed with the pyridine in the axial position and the carboxylate isostere occupying an equatorial coordination site (Figure 3.2, Figures 3.S2 - S15). Both noncyclic (**3.3**, **3.5**, **3.7**, **3.9**, **3.11**, **3.12**, **3.15**) and cyclic (**3.17**, **3.18**,

3.19, **3.20**, **3.21**, **3.23**) carboxylic acid isosteres, maintained the coordinative ability of the carboxylate upon its replacement. Fused ring systems also demonstrated similar coordination, with retention of the 5-membered chelate ring in [($Tp^{Ph,Me}$)Zn(**3.24**)]. All MBIs behaved as monoanionic ligands resulting in neutral [($Tp^{Ph,Me}$)Zn(MBI)] complexes. Overall the crystallized [($Tp^{Ph,Me}$)Zn(MBI)] complexes were similar to the [($Tp^{Ph,Me}$)Zn(**3.1**)] complex, with some interesting trends and slight differences being observed.

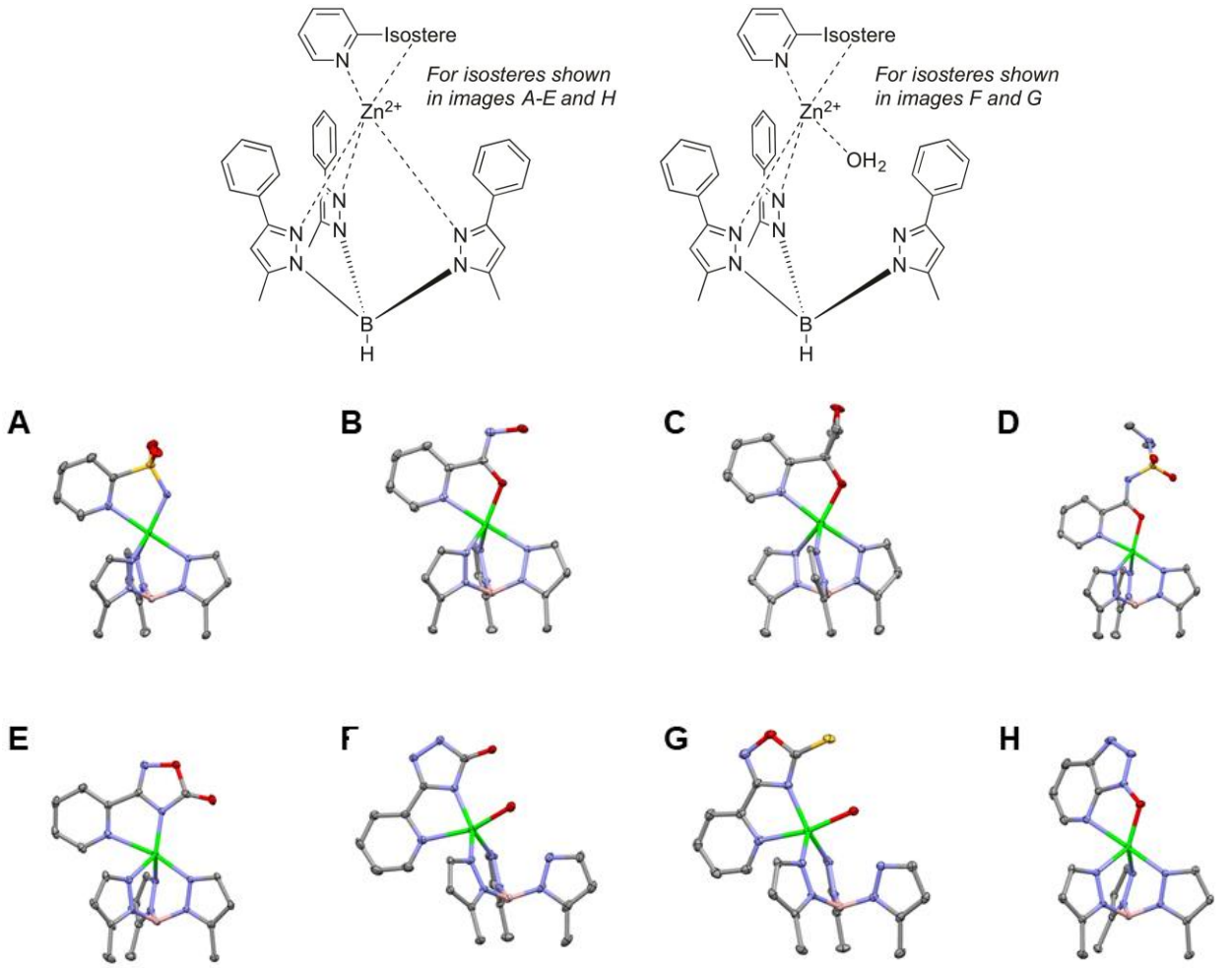

Figure 3.2. Representative examples of [(Tp^{Ph,Me})Zn(MBI)] complexes shown as chemical structures (*top*) and ORTEPs (*bottom*) with atoms as 50% thermal probability ellipsoids. A: [(Tp^{Ph,Me})Zn(**3.5**)]. B: [(Tp^{Ph,Me})Zn(**3.9**)]. C: [(Tp^{Ph,Me})Zn(**3.12**)]. D: [(Tp^{Ph,Me})Zn(**3.15**)]. E: [(Tp^{Ph,Me})Zn(**3.20**)]. F: [(Tp^{Ph,Me})Zn(**3.21**)]. G: [(Tp^{Ph,Me})Zn(**3.23**)]. H: [(Tp^{Ph,Me})Zn(**3.24**)]. Hydrogen atoms and Tp^{Ph,Me} phenyl groups have been removed for clarity. Color scheme: carbon = gray, oxygen = red, nitrogen = blue, boron = pink, sulfur = yellow, and zinc = green.

The noncyclic MBIs achieved bidentate coordination to the Zn^{2+} through the pyridine ring and a deprotonated oxygen donor atom, except for **3.5,** which exhibited bidentate coordination through the pyridine ring and a deprotonated sulfonamide nitrogen (Figure 3.2). For the noncyclic isosteres, the [(Tp^{Ph,Me})Zn(MBI)] complexes revealed that oxygen donor atoms were favored for coordinating the Zn^{2+} ion over nitrogen donor atoms. Ligands with varying substituent sizes, such

as compounds **3.7**, **3.9**, and **3.15**, all demonstrate oxygen coordination (Figure 3.2, Figure 3.S4) suggesting this preference for the oxygen donor cannot be explained by steric hindrance. A more likely explanation is that the [($Tp^{Ph,Me}$)Zn] complex has a preference for the more electronegative oxygen donor atom. In addition, the coordination motif of **3.9** was especially surprising, as it shows coordination of the picolinic isostere is preferred over coordination by the hydroxamic acid group contained within **3.9**.[20] The [($Tp^{Ph,Me}$)Zn(**3.9**)] complex presented here shows that suitable MBIs may be preferred even over widely used coordination motifs found in metalloenzyme inhibitors.

The MBIs containing cyclic isosteres (**3.17**, **3.18**, **3.19**, **3.20**, **3.21**, **3.23**) all coordinated through the pyridinyl nitrogen and a deprotonated heterocyclic nitrogen donor atom. The fused ring MBI **3.24** exhibited similar coordination as **3.2**, with bidentate coordination through the pyridinyl nitrogen and deprotonated triazolol oxygen. MBIs **3.21** and **3.23** resulted in a complex where a water molecule displaces one of the pyrazole arms of the $Tp^{Ph,Me}$ ligand (Figure 3.2). This bidentate coordination by pyrazolylborate scorpionate ligands to Zn^{2+} is uncommon and has only been observed twice crystallographically: in a homoleptic $Zn(Tp)_2$ complex,[21] and in heteroleptic ZnTp complexes with exceptional steric bulk.[22] In both of these examples an additional solvent molecule was not found coordinating the Zn^{2+} ion, as is observed in [($Tp^{Ph,Me}$)Zn(**3.21**)] and [($Tp^{Ph,Me}$)Zn(**3.23**)]. It is unlikely that the pyrazole displacement is the result of a steric clash between the exocyclic substituent of the MBIs and the substituted pyrazole ring, as the structure of [($Tp^{Ph,Me}$)Zn(**3.20**)] (Figure 3.2) shows the expected, tridentate mode of $Tp^{Ph,Me}$ binding, whilst possessing a similar exocyclic substituent. Based on these observations, the pyrazole displacement in [($Tp^{Ph,Me}$)Zn(**3.21**)] and [($Tp^{Ph,Me}$)Zn(**3.23**)] are likely due to electronic effects, although further

studies are necessary to confirm this hypothesis and whether it may be relevant to the inhibition of metalloenzymes by these MBIs.

All MBIs structurally characterized as [($Tp^{Ph,Me}$)Zn] complexes exhibited a similar bidentate coordination motif. This indicates that carboxylic acid isostere replacement does not result in a loss of metal binding ability for these compounds. Overall, these results demonstrate that isostere replacement is an effective method for opening new chemical space for metalloenzyme inhibition.

3.4 Physicochemical Properties of Metal-Binding Isosteres

Upon determining that MBIs retain the coordinative abilities of **3.1**, an evaluation of physicochemical properties was performed. The acidity (pK_a) of the acidic isostere group of each MBI was determined using UV-based or potentiometric methods (Table 3.1).[23-24] The MBIs exhibited a broad range of acidity constants (pK_a <1.5 to >12.5) demonstrating the ability to modulate this important physicochemical property. The compounds were further analyzed by determining the hydrophobicity (LogP) via a potentiometric method,[25] which combined with pK_a values was then used to derive the lipophilicity ($LogD_{7.4}$) at pH 7.4 (Table 3.1).

From the results of the physicochemical analysis of the MBIs, a wide range of pK_a, LogP, and $LogD_{7.4}$ values were achieved. In light of the wide range of pK_a values measured, (**3.12** vs. **3.23**, Table 3.1), it is apparent that changes in pK_a do not interfere with the ability of these MBIs to form metal complexes, as evidence by the results with [($Tp^{Ph,Me}$)Zn(MBI)] model compounds. Perhaps more important were the large variations in LogP and $LogD_{7.4}$ of the MBIs. LogP ranged from -0.6 to ~1.5 (**3.5** vs. **3.11**, Table 3.1) [($Tp^{Ph,Me}$)Zn(MBI)] and similarly $LogD_{7.4}$ values ranged

from -3.43 to 1.54 (**3.23** vs. **3.11**, Table 3.1). Overall, these results show it is possible to significantly modulate physicochemical properties of the metal binding motif, while still preserving metal coordination capabilities. The ability to independently modulate these features of a metal-binding motif suitable for drug development has not been previously demonstrated.

Table 3.1. Measured physicochemical properties of picolinic acid and related MBIs.

Compound	pK_a [a]	LogP [a]	$LogD_{7.4}$
3.1	<1.5	<-2	<-2
3.5	9.30	-0.59	-0.55
3.6	>12.5	-0.66	-0.66
3.7	8.39	0.07	0.02
3.9	8.29	-0.37	-0.42
3.11	11.25	1.54	1.54
3.12	12.31	0.19	0.19
3.15	4.87	0.49	-2.04
3.16	>12.5	1.29	1.29
3.18	7.88	0.97	0.84
3.19	4.04	0.62	-2.72
3.20	4.76	0.65	-1.43
3.21	8.02	0.32	0.02
3.22	5.71	1.42	-0.21
3.23	3.09	0.88	-3.43

[a]All pK_a and LogP experiments yielded standard deviations <0.05.

3.5 Metal-Binding Isostere Screening

To assess the utility of MBIs to serve as fragments for metalloenzyme targeted FBDD, the MBIs were screened against several metalloenzymes for inhibitory activity. Endo, a dinuclear Mn^{2+}/Mg^{2+} metalloenzyme was selected as it is inhibited by picolinic acid (**3.1**). In contrast, the Zn^{2+} metalloenzyme hCAII was selected because it is not effectively inhibited by picolinic acid (**1,** IC50 >1 mM, unpublished data), which would therefore reveal any unexpected (and potentially off-target) activity of the MBIs. Both Endo and hCAII were screened against **3.1** and the MBIs at a fragment concentration of 200 μM (Figure 3.3).

From the screening results against Endo, approximately half of the MBIs exhibited similar inhibitory activity as picolinic acid (generally within ~20% of the activity of **3.1**). MBIs **3.3**, **3.5**, **3.8**, **3.11**, **3.12**, **3.13**, **3.16**, **3.18**, and **3.23** exhibited poorer activity (<15% inhibition at 200 μM), while **3.9** exhibited significantly improved activity (~96% inhibition at 200 μM). The improved activity of **3.9** might originate from coordination to both Mn^{2+} ions of the dinuclear Endo active site. It is possible that the hydroxamate group of **3.9** is engaging in bidentate coordination to one ion and the pyridine and the hydroxamate carbonyl oxygen coordinate the other (Figure 3.S16).[26] Overall, a significant number (~50%) of MBIs exhibited comparable inhibitory activity as **3.1** towards Endo showing that MBIs provide versatile scaffolds for isostere replacement in metalloenzyme inhibitors.

Compound	Endo	hCAII
3.1	41	<5
3.2	41	<5
3.3	12	6
3.4	45	<5
3.5	6	100
3.6	20	6
3.7	49	<5
3.8	14	13
3.9	96	33
3.10	22	<5
3.11	<5	<5
3.12	8	6
3.13	<5	32
3.14	31	<5
3.15	22	<5
3.16	13	10
3.17		12
3.18	<5	
3.19	18	<5
3.2	30	<5
3.21	39	<5
3.22	40	<5
3.23	11	<5
3.24	22	<5

Figure 3.3. Thermoplot of screening of MBIs against Endo (200 μM) and hCAII (200 μM) with percent inhibition values included. Cells are color-coded by percent inhibition: white (<20%), yellow (20-50%), and red (51-100%). Gray cells were compounds that interfered with the assay. Percent inhibition values and standard deviations can be found in the Appendix (Table 3.S5 and Table 3.S6).

In contrast to Endo, only three MBIs (**3.5**, **3.9**, **3.13**, Figure 3.3) exhibited any significant inhibitory activity against hCAII. Only compound **3.5**, which possesses a sulfonamide isostere, showed strong inhibition of hCAII (100% inhibition at 200 μM). This was unsurprising, as aryl sulfonamides are a privileged scaffold for inhibition of carbonic anhydrases.[27] Similarly, hydroxamic acids have previously been shown to inhibit hCAII,[28] which is the isostere found in com-

pound **3.9**, which demonstrated weak inhibitory activity (~33% inhibition at 200 μM). Surprisingly, MBI **3.13** exhibited inhibitory activity (32% inhibition at 200 μM), which was unexpected as the very similar MBI **3.12** showed no activity. The observed lack of activity with **3.12** suggests that the thietane moiety of **3.13** is having some inhibitory effect. In general, isostere replacement did not result in an appearance of unexpected inhibitory activity against hCAII.

Overall, the screening results against Endo and hCAII, demonstrate that isostere replacement results in similar activity as **3.1** against different metalloenzymes. MBIs generally maintained inhibitory activity against Endo, but showed no unanticipated, emergent inhibition against hCAII. Based on these results, isostere replacement of MBPs with carboxylic acid groups results in MBIs that retain activity without introducing unexpected, off-target activity. These results establish MBIs as a new set of scaffolds for metalloenzyme FBDD.

3.6 Conclusions

Isostere replacement of MBPs to produce MBIs is a viable strategy for metalloenzyme inhibition for a large number of carboxylic acid isosteres. The broad range of isosteres utilized in this work, particularly some of the more exotic heterocycle isosteres, provide a novel source of metal binding functional groups not previously described in inorganic, bioinorganic, or medicinal chemistry. Without sacrificing inhibitory activity, MBIs can be used to modulate the physicochemical properties of metalloenzyme inhibitors at the metal binding warhead, which is frequently plagued with limited chemical diversity. Based on the success of these MBIs, isostere replacement holds great promise as a viable method for other functional groups found in MBPs. While the work presented so far demonstrates the foundations for the application of MBIs, further analysis

on more complex systems would be worthwhile. In Chapter 4, isostere replacement of carboxylic acids on a series of isosteric heteroarene MBP scaffolds is assessed to demonstrate the robustness of isostere replacement on MBP scaffolds. The purpose behind this expanded study is that often the success of an isostere replacement is dependent on the scaffold it is performed on.

3.7 Experimental

General Information. Starting materials and solvents were purchased and used without further purification from commercial suppliers (Sigma-Aldrich, Alfa Aesar, EMD, TCI, etc.). Detailed syntheses of each MBI are provided in the Appendix. [($Tp^{Ph,Me}$)ZnOH] ($Tp^{Ph,Me}$= hydrotris(5,3-methylphenylpyrazolyl)borate)) was synthesized as reported using [$Tp^{Ph,Me}$K], which was prepared as previously reported.[20] Absorbance and fluorescence activity assays were carried out using a BioTek Synergy HT plate reader.

Synthesis and Crystallization of TpZn(MBI) Model Complexes. [($Tp^{Ph,Me}$)ZnOH] (150 mg, 0.27 mmol) was dissolved in 15 mL of CH_2Cl_2 in a 50 mL round bottom flask. The MBI (0.27 mmol, 1 equiv) in 10 mL of MeOH was added and the reaction mixture was stirred overnight under a nitrogen atmosphere. The resulting mixture was evaporated to dryness via rotary evaporation and subsequently dissolved in a minimal amount (~10 mL) of benzene. The solution was filtered to remove any undissolved solids. The resulting complex in benzene was recrystallized using vapor diffusion with pentane; crystals typically formed within 1 week.

Physicochemical Properties Analysis. Physicochemical properties were determined using a Sirius T3 instrument. All titrations, both pK_a and LogP, were performed in 0.15 M KCl with 0.5 M

HCL and KOH. The pK_a was determined by analyzing each MBI sample in triplicate using potentiometric or UV-metric titrations.[23-24] Experiments were typically performed over a pH range of 2.0 to 12.0. Standard deviations were derived from fitting all three replicate experiments.

LogP was determined via potentiometric titrations in the presence of varying ratios of octanol and water.[25] The presence of octanol shifts the pK_a of ionizable species and based on the shift a LogP can be determined. Measurements for LogP determination were typically performed over a pH range of 2.0 to 12.0. Three experiments with varying ratios of water:octanol were performed, allowing for a standard deviation to be determined from the fitting of all measurements. Using the measured pK_a and LogP values, $LogD_{7.4}$ was derived. MBI sample sizes were ≤0.5 mg for both pK_a and LogP measurements.

Endonuclease Assay. Endonuclease was expressed and purified as previously reported.[11] The activity assays were carried out in black Costar 96-well plates with a total volume of 100 µL per well. Assay buffer consisted of 20 mM Tris pH 8.0, 150 mM NaCl, 2 mM $MnCl_2$, 10 mM 2-mercaptoethanol, and 0.2 % Triton-X100. Endo was included at a final concentration of 25 nM and MBIs were added from a 50 mM DMSO stock to a final concentration of 200 µM. A fluorescent ssDNA-oligo substrate [([6-FAM]AATCGCAGGCAGCACTC[TAM]), FAM = 6-Carboxyfluorescein, TAM = tetramethylrhodamine] was used to monitor enzymatic activity. After addition of substrate, fluorescence (λ_{ex} = 485 nm, λ_{em} = 528 nm) was monitored over 45 min at 37 °C. Negative control wells contained no inhibitor and were set to 100% activity. A reported pyridinone based inhibitor was included as a positive control for inhibition.[11] Percent inhibition was determined by comparing the activity of wells containing MBIs to the activity of those without.

hCAII Assay. The plasmid for recombinant expression of hCAII with a T7 RNA polymerase promotor and ampicillin resistance gene (pACA) was a gift from Thomas R. Ward (U. Basel, Switzerland). The protein for activity assays was expressed in BL21 *E. coli* cells and purified as reported previously.[29] Assays were carried out in clear-bottom Costar 96-well plates with a total volume of 100 µL per well. The assay buffer was comprised of 50 mM HEPES pH 8.0 and 100 mM $NaSO_4$. MBIs were added from a 50 mM DMSO stock to a final concentration of 200 µM and incubated with hCAII (100 nM final concentration) for 15 min at room temperature. *p*-Nitrophenyl acetate was used as the substrate (1 mM final concentration) and the absorbance at 405 nM was monitored for 20 min at 1 min intervals. Percent inhibition was determined by comparing the activity of wells containing MBIs to the activity of those without.

3.8 Appendix: Supporting Information

General Materials and Methods. Starting materials were purchased and used from commercially available suppliers (Sigma-Aldrich, Acros Organics, Matrix Scientific, others) without further purification. [($Tp^{Ph,Me}$)ZnOH] ($Tp^{Ph,Me}$= hydrotris(5,3-methylphenylpyrazolyl)borate)) was synthesized as previously reported.[20] Column Chromatography was performed using a CombiFlash R_f automated system from Teledyne Isco using prepacked silica cartridges. ^1H nuclear magnetic resonance (NMR) spectra were collected using a Varian spectrometer running at 400 MHz or a 300 MHz Bruker AVA. Mass spectrometry analysis was performed by the University of California San Diego Chemistry and Biochemistry Mass Spectrometry Facility (MMSF). Fourier-transform infrared spectroscopy (FTIR) analysis was performed using a Bruker Alpha-P spectrometer. The

purity of all synthesized compounds used in assays were determined to ≥95% by high performance liquid chromatography (HPLC).

Single Crystal X-ray Diffraction. Suitable crystals of [($Tp^{Ph,Me}$)Zn(MBI)] complexes were selected and placed on a Bruker APEX-II Ultra diffractometer with a Mo-Kα Microfocus Rotating Anode and a APEX-II CCD area detector or a Bruker Kappa diffractometer equipped with a Bruker X8 APEX II Mo sealed tube and a Bruker APEX-II CCD. The crystals were kept at 100 K during data collection. Using Olex2,[30] the structure was solved with the ShelXT[31] structure solution program using direct methods and refined with the XL[32] refinement package using least squares minimization. The crystal data file of all complexes was deposited into the Cambridge Crystallographic Data Centre (CCDC, Table 3.S1-Table 3.S4). Crystallographic data collection and refinement information is listed in Table 3.S1-Table 3.S4.

MBI Synthesis

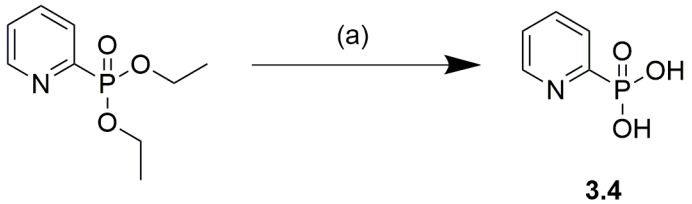

3.4

Scheme 3.S1. Synthesis of compound **3.4**. Reagents and conditions: (a) H_2O, 8 M HCl, 100℃, 12 h.

Synthesis of 3.4. Starting from pyridine *N*-oxide, diethyl pyridine-2-ylphosphonate was synthesized as previously reported.[33] Diethyl pyridine-2-ylphosphonate (0.20 g, 0.9 mmol) was dissolved in 10 mL of 8 M HCl. The mixture was stirred under nitrogen and heated to reflux for 12 h. The reaction mixture was evaporated to a solid on a rotary evaporator and coevaporated 6 times with MeOH to remove residual HCl. The solid was dissolved in ethanol (EtOH) and acetone was used to precipitate out the product as a white solid. Yield: 0.10 g (0.6 mmol, 70 %). ^{1}H NMR (300 MHz, D_2O): δ 8.68 (d, J_1 = 5.8 Hz, 1H), 8.54 (tdd, J_1 = 7.9, J_2 = 2.7, J_3 = 1.5 Hz, 1H), 8.17 (t, J_1 = 7.7 Hz, 1H), 8.00 (t, J_1 = 6.3 Hz, 1H). ESI-MS(-) calculated for $[C_5H_5NO_3P]^-$ 158.00, found *m/z* 158.24 $[M\text{-}H]^-$.

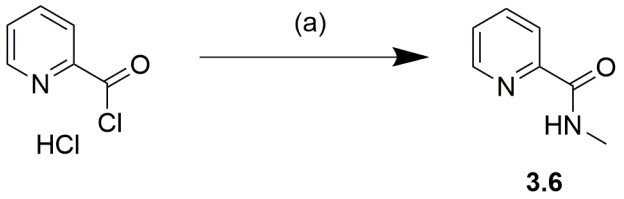

3.6

Scheme 3.S2 Synthesis of compound **3.6**. Reagents and conditions: (a) THF, TEA, methylamine, 25 ℃, overnight.

Synthesis of 3.6. Picolinoyl chloride hydrochloride (1.00 g, 5.6 mmol) was dissolved in 100 mL of tetrahydrofuran (THF) and triethylamine (TEA) (1.57 mL, 11.2 mmol). When the solution became clear, methylamine (3.10 mL, 6.2 mmol) in a 2 M THF solution was added and the mixture was stirred under nitrogen at room temperature overnight. The reaction mixture was evaporated to an oil on a rotary evaporator that was dried onto silica. The product was purified by column chromatography using a Hexanes:Ethyl Acetate (EtOAc) gradient of 0-65%. After removal of solvent the purified product was isolated as a yellow liquid. Yield: 0.52 g (3.9 mmol, 69%). ^{1}H NMR (300 MHz, DMSO): δ 8.78 (s, 1H), 8.63 (dd, J_1 = 2.8, J_2 = 1.9 Hz, 1H), 8.04 (d, J_1 = 7.3 Hz, 1H), 7.98 (td, J_1 = 7.5, J_2 = 1.6 Hz, 1H), 7.58 (ddd, J_1 = 7.1, J_2 = 4.8, J_3 = 1.5 Hz, 1H), 2.83 (d, J_1 = 4.9 Hz, 3H). ESI-MS(+) calculated for $[C_7H_9N_2O]^+$ 137.07, found *m/z* 137.06 $[M+H]^+$.

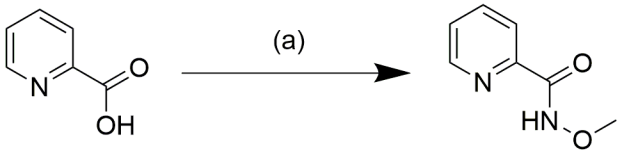

3.7

Scheme 3.S3. Synthesis of compound **3.7**. Reagents and conditions: (a) DMF, CDI, 25 ℃, 2 h, $CH_3ONH_2 \cdot HCl$, 25 ℃, overnight.

Synthesis of 3.7. Picolinic acid (0.5 g, 4.06 mmol) was dissolved in 2 mL of DMF (dry) to which Carbonyldiimidazole (CDI) (659 mg, 4.06 mmol) in 2 mL of dimethylformamide (DMF) (dry) was added slowly and stirred for 2 h under nitrogen. *O*-Methylhydroxylamine hydrochloride (678 mg, 8.12 mmol) was added and stirred overnight under nitrogen. The reaction was dried down via rotary evaporation to an oil which was loaded onto silica. The product was purified by column chromatography using a Hexanes:EtOAc gradient 0-60% with product eluting as the only major peak. After removal of solvent the product was obtained as a colorless oil. Yield: 0.41 g (2.7 mmol, 67 %). ^{1}H NMR (300 MHz, $CDCl_3$): δ 10.33 (s, 1H), 8.53 (d, J_1 = 4.5 Hz, 1H), 8.19 (d, J_1 = 7.8 Hz, 1H), 7.88 (td, J_1 = 7.8, J_2 = 1.7 Hz, 1H) 7.47 (ddd, J_1 = 7.6, J_2 = 4.8, J_2 = 1.2 Hz, 1H), 3.93 (s, 3H). ESI-MS(+) calculated for $[C_7H_9N_2O_2]^+$ 153.07, found *m/z* 153.08 $[M+H]^+$.

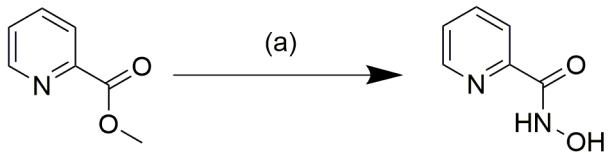

3.9

Scheme 3.S4. Synthesis of compound **3.9**. Reagents and conditions: (a) MeOH, KOH, $NH_2OH \cdot HCl$, 25 °C, overnight.

Synthesis of 3.9. Hydroxylamine hydrochloride (0.51 g, 7.3 mmol) was dissolved in 5 mL of hot MeOH. An additional 5 mL of MeOH containing KOH (0.61 g, 10.9 mmol) was added and the mixture was stirred over an ice bath for 30 min. Methyl picolinate (500 mg, 3.6 mmol) was added and the mixture was stirred under nitrogen at room temperature overnight. The reaction mixture was evaporated to an oil on a rotary evaporator that was then dried onto silica. The product was purified by column chromatography using a Hexanes:EtOAc gradient of 0-60%. After removal of solvent the purified product was isolated as a white solid. Yield: 0.42 g (3.0 mmol, 83%). ^{1}H NMR (300 MHz, DMSO-d_6): δ 11.42 (s, 1H), 9.09 (s, 1H), 8.60 (dt, J_1 = 4.7, J_2 = 1.2 Hz, 1H), 8.02 – 7.93 (m, 2H), 7.58 (dt, J_1 = 8.8, J_2 = 4.6 Hz, 1H). ESI-MS(-) calculated for $[C_6H_5N_2O_2]^-$ 137.04, found *m/z* 137.21 $[M-H]^-$.

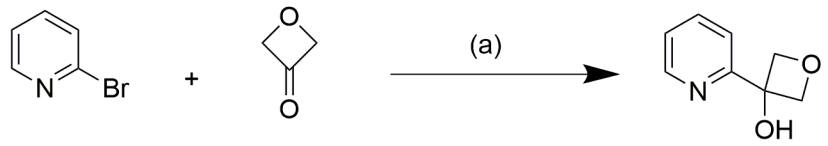

3.12

Scheme 3.S5. Synthesis of compound **3.12**. Reagents and conditions: (a) THF, *n*-BuLi, -78 °C, 2 hr, 25 °C, overnight.

Synthesis of 3.12. A solution of 2-bromopyridine (0.91 μL, 9.5 mmol) in 50 mL of THF was cooled to -78 °C and stirred for 30 min under nitrogen. 1 equiv of *n*-buthyllithium (*n*-BuLi) (2.5 M solution in hexanes, 3.8 mL, 9.5 mmol) was slowly added over a period of 5 min. The solution was stirred for 2 h at -78 °C after which oxetan-3-one (560 μL, 9.5 mmol) was added and the reaction solution was brought up to room temperature and stirred overnight under nitrogen. The reaction mixture was quenched with a saturated aqueous ammonium chloride solution and extracted with EtOAc. The organic layer was washed with brine and dried over magnesium sulfate. The organic layer was evaporated to an oil on a rotary evaporator that was then dried onto silica. The product was purified by column chromatography using a Hexanes:EtOAc gradient 0-55%. After removal of solvent the purified product was obtained as a yellow oil. Yield: 0.61 g (4.0 mmol, 42%). ^{1}H NMR (300 MHz, DMSO-d_6): δ 8.63 (ddd, J_1 = 4.8, J_2 = 1.7, J_3 = 0.9 Hz, 1H), 7.82 (td, J_1 = 7.7, J_2 = 1.8 Hz, 1H), 7.60 (dt, J_1 = 7.9, J_2 = 1.0 Hz, 1H), 7.33 (ddd, J_1 = 7.5, J_2 = 4.8, J_3 = 1.2 Hz, 1H), 6.54 (s, 1H), 4.92 (d, J_1 = 6.0 Hz, 2H), 4.66 (d, J_1 = 6.0 Hz, 2H). ESI-MS(+) calculated for $[C_8H_{10}NO_2]^+$ 152.07, found *m/z* 152.12 $[M+H]^+$. IR (neat, cm^{-1}): 3353, 2948, 2873, 1591, 1436, 1329, 1176, 1075.

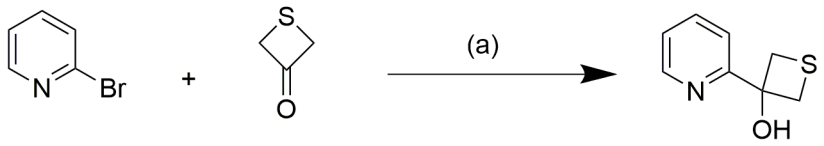

3.13

Scheme 3.S6. Synthesis of compound **3.13**. Reagents and conditions: (a) THF, *n*-BuLi, -78 °C, 2 hr, 25 °C, overnight.

Synthesis of 3.13. A solution of 2-bromopyridine (0.91 μL, 9.5 mmol) in 50 mL of THF was cooled to -78 °C and stirred for 30 min under nitrogen. 1 equiv of *n*-BuLi (2.5 M solution in hexanes, 3.8 mL, 9.5 mmol) was slowly added over a period of 5 min. The solution was stirred for 2 h at -78 °C after which thietan-3-one (0.84 g, 9.5 mmol) dissolved in 5 mL of THF was added and the reaction solution was brought up to room temperature and stirred overnight under nitrogen. The reaction mixture was quenched with saturated an aqueous ammonium chloride solution and extracted with EtOAc. The organic layer was washed with brine and dried over magnesium sulfate. The organic layer was evaporated to an oil on a rotary evaporator that was then dried onto silica. The product was purified by column chromatography using a Hexanes:EtOAc gradient 0-20%. After removal of solvent the purified product was obtained as a brown oil. Yield: 0.63 g (3.8 mmol, 40%). ^{1}H NMR (300 MHz, DMSO-d_6): δ 8.60 (ddd, J_1 = 4.8, J_2 = 1.7, J_3 = 0.9 Hz, 1H), 7.85 (td, J_1 = 7.9, J_2 = 1.8 Hz, 1H), 7.63 (dt, J_1 = 8.0, J_2 = 1.0 Hz, 1H), 7.35 (ddd, J_1 = 7.4, J_2 = 4.8, J_3 = 1.1f Hz, 1H), 6.49 (s, 1H), 3.75 (d, J_1 = 9.9 Hz, 2H), 3.42 (d, J_1 = 9.9 Hz, 2H). ESI-MS(+) calculated for $[C_8H_{10}NOS]^+$ 168.05, found *m/z* 167.99 $[M+H]^+$. IR (neat, cm^{-1}): 3345, 2937, 1591, 1434, 1388, 1209, 1064.

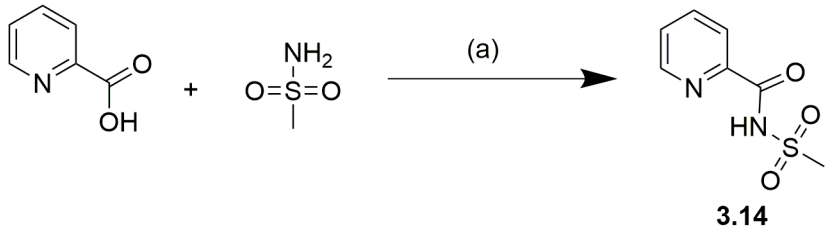

Scheme 3.S7. Synthesis of compound **3.14**. Reagents and conditions: (a) CH_2Cl_2, DCC, DMAP, 25 °C, 18 h.

Synthesis of 3.14. 2-[(Methylsulfonyl)carbamoyl)pyridine was prepared as previously reported.[34] Picolinic acid (0.31 g, 2.5 mmol) was dissolved in 50 mL of CH_2Cl_2. Methanesulfonamide (0.24 g, 2.5 mmol) was added followed by *N*,*N*-dicyclohexylcarbodiimide (DCC) (0.52 g, 2.5 mmol) and 4-(dimethylamino)pyridine (DMAP) (0.31 g, 2.5 mmol). The solution was stirred for 18 h at room temperature. The resulting mixture was filtered using filter paper and vacuum filtration, and the collected filtrate was washed with saturated sodium bicarbonate solution. The aqueous layer was washed twice with ether, acidified to pH 1.0 with 6M HCl, and extracted with ethyl acetate. The organic layer was washed with brine, dried over $MgSO_4$, and dried to a solid on a rotary evaporator. The product was recrystallized from Hexanes:EtOAc and obtained as beige crystals. Yield: 0.11 g (0.6 mmol, 22%). ^{1}H NMR (400 MHz, $CDCl_3$): δ 10.32 (s, 1H), 8.62 (ddd, J_1 = 4.8, J_2 = 1.6, J_3 = 0.9 Hz, 1H), 8.23 (dt, J_1 = 7.8, J_2 = 1.0 Hz, 1H), 7.94 (td, J_1 = 7.7, J_2 = 1.7 Hz, 1H), 7.58 (ddd, J_1 = 7.6, J_2 = 4.8, J_3 = 1.2 Hz, 1H), 3.41 (s, 3H). ESI-MS(-) calculated for $[C_7H_7N_2SO_3]^-$ 199.02, found *m/z* 199.25 $[M-H]^-$.

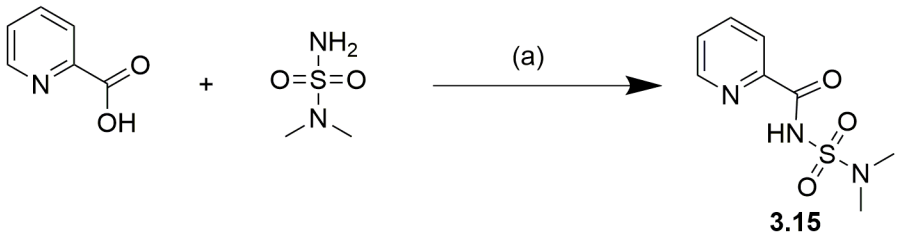

Scheme 3.S8. Synthesis of compound **3.15**. Reagents and conditions: (a) THF, CDI, 55 °C, 1 hr, DBU, 25 °C, 24 h.

Synthesis of 3.15. Picolinic acid (0.78 g, 6.3 mmol) was dissolved in 6 mL of THF. CDI (1.17 g, 7.2 mmol) was added and stirred for 20 min at room temperature until bubbles stopped forming. The reaction solution was then stirred for 1 h at 55 °C. The solution was cooled to room temperature and DBU (0.95 mL, 6.3 mmol) was added followed by the dropwise addition of *N*,*N*-dimethylsulfamide (0.94 g, 7.6 mmol) in 4 mL of THF. The reaction was stirred for 24 h at room temperature. The reaction solution was concentrated on a rotary evaporator and loaded onto silica. The product was purified by column chromatography using a Hexanes:EtOAc gradient of 0-65%. The product was recrystallized from isopropanol and obtained as a white crystalline solid. Yield: 0.64 g (2.8 mmol, 44%). ^{1}H NMR (300 MHz, DMSO-d_6): δ 11.43 (s, 1H), 8.72 (d, J_1 = 4.7 Hz, 1H), 8.08 (d, J_1 = 3.7 Hz, 2H), 7.72 (dd, J_1 = 8.8, J_2 = 4.7 Hz, 1H), 2.90 (s, 6H). ESI-MS(-) calculated for $[C_8H_{10}N_3O_3S]^-$ 228.04, found *m/z* 228.19 $[M-H]^-$. IR (neat, cm^{-1}): 3064, 1690, 1457, 1353, 1162, 1088.

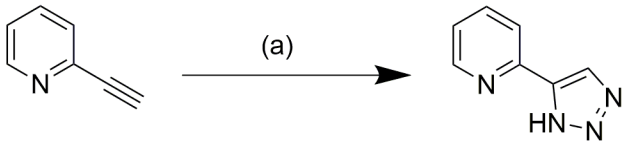

3.18

Scheme 3.S9. Synthesis of compound **3.18**. Reagents and conditions: (a) DMF:MeOH, Trimethylsilyl azide, CuI, 100 °C, overnight.

Synthesis of 3.18. 2-Ethynylpyridine (1.00 g, 9.7 mmol) was dissolved in 20 mL of a DMF:MeOH (9:1) solution. Trimethylsilyl azide (2 mL, 20 mmol) and copper(I) iodide (0.09 g, 0.5 mmol) were added and the mixture was stirred under nitrogen at 100 °C overnight. The reaction mixture was concentrated on a rotary evaporator and loaded onto silica. The product was purified by column chromatography using a Hexanes:EtOAc gradient of 0-50%. After removal of solvent the purified product was isolated as a white solid. Yield: 0.22 g (1.5 mmol, 15%). ^{1}H NMR (300 MHz, $CDCl_3$): δ 8.73 (d, J_1 = 4.4 Hz, 1H), 8.45 (s, 1H), 8.04 (d, J_1 = 7.9 Hz, 1H), 7.86 (td, J_1 = 7.8, J_2 = 1.7 Hz, 1H), 7.35 (ddd, J_1 = 7.4, J_2 = 5.0, J_3 = 1.0 Hz, 1H). ESI-MS(-) calculated for $[C_7H_5N_4]^-$ 145.05, found *m/z* 145.22 $[M-H]^-$.

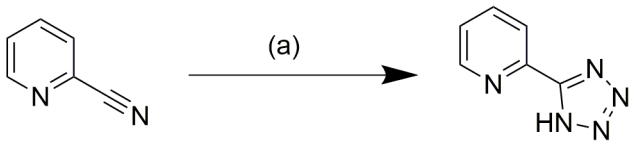

3.19

Scheme 3.S10. Synthesis of compound **3.19**. Reagents and conditions: (a) DMF, NaN_3, NH_4Cl, 110 °C, 3 h.

Synthesis of 3.19. Picolinonitrile (2.00 g, 19.2 mmol) was dissolved in 20 mL of DMF. Sodium azide (1.87 g, 28.8 mmol) and ammonium chloride (1.54 g, 28.8 mmol) were added and the mixture was stirred under nitrogen at 110 °C for 3 h. The reaction mixture was concentrated down almost to dryness on a rotary evaporator. Water was added and the solution was acidified to pH 2.0 using 6 M HCl. The product began precipitating as a solid immediately and was collected by filtration. The collected white solid was washed with water and dried. Yield: 2.83 g (14.5 mmol, 75%). ^{1}H NMR (300 MHz, DMSO-d_6): δ 8.81 (ddd, J_1 = 4.8, J_2 = 1.7, J_3 = 0.9 Hz, 1H), 8.24 (dt, J_1 = 7.9, J_2 = 1.1 Hz, 1H), 8.09 (td, J_1 = 7.7, J_2 = 1.7 Hz, 1H), 7.64 (ddd, J_1 = 7.6, J_2 = 4.8, J_3= 1.2 Hz, 1H). ESI-MS(+) calculated for $[C_6H_6N_5]^+$ 148.06, found *m/z* 148.11 $[M+H]^+$.

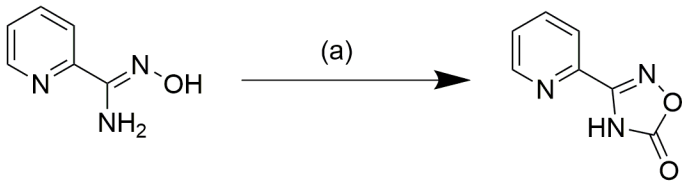

3.20

Scheme 3.S11. Synthesis of compound **3.20**. Reagents and conditions: (a) Pyridine, ethyl chloroformate, 115 °C, 6 h.

Synthesis of 3.20. 3-Pyridin-2-yl-4*H*-[1,2,4]oxadiazol-5-one (**3.20**) was prepared as previously reported.[35] *N*-hydroxypicolinimidamide (1.37 g, 10.0 mmol) was dissolved in 20 mL of dry pyridine. Ethyl chloroformate was added and the mixture was stirred under nitrogen for 6 h at reflux. The reaction mixture was concentrated and diluted with water and a precipitate formed. The precipitate was washed with water and recrystallized from water producing beige needles, which were collected by filtration. Yield: 0.89 g (5.5 mmol, 55%). ^{1}H NMR (300 MHz, DMSO-d_6): δ 13.16 (s, 1H), 8.77 (ddd, J_1 = 4.8, J_2 = 1.6, J_3 = 1.0 Hz, 1H), 8.09 - 8.02 (m, 1H), 8.00 (dt, J_1 = 7.9, J_2 =1.4 Hz, 1H), 7.67 (ddd, J_1 = 7.3, J_2 = 4.8, J_3 = 1.5 Hz, 1H). ESI-MS(+) calculated for $[C_7H_6N_3O_2]^+$ 164.05, found *m/z* 164.12 $[M+H]^+$.

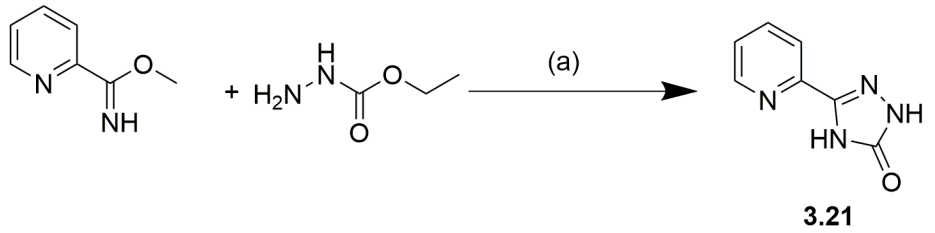

Scheme 3.S12. Synthesis of compound **3.21**. Reagents and conditions: (a) 200℃, 10 min.

Synthesis of 3.21. 5-(2-Pyridyl)-1,2,4-triazole-3-one (**3.21**) was prepared as previously reported.[15] Methyl picolinimidate (0.80 g, 5.9 mmol) and ethyl carbazate (0.61 g, 5.9 mmol) were melted together at 200 °C and stirred for 10 min. The resulting solid was recrystallized from EtOH to yield a white solid. Yield: 0.36 g (2.2 mmol, 37%). ^{1}H NMR (300 MHz, DMSO-d_6): δ 12.07 (s, 1H), 11.81 (s, 1H), 8.63 (dt, J_1 = 4.9, J_2 = 1.3 Hz, 1H), 7.93 (t, J_1 = 1.5 Hz, 1H), 7.92 (d, J_1 = 1.3 Hz, 1H), 7.52 – 7.42 (m, 1H). ESI-MS(+) calculated for $[C_7H_7N_4O]^+$ 163.06, found *m/z* 163.22 $[M+H]^+$.

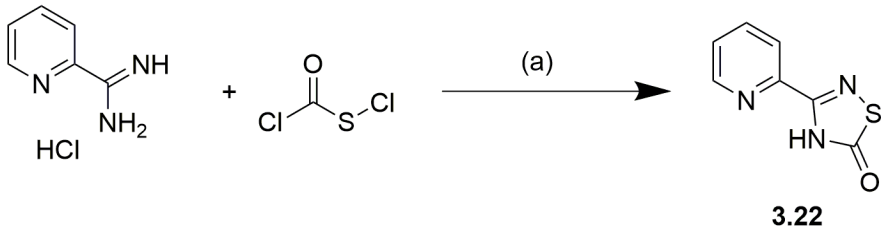

3.22

Scheme 3.S13. Synthesis of compound **3.22**. Reagents and conditions: (a) $CHCl_3$, TEA, 25℃, 3 h.

Synthesis of 3.22. Picolinimidamide hydrochloride (0.72 g, 4.6 mmol) was dissolved in 10 mL of chloroform and TEA (2.1 mL, 15 mmol). The solution was stirred on ice as chlorocarboynl-sulfenyl chloride (0.42 mL, 5.0 mmol) in 10 mL of $CHCl_3$ was added dropwise. The reaction solution was then heated to room temperature and stirred for ~3 h. The reaction mixture was evaporated to an oil on a rotary evaporator that was then dried onto silica. The mixture was purified by column chromatography using a Hexanes:EtOAc gradient 0-45%. After removal of solvent the purified product was obtained as a white solid. Yield: 0.08 g (0.4 mmol, 9 %). ^{1}H NMR (300 MHz, DMSO-d_6): δ 13.55 (s, 1H), 8.70 (d, J_1 = 3.4 Hz, 1H), 8.14 (d, J_1 = 7.5 Hz, 1H), 8.03 (t, J_1 = 7.3 Hz, 1H), 7.61 (t, J_1 = 5.7 Hz, 1H). ESI-MS(+) calculated for $[C_7H_6N_3OS]^+$ 180.02, found *m/z* 180.15 $[M+H]^+$. IR (neat, cm^{-1}): 3056, 1678, 1455, 1410.

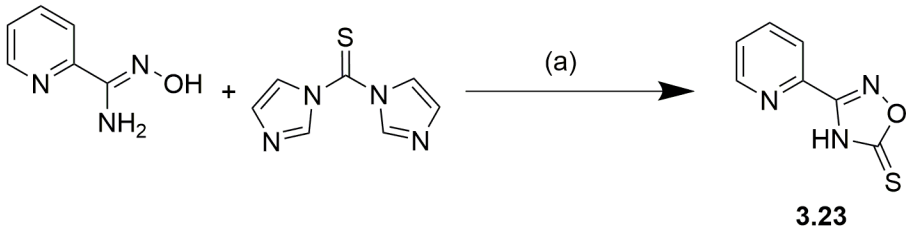

3.23

Scheme 3.S14. Synthesis of compound **3.23**. Reagents and conditions: (a) DBU, 25℃, overnight.

Synthesis of 3.23. *N*-Hydroxypicolinimidamide (1.0 g, 7.3 mmol) was dissolved in 60 mL of CH_3CN. 1,1'-Thiocarbonyldiimidazole (1.94 g, 10.9 mmol) and diazabicycloudecene (DBU) (4.4 mL, 29 mmol) were added and the mixture was stirred under nitrogen at room temperature overnight. The reaction mixture was diluted with water and acidified with 6 M HCl until a yellow precipitate formed. The precipitate was collected by filtration, washed with water, and dried resulting in a yellow solid. Yield: 0.51 g (2.9 mmol, 39%). ^{1}H NMR (300 MHz, DMSO-d_6): δ 8.80 (d, J_1= 4.7 Hz, 1H), 8.13 - 8.02 (m, 2H), 7.70 (ddd, J_1 = 6.8, J_2=4.8, J_3=2.1 Hz, 1H). ESI-MS(+) calculated for $[C_7H_6N_3OS]^+$ 180.02, found *m/z* 180.11 $[M+H]^+$. IR (neat, cm^{-1}): 3004, 1587, 1434, 1156.

Table 3.S1. Crystal data and structure refinement for [($Tp^{Ph,Me}$)Zn(**3.3**)], [($Tp^{Ph,Me}$)Zn(**3.5**)], and [($Tp^{Ph,Me}$)Zn(**3.7**)] complexes.

Compound	[($Tp^{Ph,Me}$)Zn(**3.3**)]	[($Tp^{Ph,Me}$)Zn(**3.5**)]	[($Tp^{Ph,Me}$)Zn(**3.7**)]
Identification code	1838692	1838693	1838694
Empirical formula	$C_{35}H_{32}BN_7O_3SZn$	$C_{35}H_{33}BN_8O_2SZn$	$C_{424}H_{404}B_{12}Cl_8N_{80}O_8Zn_{12}$
Formula weight	706.91	705.93	7946.01
Temperature/K	100.0	100.0	100.0
Crystal system	triclinic	monoclinic	monoclinic
Space group	P-1	$P2_1/c$	$P2_1/c$
a/Å	11.62(2)	11.6894(14)	31.866(2)
b/Å	11.74(2)	12.1114(17)	15.9078(12)
c/Å	11.97(2)	23.268(5)	19.7233(13)
α/°	88.82(3)	90	90
β/°	81.70(3)	91.331(7)	96.751(2)
γ/°	85.55(5)	90	90
Volume/$Å^3$	1611(6)	3293.3(9)	9928.7(12)
Z	2	4	1
$\rho_{calc}g/cm^3$	1.458	1.424	1.329
μ/mm^{-1}	0.876	0.856	0.834
F(000)	732.0	1464.0	4128.0
Crystal size/mm^3	0.1 × 0.05 × 0.05	0.35 × 0.15 × 0.15	0.3 × 0.1 × 0.05
Radiation	MoKα (λ = 0.71073)	MoKα (λ = 0.71073)	MoKα (λ = 0.71073)
2Θ range for data collection/°	3.44 to 50.214	3.792 to 56.502	3.45 to 46.6
Index ranges	$-13 \le h \le 13$, $-13 \le k \le 13$, $-14 \le l \le 14$	$-15 \le h \le 15$, $-16 \le k \le 16$, $-30 \le l \le 29$	$-35 \le h \le 35$, $-17 \le k \le 17$, $-21 \le l \le 17$
Reflections collected	30274	64925	94730
Independent reflections	5721 [R_{int} = 0.0372, R_{sigma} = 0.0306]	8137 [R_{int} = 0.0668, R_{sigma} = 0.0353]	14275 [R_{int} = 0.1151, R_{sigma} = 0.0868]
Data/restraints/parameters	5721/0/436	8137/0/440	14275/1300/1251
Goodness-of-fit on F^2	1.032	1.100	1.188
Final R indexes [I>=2σ (I)]	R_1 = 0.0318, wR_2 = 0.0728	R_1 = 0.0368, wR_2 = 0.0878	R_1 = 0.0893, wR_2 = 0.1778
Final R indexes [all data]	R_1 = 0.0425, wR_2 = 0.0776	R_1 = 0.0431, wR_2 = 0.0909	R_1 = 0.1325, wR_2 = 0.2019
Largest diff. peak/hole / e $Å^{-3}$	0.48/-0.39	0.49/-0.66	0.95/-1.35

Table 3.S2. Crystal data and structure refinement for [($Tp^{Ph,Me}$)Zn(**3.9**)], [($Tp^{Ph,Me}$)Zn(**3.11**)], and [($Tp^{Ph,Me}$)Zn(**3.12**)] complexes.

Compound	[($Tp^{Ph,Me}$)Zn(**3.9**)]	[($Tp^{Ph,Me}$)Zn(**3.11**)]	[($Tp^{Ph,Me}$)Zn(**3.12**)]
Identification code	1838695	1838696	1838697
Empirical formula	$C_{36}H_{33}BN_8O_2Zn$	$C_{43}H_{39}BF_3N_7OZn$	$C_{38}H_{36}BN_7O_2Zn$
Formula weight	685.88	802.99	698.92
Temperature/K	100.0	100.0	100.0
Crystal system	monoclinic	triclinic	monoclinic
Space group	$P2_1/c$	P-1	$P2_1/n$
a/Å	11.6710(6)	11.537(8)	23.6217(12)
b/Å	12.0737(7)	11.863(8)	12.1768(6)
c/Å	23.1806(12)	15.509(10)	24.0024(12)
α/°	90	85.106(11)	90
β/°	92.188(2)	77.257(18)	100.5950(10)
γ/°	90	64.911(9)	90
Volume/Å3	3264.0(3)	1875(2)	6786.3(6)
Z	4	2	8
ρcalcg/cm3	1.396	1.422	1.368
μ/mm-1	0.799	0.716	0.770
F(000)	1424.0	832.0	2912.0
Crystal size/mm3	0.15 × 0.15 × 0.15	0.15 × 0.1 × 0.05	0.25 × 0.25 × 0.25
Radiation	MoKα (λ = 0.71073)	MoKα (λ = 0.71073)	MoKα (λ = 0.71073)
2Θ range for data collection/°	3.804 to 52.86	2.692 to 52.894	2.678 to 52.842
Index ranges	$-14 \le h \le 14$, $-15 \le k \le 15$, $-28 \le l \le 28$	$-14 \le h \le 14$, $-14 \le k \le 14$, $-19 \le l \le 19$	$-29 \le h \le 29$, $-15 \le k \le 15$, $-30 \le l \le 25$
Reflections collected	52324	47643	91997
Independent reflections	6693 [R_{int} = 0.0490, R_{sigma} = 0.0301]	7723 [R_{int} = 0.0526, R_{sigma} = 0.0391]	13916 [R_{int} = 0.0819, R_{sigma} = 0.0480]
Data/restraints/parameters	6693/0/437	7723/0/512	13916/0/889
Goodness-of-fit on F2	1.044	1.014	1.024
Final R indexes [I>=2σ (I)]	R_1 = 0.0315, wR_2 = 0.0716	R_1 = 0.0325, wR_2 = 0.0690	R_1 = 0.0349, wR_2 = 0.0917
Final R indexes [all data]	R_1 = 0.0433, wR_2 = 0.0760	R_1 = 0.0471, wR_2 = 0.0739	R_1 = 0.0422, wR_2 = 0.0971
Largest diff. peak/hole / e Å-3	0.34/-0.37	0.35/-0.32	0.37/-0.40

Table 3.S3. Crystal data and structure refinement for [($Tp^{Ph,Me}$)Zn(**3.15**)], [($Tp^{Ph,Me}$)Zn(**3.17**)], [($Tp^{Ph,Me}$)Zn(**3.18**)], and [($Tp^{Ph,Me}$)Zn(**3.19**)] complexes.

Compound	[($Tp^{Ph,Me}$)Zn(**3.15**)]	[($Tp^{Ph,Me}$)Zn(**3.17**)]	[($Tp^{Ph,Me}$)Zn(**3.18**)]	[($Tp^{Ph,Me}$)Zn(**3.19**)]
Identification code	1838698	1838699	1838700	1838701
Empirical formula	$C_{41}H_{41}BN_9O_3SZn$	$C_{37.5}H_{38}BN_{10}O_2Zn$	$C_{37}H_{33}BN_{10}Zn$	$C_{36}H_{32}BN_{11}Zn$
Formula weight	816.07	736.96	693.91	694.90
Temperature/K	100.0	100.0	100.0	100.0
Crystal system	triclinic	triclinic	triclinic	monoclinic
Space group	P-1	P-1	P-1	$P2_1/n$
a/Å	12.0520(4)	11.361(4)	11.7162(8)	13.1556(10)
b/Å	17.6856(6)	12.052(4)	11.9647(12)	13.7425(13)
c/Å	19.9590(7)	13.195(4)	12.0302(12)	18.2154(15)
α/°	72.3740(10)	82.948(7)	87.009(3)	90
β/°	86.9540(10)	81.488(8)	88.700(2)	93.898(2)
γ/°	81.7720(10)	87.291(8)	82.024(2)	90
Volume/$Å^3$	4012.5(2)	1772.5(10)	1667.6(3)	3285.6(5)
Z	4	2	2	4
$\rho_{calc}g/cm^3$	1.351	1.381	1.382	1.405
μ/mm^{-1}	0.715	0.743	0.781	0.793
F(000)	1700.0	768.0	720.0	1440.0
Crystal size/mm^3	0.3 × 0.2 × 0.2	0.45 × 0.2 × 0.1	0.35 × 0.15 × 0.05	0.3 × 0.2 × 0.15
Radiation	MoKα (λ = 0.71073)	MoKα (λ = 0.71073)	MoKα (λ = 0.71073)	MoKα (λ = 0.71073)
2Θ range for data collection/°	2.438 to 52.818	3.142 to 52.036	3.442 to 50.264	3.702 to 52.73
Index ranges	$-15 \le h \le 15$, $-22 \le k \le 22$, $-24 \le l \le 24$	$-13 \le h \le 14$, $-14 \le k \le 14$, $0 \le l \le 16$	$-13 \le h \le 13$, $-14 \le k \le 14$, $-14 \le l \le 14$	$-16 \le h \le 16$, $-17 \le k \le 17$, $-22 \le l \le 22$
Reflections collected	56186	14236	36919	34762
Independent reflections	16419 [R_{int} = 0.0340, R_{sigma} = 0.0379]	6945 [R_{int} = 0.0131, R_{sigma} = 0.0306]	5922 [R_{int} = 0.0805, R_{sigma} = 0.0650]	6676 [R_{int} = 0.0430, R_{sigma} = 0.0354]
Data/restraints/parameters	16419/0/1019	6945/0/489	5922/0/445	6676/0/445
Goodness-of-fit on F^2	1.016	1.076	1.034	1.052
Final R indexes [I>=2σ (I)]	R_1 = 0.0316, wR_2 = 0.0705	R_1 = 0.0412, wR_2 = 0.0984	R_1 = 0.0391, wR_2 = 0.0695	R_1 = 0.0347, wR_2 = 0.0783
Final R indexes [all data]	R_1 = 0.0456, wR_2 = 0.0757	R_1 = 0.0566, wR_2 = 0.1126	R_1 = 0.0662, wR_2 = 0.0777	R_1 = 0.0462, wR_2 = 0.0828
Largest diff. peak/hole / e $Å^{-3}$	0.38/-0.40	0.51/-0.65	0.35/-0.42	0.44/-0.36

Table 3.S4. Crystal data and structure refinement for [($Tp^{Ph,Me}$)Zn(**3.20**)], [($Tp^{Ph,Me}$)Zn(**3.21**)], [($Tp^{Ph,Me}$)Zn(**3.23**)], and [($Tp^{Ph,Me}$)Zn(**3.24**)] complexes.

Compound	[($Tp^{Ph,Me}$)Zn(**3.20**)]	[($Tp^{Ph,Me}$)Zn(**3.21**)]	[($Tp^{Ph,Me}$)Zn(**3.23**)]	[($Tp^{Ph,Me}$)Zn(**3.24**)]
Identification code	1838702	1838703	1838704	1838705
Empirical formula	$C_{37}H_{32}BN_9O_2Zn$	$C_{40}H_{38}BN_{10}O_2Zn$	$C_{320}H_{296}B_8N_{72}O_{16}S_8Zn_8$	$C_{35}H_{31}BN_{10}OZn$
Formula weight	710.93	766.98	6272.19	683.88
Temperature/K	100.0	100.0	100.0	100.0
Crystal system	monoclinic	monoclinic	monoclinic	monoclinic
Space group	$P2_1/n$	C2/c	C2/c	$P2_1/c$
a/Å	13.3934(9)	32.381(6)	21.357(4)	11.6817(10)
b/Å	13.7607(10)	12.821(2)	12.077(2)	12.0790(10)
c/Å	18.2199(14)	19.375(3)	31.551(6)	23.562(2)
α/°	90	90	90	90
β/°	93.762(2)	110.645(4)	109.06(3)	93.1460(10)
γ/°	90	90	90	90
Volume/$Å^3$	3350.7(4)	7527(2)	7692(3)	3319.7(5)
Z	4	8	1	4
$\rho_{calc}g/cm^3$	1.409	1.354	1.354	1.368
μ/mm^{-1}	0.782	0.703	0.741	0.785
F(000)	1472.0	3192.0	3256.0	1416.0
Crystal size/mm^3	0.075 × 0.075 × 0.075	0.1 × 0.1 × 0.1	0.25 × 0.25 × 0.25	0.6 × 0.5 × 0.5
Radiation	MoKα (λ = 0.71073)	MoKα (λ = 0.71073)	MoKα (λ = 0.71073)	MoKα (λ = 0.71073)
2Θ range for data collection/°	3.662 to 52.042	4.368 to 50.052	3.93 to 52.826	3.79 to 50.104
Index ranges	$-16 \le h \le 16$, $-16 \le k \le 16$, $-15 \le l \le 22$	$-38 \le h \le 38$, $-15 \le k \le 15$, $-23 \le l \le 23$	$-26 \le h \le 26$, $-15 \le k \le 15$, $-39 \le l \le 39$	$-13 \le h \le 12$, $-14 \le k \le 14$, $-27 \le l \le 28$
Reflections collected	39332	45788	41283	35599
Independent reflections	6604 [R_{int} = 0.0578, R_{sigma} = 0.0427]	6649 [R_{int} = 0.1118, R_{sigma} = 0.0841]	7856 [R_{int} = 0.0780, R_{sigma} = 0.0572]	5861 [R_{int} = 0.0486, R_{sigma} = 0.0343]
Data/restraints/parameters	6604/0/458	6649/0/502	7856/2/500	5861/0/436
Goodness-of-fit on F^2	1.025	1.035	1.043	1.025
Final R indexes [I>=2σ (I)]	R_1 = 0.0325, wR_2 = 0.0732	R_1 = 0.0503, wR_2 = 0.1216	R_1 = 0.0377, wR_2 = 0.0953	R_1 = 0.0317, wR_2 = 0.0709
Final R indexes [all data]	R_1 = 0.0442, wR_2 = 0.0790	R_1 = 0.0745, wR_2 = 0.1359	R_1 = 0.0441, wR_2 = 0.0997	R_1 = 0.0442, wR_2 = 0.0764
Largest diff. peak/hole / e $Å^{-3}$	0.38/-0.34	0.61/-1.27	0.38/-0.41	0.26/-0.34

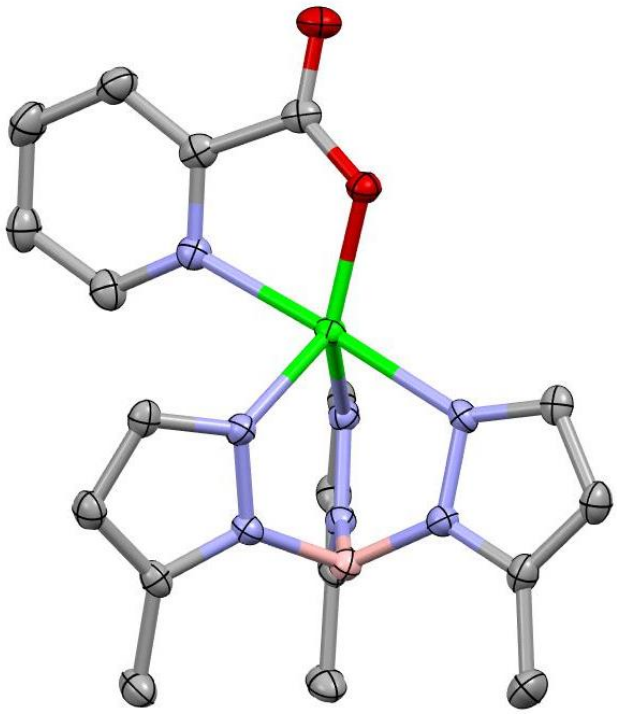

Figure 3.S1. Previously reported structure of [($Tp^{Ph,Me}$)Zn(**3.1**)] rendered as an ORTEP with atoms at 50% thermal probability ellipsoids.[18] Hydrogen atoms and $Tp^{Ph,Me}$ phenyl groups have been removed for clarity. Color scheme: carbon = gray, oxygen = red, nitrogen = blue, boron = pink, and zinc = green.

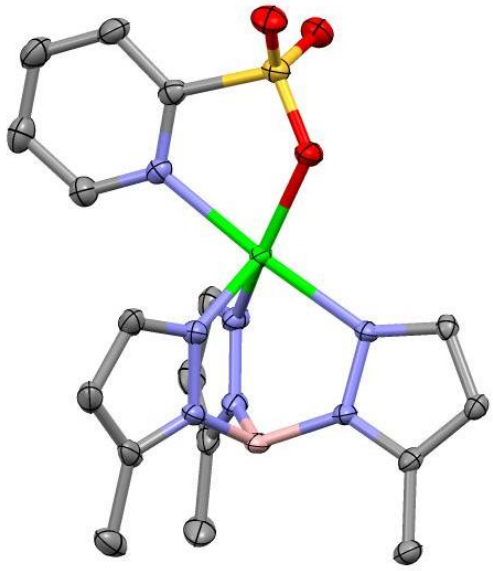

Figure 3.S2. Structure of [($Tp^{Ph,Me}$)Zn(**3.3**)] rendered as an ORTEP with atoms at 50% thermal probability ellipsoids. Hydrogen atoms and $Tp^{Ph,Me}$ phenyl groups have been removed for clarity. The asymmetric unit consists only of the complex. Color scheme: carbon = gray, sulfur = yellow, oxygen = red, nitrogen = blue, boron = pink, and zinc = green.

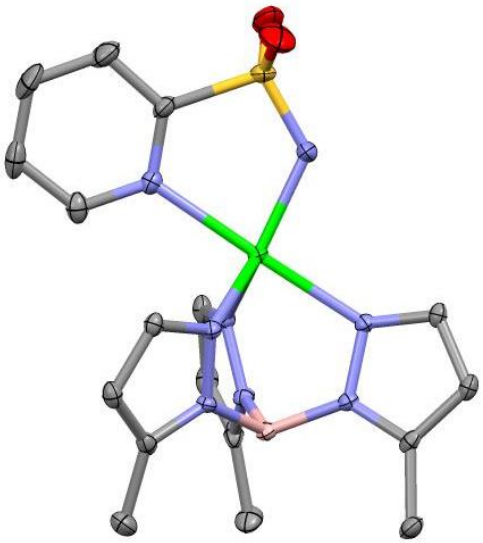

Figure 3.S3. Structure of [($Tp^{Ph,Me}$)Zn(**3.5**)] rendered as an ORTEP with atoms at 50% thermal probability ellipsoids. Hydrogen atoms and $Tp^{Ph,Me}$ phenyl groups have been removed for clarity. The asymmetric unit consists only of the complex. Color scheme: carbon = gray, sulfur = yellow, oxygen = red, nitrogen = blue, boron = pink, and zinc = green.

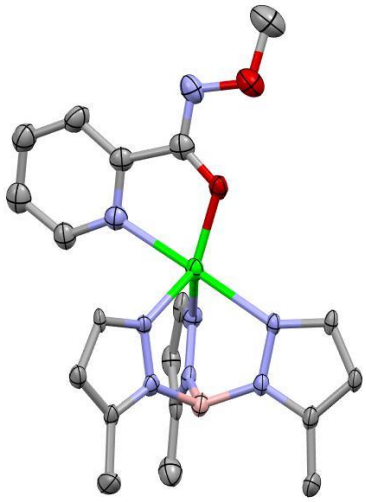

Figure 3.S4. Structure of [(Tp^{Ph,Me})Zn(**3.7**)] rendered as an ORTEP with atoms at 50% thermal probability ellipsoids. Hydrogen atoms and Tp^{Ph,Me} phenyl groups have been removed for clarity. The asymmetric unit consists of the complex, two [(Tp^{Ph,Me})Zn(Cl)] complexes (not shown), and two benzene molecules (not shown). Color scheme: carbon = gray, oxygen = red, nitrogen = blue, boron = pink, and zinc = green.

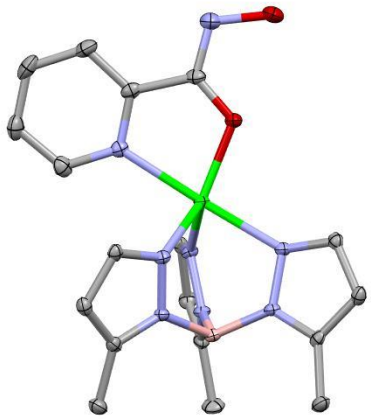

Figure 3.S5. Structure of [(Tp^{Ph,Me})Zn(**3.9**)] rendered as an ORTEP with atoms at 50% thermal probability ellipsoids. Hydrogen atoms and Tp^{Ph,Me} phenyl groups have been removed for clarity. The asymmetric unit consists only of the complex. Color scheme: carbon = gray, oxygen = red, nitrogen = blue, boron = pink, and zinc = green.

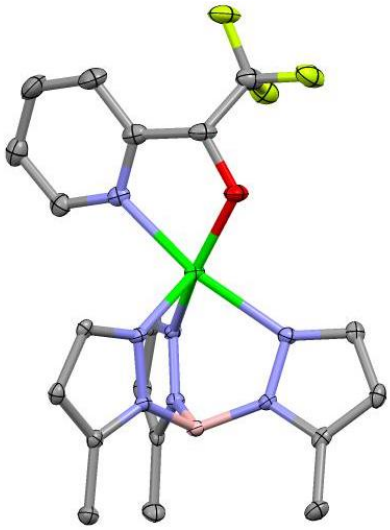

Figure 3.S6. Structure of [($Tp^{Ph,Me}$)Zn(**3.11**)] rendered as an ORTEP with atoms at 50% thermal probability ellipsoids. Hydrogen atoms and $Tp^{Ph,Me}$ phenyl groups have been removed for clarity. The asymmetric unit consists of the complex and a molecule of benzene (not shown). Color scheme: carbon = gray, fluorine = yellow, oxygen = red, nitrogen = blue, boron = pink, and zinc = green.

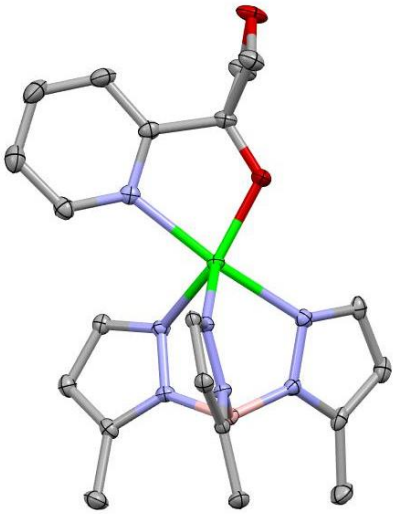

Figure 3.S7. Structure of [($Tp^{Ph,Me}$)Zn(**3.12**)] rendered as an ORTEP with atoms at 50% thermal probability ellipsoids. Hydrogen atoms and $Tp^{Ph,Me}$ phenyl groups have been removed for clarity. The asymmetric unit consists of two complexes (one not shown). Color scheme: carbon = gray, oxygen = red, nitrogen = blue, boron = pink, and zinc = green.

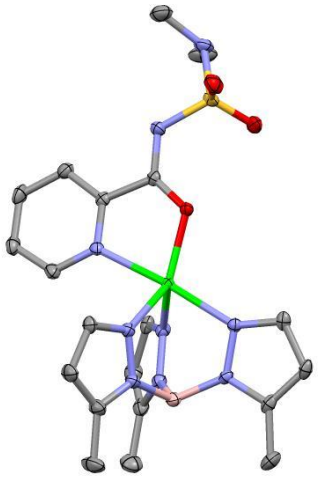

Figure 3.S8. Structure of [($Tp^{Ph,Me}$)Zn(**3.15**)] rendered as an ORTEP with atoms at 50% thermal probability ellipsoids. Hydrogen atoms and $Tp^{Ph,Me}$ phenyl groups have been removed for clarity. The asymmetric unit consists of two complexes (one not shown) and two and a half molecules of benzene (not shown). Color scheme: carbon = gray, sulfur = yellow, oxygen = red, nitrogen = blue, boron = pink, and zinc = green.

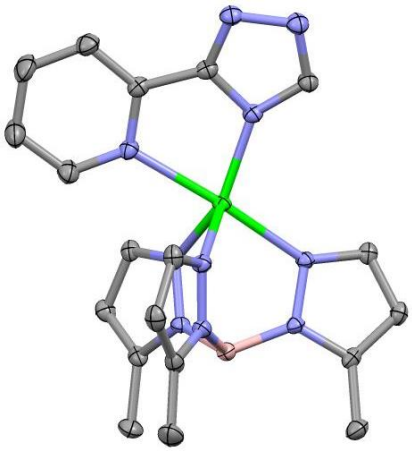

Figure 3.S9. Structure of [($Tp^{Ph,Me}$)Zn(**3.17**)] rendered as an ORTEP with atoms at 50% thermal probability ellipsoids. Hydrogen atoms and $Tp^{Ph,Me}$ phenyl groups have been removed for clarity. The asymmetric unit consists of the complex, mixed occupancy solvent molecules (MeOH: water, 50:50) (not shown), and a full occupancy water molecule (not shown) with both solvent molecules hydrogen binding with the complex. Color scheme: carbon = gray, nitrogen = blue, boron = pink, and zinc = green.

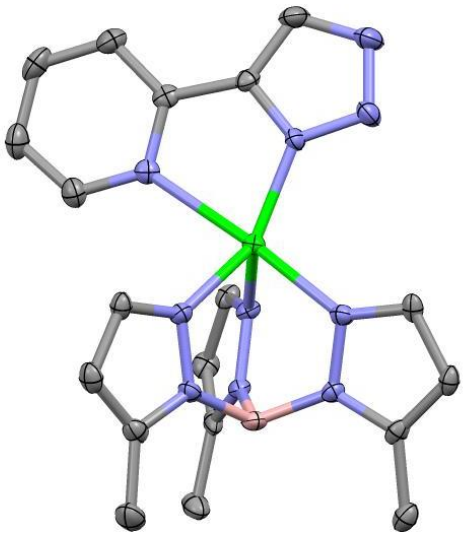

Figure 3.S10. Structure of [($Tp^{Ph,Me}$)Zn(**3.18**)] rendered as an ORTEP with atoms at 50% thermal probability ellipsoids. Hydrogen atoms and $Tp^{Ph,Me}$ phenyl groups have been removed for clarity. The asymmetric unit consists only of the complex. Color scheme: carbon = gray, nitrogen = blue, boron = pink, and zinc = green.

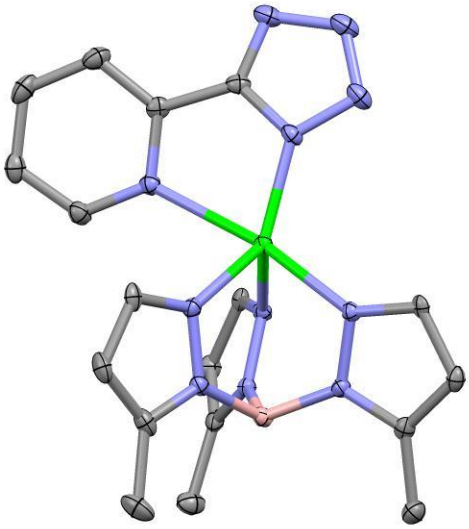

Figure 3.S11. Structure of [($Tp^{Ph,Me}$)Zn(**3.19**)] rendered as an ORTEP with atoms at 50% thermal probability ellipsoids. Hydrogen atoms and $Tp^{Ph,Me}$ phenyl groups have been removed for clarity. The asymmetric unit consists only of the complex. Color scheme: carbon = gray, nitrogen = blue, boron = pink, and zinc = green.

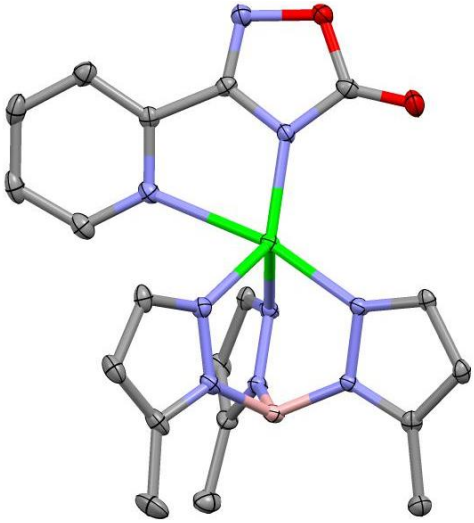

Figure 3.S12. Structure of [(Tp^{Ph,Me})Zn(**3.20**)] rendered as an ORTEP with atoms at 50% thermal probability ellipsoids. Hydrogen atoms and Tp^{Ph,Me} phenyl groups have been removed for clarity. The asymmetric unit consists of two complexes (one not shown). Color scheme: carbon = gray, oxygen = red, nitrogen = blue, boron = pink, and zinc = green.

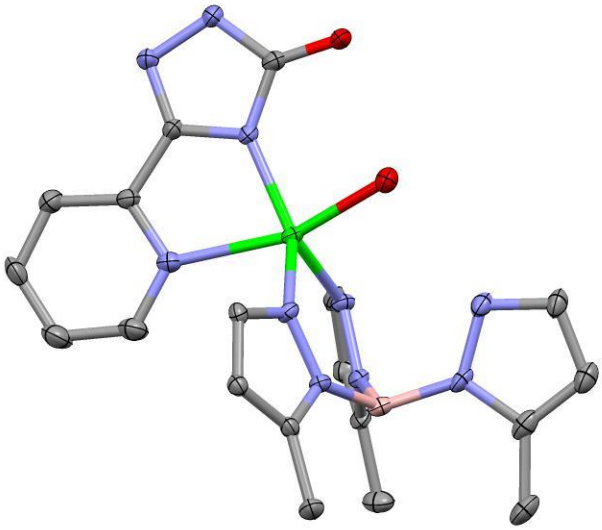

Figure 3.S13. Structure of [(Tp^{Ph,Me})Zn(**3.21**)] rendered as an ORTEP with atoms at 50% thermal probability ellipsoids. Hydrogen atoms and Tp^{Ph,Me} phenyl groups have been removed for clarity. The asymmetric unit consists of the complex and half a molecule of benzene (not shown). Color scheme: carbon = gray, oxygen = red, nitrogen = blue, boron = pink, and zinc = green.

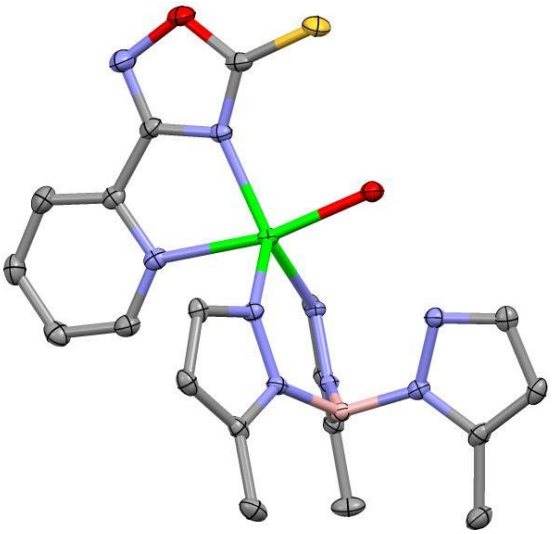

Figure 3.S14. Structure of [(Tp^{Ph,Me})Zn(**3.23**)] rendered as an ORTEP with atoms at 50% thermal probability ellipsoids. Hydrogen atoms and Tp^{Ph,Me} phenyl groups have been removed for clarity. The asymmetric unit consists of the complex and half molecule of benzene (not shown). Color scheme: carbon = gray, sulfur = yellow, oxygen = red, nitrogen = blue, boron = pink, and zinc = green.

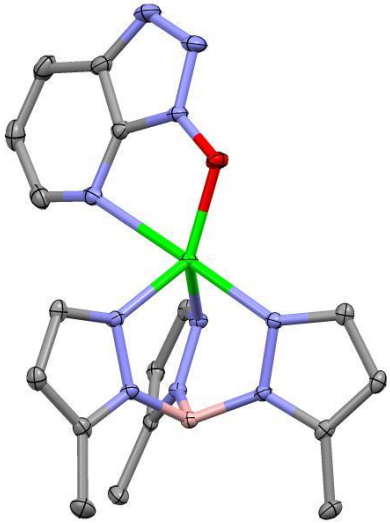

Figure 3.S15. Structure of [(Tp^{Ph,Me})Zn(**3.24**)] rendered as an ORTEP with atoms at 50% thermal probability ellipsoids. Hydrogen atoms and Tp^{Ph,Me} phenyl groups have been removed for clarity. The asymmetric unit consists only of the complex. Color scheme: carbon = gray, sulfur = yellow, oxygen = red, nitrogen = blue, boron = pink, and zinc = green.

Table 3.S5. Percent inhibition of **3.1** and MBIs (200 μM) against Endo.

MBI	**3.1**	**3.2**	**3.3**	**3.4**	**3.5**	**3.6**
Mean	41	41	12	45	6	20
SD	6	5	7	5	9	11
MBI	**3.7**	**3.8**	**3.9**	**3.10**	**3.11**	**3.12**
Mean	49	14	96	22	-4	8
SD	4	4	1	4	6	4
MBI	**3.13**	**3.14**	**3.15**	**3.16**	**3.17**	**3.18**
Mean	0	31	22	13	NA	5
SD	4	3	2	3	NA	10
MBI	**3.19**	**3.20**	**3.21**	**3.22**	**3.23**	**3.24**
Mean	18	30	39	40	11	22
SD	6	4	10	4	5	4

Table 3.S6. Percent inhibition of **3.1** and MBIs (200 μM) against hCAII.

MBI	**3.1**	**3.2**	**3.3**	**3.4**	**3.5**	**3.6**
Mean	2	5	6	2	100	6
SD	2	4	4	1	0	3
MBI	**3.7**	**3.8**	**3.9**	**3.10**	**3.11**	**3.12**
Mean	3	13	33	5	5	6
SD	5	4	4	3	3	3
MBI	**3.13**	**3.14**	**3.15**	**3.16**	**3.17**	**3.18**
Mean	32	2	4	10	12	NA
SD	0	1	1	2	2	NA
MBI	**3.19**	**3.20**	**3.21**	**3.22**	**3.23**	**3.24**
Mean	1	3	1	1	3	3
SD	0	3	1	1	2	2

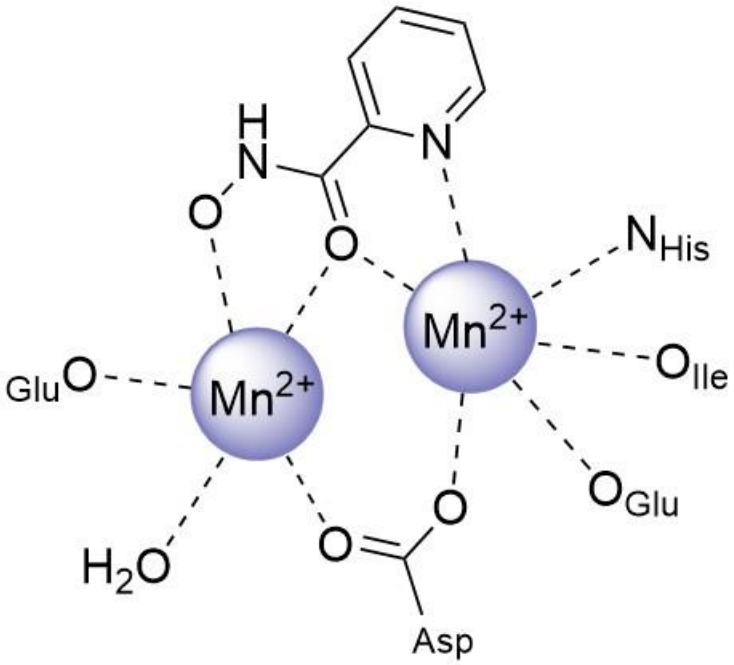

Figure 3.S16. Proposed mode of coordination of **3.9** to the active site of Endo, with the hydroxamate engaging in bidentate coordination to one active site Mn^{2+} and the pyridine and hydroxamate carbonyl coordinating in a bidentate fashion to the other Mn^{2+}.

3. 9 Acknowledgments

Chapter 3 is a reprint of the material published in the following publication, "Metal-Binding Isosteres as New Scaffolds for Metalloenzyme Inhibitors" Benjamin L. Dick, Seth M. Cohen. *Inorg. Chem.* 2018, *57* (15), 9538-9543. The dissertation author was the primary author and researcher of this paper and gratefully acknowledges the contributions of coauthor Seth M. Cohen. The permission to reproduce this paper was granted by the American Chemical Society. Copyright 2018, American Chemical Society.

3.10 References

1. Patani, G. A.; LaVoie, E. J., Bioisosterism: A Rational Approach in Drug Design. *Chem. Rev.* **1996,** *96*, 3147-3176.

2. Meanwell, N. A., Synopsis of Some Recent Tactical Application of Bioisosteres in Drug Design. *J. Med. Chem.* **2011,** *54*, 2529–2591.

3. Kalgutkar, A. S.; Scott Daniels, J., Chapter 3 Carboxylic Acids and Their Bioisosteres. In *Metabolism, Pharmacokinetics and Toxicity of Functional Groups: Impact of Chemical Building Blocks on ADMET*, The Royal Society of Chemistry: 2010; pp 99-167.

4. Lassila, T.; Hokkanen, J.; Aatsinki, S. M.; Mattila, S.; Turpeinen, M.; Tolonen, A., Toxicity of Carboxylic Acid-Containing Drugs: The Role of Acyl Migration and CoA Conjugation Investigated. *Chem. Res. Toxicol.* **2015,** *28*, 2292-2303.

5. Pajouhesh, H.; Lenz, G. R., Medicinal Chemical Properties of Successful Central Nervous System Drugs. *NeuroRx* **2005,** *2*, 541-553.

6. Rautio, J.; Kumpulainen, H.; Heimbach, T.; Oliyai, R.; Oh, D.; Jarvinen, T.; Savolainen, J., Prodrugs: Design and Clinical Applications. *Nat. Rev. Drug Discovery* **2008,** *7*, 255-270.

7. Ballatore, C.; Huryn, D. M.; Smith, A. B., Carboxylic Acid (Bio)Isosteres in Drug Design. *ChemMedChem* **2013,** *8*, 385-395.

8. Lassalas, P.; Gay, B.; Lasfargeas, C.; James, M. J.; Tran, V.; Vijayendran, K. G.; Brunden, K. R.; Kozlowski, M. C.; Thomas, C. J.; Smith, A. B., 3rd; Huryn, D. M.; Ballatore, C., Structure Property Relationships of Carboxylic Acid Isosteres. *J. Med. Chem.* **2016,** *59*, 3183-3203.

9. Cohen, S. M., A Bioinorganic Approach to Fragment-Based Drug Discovery Targeting Metalloenzymes. *Acc. Chem. Res.* **2017,** *50*, 2007-2016.

10. Chen, A. Y.; Thomas, P. W.; Stewart, A. C.; Bergstrom, A.; Cheng, Z.; Miller, C.; Bethel, C. R.; Marshall, S. H.; Credille, C. V.; Riley, C. L.; Page, R. C.; Bonomo, R. A.; Crowder, M. W.; Tierney, D. L.; Fast, W.; Cohen, S. M., Dipicolinic Acid Derivatives as Inhibitors of New Delhi Metallo-beta-lactamase-1. *J. Med. Chem.* **2017,** *60*, 7267-7283.

11. Credille, C. V.; Chen, Y.; Cohen, S. M., Fragment-Based Identification of Influenza Endonuclease Inhibitors. *J. Med. Chem.* **2016,** *59*, 6444-6454.

12. Perez, C.; Li, J.; Parlati, F.; Rouffet, M.; Ma, Y.; Mackinnon, A. L.; Chou, T. F.; Deshaies, R. J.; Cohen, S. M., Discovery of an Inhibitor of the Proteasome Subunit Rpn11. *J. Med. Chem.* **2017,** *60*, 1343-1361.

13. Credille, C. V.; Morrison, C. N.; Stokes, R. W.; Dick, B. L.; Feng, Y.; Sun, J.; Chen, Y.; Cohen, S. M., SAR Exploration of Tight-Binding Inhibitors of Influenza Virus PA Endonuclease. *J. Med. Chem.* **2019,** *62* (21), 9438-9449.

14. Jacobsen, J. A.; Fullagar, J. L.; Miller, M. T.; Cohen, S. M., Identifying Chelators for Metalloprotein Inhibitors Using a Fragment-Based Approach. *J. Med. Chem.* **2011,** *54*, 591-602.

15. Dowell, R. I.; Hales, N. H.; Tucker, H., Novel Inhibitors of Prolyl 4-Hydroxylase. Part 4 Pyridine-2-Carboxylic Acid Analogues with Alternative 2-Substituents. *Eur. J. Med. Chem.* **1993,** *28*, 513-516.

16. Pichota, A.; Duraiswamy, J.; Yin, Z.; Keller, T. H.; Alam, J.; Liung, S.; Lee, G.; Ding, M.; Wang, G.; Chan, W. L.; Schreiber, M.; Ma, I.; Beer, D.; Ngew, X.; Mukherjee, K.; Nanjundappa, M.; Teo, J. W.; Thayalan, P.; Yap, A.; Dick, T.; Meng, W.; Xu, M.; Koehn, J.; Pan, S. H.; Clark, K.; Xie, X.; Shoen, C.; Cynamon, M., Peptide Deformylase Inhibitors of Mycobacterium Tuberculosis: Synthesis, Structural Investigations, and Biological Results. *Bioorg. Med. Chem. Lett.* **2008,** *18*, 6568-6572.

17. Puerta, D. T.; Cohen, S. M., Examination of Novel Zinc-Binding Groups for Use in Matrix Metalloproteinase Inhibitors. *Inorg. Chem.* **2003,** *42*, 3423-3430.

18. Jacobsen, F. E.; Lewis, J. A.; Cohen, S. M., A New Role for Old Ligands: Discerning Chelators for Zinc Metalloproteinases. *J. Am. Chem. Soc.* **2006,** *128*, 3156-3157.

19. Sun Cao, P.; Sommer, R. D.; Grice, K. A., Structural Comparison of Suberanilohydroxamic acid (SAHA) and Other Zinc-Enzyme Inhibitors Bound to a Monomeric Zinc Species. *Polyhedron* **2016,** *114*, 344-350.

20. Puerta, D. T.; Cohen, S. M., [(TpMe,Ph)2Zn2(H3O2)]ClO4: A New H3O2 Species Relevant to Zinc Proteinases. *Inorg. Chim. Acta* **2002,** *337*, 459-462.

21. Kremer-Aach, A.; Kläui, W.; Bell, R.; Strerath, A.; Wunderlich, H.; Mootz, D., Cobalt as a Probe for Zinc in Metalloenzyme Model Compounds? A Comparison of Spectroscopic Features and Coordination Geometry of Four- and Five-Coordinate Complexes. Crystal and Molecular Structures of [Co(η3-TpPh)(η2-TpPh)], [(η3-TpPh)Zn(anthranilate)], and [(η3-TpPh)M(η2-acac)] (TpPh = Hydrotris(3-phenylpyrazol-1-yl)borate, acac = Pentane-2,4-dionate, and M = Zn, Co). *Inorg. Chem.* **1997,** *36*, 1552-1563.

22. Rombach, M.; Gelinsky, M.; Vahrenkamp, H., Coordination Modes of Aminoacids to Zinc. *Inorg. Chim. Acta* **2002,** *334*, 25-33.

23. Tam, K. Y.; Takacs-Novak, K., Multi-Wavelength Spectrophotometric Determination of Acid Dissociation Constants: A Validation Study. *Anal. Chim. Acta* **2001,** *434*, 157-167.

24. Schonherr, D.; Wollatz, U.; Haznar-Garbacz, D.; Hanke, U.; Box, K. J.; Taylor, R.; Ruiz, R.; Beato, S.; Becker, D.; Weitschies, W., Characterisation of Selected Active Agents Regarding pK(a) Values, Solubility Concentrations and pH Profiles by SiriusT3. *Eur. J. Pharm. Biopharm.* **2015,** *92*, 155-170.

25. Slater, B.; Mccormack, A.; Avdeef, A.; Comer, J. E. A., Ph-Metric Log-P .4. Comparison of Partition-Coefficients Determined by Hplc and Potentiometric Methods to Literature Values. *J. Pharm. Sci.* **1994,** *83*, 1280-1283.

26. DuBois, R. M.; Slavish, P. J.; Baughman, B. M.; Yun, M. K.; Bao, J.; Webby, R. J.; Webb, T. R.; White, S. W., Structural and Biochemical Basis for Development of Influenza Virus Inhibitors Targeting the PA Endonuclease. *PLoS Pathog.* **2012,** *8*, e1002830.

27. Supuran, C. T.; Scozzafava, A.; Casini, A., Carbonic Anhydrase Inhibitors. *Med. Res. Rev.* **2003,** *23*, 146-189.

28. Di Fiore, A.; Maresca, A.; Supuran, C. T.; De Simone, G., Hydroxamate Represents a Versatile Zinc Binding Group for the Development of New Carbonic Anhydrase Inhibitors. *Chem. Commun.* **2012,** *48*, 8838-8840.

29. Monnard, F. W.; Heinisch, T.; Nogueira, E. S.; Schirmer, T.; Ward, T. R., Human Carbonic Anhydrase II as a Host for Piano-Stool Complexes Bearing a Sulfonamide Anchor. *Chem. Commun.* **2011,** *47*, 8238-8240.

30. Dolomanov, O. V.; Bourhis, L. J.; Gildea, R. J.; Howard, J. A. K.; Puschmann, H., OLEX2: A Complete Structure Solution, Refinement and Analysis Program. *J. Appl. Crystal.* **2009,** *42*, 339-341.

31. Sheldrick, G., Crystal Structure Refinement with SHELXL. *Acta Crystal. Sec. C* **2015,** *71*, 3-8.

32. Sheldrick, G., A Short History of SHELX. *Acta Crystal. Sec. A* **2008,** *64*, 112-122.

33. Lee, S. J.; Kim, H. S.; Yang, H. W.; Yoo, B. W.; Yoon, C. M., Synthesis of Diethyl Pyridin-2-ylphosphonates and Quinolin-2-ylphosphonates by Deoxygenative Phosphorylation of the Corresponding N-Oxides. *Bull. Korean Chem. Soc.* **2014,** *35*, 2155-2158.

34. Dowell, R. I.; Hadley, E. M., Novel Inhibitors of Prolyl 4-Hydroxylase. *J. Med. Chem.* **1992,** *35*, 800-804.

35. Gobis, K.; Foks, H.; Kedzia, A.; Wierzbowska, M.; Zwolska, Z., Synthesis and Antibacterial Activity of Novel Pyridine and Pyrazine Derivatives Obtained from Amidoximes. *J. Heterocyclic Chem.* **2009,** *46,* 1271-1279.

Chapter 4: Effect of Heterocycle Content on Metal-Binding Isostere Coordination

4.1 Introduction

As discussed in Chapter 1, clinically approved metalloenzyme inhibitors are limited in scope, specifically with respect to the metal binding motif, which are often dominated by a select few metal binding functional groups.[1-2] This overreliance on a limited set of metal binding functional groups (a.k.a., metal-binding pharmacophores, MBPs) capable of binding active site metal ions is a potential barrier to developing next-generation metalloenzyme inhibitors. As already described, efforts to apply fragment-based drug discovery (FBDD) to metalloenzymes has produced new libraries of potential MBPs.[3-5] However, some new MBPs may possess physiochemical properties that limit their viability for use in drug candidates.[6-7]

As discussed in Chapter 1, in medicinal chemistry, functional groups that adversely modulate the pharmacological properties of a drug candidate or introduce clear pharmacological liabilities, are often replaced with alternate functional groups with broadly similar properties referred to as bioisosteres (in this chapter, the terms isostere will be used to refer to both isosteres and bioisosteres).[8-9] For example, carboxylic acids are often replaced with other acidic functional groups, such as tetrazoles that possess some similarities (i.e., pK_a), but differ in other aspects (i.e., lipophilicity).[10-11] As described in Chapter 3, in an effort to increase the chemical diversity and to improve the drug-likeness of MBPs, carboxylic acid isostere replacement was applied to the pyridine-2-carboxylic acid (picolinic acid) MBP, generating a novel set of metal-binding isosteres (MBIs).[12] This exercise in isostere replacement was successful in generating a set of viable metal coordinating motifs varying in their physicochemical properties (i.e., pK_a, LogP, Log$D_{7.4}$) without compromising their metalloenzyme inhibitory activity.

In this chapter, a more diverse series of nitrogen heterocycle scaffolds containing a carboxylic acid were explored for isostere replacement, in order to demonstrate a potential broader

applicability to metalloenzyme inhibition. MBIs were synthesized and their metal binding ability assessed via examining bioinorganic model complexes. Certain MBIs had their physicochemical properties determined and coordination chemistry behaviour analysed via computational methods. This expanded study examines a wide variety of heteroarene scaffolds allowing for a study of the effects of isostere replacement on the coordination abilities of the resulting MBIs and shows that the effect of isostere replacement is context dependent.[13] The findings presented here demonstrate that while the application of isostere replacement to MBPs may be a straightforward concept, the coordination behaviour and physiochemical properties are dependent on the parent scaffold and require consideration when employed in metalloenzyme drug discovery.

4.2 Scaffold Selection and Metal-Binding Isostere Synthesis

Carboxy-substituted heteroarene MBPs were examined as possible candidates for MBI development. The candidates for study included indazole-3-carboxylic acid (**4.1**), benzimidazole-2-carboxylic acid (**4.2**), 1,2-benzisothiazole-3-carboxylic acid (**3**), benzothiazole-2-carboxylic acid (**4.4**), and 1,2-benzisoxazole-3-carboxylic acid (**5**) (Figure 4.1). Benzoxazole-2-carboxylic acid would be a logical addition to this series, but was not included as the scaffold is known to undergo degradation via decarboxylation.[14] Compounds **4.1**, **4.2**, **4.4**, and **4.5** were commercially available, while **4.3** was synthesized according to a published procedure.[15] A series of both acyclic (A and B series) and cyclic (C and D series) isosteres were selected for synthesis. For the acyclic MBIs the starting material was generally the corresponding carboxylic acid (**4.1**, **4.2**, **4.3**, **4.4**, and **4.5**). The corresponding *O*-methyl indazole-3-hydroxamic acid (**4.1a**) and *O*-methyl benzimidazole-2-hydroxamic acid (**4.2a**) were generated from the carboxylic acid using peptide coupling conditions. *O*-methyl 1,2-benzisothiazole-3-hydroxamic acid (**4.3a**) and *O*-methyl

benzothiazole-2-hydroxamic acid (**4.4a**) were synthesized from the carboxylic acid using acid chloride coupling conditions. The indazole-3-hydroxamic acid (**4.1b**) and benzimidazole-2-hydroxamic acid (**4.2b**) were generated from the carboxylic acid using peptide coupling conditions. 1,2-Benzisothiazole-3-hydroxamic acid (**4.3b**) was synthesized from the carboxylic acid using acid chloride coupling. Benzothiazole-2-hydroxamic acid (**4.4b**) was synthesized from ethyl benzothiazole-2-carboxylate and hydroxylamine under basic conditions. The *O*-methyl 1,2-benzisoxazole-3-hydroxamic acid (**4.5a**) and 1,2-benzisoxazole-3-hydroxamic acid (**4.5b**) were both synthesized from **4.5** by generating the acid chloride and combining it with the corresponding hydroxyl amine.

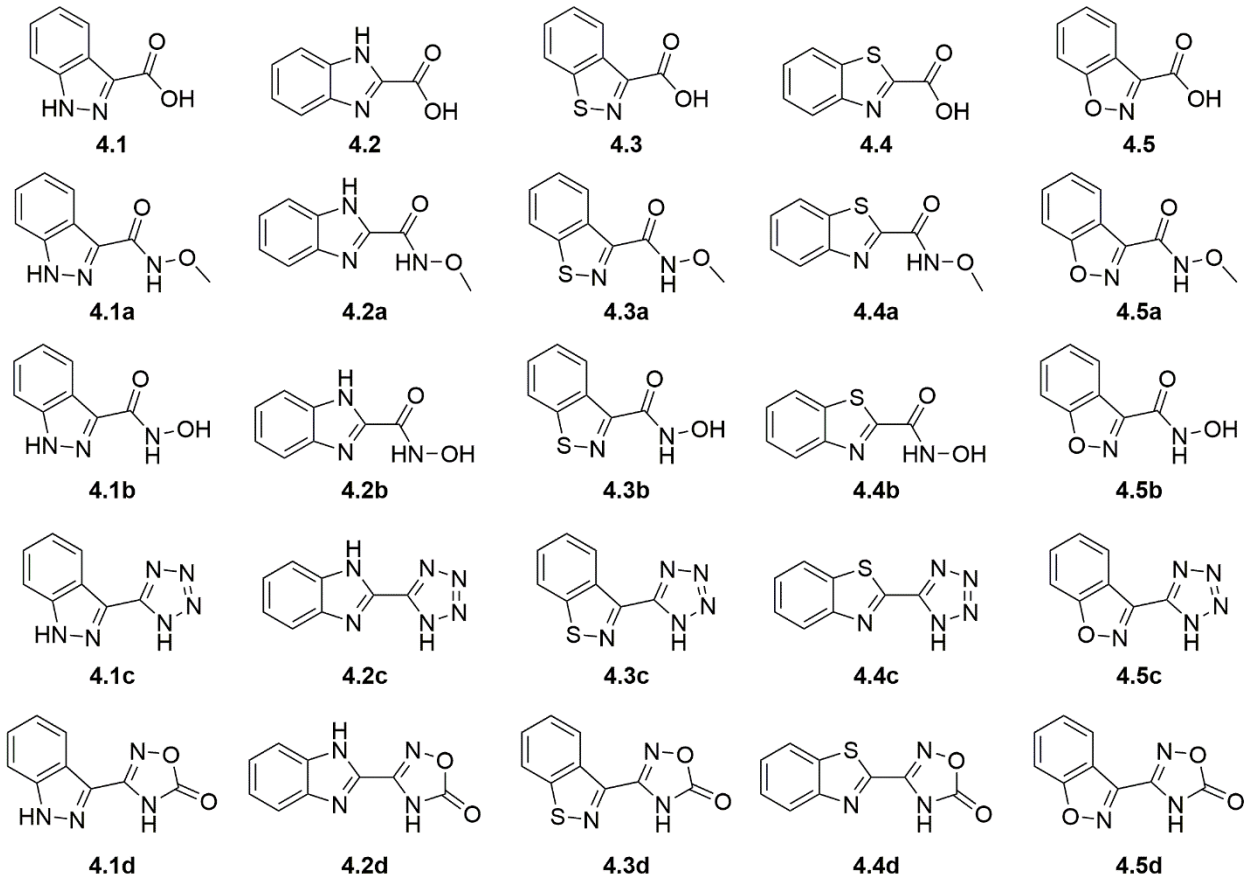

Figure 4.1. Heterocyclic MBPs (*top row*, compounds **4.1**-**4.5**) that were chosen for MBI development (*all other rows*).

The cyclic MBIs (C and D series, Figure 4.1) of **4.1**, **4.2**,[16] **4.3**,[17] and **4.4**[18] were all synthesized starting from the commercially available or published synthesis of the corresponding nitrile derivatives. The nitrile derivative of **4.5** was prepared in a similar fashion starting from **4.5** (synthetic details can be found in the Appendix). The tetrazole series was synthesized from the corresponding nitriles via a 3+2 cycloaddition with sodium azide yielding the indazole-3-tetrazole (**4.1c**), benzimidazole-2-tetrazole (**4.2c**), 1,2-benzisothiazole-3-tetrazole (**4.3c**), benzothiazole-2-tetrazole (**4.4c**), and 1,2-benzisoxazole-3-tetrazole (**4.5c**). To obtain each oxadiazolone derivative, the *N'*-hydroxy amidine was first synthesized for each scaffold from the respective nitrile using

hydroxylamine, which was isolated and then cyclized with ethyl chloroformate yielding the indazole-3-oxadiazolone (**4.1d**), benzimidazole-2-oxadiazolone (**4.2d**), 1,2-benzisothiazole-3-oxadiazolone (**4.3d**), benzothiazole-2-oxadiazolone (**4.4d**), and 1,2-benzisoxazole-3-oxadiazolone (**4.5d**).

4.3 Synthesis and Characterization of Model Complexes

To determine the metal binding ability of each MBI in a bioinorganic context, [$Tp^{Ph,Me}$Zn(MBI)] ($Tp^{Ph,Me}$ = hydrotris(5,3-methylphenylpyrazolyl)borate) complexes were prepared (Note: Brackets are used when referring to synthesized complexes). These model complexes are mimetic of a tris(histidine) Zn^{2+} metalloenzyme active site and are useful for characterizing MBI coordination chemistry.[12, 19] The [$Tp^{Ph,Me}$Zn(MBP)] complexes of **4.1**, **4.2**, **4.3**, **4.4**, and **4.5** were prepared and crystallized. It was found that almost all of these MBPs coordinate in a bidentate fashion via the nitrogen atom of the heterocycle and the carboxylate oxygen (Figure 4.2). The only exception was for [$Tp^{Ph,Me}$Zn(**4.5**)], which coordinated to the Zn^{2+} ion in a predominantly monodentate fashion through the carboxylate donor (Figure 4.2), indicating the 1,2-benzisoxazole scaffold has significantly decreased coordination ability. Interestingly, the Zn-heteroarene nitrogen bond distances for the *N,S* heteroarenes (**4.3** and **4.4**) were slightly longer than the corresponding *N,N* heteroarenes (**4.1** and **4.2**), by about 0.10 to 0.15 Å, while the Zn-carboxylate bond distances exhibited a smaller deviation (~0.05 Å) (Table 4.S6). This difference in bond lengths suggest an overall decrease in the donor ability of the *N,S* heterocycle scaffolds relative to the *N,N* scaffolds.

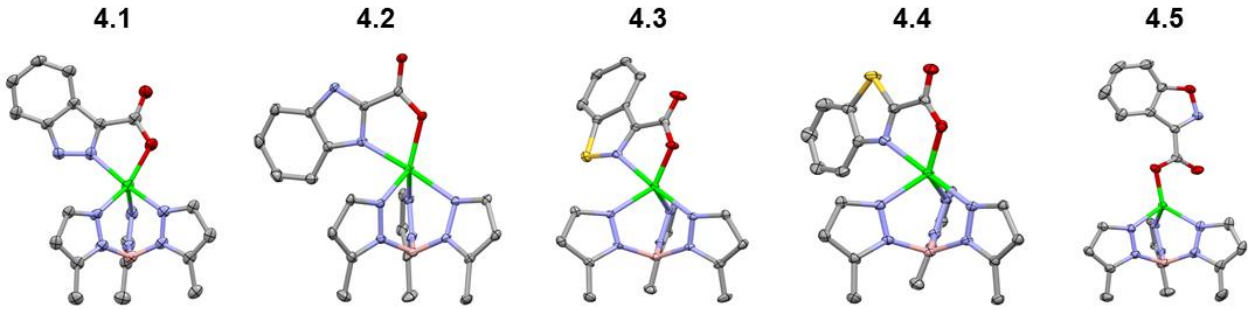

Figure 4.2. Crystal structure of [$Tp^{Ph,Me}$Zn(MBP)] complexes of **4.1**, **4.2**, **4.3**, **4.4**, and **4.5**. Phenyl groups of $Tp^{Ph,Me}$ have been removed for clarity.

Next, the coordination ability of the *O*-methyl hydroxamate MBIs (A series) were analysed (Figure 4.3). The X-ray structures of [$Tp^{Ph,Me}$Zn(MBI)] with **4.2a**, **4.3a**, and **4.4a** exhibit the same bidentate coordination (through the heterocycle and the carbonyl oxygen of the *O*-methyl hydroxamate) that was observed for the pyridine scaffold.[12] Interestingly, the structures of the [$Tp^{Ph,Me}$Zn(MBI)] complexes of **4.1a** and **4.5a** show bidentate coordination only through the oxygen donor atoms of the *O*-methyl hydroxamate. The bidentate coordination through the *O*-methyl hydroxamate has only rarely been observed crystallographically and not in the presence of alternative coordination motifs.[20-21] This bidentate coordination through an ether-like coordination motif (**4.1a** and **4.5a**), when there is a suitable nitrogen heterocycle donor available, suggests that the coordination ability of the nitrogen atoms are compromised due to electronic effects. Additionally, it is unlikely that sterics play a significant role in the observed coordination chemistry, as in the case of comparing the difference in coordination between **4.1a** to **4.3a**, the only difference in both structures is a single atom substitution (N versus S). To further probe the effect of isostere replacement on each scaffold, the hydroxamate series of isosteres was analysed crystallographically, as the hydroxamate is a stronger ligand than the respective *O*-methyl hydroxamate.

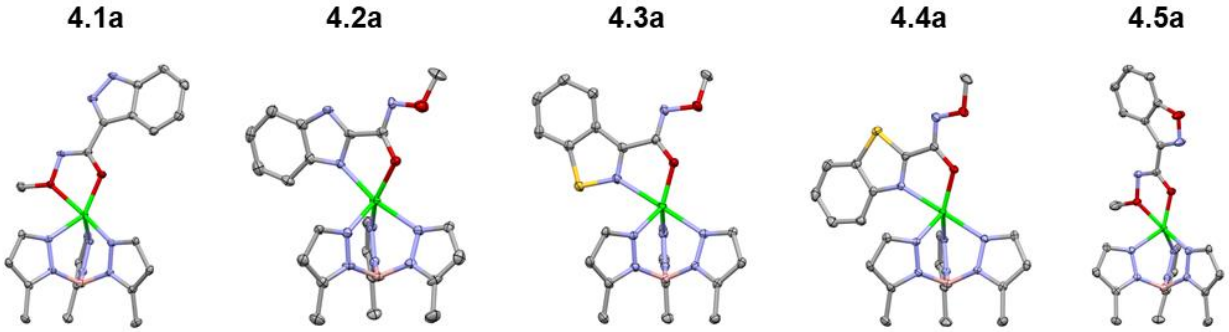

Figure 4.3. Crystal structure of [Tp^{Ph,Me}Zn(MBI)] complexes of **4.1a**, **4.2a**, **4.3a**, **4.4a**, and **4.5a**. Phenyl groups of Tp^{Ph,Me} have been removed for clarity.

The [Tp^{Ph,Me}Zn(MBI)] complexes with the hydroxamate series (**4.1b**, **4.2b**, **4.3b**, **4.4b,** and **4.5b**) exhibited similar trends as was observed with the *O*-methyl hydroxamate series, with one exception. Compounds **4.1b** and **4.5b** were observed to coordinate through the hydroxamate only and **4.2b** and **4.4b** were bound through the heterocycle and the hydroxamate (Figure 4.4), which are all consistent with the *O*-methyl hydroxamate series. In contrast, **4.3b** did not coordinate in the same manner as **4.3a**, but rather was coordinated to the Zn^{2+} center through the hydroxamic acid in a bidentate fashion (like **4.1b** and **4.5b**).

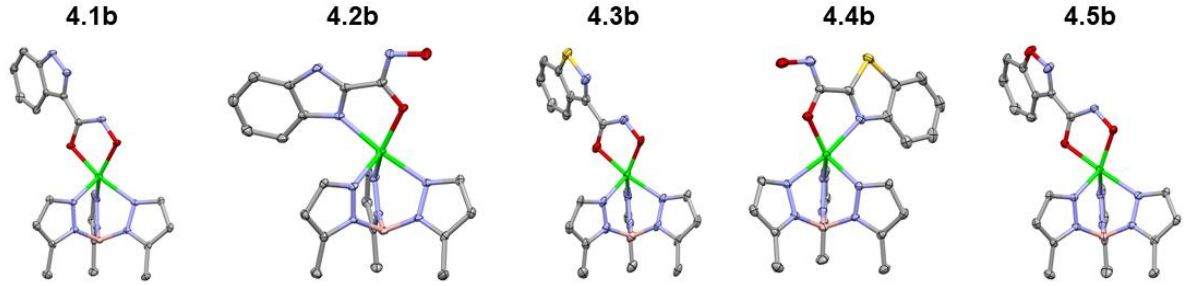

Figure 4.4. Crystal structure of [Tp^{Ph,Me}Zn(MBI)] complexes of **4.1b**, **4.2b**, **4.3b**, **4.4b**, and **4.5b**. Phenyl groups of Tp^{Ph,Me} have been removed for clarity.

To gain further insight into the coordinative ability of these MBIs, heterocyclic MBIs (C and D Series) were analysed crystallographically (Figure 4.5, Figure 4.6). Interestingly, the coordination mode of **4.1c** was almost monodentate in character with a Zn-heterocycle bond distance of 2.61 Å. The coordination mode of **4.2c** was clearly bidentate in character, with a Zn-heterocycle bond distance of 2.28 Å, as had been observed before with the pyridine-2-tetrazole complex.[12] The complex with **4.3c** again showed monodentate binding with the Zn-heterocycle distance ~3.05 Å, while the complex with **4.4c** exhibited bidentate binding with an elongated Zn-heterocycle distance of 2.48 Å. The [$Tp^{Ph,Me}$Zn(MBI)] complex with **4.5c** again presented monodentate coordination with a Zn-heterocycle distance of 3.17 Å. To evaluate whether these coordination trends were due to a steric effect, a more sterically bulky heterocycle isostere, oxadiazolone, was investigated. The oxadiazolone [$Tp^{Ph,Me}$Zn(MBI)] complexes (Figure 4.6) exhibited the same coordination motifs and bond distances as the tetrazole complexes, suggesting an important electronic contribution to the observed coordination trends and no significant steric impediments.

Based on the [$Tp^{Ph,Me}$Zn(MBI)] structures of both the acyclic and cyclic MBI complexes, it is evident that the heterocyclic scaffold greatly influences MBI binding. The heteroarenes presenting a 1,3-heteroatom arrangement (Series 2 and 4) appear to retain bidentate coordination and short metal-ligand bond distances. In contrast, the heteroarenes bearing a 1,2 arrangement of heteroatoms vary significantly in their preferred coordination mode and bond distances. For example, the series based on the 1,2-benzisoxazole scaffold (**4.5a-4.5d**) exhibited either monodentate coordination or coordination through the isostere replacement alone (**4.5a** and **4.5b**). These results suggest that retention of coordination geometry upon carboxylate replacement is dependent on the coordination character/ability of the parent scaffold, which appears to be affected

by heteroatom identity and pattern within the heterocycle scaffold. Taken together, these crystallographic complexes suggest the [$Tp^{Ph,Me}$Zn(MBI)] model complex is a useful evaluative tool for metal binding, and may be useful to recapitulate coordinative behaviour of similar substitutions in metalloenzyme inhibitors.[22] To further understand the electronic effect of each isostere replacement, the physicochemical properties of the MBIs were measured.

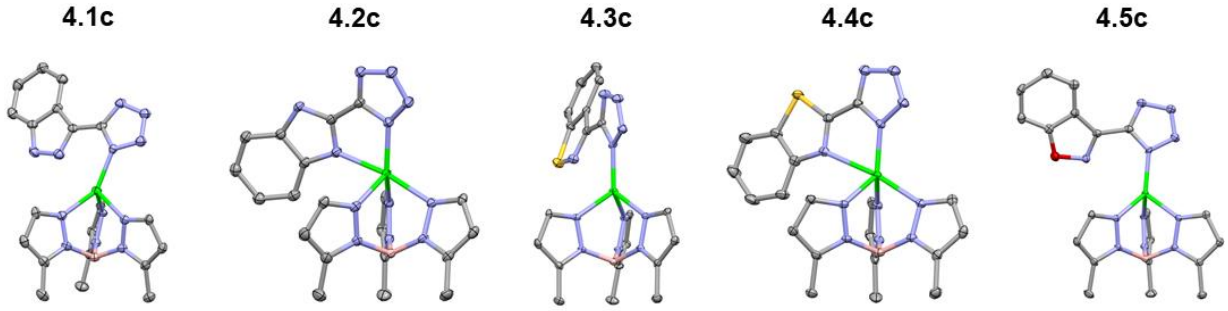

Figure 4.5. Crystal structure of [$Tp^{Ph,Me}$Zn(MBI)] complexes of **4.1c**, **4.2c**, **4.3c**, **4.4c**, and **4.5c**. Phenyl groups of $Tp^{Ph,Me}$ have been removed for clarity.

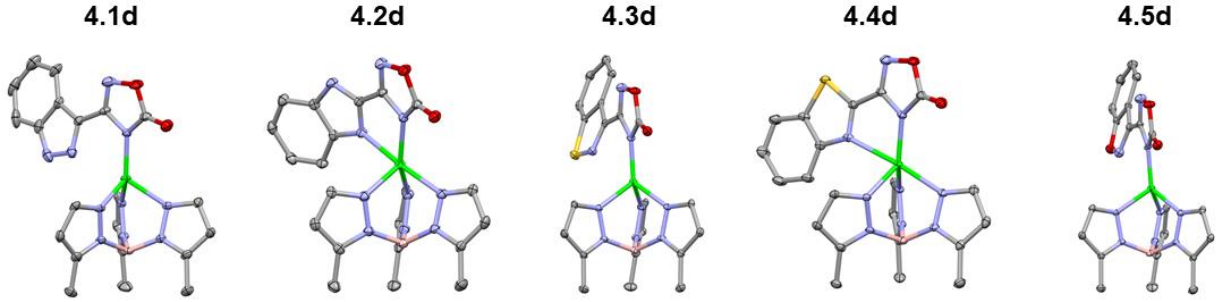

Figure 4.6. Crystal structure of [$Tp^{Ph,Me}$Zn(MBI)] complexes of **4.1d**, **4.2d**, **4.3d**, **4.4d**, and **4.5d**. Phenyl groups of $Tp^{Ph,Me}$ have been removed for clarity.

4.4 Physicochemical Analysis

Upon determining that the MBIs of the different series have different coordination abilities to the $Tp^{Ph,Me}Zn$ bioinorganic model system, an evaluation of physicochemical properties was performed. The acidity (pK_a) of the isostere groups of the *O*-methyl hydroxamic ester (**4.1a**-**4.5a**) and oxadiazolone MBIs (**4.1d**-**4.5d**) were determined as representative sets. Acidity was measured using a potentiometric method with or without methanol as a cosolvent (Table 4.1).[23] The compounds were also evaluated for their lipophilicity (LogP) via a potentiometric method, which was combined with the measured pK_a value to determine $LogD_{7.4}$ (Table 4.1).

The physicochemical values between MBIs vary significantly, even in cases where the only difference between compounds is a single atom replacement. Comparing isomeric MBIs such as, **4.1a** and **4.2a**, yields an interesting trend with the 1,3-heteroatom arrangement (**4.2a**) MBIs possessing a substantially lower pK_a value than the corresponding 1,2-isomer (**4.1a**). Interestingly, single atom substitutions had a strong effect on the logP values, causing a significant shift in some cases (**4.2d** versus **4.4d**). These observed differences were also apparent in the $LogD_{7.4}$ values, as they are derived from both measurements. Overall, the pK_a values are significantly affected by the heteroatom positioning and identity, yielding a set of substituted heteroarenes that span a range of two pK_a units, suggesting the heteroarene scaffold strongly affects the electronics of the isostere replacement and vice versa. To better understand how electronic effects are influenced by the positioning and identity of the heteroatoms within these heteroarene rings, computational analysis of these coordination complexes was performed.

Table 4.1. Physicochemical values from all *O*-methyl hydroxamate (**4.1a**-**4.5a**) and oxadiazolone (**4.1d**-**4.5d**) MBIs.

Compound	pK_a[a]	LogP[a]	Log$D_{7.4}$
4.1a	8.43	1.37	1.33
4.2a	7.21	1.28	0.88
4.3a	7.44	1.83	1.55
4.4a	6.34	1.91	0.81
4.5a	6.35	1.53	0.44
4.1d	4.73	2.51	-0.16
4.2d	4.04	1.55	-1.75
4.3d	4.50	2.86	0.11
4.4d	2.87	3.05	-0.43
4.5d	3.74	2.26	-0.24

[a]All pK_a and LogP experiments yielded standard deviations <0.05.

4.5 Computational Analysis

To understand the electronics of the MBIs and energetics of the resulting [$Tp^{Ph,Me}$Zn (MBI)] model complexes, an evaluation of each complex via density functional theory (DFT) was performed. All computations were performed using ωB97x-D/def2-TZVPP as it generally recapitulates the geometries observed experimentally.[24] An added benefit of performing these calculations allows the exclusion of noncovalent interactions present in the crystal structures which may influence the observed modes of coordination. A phenyl truncation of the [$Tp^{Ph,Me}$Zn(MBI)] models was used to reduce computational cost, with the phenyl substituents present on the $Tp^{Ph,Me}$ ligand being replaced with a hydrogen atom (i.e., Tp^{Me}). Additionally, the benzoxazole scaffold

(Figure 4.S26) was investigated even though it could not be accessed synthetically.[14] Further details regarding the computational methodology can be found in the Experimental.

In agreement with the bond lengths determined from X-ray crystallography (Table 4.S6), computations show that the carboxylate/isostere-metal bonds of Tp^{Me}Zn(MBP) complexes are generally shorter than the heteroarene-metal (i.e., N-Zn) bonds (Table 4.2). The greatest deviation between the experimentally and computationally determined bond lengths is observed when the ligating heteroarene engages in long range interactions with the Zn (**4.3c**, **4.3d**, **4.5c**, and **4.5d**). However, the computational results recapitulated the experimental results with respect to the observed trends in Zn-MBI bond distances, with 1,3-heteroatom arrangement MBIs (e.g. **4.2**, **4.2c**, **4.4**, **4.4c**) producing shorter Zn-heteroarene bond distances than their 1,2-isomers (e.g. **4.1**, **4.1c**, **4.3**, **4.3c**).

Table 4.2. Calculated bond lengths for select $Tp^{Me}Zn$(MBP) and $Tp^{Me}Zn$(MBI) coordination complexes using ωB97x-D/def2-TZVPP.

MBP	Zn–Carboxylate (Å)	Zn–N (heteroarene, Å)
4.1	1.953	2.255
4.2	2.021	2.161
4.3	1.959	2.261
4.4	1.994	2.193
4.5	1.955	2.319
Benzoxazole-2-carboxylic acid	1.996	2.199
MBI	Zn–Tetrazole (Å)	Zn–N (heteroarene, Å)
4.1c	1.948	2.784
4.2c	2.033	2.283
4.3c	1.951	2.706
4.4c	2.004	2.348
4.5c	1.953	2.959
Benzoxazole-2-tetrazole	1.985	2.496
MBI	Zn–Oxadiazolone (Å)	Zn–N (heteroarene, Å)
4.1d	1.942	2.776
4.2d	2.004	2.391
4.3d	1.949	2.740
4.4d	1.976	2.491
4.5d	1.940	2.910
Benzoxazole-2-oxadiazolone	1.957	2.738

Computed free energies (1 atm at 298 K) determined at the ωB97x-D/def2-TZVPP level of theory indicate that bidentate coordination through both the heteroarene and carboxylate (*N*,*O*) in the $Tp^{Me}Zn$(**1**) complex is 4.7 kcal mol^{-1} lower in electronic energy than isomeric bidentate coordination through only the carboxylate (*O*,*O*), whereas analogous coordination modes of the isomeric $Tp^{Me}Zn$(**4.5**) complexes are closer to being isoenergetic (ΔG = 1.2 kcal mol^{-1}) (Figure 4.7). These differences in relative stabilities can be attributed to differences in electronic structure of the heterocyclic ring systems. The 1,2-benzisoxazole (**4.5**) contains a more electronegative oxygen atom adjacent to the ligating nitrogen atom than the indazole (**4.1**), making it a poorer electron donor than **4.1**. Furthermore, the negative charge of the carboxylate is more effectively withdrawn in **4.5** due to the greater electron-withdrawing character of the 1,2-benzisoxazole.[25] Clearly, differences in the electronic character of heteroarene ligands **4.1**-**4.5**, **4.1a**-**4.5a**, **4.1b**-

4.5b, **4.1c-4.5c**, and **4.1d-4.5d**, not only modulate ligand–metal bond lengths, but ultimately influence the actual modes by which these ligands coordinate metal ions.

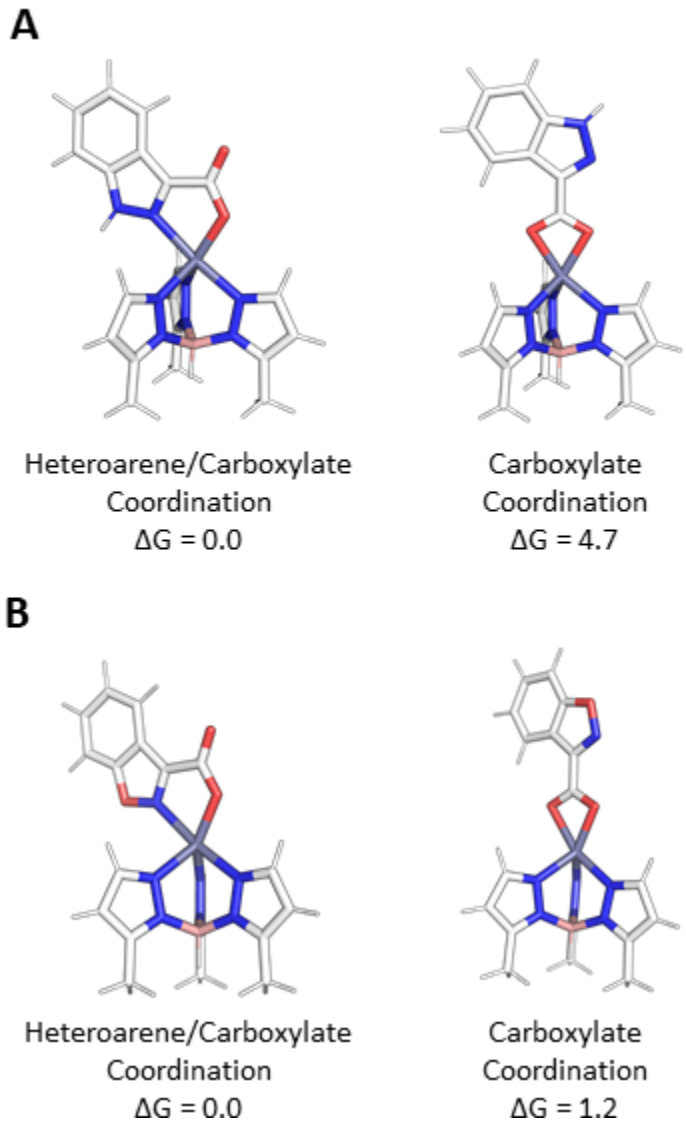

Figure 4.7. A comparison of the structures and relative free energies (kcal mol^{-1}) for carboxylate only (*O*,*O*) and isomeric heteroarene/carboxylate (*N*,*O*) coordination of (*A*) Tp^{Me}Zn(**4.2**) and (*B*) Tp^{Me}Zn(**4.5**) using ωB97x-D/def2-TZVPP level of theory.

Theory shows that regardless of the nature of the heteroarene substituent, heteroarenes with a 1,3-heteroatom arrangement (**4.2**, **4.4**, and benzoxazole-2-carboxylic acid) coordinate with

shorter bond lengths to the Zn^{2+} center than do their 1,2-isomers (**4.1**, **4.3**, and **4.5**). In examining the isomeric pairs (**4.1** vs. **4.2**) the computed energy difference is largest when comparing 1,2-benzisoxazole-containing complexes, $Tp^{Me}Zn$(**4.5**), $Tp^{Me}Zn$(**4.5c**), and $Tp^{Me}Zn$(**4.5d**), to their benzoxazole isomers (Figure 4.8, Figure 4.S27-S28). In contrast, the corresponding energy differences between isomeric benzothiazole- and 1,2-benzisothiazole-ligated $Tp^{Ph,Me}Zn$(MBI) complexes (e.g., $Tp^{Ph,Me}Zn$(**4.4**) and $Tp^{Ph,Me}Zn$(**4.3**)) are much smaller, ranging in energy from ~4 to ~9 kcal mol^{-1}. These energetic preferences can be attributed to differences in the aromaticity of the heteroarenes. For instance, benzimidazole-ligated complexes, like $Tp^{Ph,Me}Zn$(**4.2c**) are more stable than the those that featuring an indazole ligand (e.g., $Tp^{Ph,Me}Zn$(**4.1c**)) because through greater electron delocalization **4.2c** more effectively shifts electron density toward the coordinating nitrogen atom of the heteroarene than its isomer **4.1c**. A smaller difference in the stability of $Tp^{Ph,Me}Zn$(**4.4c**) and $Tp^{Ph,Me}Zn$(**4.3c**) pair of complexes is due to both the reduced aromaticity of the benzothiazole (**4.4**) moiety and the reduced electronegativity of sulfur.[25-26] These computational data provide a rationalization for the tighter coordination, and likely better donor ability, observed for the benzimidazole and benzothiazole MBPs/MBIs (**4.2**, **4.4**, **4.2c**, **4.4c**, **4.2d**, **4.4d**).

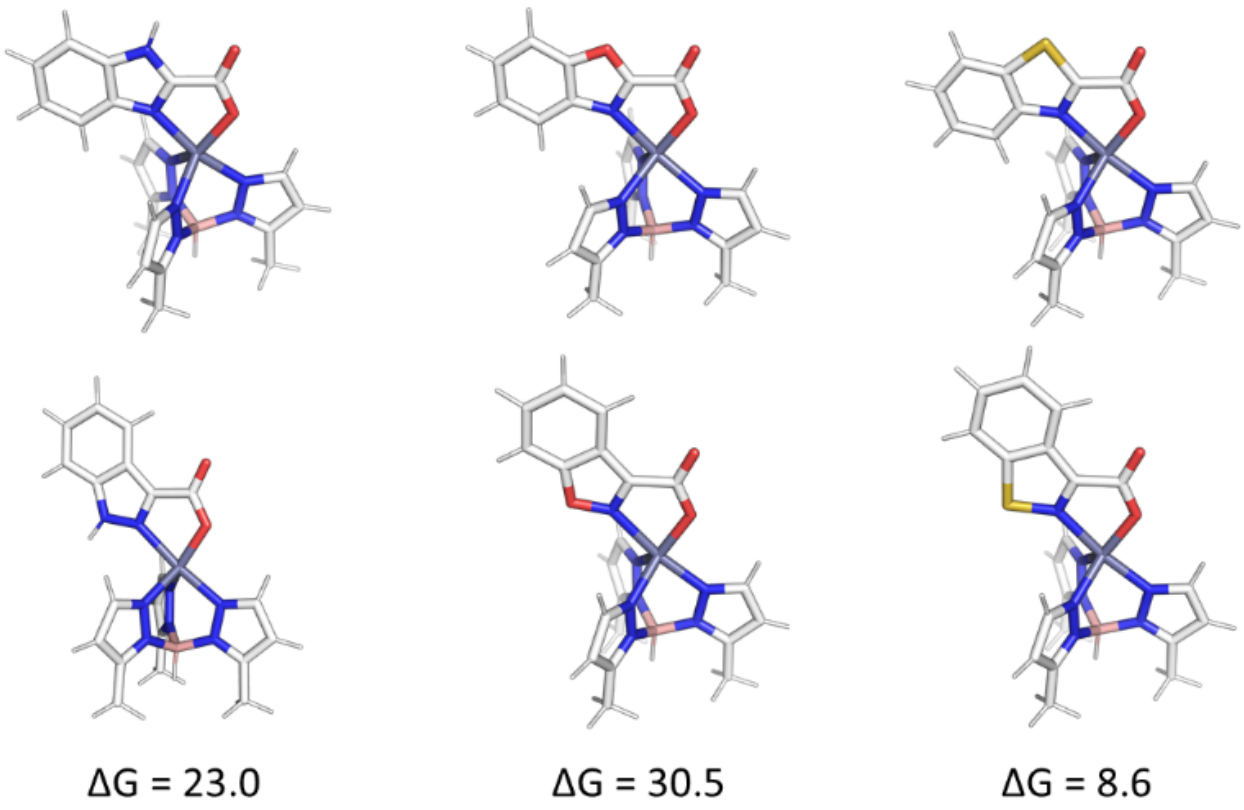

Figure 4.8. ωB97x-D/def2-TZVPP-optimized geometries of: isomeric Tp^{Me}Zn(**4.2**) and Tp^{Me}Zn(**4.1**) (*top and bottom left*, respectively), isomeric Tp^{Me}Zn(benzoxazole-2-carboxylic acid) and Tp^{Me}Zn(**4.5**) (*top and bottom middle*, respectively), and isomeric Tp^{Me}Zn(**4.4**) and Tp^{Me}Zn(**4.5**) (*top and bottom right*, respectively). Energies (in kcal mol^{-1}) are free energies determined at the ωB97x-D/def2-TZVPP level of theory.

Computational analysis of the $Tp^{Ph,Me}$Zn(MBI) complexes with ligands **4.1a**-**4.5a** and **4.1b**-**4.5b** is complicated by the possibility of multiple coordination modes (e.g., *N,O* or *N,N* coordination), various coordination geometries, and conformational flexibility of the hydroxamate and hydroxamic methyl ester ligands. As shown in Figure 4.9, computational modelling of the phenyl truncated complex Tp^{Me}Zn(**4.1a**), reveals the crystallographically observed mode of coordination is the lowest energy mode of coordination predicted computationally. Because there were many computationally observed modes of coordination with [$Tp^{Ph,Me}$Zn(MBI)] complexes

with ligands **4.1a**-**4.5a** and **4.1b**-**4.5b**, geometry optimizations were performed on the complete, phenyl-substituted $Tp^{Ph,Me}Zn$(**4.1a**) complex. The inclusion of the phenyl substituents also correctly predicts that the preferred coordination geometry involving heteroarene coordination via the heteroarene nitrogen atom and the *O*-methyl hydroxamate oxygen atom of **4.1a**. Interestingly, these calculations show that the phenyl substituents reduce the energetic differences between the various possible modes of coordination by ~1 kcal/mol, relative to the $Tp^{Me}Zn$(**4.1a**) results. Overall, these computational analyses suggest that while the phenyl groups contribute slightly to the observed modes of coordination, the major driving force behind MBI coordination is ligand electronics.

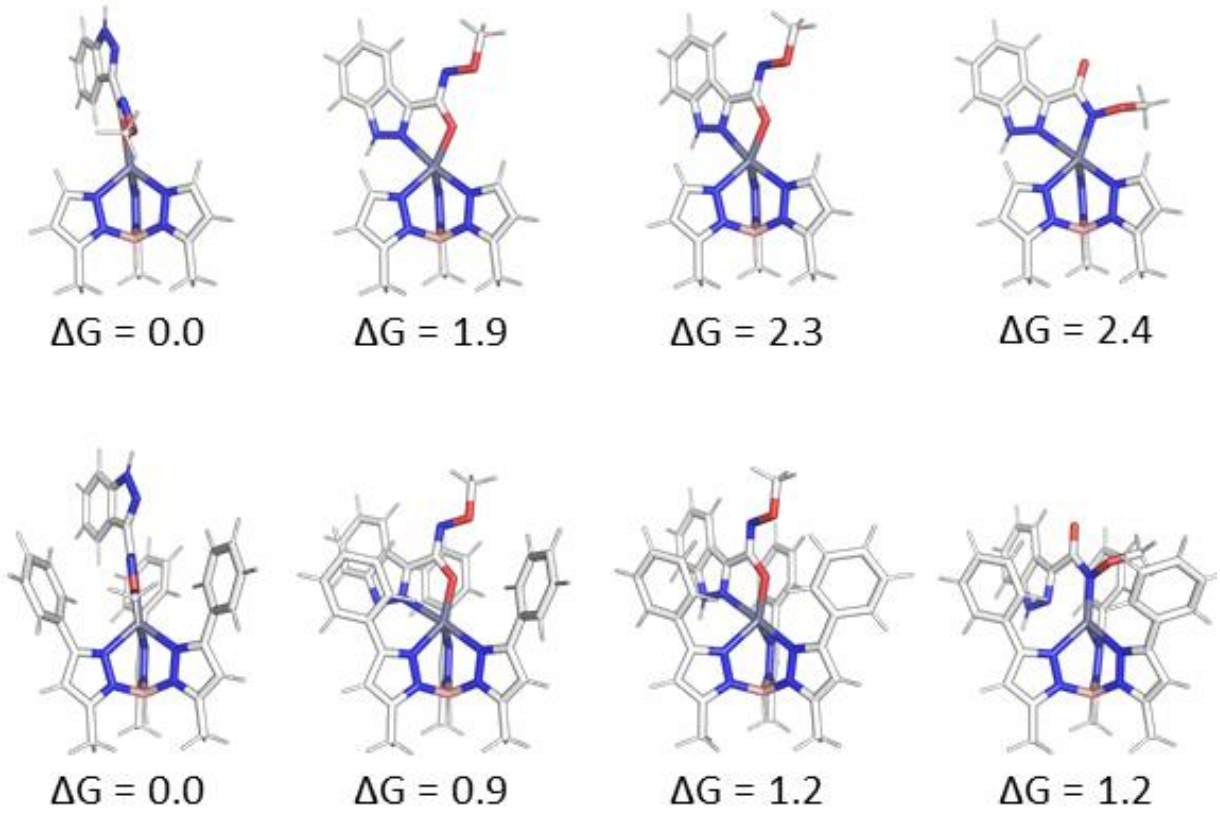

Figure 4.9. A comparison of various coordination modes of phenyl-truncated $Tp^{Me}Zn$(**4.1a**) (*top*) and phenyl substituted $Tp^{Me,Ph}Zn$(**4.1a**) (*bottom*) complexes. Relative free energies, in kcal mol^{-1}, determined using ωB97x-D/def2-TZVPP level of theory are reported below each structure.

4.6 Conclusions

The development of a series of MBIs based on a diverse range of heteroarene scaffolds was shown to produce an interesting range of expected, as well as unexpected, coordination modes. DFT calculations were able to reproduce the experimental results from X-ray crystallography. From these data it was determined that the content and arrangement of the heteroarene significantly modifies the coordination ability of the resulting MBP or MBI. Specifically, the heteroarene aromaticity and subsequent donation ability of the heteroarene donor atom(s) was determined to be essential in dictating the resulting mode of coordination to a bioinorganic model complex. This dependence on the electronic character of each scaffold is a direct example of the "context dependence" success of isostere replacement. These results and analyses provided here allow for an understanding and prediction of future MBI success. In addition, the results described here can be applied to MBP development. This work demonstrates that MBIs are useful scaffolds for FBDD of metalloenzymes, but the effect of isosteres on metal coordination must be understood to successfully implement the use of isosteres for metalloenzyme inhibition. In Chapter 5, the preliminary appliction of isostere replacement in a structure based inhibitor development campaign will be explored.

4.7 Experimental

General Information. Starting materials and solvents were purchased and used without further purification from commercial suppliers (Sigma-Aldrich, Alfa Aesar, EMD, TCI, etc.). Detailed synthetic routes for each MBI are provided in the Appendix. [($Tp^{Ph,Me}$)ZnOH] ($Tp^{Ph,Me}$ =

hydrotris(5,3-methylphenylpyrazolyl)borate)) was synthesized as reported using [KTp^{Ph,Me}], which was prepared as previously reported.[27]

General Synthesis and Crystallization of [Tp^{Ph,Me}Zn(MBI)] Model Complexes. [(Tp^{Ph,Me})ZnOH] (60 mg, 0.11 mmol) was dissolved in 15 mL of CH_2Cl_2 in a 50 mL round-bottom flask. The MBP/MBI (0.11 mmol, 1 equiv) in 10 mL of MeOH was added, and the reaction mixture was stirred overnight under a nitrogen atmosphere (Note: in a select few cases to conserve material the amounts of [(Tp^{Ph,Me})ZnOH] and MBI were halved while keeping solvent volumes constant). The resulting mixture was evaporated to dryness via rotary evaporation and subsequently a minimal amount (~5 mL) of benzene was added, if that was insufficient to dissolve the residue a minimal amount of MeOH was added (~1-3 mL). The solution was filtered via filter paper and vacuum filtration to remove any undissolved solids. The resulting complex in benzene or benzene/MeOH was recrystallized using vapor diffusion with pentane; crystals typically formed within one week.

Physicochemical Properties Analysis. Physicochemical properties were determined using a Sirius T3 instrument. All titrations, both pK_a and logP, were performed in 0.15 M KCl with 0.5 M HCl and KOH. The pK_a of a compound was determined by analysing each MBI sample in triplicate using potentiometric titrations.[23] Experiments were typically performed over a pH range of 2.0−12.0. Standard deviations were derived from fitting all three replicate experiments. For water insoluble compounds cosolvents were applied and the obtained apparent pK_a (psK_a) was extrapolated to the aqueous pK_a by the Yasuda–Shedlovsky procedure.[28-29] LogP was determined

via potentiometric titrations in the presence of varying ratios of octanol and water.[30] The presence of octanol shifts the pK_a of ionizable species, and based on the shift, a logP can be determined. Measurements for logP determination were typically performed over a pH range of 2.0−12.0. Three experiments with varying ratios of water:octanol were performed, allowing for a standard deviation to be determined from the fitting of all measurements. MBI sample sizes were ≤0.5 mg for both pK_a and logP measurements.

Computational Methodology. All DFT computations were performed using Gaussian 09.[31] All geometry optimizations were performed at the ωB97x-D/def2-TZVPP level of theory.[24, 32-33] Unless otherwise indicated all structures and energies were determined using the ωB97x-D/def2-TZVPP method. Frequency calculations were performed to confirm that each structure was in fact a local minimum (stationary point) on the potential energy surface. Initial coordinates for computation were prepared using Gaussview 5.0.9 and Avogadro 1.2.0.[34-36] Pymol 2.3 was used to render images of the DFT-optimized structures presented herein.[37]

4.8 Appendix: Supporting Information

General Materials and Methods. Starting materials were purchased and used from commercially available suppliers (Sigma-Aldrich, Acros Organics, Matrix Scientific, others) without further purification. [($Tp^{Ph,Me}$)ZnOH] ($Tp^{Ph,Me}$= hydrotris(5,3-methylphenylpyrazolyl)borate)) was synthesized as previously reported.[27] Column chromatography was performed using a CombiFlash R_f automated system from Teledyne Isco using prepacked silica cartridges. ^{1}H nuclear magnetic resonance (NMR) spectra were collected using a Varian spectrometer running at

400 MHz, a Varian spectrometer running at 500 MHz, or a 300 MHz Bruker AVA. ^{13}C NMR spectra were collected using a Varian spectrometer running at 126 MHz. Mass spectrometry analysis was performed by the University of California San Diego Chemistry and Biochemistry Mass Spectrometry Facility (MMSF).

Single Crystal X-ray Diffraction. Suitable crystals of [($Tp^{Ph,Me}$)Zn(MBI)] complexes were selected and placed on a Bruker APEX-II Ultra diffractometer with a Mo-Kα Microfocus Rotating Anode and an APEX-II CCD area detector or a Bruker Kappa diffractometer equipped with a Bruker X8 APEX II Mo sealed tube and a Bruker APEX-II CCD. The crystals were kept at 100 K during data collection. Using Olex2,[38] the structure was solved with the ShelXT[39] structure solution program using direct methods and refined with the XL[40] refinement package using least squares minimization. The crystal data file of all complexes was deposited into the Cambridge Crystallographic Data Centre (CCDC, Table 4.S1-4.S5). Crystallographic data collection and refinement information is listed in Table 4.S1-Table 4.S5. Disordered solvent was treated with the PLATON SQUEEZE function in the [($Tp^{Ph,Me}$)Zn(**4.3b**)] and [($Tp^{Ph,Me}$)Zn(**4.5b**)] structures with 39 and 43 electrons squeezed respectively.[41]

Table 4.S1. Crystal data and structure refinement for [(Tp^{Ph,Me})Zn(indazole)] complexes.

Compound	[(Tp^{Ph,Me})Zn(**4.1**)]	[(Tp^{Ph,Me})Zn(**4.1a**)]	[(Tp^{Ph,Me})Zn(**4.1b**)]	[(Tp^{Ph,Me})Zn(**4.1c**)]	[(Tp^{Ph,Me})Zn(**4.1d**)]
CCDC code	1999816	1999818	1999817	1999819	1999820
Empirical formula	$C_{42}H_{40}BN_8O_3Zn$	$C_{40}H_{40}BN_9O_3Zn$	$C_{39}H_{38}BN_9O_3Zn$	$C_{38}H_{34}BN_{12}O_{0.5}Zn$	$C_{40.5}H_{39}BN_{10}O_{3.5}Zn$
Formula weight	781.00	770.99	756.96	742.95	797.99
Temperature/K	100.0	100.0	100.0	100.0	100.0
Crystal system	monoclinic	triclinic	triclinic	monoclinic	monoclinic
Space group	$P2_1/n$	P-1	P-1	C2/c	$P2_1/c$
a/Å	11.1116(16)	11.652(4)	11.5454(6)	21.265(2)	22.1038(7)
b/Å	22.132(3)	12.368(4)	12.4466(6)	12.2666(12)	18.2437(6)
c/Å	16.382(2)	13.917(4)	13.3968(7)	26.802(3)	20.8443(7)
α/°	90	92.104(6)	87.8610(10)	90	90
β/°	105.947(5)	105.552(4)	72.8450(10)	96.968(2)	110.7280(10)
γ/°					
Volume/Å^3	3873.7(9)	1870.4(10)	1838.16(16)	6939.8(12)	7861.5(4)
Z	4	2	2	8	8
ρ_{calc}g/cm^3	1.339	1.369	1.368	1.422	1.348
μ/mm^{-1}	0.684	0.708	0.719	0.758	0.678
F(000)	1628.0	804.0	788.0	3080.0	3320.0
Crystal size/mm^3	0.5 × 0.25 × 0.15	0.08 × 0.08 × 0.08	0.05 × 0.05 × 0.05	0.4 × 0.3 × 0.1	0.2 × 0.02 × 0.01
Radiation	MoKα (λ = 0.71073)	MoKα (λ = 0.71073)	MoKα (λ = 0.71073)	MoKα (λ = 0.71073)	MoKα (λ = 0.71073)
2Θ range for data collection/°	5.172 to 51.604	3.054 to 52.81	3.184 to 50.73	3.062 to 51.36	2.978 to 51.394
Index ranges	$-13 \le h \le 13$, $-27 \le k \le 26$, $-20 \le l \le 20$	$-14 \le h \le 14$, $-15 \le k \le 15$, $-17 \le l \le 17$	$-13 \le h \le 13$, $-14 \le k \le 14$, $-16 \le l \le 15$	$-25 \le h \le 25$, $-14 \le k \le 14$, $-32 \le l \le 32$	$-26 \le h \le 26$, $-22 \le k \le 15$, $-25 \le l \le 19$
Reflections collected	36424	46382	11609	34629	48279
Independent reflections	7278 [R_{int} = 0.0636, R_{sigma} = 0.0592]	7674 [R_{int} = 0.0515, R_{sigma} = 0.0338]	6726 [R_{int} = 0.0270, R_{sigma} = 0.0452]	6569 [R_{int} = 0.0665, R_{sigma} = 0.0527]	14813 [R_{int} = 0.0602, R_{sigma} = 0.0776]
Data/restraints/parameters	7278/9/501	7674/0/493	6726/0/483	6569/0/480	14813/0/1021
Goodness-of-fit on F^2	1.038	1.046	1.062	1.038	1.090
Final R indexes [I>=2σ (I)]	R_1 = 0.0543, wR_2 = 0.1275	R_1 = 0.0306, wR_2 = 0.0721	R_1 = 0.0335, wR_2 = 0.0711	R_1 = 0.0413, wR_2 = 0.0827	R_1 = 0.0514, wR_2 = 0.1219
Final R indexes [all data]	R_1 = 0.0836, wR_2 = 0.1428	R_1 = 0.0379, wR_2 = 0.0762	R_1 = 0.0455, wR_2 = 0.0749	R_1 = 0.0629, wR_2 = 0.0902	R_1 = 0.0913, wR_2 = 0.1507
Largest diff. peak/hole / e Å^{-3}	0.70/-1.08	0.61/-0.29	0.53/-0.32	0.31/-0.41	0.71/-0.73

Table 4.S2. Crystal data and structure refinement for [(Tp^{Ph,Me})Zn(benzimidazole)] complexes.

Compound	[(Tp^{Ph,Me})Zn(**4.2**)]	[(Tp^{Ph,Me})Zn(**4.2a**)]	[(Tp^{Ph,Me})Zn(**4.2b**)]	[(Tp^{Ph,Me})Zn(**4.2c**)]	[(Tp^{Ph,Me})Zn(**4.2d**)]
CCDC code	1999824	1999822	1999840	1999823	1999821
Empirical formula	$C_{53}H_{48}BN_8O_2Zn$	$C_{48}H_{45}BN_9O_2Zn$	$C_{50}H_{46}BN_9O_2Zn$	$C_{91}H_{81}B_2N_{24}Zn_2$	$C_{39}H_{33}BN_{10}O_2Zn$
Formula weight	905.17	856.11	881.14	1663.15	749.93
Temperature/K	100.0	100.0	100.0	100.0	100.0
Crystal system	triclinic	triclinic	triclinic	triclinic	monoclinic
Space group	P-1	P-1	P-1	P-1	$P2_1/c$
a/Å	11.7557(10)	11.951(7)	11.902(2)	14.290(3)	19.2031(17)
b/Å	13.3890(16)	12.222(7)	13.512(3)	16.009(4)	17.4413(16)
c/Å	16.6386(11)	33.40(2)	15.071(2)	20.236(5)	10.8662(10)
α/°	67.385(4)	96.044(11)	65.558(5)	111.296(6)	90
β/°	74.545(2)	90.661(10)	87.822(5)	101.338(4)	103.602(3)
γ/°	89.452(4)	117.154(13)	87.374(8)	94.752(4)	90
Volume/Å^3	2317.3(4)	4307(4)	2203.5(7)	4168.3(16)	3537.3(6)
Z	2	4	2	2	4
ρ_{calc}g/cm^3	1.297	1.320	1.328	1.325	1.408
μ/mm^{-1}	0.581	0.621	0.609	0.638	0.746
F(000)	946.0	1788.0	920.0	1730.0	1552.0
Crystal size/mm^3	0.2 × 0.2 × 0.2	0.1 × 0.1 × 0.03	0.5 × 0.2 × 0.2	0.3 × 0.2 × 0.15	0.25 × 0.25 × 0.07
Radiation	MoKα (λ = 0.71073)	MoKα (λ = 0.71073)	MoKα (λ = 0.71073)	MoKα (λ = 0.71073)	MoKα (λ = 0.71073)
2Θ range for data collection/°	3.314 to 52.814	2.458 to 48.452	3.416 to 51.494	2.77 to 52.684	4.364 to 52.952
Index ranges	-14 ≤ h ≤ 14, -16 ≤ k ≤ 16, -20 ≤ l ≤ 20	-13 ≤ h ≤ 13, -14 ≤ k ≤ 14, -38 ≤ l ≤ 38	-11 ≤ h ≤ 14, -16 ≤ k ≤ 16, -18 ≤ l ≤ 18	-17 ≤ h ≤ 17, -19 ≤ k ≤ 19, -25 ≤ l ≤ 25	-22 ≤ h ≤ 24, -21 ≤ k ≤ 21, -13 ≤ l ≤ 13
Reflections collected	42525	61119	43680	83446	53135
Independent reflections	9499 [R_{int} = 0.0647, R_{sigma} = 0.0436]	13796 [R_{int} = 0.0983, R_{sigma} = 0.0998]	8391 [R_{int} = 0.0610, R_{sigma} = 0.0563]	16899 [R_{int} = 0.0635, R_{sigma} = 0.0429]	7284 [R_{int} = 0.0621, R_{sigma} = 0.0428]
Data/restraints/parameters	9499/0/589	13796/285/1230	8391/0/572	16899/84/1073	7284/0/481
Goodness-of-fit on F^2	1.055	1.025	1.033	1.040	1.038
Final R indexes [I>=2σ (I)]	R_1 = 0.0326, wR_2 = 0.0869	R_1 = 0.0568, wR_2 = 0.0986	R_1 = 0.0404, wR_2 = 0.0839	R_1 = 0.0341, wR_2 = 0.0840	R_1 = 0.0421, wR_2 = 0.0958
Final R indexes [all data]	R_1 = 0.0360, wR_2 = 0.0896	R_1 = 0.1049, wR_2 = 0.1126	R_1 = 0.0622, wR_2 = 0.0926	R_1 = 0.0430, wR_2 = 0.0896	R_1 = 0.0622, wR_2 = 0.1038
Largest diff. peak/hole / e Å^{-3}	0.36/-0.28	0.43/-0.44	0.62/-0.52	0.52/-0.40	0.89/-0.42

Table 4.S3. Crystal data and structure refinement for [(Tp^{Ph,Me})Zn(1,2-benzisothiazole)] complexes.

Compound	[(Tp^{Ph,Me})Zn(**4.3**)]	[(Tp^{Ph,Me})Zn(**4.3a**)]	[(Tp^{Ph,Me})Zn(**4.3b**)]	[(Tp^{Ph,Me})Zn(**4.3c**)]	[(Tp^{Ph,Me})Zn(**4.3d**)]
CCDC code	1999829	1999827	1999828	1999826	1999825
Empirical formula	$C_{38}H_{32}BN_7O_2SZn$	$C_{45}H_{41}BN_8O_2SZn$	$C_{39}H_{36}BN_8O_3SZn$	$C_{38}H_{32}BN_{11}SZn$	$C_{39}H_{32}BN_9O_2SZn$
Formula weight	726.94	834.10	773.00	750.98	766.97
Temperature/K	100.0	100.0	100.0	100.0	100.0
Crystal system	monoclinic	triclinic	triclinic	triclinic	triclinic
Space group	$P2_1/c$	P-1	P-1	P-1	P-1
a/Å	25.354(4)	11.7747(6)	11.767(3)	11.3854(9)	11.3437(6)
b/Å	12.7294(11)	12.2627(6)	13.044(3)	12.2324(9)	12.4724(6)
c/Å	21.364(3)	16.6658(8)	14.552(4)	12.9278(11)	13.2663(7)
α/°	90	88.998(2)	110.451(4)	95.296(2)	93.307(2)
β/°	99.223(5)	71.4110(10)	94.891(5)	103.872(2)	106.813(2)
γ/°	90	63.5020(10)	107.004(4)	100.760(2)	102.442(2)
Volume/Å^3	6805.8(15)	2019.04(17)	1957.2(9)	1699.4(2)	1740.01(16)
Z	8	2	2	2	2
ρ_{calc}g/cm^3	1.419	1.372	1.312	1.468	1.464
μ/mm^{-1}	0.830	0.710	0.728	0.832	0.817
F(000)	3008.0	868.0	802.0	776.0	792.0
Crystal size/mm^3	0.4 × 0.175 × 0.1	0.1 × 0.04 × 0.04	0.80 × 0.40 × 0.20	0.05 × 0.03 × 0.03	0.12 × 0.06 × 0.06
Radiation	MoKα (λ = 0.71073)	MoKα (λ = 0.71073)	MoKα (λ = 0.71073)	MoKα (λ = 0.71073)	MoKα (λ = 0.71073)
2Θ range for data collection/°	3.59 to 52.736	2.606 to 52.874	3.054 to 50.844	3.28 to 53.522	3.234 to 52.242
Index ranges	-31 ≤ h ≤ 31, -15 ≤ k ≤ 15, -26 ≤ l ≤ 26	-14 ≤ h ≤ 14, -15 ≤ k ≤ 15, -20 ≤ l ≤ 20	-14 ≤ h ≤ 14, -15 ≤ k ≤ 15, -17 ≤ l ≤ 16	-14 ≤ h ≤ 14, -15 ≤ k ≤ 15, -16 ≤ l ≤ 16	-14 ≤ h ≤ 14, -15 ≤ k ≤ 15, -14 ≤ l ≤ 16
Reflections collected	85431	25629	25768	19604	17297
Independent reflections	13899 [R_{int} = 0.0779, R_{sigma} = 0.0624]	8307 [R_{int} = 0.0309, R_{sigma} = 0.0335]	7169 [R_{int} = 0.0649, R_{sigma} = 0.0718]	7243 [R_{int} = 0.0441, R_{sigma} = 0.0655]	6893 [R_{int} = 0.0329, R_{sigma} = 0.0474]
Data/restraints/parameters	13899/0/907	8307/0/527	7169/0/486	7243/0/472	6893/0/481
Goodness-of-fit on F^2	1.017	1.048	1.027	0.912	1.015
Final R indexes [I>=2σ (I)]	R_1 = 0.0404, wR_2 = 0.0797	R_1 = 0.0313, wR_2 = 0.0704	R_1 = 0.0594, wR_2 = 0.1497	R_1 = 0.0423, wR_2 = 0.0900	R_1 = 0.0337, wR_2 = 0.0700
Final R indexes [all data]	R_1 = 0.0778, wR_2 = 0.0914	R_1 = 0.0409, wR_2 = 0.0742	R_1 = 0.0876, wR_2 = 0.1654	R_1 = 0.0681, wR_2 = 0.1013	R_1 = 0.0474, wR_2 = 0.0749
Largest diff. peak/hole / e Å^{-3}	0.35/-0.47	0.38/-0.27	1.35/-0.95	0.39/-0.53	0.37/-0.31

Table 4.S4. Crystal data and structure refinement for [(Tp^{Ph,Me})Zn(benzothiazole)] complexes.

Compound	[(Tp^{Ph,Me})Zn(**4.4**)]	[(Tp^{Ph,Me})Zn(**4.4a**)]	[(Tp^{Ph,Me})Zn(**4.4b**)]	[(Tp^{Ph,Me})Zn(**4.4c**)]	[(Tp^{Ph,Me})Zn(**4.4d**)]
CCDC code	1999834	1999830	1999833	1999831	1999832
Empirical formula	$C_{38}H_{32}BN_7O_2SZn$	$C_{45}H_{41}BN_8O_2SZn$	$C_{44}H_{39}BN_8O_2SZn$	$C_{44}H_{38}BN_{11}SZn$	$C_{45}H_{38}BN_9O_2SZn$
Formula weight	726.94	834.10	820.07	829.09	845.08
Temperature/K	100.0	100.0	100.0	100.0	100.0
Crystal system	monoclinic	monoclinic	monoclinic	monoclinic	monoclinic
Space group	$P2_1/n$	$P2_1/n$	$P2_1/c$	$P2_1/n$	$P2_1/n$
a/Å	11.8071(5)	13.2942(13)	18.2805(12)	11.4626(11)	11.5071(9)
b/Å	20.2004(10)	16.9309(19)	24.6819(16)	24.908(3)	24.8201(16)
c/Å	14.5401(11)	18.117(2)	17.9965(11)	14.0421(15)	14.2983(10)
α/°	90	90	90	90	90
β/°	95.990(2)	90.612(4)	103.0430(10)	92.074(4)	93.957(2)
γ/°	90	90	90	90	90
Volume/Å^3	3449.0(3)	4077.5(8)	7910.5(9)	4006.5(7)	4074.0(5)
Z	4	4	8	4	4
ρ_{calc}g/cm^3	1.400	1.359	1.377	1.375	1.378
μ/mm^{-1}	0.819	0.703	0.723	0.713	0.705
F(000)	1504.0	1736.0	3408.0	1720.0	1752.0
Crystal size/mm^3	0.4 × 0.4 × 0.4	0.6 × 0.6 × 0.2	0.1 × 0.1 × 0.05	1 × 0.5 × 0.5	0.5 × 0.3 × 0.3
Radiation	MoKα (λ = 0.71073)	MoKα (λ = 0.71073)	MoKα (λ = 0.71073)	MoKα (λ = 0.71073)	MoKα (λ = 0.71073)
2Θ range for data collection/°	3.464 to 51.348	3.292 to 53.464	4.694 to 54.25	3.332 to 52.824	3.294 to 52.84
Index ranges	-13 ≤ h ≤ 14, -22 ≤ k ≤ 24, -17 ≤ l ≤ 17	-15 ≤ h ≤ 16, -21 ≤ k ≤ 21, -22 ≤ l ≤ 22	-23 ≤ h ≤ 23, -31 ≤ k ≤ 31, -22 ≤ l ≤ 23	-14 ≤ h ≤ 13, -31 ≤ k ≤ 31, -17 ≤ l ≤ 16	-14 ≤ h ≤ 14, -31 ≤ k ≤ 31, -17 ≤ l ≤ 17
Reflections collected	69989	57223	51632	46011	78142
Independent reflections	6548 [R_{int} = 0.0406, R_{sigma} = 0.0169]	8665 [R_{int} = 0.0560, R_{sigma} = 0.0414]	17388 [R_{int} = 0.0483, R_{sigma} = 0.0567]	8205 [R_{int} = 0.0530, R_{sigma} = 0.0455]	8347 [R_{int} = 0.0423, R_{sigma} = 0.0245]
Data/restraints/parameters	6548/30/454	8665/0/527	17388/0/1035	8205/0/526	8347/0/535
Goodness-of-fit on F^2	1.053	1.016	1.025	1.019	1.029
Final R indexes [I>=2σ (I)]	R_1 = 0.0259, wR_2 = 0.0670	R_1 = 0.0332, wR_2 = 0.0703	R_1 = 0.0386, wR_2 = 0.0903	R_1 = 0.0363, wR_2 = 0.0743	R_1 = 0.0286, wR_2 = 0.0637
Final R indexes [all data]	R_1 = 0.0280, wR_2 = 0.0683	R_1 = 0.0491, wR_2 = 0.0764	R_1 = 0.0583, wR_2 = 0.0987	R_1 = 0.0549, wR_2 = 0.0807	R_1 = 0.0381, wR_2 = 0.0682
Largest diff. peak/hole / e Å^{-3}	0.53/-0.41	0.30/-0.35	0.81/-0.54	0.40/-0.33	0.30/-0.33

Table 4.S5. Crystal data and structure refinement for [(Tp^{Ph,Me})Zn(1,2-benzisoxazole)] complexes.

Compound	[(Tp^{Ph,Me})Zn(**4.5**)]	[(Tp^{Ph,Me})Zn(**4.5a**)]	[(Tp^{Ph,Me})Zn(**4.5b**)]	[(Tp^{Ph,Me})Zn(**4.5c**)]	[(Tp^{Ph,Me})Zn(**4.5d**)]
CCDC code	1999839	199836	1999838	1999837	1999835
Empirical formula	$C_{43.5}H_{41}BN_7O_3Zn$	$C_{45}H_{41}BN_8O_3Zn$	$C_{38}H_{35}BN_8O_4Zn$	$C_{38}H_{32}BN_{11}OZn$	$C_{39}H_{32}BN_9O_{2.96}Zn$
Formula weight	786.01	818.04	743.92	734.92	750.91
Temperature/K	100.0	100.0	100.0	100.0	100.0
Crystal system	monoclinic	triclinic	triclinic	triclinic	triclinic
Space group	$P2_1/n$	P-1	P-1	P-1	P-1
a/Å	15.5694(12)	11.7292(11)	11.930(2)	11.4597(7)	11.529(3)
b/Å	14.5978(11)	11.9654(12)	13.078(2)	12.2118(8)	12.532(3)
c/Å	17.7711(14)	16.3974(16)	14.235(3)	12.9190(8)	13.170(3)
α/°	90	100.704(3)	107.583(6)	95.428(2)	92.476(9)
β/°	106.120(2)	96.654(3)	93.055(6)	104.427(2)	108.327(9)
γ/°	90	114.105(3)	106.031(6)	100.399(2)	103.041(8)
Volume/Å^3	3880.2(5)	2016.3(3)	2012.0(6)	1703.57(19)	1746.3(7)
Z	4	2	2	2	2
ρ_{calc}g/cm^3	1.346	1.347	1.228	1.433	1.428
μ/mm^{-1}	0.683	0.661	0.657	0.772	0.757
F(000)	1640.0	852.0	772.0	760.0	776.0
Crystal size/mm^3	0.4 × 0.35 × 0.2	0.4 × 0.35 × 0.35	0.2 × 0.1 × 0.1	0.3 × 0.2 × 0.2	0.2 × 0.2 × 0.2
Radiation	MoKα (λ = 0.71073)	MoKα (λ = 0.71073)	MoKα (λ = 0.71073)	MoKα (λ = 0.71073)	MoKα (λ = 0.71073)
2Θ range for data collection/°	4.088 to 52.04	4.056 to 52.78	4.138 to 52.292	3.428 to 51.358	3.846 to 52.8
Index ranges	-18 ≤ h ≤ 19, -18 ≤ k ≤ 18, -21 ≤ l ≤ 21	-14 ≤ h ≤ 14, -14 ≤ k ≤ 14, -20 ≤ l ≤ 20	-14 ≤ h ≤ 14, -16 ≤ k ≤ 16, -17 ≤ l ≤ 17	-13 ≤ h ≤ 13, -14 ≤ k ≤ 14, -15 ≤ l ≤ 15	-14 ≤ h ≤ 14, -15 ≤ k ≤ 15, -16 ≤ l ≤ 16
Reflections collected	47206	53797	47161	38782	16915
Independent reflections	7655 [R_{int} = 0.0377, R_{sigma} = 0.0300]	8246 [R_{int} = 0.0295, R_{sigma} = 0.0195]	7991 [R_{int} = 0.0534, R_{sigma} = 0.0423]	6459 [R_{int} = 0.0355, R_{sigma} = 0.0246]	7129 [R_{int} = 0.0428, R_{sigma} = 0.0671]
Data/restraints/parameters	7655/39/531	8246/72/558	7991/0/481	6459/0/472	7129/0/482
Goodness-of-fit on F^2	1.007	0.997	1.037	1.041	1.016
Final R indexes [I>=2σ (I)]	R_1 = 0.0365, wR_2 = 0.0832	R_1 = 0.0279, wR_2 = 0.0701	R_1 = 0.0334, wR_2 = 0.0731	R_1 = 0.0269, wR_2 = 0.0655	R_1 = 0.0410, wR_2 = 0.0784
Final R indexes [all data]	R_1 = 0.0570, wR_2 = 0.0941	R_1 = 0.0334, wR_2 = 0.0734	R_1 = 0.0474, wR_2 = 0.0778	R_1 = 0.0315, wR_2 = 0.0676	R_1 = 0.0607, wR_2 = 0.0859
Largest diff. peak/hole / e Å^{-3}	1.00/-0.71	0.42/-0.33	0.45/-0.36	0.31/-0.26	0.39/-0.34

Table 4.S6. MBP/MBI coordinating bond distances.

MBPs	Zn-Carboxylate Bond (Å)	Zn-Heterocycle Bond (Å)
4.1	2.011	2.136
4.2	2.007	2.15
4.3	1.950 (1.930)	2.249 (2.339)
4.4	1.967	2.308
4.5	1.941	NA
A Series MBIs	Zn-C-O Bond(Å)	Zn-Heterocycle/N-O Bond (Å)
4.1a	1.928	2.227
4.2a	2.003 (1.951)	2.093 (2.128)
4.3a	1.92	2.321
4.4a	1.949	2.241
4.5a	1.897	2.43
B Series MBIs	Zn-C-O Bond(Å)	Zn-Heterocycle/N-O Bond (Å)
4.1b	2.088	2
4.2b	2.009	2.123
4.3b	2.131	1.953
4.4b	1.980 (1.979)	2.183 (2.170)
4.5b	2.12	1.989
C Series MBIs	Zn-Tetrazole Bond(Å)	Zn-Heterocycle Bond (Å)
4.1c	1.992	2.61
4.2c	2.032 (2.027)	2.277 (2.232)
4.3c	1.956	3.046
4.4c	1.985	2.488
4.5c	1.961	3.174
D Series MBIs	Zn-Oxadiazolone Bond(Å)	Zn-Heterocycle Bond (Å)
4.1d	1.953 (1.954)	2.654 (2.621)
4.2d	2.045	2.23
4.3d	1.94	2.988
4.4d	1.988	2.425
4.5d	1.951	3.187

[a] Structures with more than one complex in the asymmetric unit have all observed bond distances reported.

MBI Synthesis

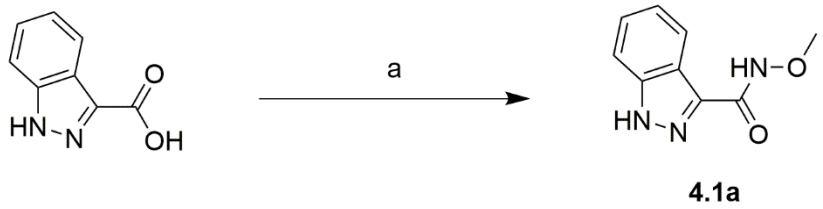

4.1a

Scheme 4.S1. Synthesis of compound **4.1a**. Reagents and conditions: (a) DMF, CDI, 25 ℃, 1 h, $CH_3ONH_2 \cdot HCl$, 25 ℃, overnight.

***O*-methyl indazole-3-hydroxamic acid (4.1a).** In a round bottom flask indazole-3-carboxylic acid (300 mg, 1 equiv, 1.9 mmol) was dissolved in 10 mL of DMF. CDI (300 mg, 1 equiv, 1.9 mmol) was added to the solution and stirred for 1 h under nitrogen at room temperature. *O*-methylhydroxylamine hydrochloride (309 mg, 2 equiv, 3.7 mmol) was added to the reaction and stirred overnight under nitrogen at room temperature. The reaction was dried down via rotary evaporation to a yellow-brown oil and loaded onto silica. The product was purified via column chromatography using a 0-100% Hexanes:EtOAc gradient. The fractions containing product were dried down via rotary evaporation to obtain a white solid. Yield: 197 mg (56%). ^{1}H NMR (300 MHz, DMSO-d_6): δ 13.63 (s, 1H), 11.76 (s, 1H), 8.13 (d, J = 8.2 Hz, 1H), 7.63 (d, J = 8.4 Hz, 1H), 7.47 – 7.37 (m, 1H), 7.31 – 7.22 (m, 1H), 3.73 (s, 3H). ^{13}C NMR (126 MHz, DMSO-d_6): δ 160.4, 140.7, 137.0, 126.5, 121.9, 121.7, 121.3, 110.7. ESI-MS(+) calculated for $[C_9H_{10}N_3O_2]^+$ 192.08, found *m/z* 192.05 $[M+H]^+$.

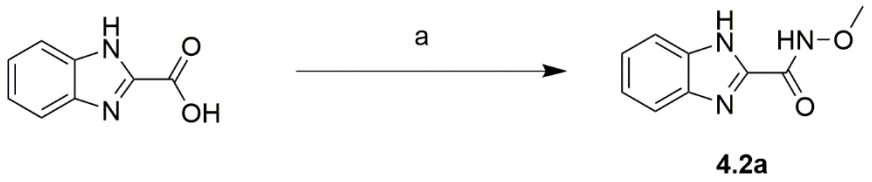

Scheme 4.S2. Synthesis of compound **4.2a**. Reagents and conditions: (a) DMF, CDI, 25 ℃ 1 h, $CH_3ONH_2 \cdot HCl$, 25 ℃, overnight.

***O*-methyl benzimidazole-2-hydroxamic acid (4.2a).** In a round bottom flask benzimidazole-2-carboxylic acid (300 mg, 1 equiv, 1.9 mmol) was dissolved in 10 mL of DMF. CDI (300 mg, 1 equiv, 1.9 mmol) was added to the solution and stirred for 1 h under nitrogen at room temperature. *O*-methylhydroxylamine hydrochloride (310 mg, 2 equiv, 3.7 mmol) was added to the reaction mixture and stirred overnight under nitrogen at room temperature. The reaction mixture was then dried down via rotary evaporation giving a brown oil that was purified via column chromatography using a 0-60% Hexanes:EtOAc gradient. The fractions containing product were dried down via rotary evaporation to obtain a tan solid. Yield: 160 mg (45%). ^{1}H NMR (300 MHz, DMSO-d_6): δ 13.38 (s, 1H), 12.39 (s, 1H), 7.63 (d, J = 45.7 Hz, 2H), 7.31 (s, 2H), 3.74 (s, 3H). ^{13}C NMR (126 MHz, DMSO-d6): δ 167.9, 161.9, 157.9, 140.8, 132.5, 132.2, 129.2, 128.2, 68.7. ESI-MS(+) calculated for $[C_9H_{10}N_3O_2]^+$ 192.08, found *m/z* 192.07 $[M+H]^+$.

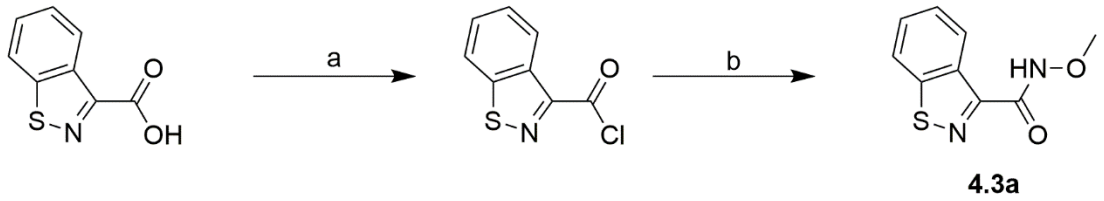

Scheme 4.S3. Synthesis of compound **4.3a**. Reagents and conditions: (a) CH_2Cl_2, $(COCl)_2$, DMF (cat.), 25 ℃, 3 h; (b) CH_2Cl_2, $CH_3ONH_2 \cdot HCl$, TEA, 25 ℃, overnight.

***O*-methyl 1,2-benzisothiazole-3-hydroxamic acid (4.3a).** To a solution of 1,2-benzisothiazole-3-carboxylic acid (300 mg, 1 equiv, 1.7 mmol) in 25 mL of CH_2Cl_2, oxalyl chloride (637 mg, 0.440 mL, 3 equiv, 5.0 mmol) was slowly added along with 5 drops of DMF. The solution was stirred for 3 h at room temperature under nitrogen. The reaction mixture was then evaporated to provide the crude acid chloride which was moved forward to the next step. The dried solids were dissolved in 25 mL of CH_2Cl_2 and *O*-methylhydroxylamine hydrochloride (168 mg, 1.2 equiv, 2.0 mmol) and triethylamine (678 mg, 0.933 mL, 4 equiv, 6.7 mmol) were added. The mixture was stirred overnight at room temperature under nitrogen. The reaction mixture was washed with a saturated brine solution and the organic layer was dried over $MgSO_4$. The organic layer was then dried down via rotary evaporation and loaded onto silica. The product was purified via column chromatography using a 0-40% Hexanes:EtOAc gradient. The fractions containing product were dried down via rotary evaporation. The product was recrystallized in isopropyl alcohol and obtained as a white solid. Yield: 83 mg (24%). ^{1}H NMR (300 MHz, DMSO-d_6): δ 12.20 (s, 1H), 8.67 (d, J = 8.1 Hz, 1H), 8.34 – 8.30 (m, 1H), 7.73 – 7.58 (m, 2H), 3.77 (s, 3H). ^{13}C NMR (126 MHz, DMSO-d6): δ 158.3, 155.1, 152.6, 133.8, 128.4, 126.1, 125.4, 120.8, 63.4. ESI-MS(+) calculated for $[C_9H_9N_2O_2S]^+$ 209.04, found *m/z* 208.98 $[M+H]^+$.

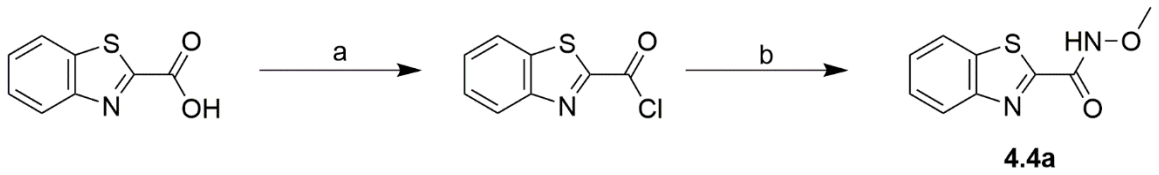

4.4a

Scheme 4.S4. Synthesis of compound **4.4a**. Reagents and conditions: (a) CH_2Cl_2, $(COCl)_2$, DMF (cat.), 25 ℃, 3 h; (b) CH_2Cl_2, $CH_3ONH_2 \cdot HCl$, TEA, 25 ℃, 2 h.

***O*-methyl benzothiazole-2-hydroxamic acid (4.4a).** To a solution of benzothiazole-2-carboxylic acid (500 mg, 1 equiv, 2.79 mmol) in 50 mL of CH_2Cl_2, oxalyl chloride (1.06 g, 0.733 mL, 3 equiv, 8.37 mmol) was slowly added along with 5 drops of DMF. The reaction as stirred for 3 h at room temperature under nitrogen. The reaction mixture was then dried down to a solid via rotary evaporation to provide the crude acid chloride which was moved forward onto the next step. To a solution of the crude acid chloride dissolved in 50 mL of CH_2Cl_2, *O*-methylhydroxylamine hydrochloride (280 mg, 1.2 equiv, 3.4 mmol) and TEA (678 mg, 0.93 mL, 2.4 equiv, 6.7 mmol) were added. The reaction was stirred at room temperature for 2 h. The reaction solution was then washed with a saturated brine solution, dried over $MgSO_4$, and dried down to a brown solid and loaded onto silica. The product was purified via column chromatography using a gradient of 0-60% Hexanes:EtOAc. The fractions containing product were dried down via rotary evaporation to obtain a tan solid. Yield: 326 mg (56%). ^{1}H NMR (300 MHz, DMSO-d_6): δ 12.61 (s, 1H), 8.28 – 8.22 (m, 1H), 8.17 – 8.10 (m, 1H), 7.69 – 7.55 (m, 2H), 3.76 (s, 3H). ^{13}C NMR (126 MHz, DMSO-d6): δ 162.8, 156.7, 152.7, 135.7, 127.3, 127.0, 124.0, 123.1, 63.5. ESI-MS(+) calculated for $[C_9H_9N_2O_2S]^+$ 209.04, found *m/z* 208.98 $[M+H]^+$.

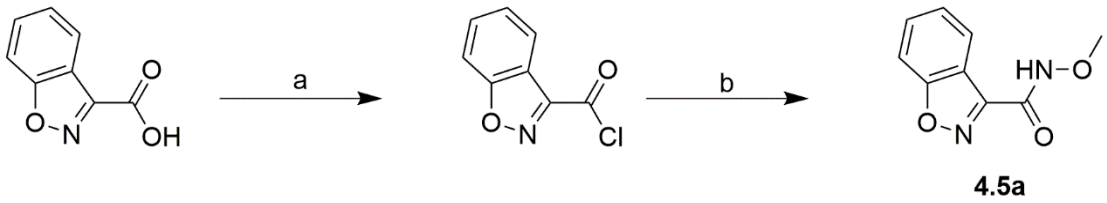

Scheme 4.S5. Synthesis of compound **4.5a**. Reagents and conditions: (a) CH_2Cl_2, $SOCl_2$, DMF (cat.), 25 ℃, 3-4 h; (b) CH_2Cl_2, $CH_3ONH_2 \cdot HCl$, TEA, 25 ℃, 2 h.

***O*-methyl 1,2-benzisothiazole-3-hydroxamic acid (4.5a).** In a round bottom flask 1,2-benzisoxazole-3-carboxylic acid (300 mg, 1 equiv, 1.84 mmol) was dissolved in CH_2Cl_2 (10 mL). Thionyl chloride (3.3 g, 2.0 mL, 15 equiv, 28 mmol) was added slowly along with a few drops of DMF. The reaction mixture was then stirred at room temperature under a nitrogen atmosphere for 3 to 4 hr. The reaction mixture was dried down to a tan residue and redissolved in CH_2Cl_2 (10 mL). *O*-methylhydroxylamine hydrochloride (307 mg, 2 equiv, 3.68 mmol) and TEA (744 mg, 1.0 mL, 4 equiv, 7.36 mmol) were added and the reaction was stirred at room temperature overnight under a nitrogen atmosphere. The reaction mixture was dried down via rotary evaporation and loaded onto silica. The product was isolated via column chromatography using a 0-20% Hexanes:EtOAc gradient. Fractions containing product were dried down via rotary evaporation to obtain a white solid. The product was recrystallized in Hexanes:EtOAc resulting in clear block crystals which were collected via filtration. Yield: 80 mg (23%). ^{1}H NMR (500 MHz, DMSO-d_6): δ 12.46 (s, 1H), 8.08 (dd, J = 8.0, 0.9 Hz, 1H), 7.88 (d, J = 8.5 Hz, 1H), 7.77 – 7.72 (m, 1H), 7.54 – 7.49 (m, 1H), 3.78 (s, 3H). ^{13}C NMR (126 MHz, DMSO-d6): δ 162.9, 155.8, 150.8, 131.2, 125.3, 123.0, 119.4, 110.1, 63.6. ESI-MS(+) calculated for $[C_9H_9N_2O_3]^+$ 193.06, found *m/z* 193.22 $[M+H]^+$.

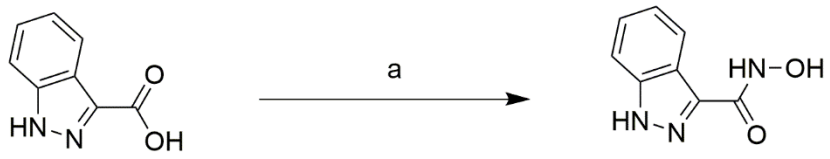

4.1b

Scheme 4.S6. Synthesis of compound **4.1b**. Reagents and conditions: (a) DMF, CDI, 25 ℃, 1 h, $NH_2OH \cdot HCl$, 25 ℃, overnight.

Indazole-3-hydroxamic acid (4.1b). To a solution of indazole-3-carboxylic acid (500 mg, 1 equiv, 3.1 mmol) dissolved in 10 mL of DMF, CDI (500 mg, 1 equiv, 3.1 mmol) was added and the solution was stirred for 1 h under nitrogen at room temperature. Hydroxylamine hydrochloride (429 mg, 2 equiv, 6.2 mmol) was added to the reaction and the mixture was stirred overnight under nitrogen at room temperature. The reaction mixture was dried via rotary evaporation and loaded onto silica. The product was purified via column chromatography using a 0-100% Hexanes:EtOAc gradient. The fractions containing product were dried down via rotary evaporation and the product was isolated by dissolving the solid in a minimal amount of MeOH and titrating with chloroform resulting in the product precipitating out as a white solid which was collected via vacuum filtration and dried. Yield: 110 mg (20%). ^{1}H NMR (300 MHz, DMSO-d_6): δ 13.52 (s, 1H), 11.14 (s, 1H), 9.00 (s, 1H), 8.12 (d, J = 8.1 Hz, 1H), 7.61 (d, J = 8.4 Hz, 1H), 7.42 (t, J = 7.9 Hz, 1H), 7.24 (t, J = 7.5 Hz, 1H). ^{13}C NMR (126 MHz, DMSO-d6): δ 160.4, 140.7, 137.0, 126.5, 121.9, 121.7, 121.3, 110.7. ESI-MS(+) calculated for $[C_8H_8N_3O_2]^+$ 178.06, found *m/z* 178.07 $[M+H]^+$.

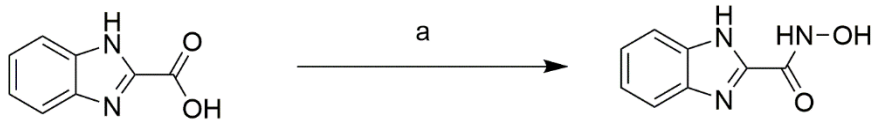

4.2b

Scheme 4.S7. Synthesis of compound **4.2b**. Reagents and conditions: (a) DMF, CDI, 25 ℃, 1 h, $NH_2OH \cdot HCl$, 25 ℃, overnight.

Benzimidazole-2-hydroxamic acid (4.2b). To a solution of benzimidazole-2-carboxylic acid (500 mg, 1 equiv, 3.1 mmol) dissolved in 10 mL of DMF, CDI (500 mg, 1 equiv, 3.08 mmol) was added to the solution and stirred for 1 h under nitrogen at room temperature. Hydroxylamine hydrochloride (429 mg, 2.0 equiv, 6.17 mmol) was added to the reaction mixture and stirred overnight under nitrogen at room temperature. The reaction solution was dried down to a brown residue and loaded onto silica. The product was purified via column chromatography using a 0-100% Hexanes:EtOAc gradient. The fractions containing product were dried down via rotary evaporation to obtain a solid that was dissolved in a minimal amount of MeOH and titrated with CH_2Cl_2 resulting in a white precipitate that was collected via filtration. Yield: 204 mg (37%). ^{1}H NMR (300 MHz, DMSO-d_6): δ 13.25 (s, 1H), 11.78 (s, 1H), 9.33 (s, 1H), 7.62 (d, J = 44.4 Hz, 2H), 7.29 (d, J = 4.9 Hz, 2H). ^{13}C NMR (126 MHz, DMSO-d6): δ 156.9, 145.0, 143.0, 134.5, 124.4, 122.9, 120.2, 112.8. ESI-MS(+) calculated for $[C_8H_{10}N_3O_2]^+$ 178.06, found m/z 178.11 $[M+H]^+$.

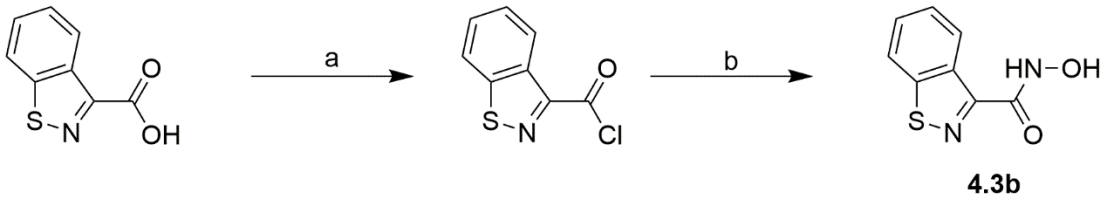

Scheme 4.S8. Synthesis of compound **4.3b**. Reagents and conditions: (a) CH_2Cl_2, $(COCl)_2$, DMF (cat.), 25 ℃, 3 h; (b) CH_2Cl_2, $NH_2OH{\cdot}HCl$, TEA, 25 ℃, overnight.

1,2-Benzisothiazole-3-hydroxamic acid (4.3b). To a solution of 1,2-benzisothiazole-3-carboxylic acid (300 mg, 1 equiv, 1.7 mmol) in 25 mL of CH_2Cl_2, oxalyl chloride (637 mg, 0.440 mL, 3 equiv, 5.0 mmol) was slowly added along with 5 drops of DMF. The solution was stirred for 3 h at room temperature under nitrogen. The reaction mixture was then dried down to a solid via rotary evaporation to provide the crude acid chloride which was moved forward onto the next step. The dried solid was dissolved in 25 mL of CH_2Cl_2 and hydroxylamine hydrochloride (140 mg, 1.2 equiv, 2.0 mmol) and TEA (678 mg, 0.933 mL, 4 equiv, 6.7 mmol) were added. The mixture was stirred overnight at room temperature under nitrogen. The reaction mixture was washed with a saturated brine solution and the organic layer was dried over $MgSO_4$. The organic layer was then dried down via rotary evaporation and loaded onto silica. The product was purified via column chromatography using a 0-60% Hexanes:EtOAc gradient. The fractions containing product were dried down via rotary evaporation to obtain a solid. The product was then recrystallized using isopropyl alcohol yielding an off-white solid. Yield: 117 mg (36%). ^{1}H NMR (300 MHz, DMSO-d_6): δ 11.57 (s, 1H), 9.34 (s, 1H), 8.63 (d, J = 8.0 Hz, 1H), 8.30 (d, J = 8.2 Hz, 1H), 7.71 – 7.52 (m, 2H). ^{13}C NMR (126 MHz, DMSO-d6): δ 158.8, 155.9, 152.5, 133.9, 128.3, 126.0, 125.4, 120.7. ESI-MS(+) calculated for $[C_8H_7N_2O_2S]^+$ 195.02, found *m/z* 195.02 $[M+H]^+$.

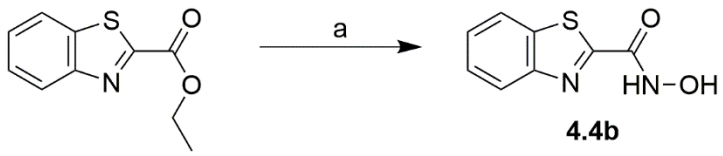

4.4b

Scheme 4.S9. Synthesis of compound **4.4b**. Reagents and conditions: (a) MeOH, KOH, NH_3OH ·HCl, 60 ℃, 24 h, KOH, NH_2OH·HCl 60 ℃, overnight.

Benzothiazole-2-hydroxamic acid (4.4b). To a solution of hydroxylamine hydrochloride (335 mg, 1 equiv, 4.8 mmol) in MeOH (50 mL), ethyl benzothiazole-2-carboxylate (1.00 g, 1 equiv, 4.8 mmol) and potassium hydroxide (271 mg, 1 equiv, 4.83 mmol) were added. The reaction mixture was stirred for 24 h at 60 ℃. By TLC the starting material was not consumed, so more KOH (948 mg, 3.5 equiv, 16.9 mmol) and hydroxylamine hydrochloride (336 mg, 1 equiv, 4.83 mmol) were added and the reaction was stirred while being heated to 60 ℃ overnight. The reaction was dried down via rotary evaporation and the residue was dissolved in water and acidified with HCl to pH ~7. The aqueous layer was extracted with EtOAc and then dried over $MgSO_4$. The material was loaded onto silica and purified via column chromatography using a CH_2Cl_2:MeOH gradient of 0-10%. The fractions containing product were dried down via rotary evaporation to obtain an off-white solid. Yield: 190 mg (20%). ^{1}H NMR (300 MHz, DMSO-d_6): δ 12.02 (s, 1H), 9.52 (s, 1H), 8.27 – 8.19 (m, 1H), 8.15 – 8.08 (m, 1H), 7.67 – 7.53 (m, 2H). ^{13}C NMR (126 MHz, DMSO-d6): δ 163.5, 156.9, 152.9, 135.6, 127.1, 126.8, 123.9, 123.0. ESI-MS(+) calculated for $[C_8H_7N_2O_2S]^+$ 195.02, found *m/z* 195.11 $[M+H]^+$.

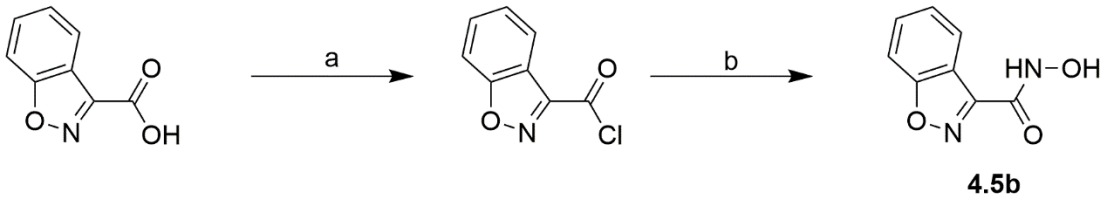

Scheme 4.S10. Synthesis of compound **4.5b**. Reagents and conditions: (a) CH_2Cl_2, $SOCl_2$, DMF (cat.), 25 ℃, 3-4 h; (b) CH_2Cl_2, $NH_2OH{\cdot}HCl$, TEA, 25 ℃, overnight.

1,2-Benzisoxazole-3-hydroxamic acid (4.5b). In a round bottom flask benzisoxazole-3-carboxylic acid (300 mg, 1 equiv, 1.84 mmol) was dissolved in CH_2Cl_2 (10 mL). Thionyl chloride (3.3 g, 2.0 mL, 15 equiv, 28 mmol) was added slowly along with a few drops of DMF, the reaction mixture was stirred at room temperature under a nitrogen atmosphere for 3 to 4 hr. The reaction mixture was dried down to a tan residue and redissolved in CH_2Cl_2 (10 mL). Hydroxylamine hydrochloride (256 mg, 2 equiv, 3.68 mmol) and TEA (744 mg, 1.0 mL, 4 equiv, 7.36 mmol) were added and the reaction was stirred at room temperature overnight under a nitrogen atmosphere. The reaction mixture was dried down via rotary evaporation and loaded onto silica. The product was isolated via column chromatography using a 0-30% Hexanes:EtOAc gradient. Fractions containing product were dried down via rotary evaporation to obtain an off-white solid. Yield: 100 mg (31%). ^{1}H NMR (500 MHz, DMSO-d_6): δ 11.84 (s, 1H), 9.61 (s, 1H), 8.04 (d, J = 8.0 Hz, 1H), 7.86 (d, J = 8.5 Hz, 1H), 7.74 (m, 1H), 7.50 (t, J = 7.5 Hz, 1H). ^{13}C NMR (126 MHz, DMSO-d6): δ 163.2, 156.5, 151.8, 131.6, 125.5, 123.4, 120.0, 110.5. ESI-MS(+) calculated for $[C_8H_7N_2O_3]^+$ 179.05, found *m/z* 179.10 $[M+H]^+$.

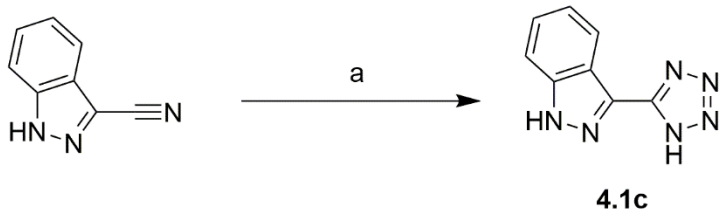

4.1c

Scheme 4.S11. Synthesis of compound **4.1c**. Reagents and conditions: (a) DMF, NaN_3, NH_4Cl, 110 ℃, overnight.

Indazole-3-tetrazole (4.1c). To a solution of indazole-3-carbonitrile (400 mg, 1 equiv, 2.8 mmol) dissolved in 10 mL of DMF, sodium azide (236 mg, 1.3 equiv, 3.6 mmol) and ammonium chloride (194 mg, 1.3 equiv, 3.6 mmol) were added. The solution was stirred at 110 ℃ overnight under nitrogen. The mixture was concentrated down via rotary evaporation almost to dryness. Water was added to the residue and the solution was then acidified, resulting in the product precipitating as an off-white solid that was collected via filtration. Yield: 400 mg (77%). ^{1}H NMR (300 MHz, DMSO-d_6): δ 13.97 (s, 1H), 8.29 (d, J = 8.3 Hz, 1H), 7.72 (d, J = 8.5 Hz, 1H), 7.57 – 7.48 (m, 1H), 7.40 – 7.31 (m, J = 7.9, 6.9, 0.9 Hz, 1H). ^{13}C NMR (126 MHz, DMSO-d6): δ 150.8, 141.5, 130.9, 127.7, 123.0, 121.2, 121.0, 111.4. ESI-MS(+) calculated for $[C_8H_7N_6]^+$ 187.07, found m/z 187.08$[M+H]^+$.

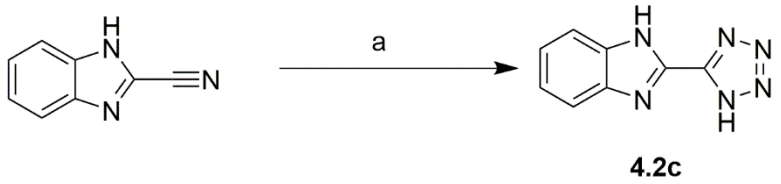

Scheme 4.S12. Synthesis of compound **4.2c**. Reagents and conditions: (a) DMF, NaN_3, NH_4Cl, 110 °C, overnight.

Benzimidazole-2-tetrazole (4.2c). To a solution of benzimidazole-2-carbonitrile (200 mg, 1 equiv, 1.4 mmol) dissolved in 10 mL of DMF, sodium azide (118 mg, 1.3 equiv, 1.8 mmol) and ammonium chloride (97 mg, 1.3 equiv, 1.8 mmol) were added. The solution was stirred at 110 °C overnight under nitrogen. The mixture was concentrated down via rotary evaporation almost to dryness, then water was added (20 mL) and a few drops of 1 M NaOH to dissolve residual solids. The solution was then acidified, resulting in the product precipitating as an off-white solid that was collected via filtration. Yield: 230 mg (88%). ^{1}H NMR (300 MHz, DMSO-d_6): δ 7.72 (dd, J = 6.1, 3.2 Hz, 2H), 7.43 (dd, J = 6.1, 3.2 Hz, 2H). ^{13}C NMR (126 MHz, DMSO-d6): δ 149.2, 140.4, 135.6, 124.6, 115.1. ESI-MS(+) calculated for $[C_8H_7N_6]^+$ 187.07, found m/z 187.11$[M+H]^+$.

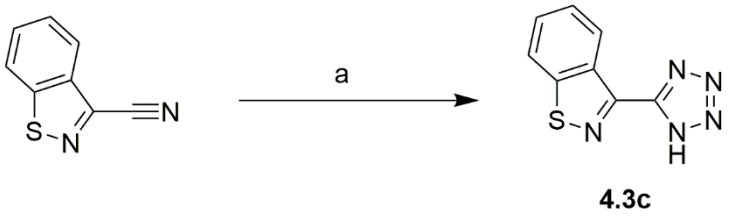

4.3c

Scheme 4.S13. Synthesis of compound **4.3c**. Reagents and conditions: (a) DMF, NaN_3, NH_4Cl, 110 ℃, overnight.

1,2-Benzisothiazole-3-tetrazole (4.3c). To a 50 mL round bottom flask 1,2-benzisothiazole-3-carbonitrile (200 mg, 1 equiv, 1.25 mmol), sodium azide (106 mg, 1.3 equiv, 1.62 mmol), ammonia hydrochloride (86.8 mg, 1.3 equiv, 1.62 mmol), and DMF (10 mL) were added. The solution was heated to 110 ºC overnight, under nitrogen while being stirred. The mixture was then concentrated down via rotary evaporation to almost dryness, then water was added (20 mL) and a few drops of 1 M NaOH to dissolve any solids. The solution was then acidified, resulting in the product precipitating as an off-white powder that was collected by filtration. Yield: 250 mg (99%). ^{1}H NMR (300 MHz, DMSO-d_6): δ 8.97 (d, J = 7.8 Hz, 1H), 8.40 (d, J = 7.7 Hz, 1H), 7.83 – 7.66 (m, 2H). ^{13}C NMR (126 MHz, DMSO-d6): δ 153.1, 151.3, 148.6, 132.9, 128.9, 126.7, 125.1, 121.1. ESI-MS(+) calculated for $[C_8H_6N_5S]^+$ 204.03, found m/z 204.17$[M+H]^+$.

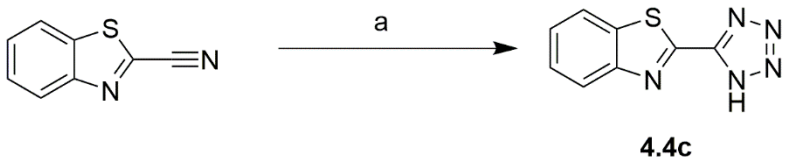

4.4c

Scheme 4.S14. Synthesis of compound **4.4c**. Reagents and conditions: (a) DMF, NaN_3, NH_4Cl, 110 ℃, overnight.

Benzothiazole-2-tetrazole (4.4c). To a solution of benzothiazole-2-carbonitrile (200 mg, 1 equiv, 1.3 mmol) dissolved in 10 mL of DMF, sodium azide (106 mg, 1.3 equiv, 1.6 mmol) and ammonium chloride (87 mg, 1.3 equiv, 1.6 mmol) were added. The solution was stirred at 110 ℃ overnight under nitrogen. The mixture was concentrated down via rotary evaporation almost to dryness, then water was added (20 mL) and a few drops of 1 M NaOH to dissolve residual solids. The solution was then acidified, resulting in the product precipitating as an off-white solid that was collected via filtration. Yield: 246 mg (97%). ^{1}H NMR (300 MHz, DMSO-d_6): δ 8.35 – 8.27 (m, 1H), 8.25 – 8.18 (m, 1H), 7.72 – 7.58 (m, 2H). ^{13}C NMR (126 MHz, DMSO-d6): δ 152.8, 152.0, 146.7, 134.8, 127.4, 127.1, 123.7, 123.1. ESI-MS(+) calculated for $[C_8H_6N_5S]^+$ 204.03, found *m/z* 204.02 $[M+H]^+$.

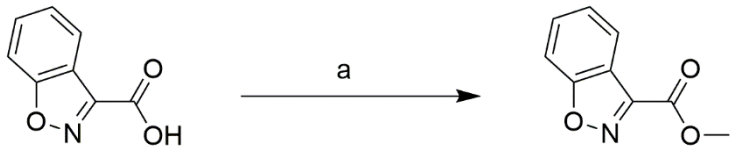

Scheme 4.S15. Synthesis of methyl 1,2-benzisoxazole-3-carboxylate. Reagents and conditions: (a) MeOH, H_2SO_4, reflux, overnight.

Methyl 1,2-benzisoxazole-3-carboxylate. In a round bottom flask 1,2-benzisoxazole-3-carboxylic acid (500 mg, 1 equiv, 3.07 mmol) was dissolved in MeOH (100 mL) and sulfuric acid (15.0 mg, 0.008 mL, 0.05 equiv, 0.15 mmol) was added. The reaction mixture was heated to reflux while being stirred overnight under nitrogen. The reaction mixture was dried down to a white solid via rotary evaporation and then dissolved in EtOAc and water. The organic layer was separated, and the aqueous layer was washed with EtOAc. All the organic layers were combined and washed with water, then brine, and then dried with anhydrous $MgSO_4$ and filtered. The filtrate was dried down via rotary evaporation to obtain the product as an off-white solid. Yield: 480 mg (88%). ^{1}H NMR (500 MHz, DMSO-d_6): δ 8.12 – 8.08 (m, 1H), 7.94 – 7.90 (m, H), 7.79 – 7.74 (m, 1H), 7.58 – 7.53 (m, 1H), 4.01 (s, 3H). ^{13}C NMR (126 MHz, DMSO-d6): δ 164.1, 160.3, 150.7, 131.7, 126.1, 123.4, 119.5, 110.8, 53.6. ESI-MS(+) calculated for $[C_9H_8NO_3]^+$ 178.05, found *m/z* 178.09 $[M+H]^+$.

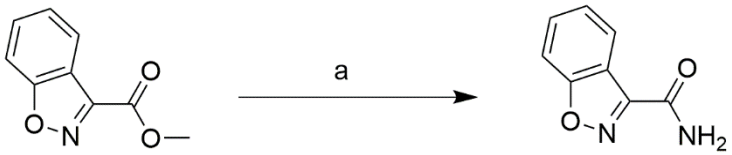

Scheme 4.S16. Synthesis of 1,2-benzisoxazole-3-carboxamide. Reagents and conditions: (a) MeOH, NH_3, 25℃, overnight.

1,2-Benzisoxazole-3-carboxamide. In a round bottom flask methyl 1,2-benzisoxazole-3-carboxylate (100 mg, 1 equiv, 0.56 mmol) was dissolved in a 7 M ammonia (12 g, 15 mL, 200 equiv, 0.1 mol) solution in MeOH. The mixture was stirred overnight in a capped vessel at room temperature. The reaction mixture was then dried down via rotary evaporation to obtain the product as a white solid in quantitative yield. Yield: 92 mg (100%). ^{1}H NMR (500 MHz, DMSO-d_6): δ 8.43 (s, 1H), 8.12 – 8.08 (m, 1H), 8.07 (s, 1H), 7.87 – 7.83 (m, 1H), 7.74 – 7.70 (m, 1H), 7.51 – 7.47 (m, 1H). ^{13}C NMR (126 MHz, DMSO-d6): δ 163.6, 160.9, 152.7, 131.3, 125.5, 123.8, 120.0, 110.4. ESI-MS(+) calculated for $[C_8H_7N_2O_2]^+$ 163.05, found *m/z* 163.11 $[M+H]^+$.

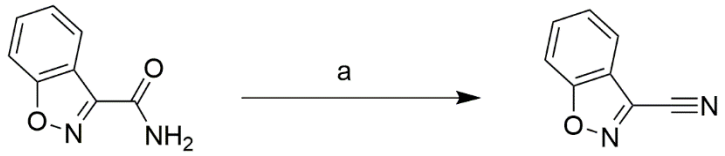

Scheme 4.S17. Synthesis of 1,2-benzisoxazole-3-carbonitrile. Reagents and conditions: (a) $POCl_3$, ACN, 65 ℃, overnight.

1,2-Benzisoxazole-3-carbonitrile. In a round bottom flask 1,2-benzisoxazole-3-carboxamide (100 mg, 1 equiv, 0.56 mmol) was dissolved in acetonitrile (ACN) (5 mL) and phosphoryl trichloride (3.3 g, 2.0 mL, 35 equiv, 21 mmol) was added slowly. The reaction was then stirred under an argon atmosphere at while being heated to 65 ºC overnight. The reaction mixture was then dried down via rotary evaporation to a residue. The residue was then dissolved in EtOAc and extracted with saturated sodium bicarbonate. The organic layer was collected, and the aqueous layer was extracted again with EtOAc. All organic layers were combined and washed with water, then brine, and then dried with $MgSO_4$. The organic layers were dried down to yield the product as a white-yellow solid. Yield: 72 mg (81%). ^{1}H NMR (500 MHz, DMSO-d_6): δ 8.11 – 8.08 (m, 1H), 8.06 – 8.04 (m, 1H), 7.89 – 7.85 (m, 1H), 7.65 – 7.61 (m, 1H). ^{13}C NMR (126 MHz, DMSO-d6): δ 163.7, 136.3, 133.0, 126.9, 121.9, 120.3, 111.2, 110.3. Compound was not detected by MS but moved forward anyway.

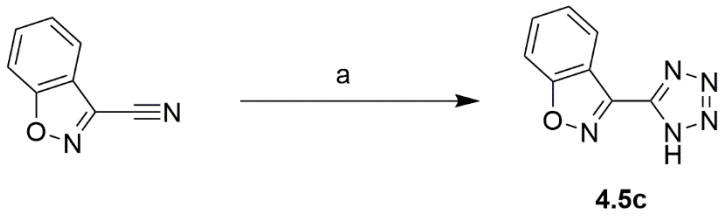

4.5c

Scheme 4.S18. Synthesis of compound **4.5c**. Reagents and conditions: (a) DMF, NaN_3, NH_4Cl, 110 ℃, overnight.

1,2-Benzisoxazole-3-tetrazole (4.5c). To a 50 mL round bottom flask 1,2-benzisoxazole-3-carbonitrile (65 mg, 1 equiv, 0.45 mmol), sodium azide (38 mg, 1.3 equiv, 0.59 mmol), ammonia hydrochloride (31 mg, 1.3 equiv, 0.59 mmol), and DMF (6 mL) were added. The solution was heated to 110 ºC overnight, under nitrogen while being stirred. The mixture was then concentrated down via rotary evaporation to almost dryness, then water was added (20 mL) and a few drops of 1 M NaOH to dissolve any solids. The solution was then acidified, resulting in the product precipitating as an off-white powder that was collected by filtration. Yield: 26 mg (31%). ^{1}H NMR (500 MHz, DMSO-d_6): δ 8.36 (d, J = 8.0 Hz, 1H), 7.94 (d, J = 8.5 Hz, 1H), 7.81 (t, J = 7.7 Hz, 1H), 7.59 (t, J = 7.5 Hz, 1H). ^{13}C NMR (126 MHz, DMSO-d6): δ 163.7, 149.2, 147.0, 132.1, 125.9, 123.5, 119.4, 110.7. ESI-MS(+) calculated for $[C_8H_4N_5O]^+$ 186.04, found *m/z* 186.15 $[M-H]^-$.

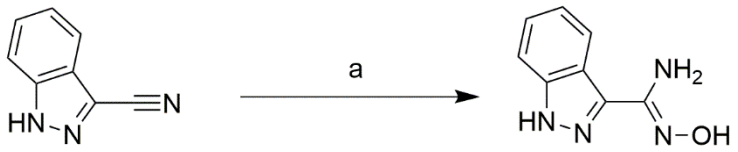

Scheme 4.S19. Synthesis of *N'*-hydroxy indazole-3-amidine. Reagents and conditions: (a) EtOH, K_2CO_3, $CH_3ONH_3 \cdot HCl$, 80 °C, overnight.

***N'*-hydroxy indazole-3-amidine.** To a solution of indazole-3-carbonitrile (300 mg, 1 equiv, 2.1 mmol) dissolved in 15 mL of EtOH, potassium carbonate (319 mg, 1.1 equiv, 2.3 mmol) and hydroxylamine hydrochloride (291 mg, 2 equiv, 4.2 mmol) were added. The mixture was stirred and heated to reflux overnight under nitrogen. The resulting mixture was filtered and washed with MeOH. The filtrate was collected and dried down to a solid via rotary evaporation. The solid was dissolved in basic water and extracted with CH_2Cl_2 twice. The aqueous layer was acidified to weakly acidic (pH ~6) and extracted with EtOAc twice. The organic layers were combined, dried using $MgSO_4$, and dried down via rotary evaporation to yield the product as a tan solid. Yield: 320 mg (87%). ^{1}H NMR (300 MHz, DMSO-d_6): δ 13.20 (s, 1H), 9.77 (s, 1H), 8.10 (d, J = 8.2 Hz, 1H), 7.54 (d, J = 8.4 Hz, 1H), 7.41 – 7.27 (m, 1H), 7.21 – 7.05 (m, 1H), 5.67 (s, 2H). ^{13}C NMR (126 MHz, DMSO-d6): δ 148.0, 141.2, 137.6, 126.4, 122.5, 121.0, 119.6, 110.3. ESI-MS(+) calculated for $[C_8H_9N_4O]^+$ 177.08, found *m/z* 177.15 $[M+H]^+$.

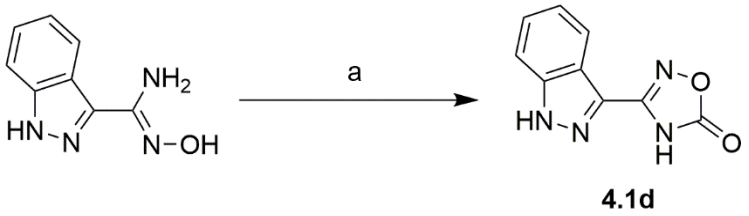

4.1d

Scheme 4.S20. Synthesis of compound **4.1d**. Reagents and conditions: (a) Pyridine, ethyl chloroformate, 115 ℃, 8 h.

Indazole-3-oxadiazolone (4.1d). To a solution of *N'*-hydroxy indazole-3-amidine (150 mg, 1 equiv, 0.9 mmol) dissolved in 5 mL of anhydrous pyridine, ethyl chloroformate (92 mg, 0.082 mL, 1 equiv, 0.9 mmol) was added. The reaction mixture was stirred and heated to reflux for 8 h. The reaction mixture was dried down to a brown oil via rotary evaporation. The product was recrystallized from a water:isopropanol mixture, yielding the product as an off-white solid that was collected via filtration. Yield: 87 mg (51%). ^{1}H NMR (300 MHz, DMSO-d_6): δ 14.06 (s, 1H), 13.17 (s, 1H), 8.01 (d, J = 8.2 Hz, 1H), 7.72 (d, J = 8.5 Hz, 1H), 7.56 – 7.48 (m, 1H), 7.39 – 7.30 (m, 1H). ^{13}C NMR (126 MHz, DMSO-d6): δ 159.5, 154.1, 141.1, 129.4, 127.5, 122.9, 120.6, 119.8, 111.2. ESI-MS(-) calculated for $[C_9H_5N_4O_2]^-$ 201.04, found m/z 201.12 $[M-H]^-$.

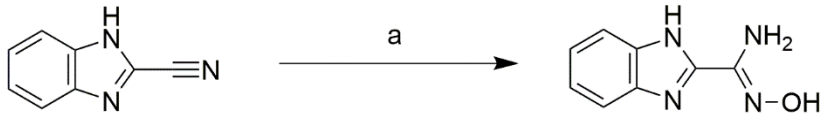

Scheme 4.S21. Synthesis of *N'*-hydroxy benzimidazole-2-amidine. Reagents and conditions: (a) EtOH, K_2CO_3, $CH_3ONH_3 \cdot HCl$, 80 ℃, overnight.

***N'*-hydroxy benzimidazole-2-amidine.** In a round bottom flask benzimidazole-2-carbonitrile (500 mg, 1 equiv, 3.49 mmol) was dissolved in 50 mL of EtOH. Hydroxylamine hydrochloride (485 mg, 2 equiv, 6.99 mmol) and potassium carbonate (483 mg, 1 equiv, 3.49 mmol) were added to the solution and stirred while the mixture was heated to reflux (90 ºC) overnight. The reaction mixture was dried down via rotary evaporation and then the resulting solid was dissolved in water and EtOAc. The aqueous layer was adjusted to neutral pH and the organic layer was dried with $MgSO_4$. The organic layer was dried down via rotary evaporation and loaded onto silica. The product was purified via column chromatography using a 0-70% Hexanes:EtOAc gradient. The fractions containing product were dried down via rotary evaporation and the product was then recrystallized from EtOAc, yielding a white solid that was collected via filtration. Yield: 350 mg (57%). ^{1}H NMR (300 MHz, DMSO-d_6): δ 12.54 (s, 1H), 10.05 (s, 1H), 7.64 (d, J = 7.5 Hz, 1H), 7.46 (d, J = 7.3 Hz, 1H), 7.27 – 7.14 (m, 2H), 5.89 (s, 2H). ^{13}C NMR (126 MHz, DMSO-d6): δ 146.2, 145.0, 134.9, 122.8, 123.4, 122.1, 119.3, 112.2. ESI-MS(+) calculated for $[C_8H_9N_4O]^+$ 177.08, found m/z 177.18 $[M+H]^+$.

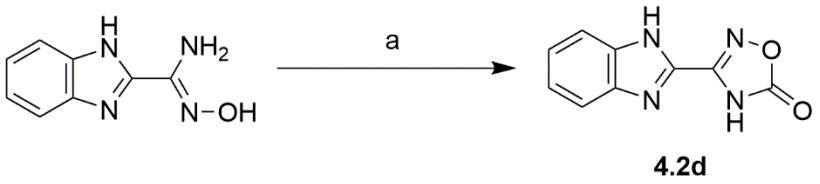

Scheme 4.S22. Synthesis of compound **4.2d**. Reagents and conditions: (a) Pyridine, ethyl chloroformate, 115 ℃, 8 h.

Benzimidazole-2-oxadiazolone. To a solution of *N'*-hydroxy benzimidazole-2-amidine (200 mg, 1 equiv, 1.14 mmol) dissolved in anhydrous pyridine (25 mL), ethyl chloroformate (148 mg, 0.131 mL, 1.2 equiv, 1.36 mmol) was added. The reaction was then heated to reflux and stirred overnight. The reaction mixture was dried down via rotary evaporation to a residue. The residue was dissolved in 1 M KOH and then the solution was acidified using HCl, resulting in a brown precipitate forming that was collected via filtration. Yield: 70 mg (31%). ^{1}H NMR (500 MHz, DMSO-d_6): δ 13.60 (s, 1H), 7.68 (s, 2H), 7.37 – 7.33 (m, 2H). ESI-MS(+) calculated for $[C_9H_7N_4O_2]^+$ 203.06, found m/z 203.19 $[M+H]^+$.

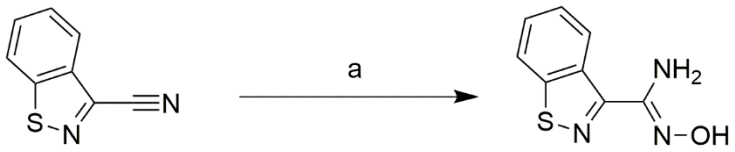

Scheme 4.S23. Synthesis of *N'*-hydroxy 1,2-benzisothiazole-3-amidine. Reagents and conditions: (a) EtOH, K_2CO_3, $CH_3ONH_3 \cdot HCl$, 80 ℃, overnight.

***N'*-hydroxy 1,2-benzisothiazole-3-amidine.** In a round bottom flask 1,2-benzisothiazole-3-carbonitrile (500 mg, 1 equiv, 3.12 mmol) was dissolved in 50 mL of EtOH. Hydroxylamine hydrochloride (434 mg, 2 equiv, 6.24 mmol) and potassium carbonate (431 mg, 1 equiv, 3.12 mmol) were added to the solution and stirred while the mixture was heated to reflux (90 ºC) overnight. The reaction mixture was dried down via rotary evaporation and then the resulting solid was dissolved in water and EtOAc. The aqueous layer was adjusted to neutral pH and the organic layer was dried with $MgSO_4$. The organic layer was dried down and the product was obtained as a white solid. Yield: 450 mg (75%). ^{1}H NMR (500 MHz, DMSO-d_6): δ 10.27 (s, 1H), 8.80 (d, J = 8.2 Hz, 1H), 8.22 (d, J = 8.2 Hz, 1H), 7.64 – 7.58 (m, 1H), 5.96 (s, 2H). ^{13}C NMR (126 MHz, DMSO-d6): δ 155.9, 152.9, 149.4, 132.7, 128.4, 127.2, 126.0, 120.9. ESI-MS(+) calculated for $[C_8H_8N_3OS]^+$ 194.04, found m/z 194.13 $[M+H]^+$.

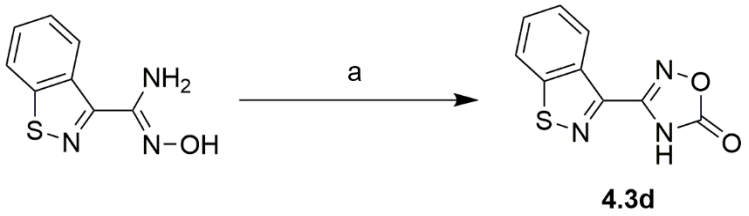

Scheme 4.S24. Synthesis of compound **4.3d**. Reagents and conditions: (a) Pyridine, ethyl chloroformate, 115 ℃, overnight.

1,2-benzisothiazole-3-oxadiazolone (4.3d). To a solution of *N'*-hydroxy 1,2-benzisothiazole-3-amidine (230 mg, 1 equiv, 1.19 mmol) dissolved in anhydrous pyridine (25 mL), ethyl chloroformate (155 mg, 0.137 mL, 1.2 equiv, 1.43 mmol) was added. The reaction was then heated to reflux and stirred overnight. The reaction mixture was dried down via rotary evaporation to a residue. The residue was dissolved in 1 M KOH and then the solution was acidified using HCl, resulting in a brown precipitate forming that was collected via filtration. Yield: 212 mg (81%). ^{1}H NMR (500 MHz, DMSO-d_6): δ 13.50 (s, 1H), 8.59 (d, J = 8.2 Hz, 1H), 8.39 (d, J = 8.3 Hz, 1H), 7.77 – 7.71 (m, 1H), 7.69 – 7.64 (m, 1H). ^{13}C NMR (126 MHz, DMSO-d6): δ 159.1, 154.5, 153.0, 147.2, 132.0, 128.9, 126.8, 124.6, 121.3. ESI-MS(+) calculated for $[C_9H_6N_3O_2S]^+$ 220.02, found m/z 220.11 $[M+H]^+$.

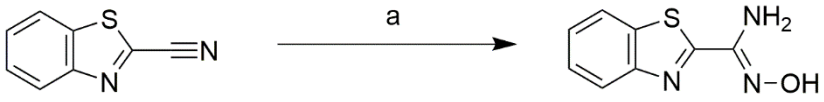

Scheme 4.S25. Synthesis of *N'*-hydroxy benzothiazole-2-amidine. Reagents and conditions: (a) EtOH, K_2CO_3, $CH_3ONH_3 \cdot HCl$, 80 °C, overnight.

***N'*-hydroxy benzothiazole-2-amidine.** In a round bottom flask benzothiazole-2-carbonitrile (500 mg, 1 equiv, 3.12 mmol) was dissolved in 50 mL of EtOH. Hydroxylamine hydrochloride (434 mg, 2 equiv, 6.24 mmol) and potassium carbonate (431 mg, 1 equiv, 3.12 mmol) were added to the solution and stirred while the mixture was heated to reflux (80 ºC) overnight. The reaction mixture was dried down via rotary evaporation and then the resulting solid was dissolved in water and EtOAc. The aqueous layer was adjusted to neutral pH and the organic layer was dried with $MgSO_4$. The organic layer was dried down via rotary evaporation and the product was obtained as a white solid. Yield: 580 mg (96%). ^{1}H NMR (400 MHz, DMSO-d_6): δ 10.48 (s, 1H), 8.08 (d, J = 7.8 Hz, 1H), 8.00 (d, J = 8.1 Hz, 1H), 7.49 (dt, J = 15.0, 6.9 Hz, 2H), 6.11 (s, 2H). ^{13}C NMR (126 MHz, DMSO-d6): δ 162.3, 152.3, 147.3, 134.2, 126.4, 126.1, 122.9, 122.3. ESI-MS(+) calculated for $[C_8H_8N_3OS]^+$ 194.04, found m/z 194.32 $[M+H]^+$.

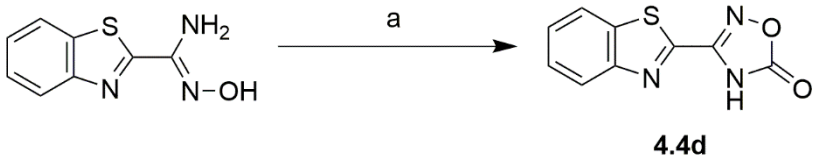

4.4d

Scheme 4.S26. Synthesis of compound **4.4d**. Reagents and conditions: (a) Pyridine, ethyl chloroformate, 115 ℃, 8 h.

Benzothiazole-2-oxadiazolone (4.4d). To a solution of *N'*-hydroxy benzothiazole-2-amidine (200 mg, 1 equiv, 1.04 mmol) dissolved in anhydrous pyridine (25 mL), ethyl chloroformate (225 mg, 0.199 mL, 2.0 equiv, 2.07 mmol) was added. The reaction was then heated to reflux and stirred overnight. The reaction mixture was dried down via rotary evaporation to a residue. The residue was dissolved in 1 M KOH and then the solution was acidified using HCl, resulting in a brown precipitate forming that was collected via filtration. Yield: 215 mg (95%). ^{1}H NMR (500 MHz, DMSO-d_6): δ 13.88 (s, 1H), 8.32 – 8.28 (m, 1H), 8.21 – 8.18 (m, 1H), 7.70 – 7.62 (m, 2H). ^{13}C NMR (126 MHz, DMSO-d6): δ 159.4, 154.5, 152.1, 151.6, 134.4, 127.8, 127.6, 123.9, 123.2. ESI-MS(+) calculated for $[C_9H_6N_3O_2S]^+$ 220.02, found m/z 220.19 $[M+H]^+$.

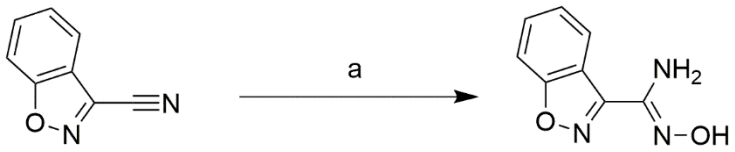

Scheme 4.S27. Synthesis of *N'*-hydroxy 1,2-benzisoxazole-3-amidine. Reagents and conditions: (a) EtOH, K_2CO_3, $CH_3ONH_3 \cdot HCl$, 80 °C, overnight.

***N'*-hydroxy 1,2-benzisoxazole-3-amidine.** In a round bottom flask 1,2-benzisothiazole-3-carbonitrile (200 mg, 1 equiv, 1.25 mmol) was dissolved in 50 mL of EtOH. Hydroxylamine hydrochloride (174 mg, 2 equiv, 2.50 mmol) and potassium carbonate (173 mg, 1 equiv, 1.25 mmol) were added to the solution and stirred while the mixture was heated to reflux (90 ºC) overnight. The reaction mixture was dried down via rotary evaporation and then the resulting solid was dissolved in water and EtOAc. The organic layer was collected and the aqueous layer was washed with EtOAc then all the organic layers were collected and dried with $MgSO_4$. The combined organic layers were dried down via rotary evaporation and the product was loaded onto silica and purified via column chromatography utilizing a 0-40% Hexanes:EtOAc gradient. Fractions containing the product were dried down via rotary evaporation and the product was obtained as a white solid. Yield: 151 mg (63%). ^{1}H NMR (500 MHz, DMSO-d_6): δ 10.55 (s, 1H), 8.12 – 8.08 (m, 1H), 7.79 (d, J = 8.5 Hz, 1H), 7.67 (t, J = 7.8 Hz, 1H), 7.43 (t, J = 7.5 Hz, 1H), 6.08 (s, 2H).z. ^{13}C NMR (126 MHz, DMSO-d6): δ 163.2, 151.8, 145.3, 131.0, 125.0, 124.8, 119.1, 110.3. ESI-MS(+) calculated for $[C_8H_8N_3O_2]^+$ 178.06, found m/z 178.20 $[M+H]^+$.

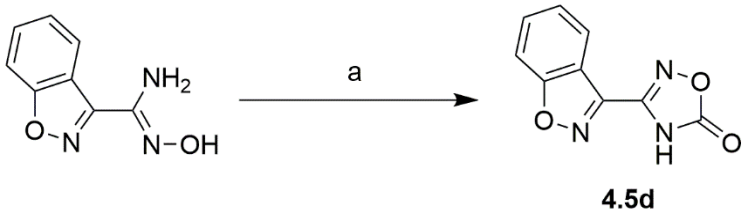

4.5d

Scheme 4.S28. Synthesis of compound **4.5d**. Reagents and conditions: (a) Pyridine, ethyl chloroformate, 115 ℃, overnight.

1,2-benzisoxazole-3-oxadiazolone (4.5d). To a solution of *N*'-hydroxy 1,2-benzisoxazole-3-amidine (125 mg, 1 equiv, 0.65 mmol) dissolved in anhydrous pyridine (25 mL), ethyl chloroformate (140 mg, 0.124 mL, 2.0 equiv, 1.29 mmol) was added. The reaction was then heated to reflux and stirred overnight. The reaction mixture was dried down via rotary evaporation to a residue. The residue was dissolved in 1 M KOH and then the solution was extracted with EtOAc. The aqueous layer was then acidified using HCl, resulting in a white precipitate forming that was collected via filtration. Yield: 40 mg (28%). ^{1}H NMR (500 MHz, DMSO-d_6): δ 8.12 – 8.07 (m, 1H), 8.00 – 7.94 (m, 1H), 7.85 – 7.79 (m, 1H), 7.61 – 7.56 (m, 1H). ^{13}C NMR (126 MHz, DMSO-d6): δ 163.4, 159.34, 151.2, 145.4, 132.0, 126.0, 122.8, 117.7, 110.5. ESI-MS(-) calculated for $[C_9H_4N_3O_3]^-$ 202.03, found m/z 202.22 $[M-H]^-$.

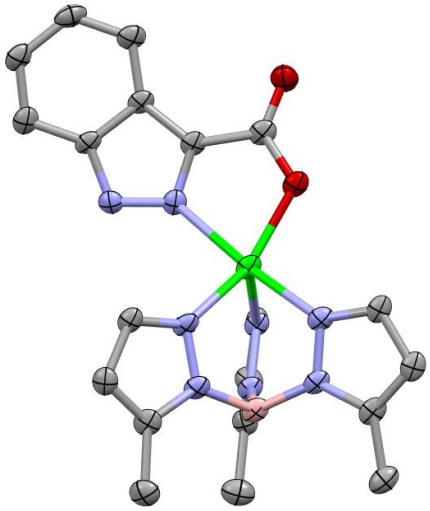

Figure 4.S1. Structure of [(Tp^{Ph,Me})Zn(**4.1**)] rendered as an ORTEP with atoms at 50% thermal probability ellipsoids. Hydrogen atoms and Tp^{Ph,Me} phenyl groups have been removed for clarity. The asymmetric unit consists of the complex, a molecule of MeOH (not shown), and half a molecule of benzene (not shown). Color scheme: carbon = gray, oxygen = red, nitrogen = blue, boron = pink, and zinc = green.

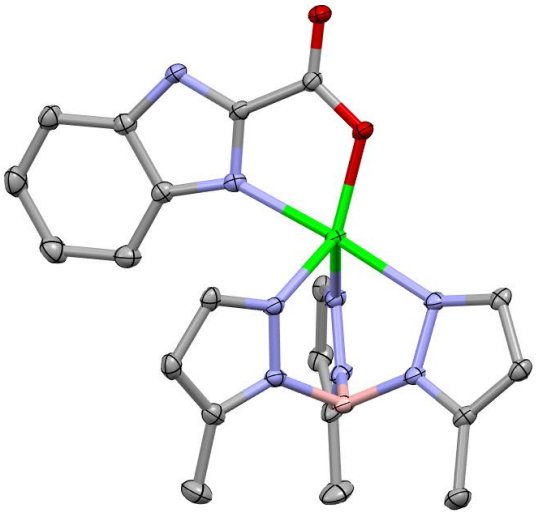

Figure 4.S2. Structure of [(Tp^{Ph,Me})Zn(**4.2**)] rendered as an ORTEP with atoms at 50% thermal probability ellipsoids. Hydrogen atoms and Tp^{Ph,Me} phenyl groups have been removed for clarity. The asymmetric unit consists of the complex and two and a half molecules of benzene (not shown). Color scheme: carbon = gray, oxygen = red, nitrogen = blue, boron = pink, and zinc = green.

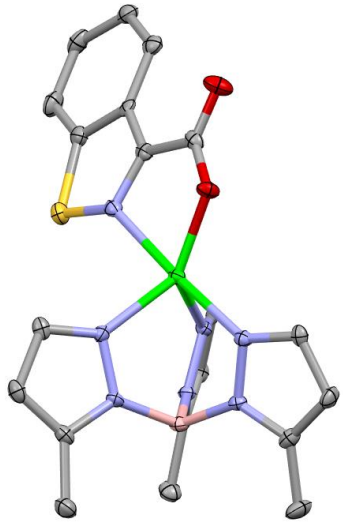

Figure 4.S3. Structure of [($Tp^{Ph,Me}$)Zn(**4.3**)] rendered as an ORTEP with atoms at 50% thermal probability ellipsoids. Hydrogen atoms and $Tp^{Ph,Me}$ phenyl groups have been removed for clarity. The asymmetric unit consists of two complexes (one not shown). Color scheme: carbon = gray, sulfur = yellow, oxygen = red, nitrogen = blue, boron = pink, and zinc = green.

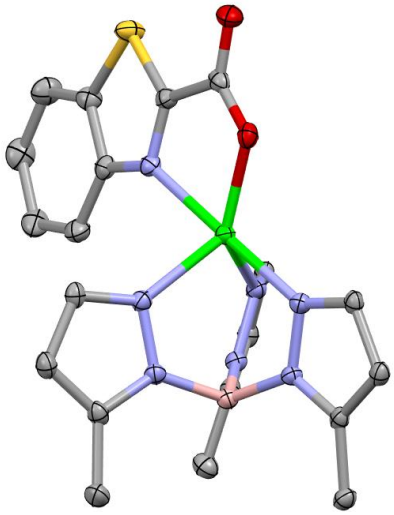

Figure 4.S4. Structure of [($Tp^{Ph,Me}$)Zn(**4.4**)] rendered as an ORTEP with atoms at 50% thermal probability ellipsoids. Hydrogen atoms and $Tp^{Ph,Me}$ phenyl groups have been removed for clarity. The asymmetric unit consists only of the complex. Color scheme: carbon = gray, sulfur = yellow, oxygen = red, nitrogen = blue, boron = pink, and zinc = green.

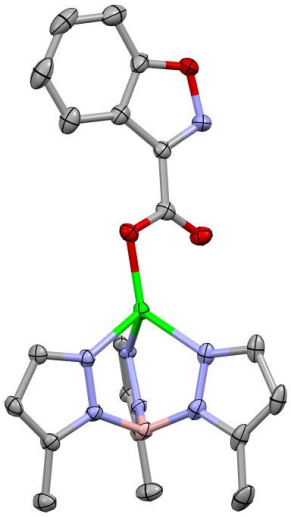

Figure 4.S5. Structure of [(Tp^{Ph,Me})Zn(**4.5**)] rendered as an ORTEP with atoms at 50% thermal probability ellipsoids. Hydrogen atoms and Tp^{Ph,Me} phenyl groups have been removed for clarity. The asymmetric unit consists of the complex and mixed occupancy solvent (benzene/pentane) molecule (not shown). Color scheme: carbon = gray, oxygen = red, nitrogen = blue, boron = pink, and zinc = green.

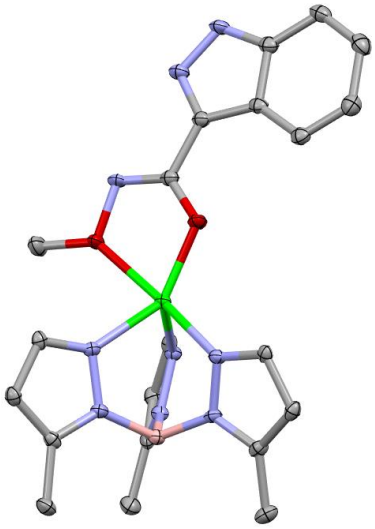

Figure 4.S6. Structure of [(Tp^{Ph,Me})Zn(**4.1a**)] rendered as an ORTEP with atoms at 50% thermal probability ellipsoids. Hydrogen atoms and Tp^{Ph,Me} phenyl groups have been removed for clarity. The asymmetric unit consists of the complex and a molecule of MeOH (not shown). Color scheme: carbon = gray, oxygen = red, nitrogen = blue, boron = pink, and zinc = green.

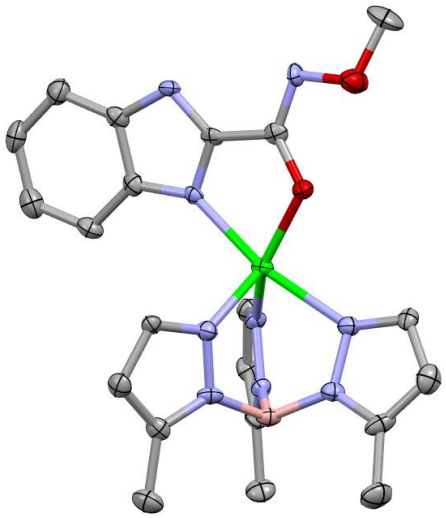

Figure 4.S7. Structure of [($Tp^{Ph,Me}$)Zn(**4.2a**)] rendered as an ORTEP with atoms at 50% thermal probability ellipsoids. Hydrogen atoms and $Tp^{Ph,Me}$ phenyl groups have been removed for clarity. The asymmetric unit consists of two complexes (one not shown) and three molecules of benzene (not shown). Color scheme: carbon = gray, oxygen = red, nitrogen = blue, boron = pink, and zinc = green.

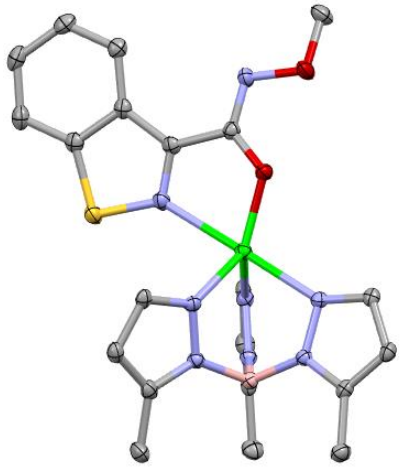

Figure 4.S8. Structure of [($Tp^{Ph,Me}$)Zn(**4.3a**)] rendered as an ORTEP with atoms at 50% thermal probability ellipsoids. Hydrogen atoms and $Tp^{Ph,Me}$ phenyl groups have been removed for clarity. The asymmetric unit consists of the complex and a molecule of benzene (not shown). Color scheme: carbon = gray, sulfur = yellow, oxygen = red, nitrogen = blue, boron = pink, and zinc = green.

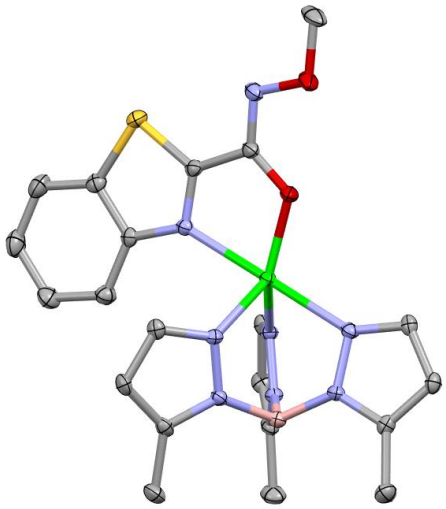

Figure 4.S9. Structure of [($Tp^{Ph,Me}$)Zn(**4.4a**)] rendered as an ORTEP with atoms at 50% thermal probability ellipsoids. Hydrogen atoms and $Tp^{Ph,Me}$ phenyl groups have been removed for clarity. The asymmetric unit consists of the complex and a molecule of benzene (not shown). Color scheme: carbon = gray, sulfur = yellow, oxygen = red, nitrogen = blue, boron = pink, and zinc = green.

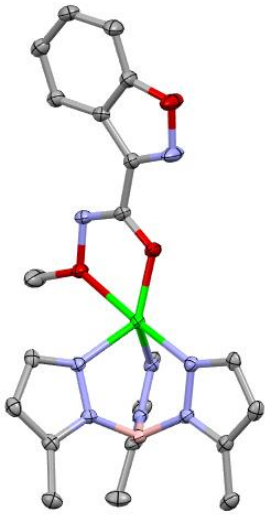

Figure 4.S10. Structure of [($Tp^{Ph,Me}$)Zn(**4.5a**)] rendered as an ORTEP with atoms at 50% thermal probability ellipsoids. Hydrogen atoms and $Tp^{Ph,Me}$ phenyl groups have been removed for clarity. The asymmetric unit consists of the complex and a molecule of benzene (not shown). Color scheme: carbon = gray, oxygen = red, nitrogen = blue, boron = pink, and zinc = green.

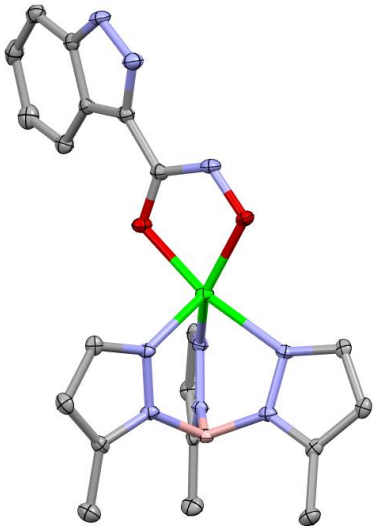

Figure 4.S11. Structure of [($Tp^{Ph,Me}$)Zn(**4.1b**)] rendered as an ORTEP with atoms at 50% thermal probability ellipsoids. Hydrogen atoms and $Tp^{Ph,Me}$ phenyl groups have been removed for clarity. The asymmetric unit consists of the complex and a molecule of MeOH (not shown). Color scheme: carbon = gray, oxygen = red, nitrogen = blue, boron = pink, and zinc = green.

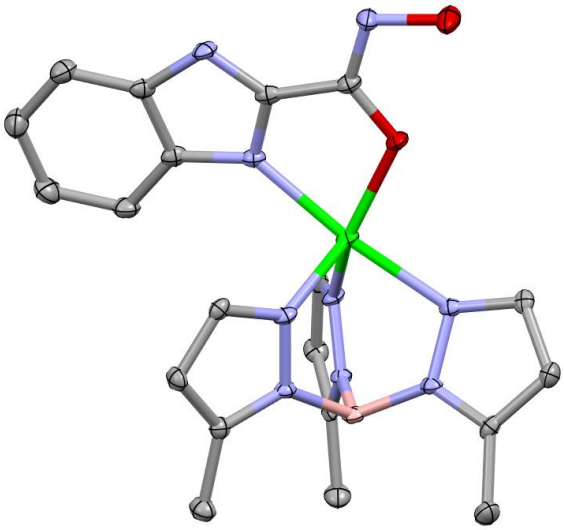

Figure 4.S12. Structure of [($Tp^{Ph,Me}$)Zn(**4.2b**)] rendered as an ORTEP with atoms at 50% thermal probability ellipsoids. Hydrogen atoms and $Tp^{Ph,Me}$ phenyl groups have been removed for clarity. The asymmetric unit consists of the complex and two molecules of benzene (not shown). Color scheme: carbon = gray, oxygen = red, nitrogen = blue, boron = pink, and zinc = green.

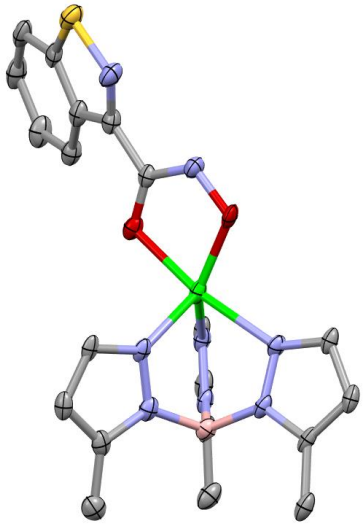

Figure 4.S13. Structure of [($Tp^{Ph,Me}$)Zn(**4.3b**)] rendered as an ORTEP with atoms at 50% thermal probability ellipsoids. Hydrogen atoms and $Tp^{Ph,Me}$ phenyl groups have been removed for clarity. The asymmetric unit consists of the complex and a molecule of MeOH (not shown). Color scheme: carbon = gray, sulfur = yellow, oxygen = red, nitrogen = blue, boron = pink, and zinc = green.

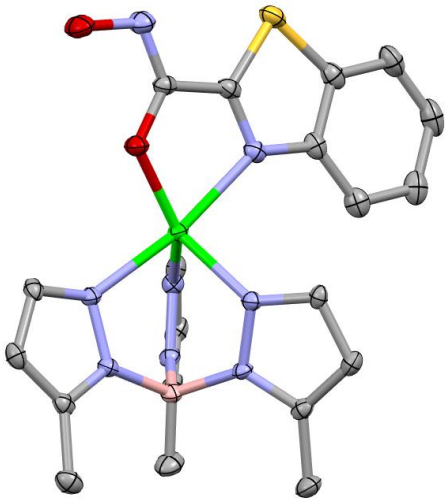

Figure 4.S14. Structure of [($Tp^{Ph,Me}$)Zn(**4.4b**)] rendered as an ORTEP with atoms at 50% thermal probability ellipsoids. Hydrogen atoms and $Tp^{Ph,Me}$ phenyl groups have been removed for clarity. The asymmetric unit consists of two complexes (one not shown) and two molecules of benzene (not shown). Color scheme: carbon = gray, sulfur = yellow, oxygen = red, nitrogen = blue, boron = pink, and zinc = green.

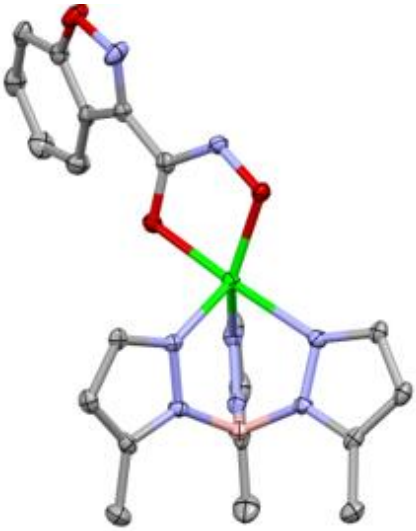

Figure 4.S15. Structure of [($Tp^{Ph,Me}$)Zn(**4.5b**)] rendered as an ORTEP with atoms at 50% thermal probability ellipsoids. Hydrogen atoms and $Tp^{Ph,Me}$ phenyl groups have been removed for clarity. The asymmetric unit consists of the complex and a molecule of water (not shown). Color scheme: carbon = gray, oxygen = red, nitrogen = blue, boron = pink, and zinc = green.

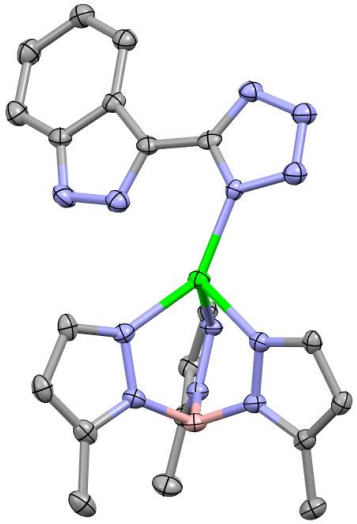

Figure 4.S16. Structure of [($Tp^{Ph,Me}$)Zn(**4.1c**)] rendered as an ORTEP with atoms at 50% thermal probability ellipsoids. Hydrogen atoms and $Tp^{Ph,Me}$ phenyl groups have been removed for clarity. The asymmetric unit consists of the complex and a molecule of water (not shown). Color scheme: carbon = gray, nitrogen = blue, boron = pink, and zinc = green.

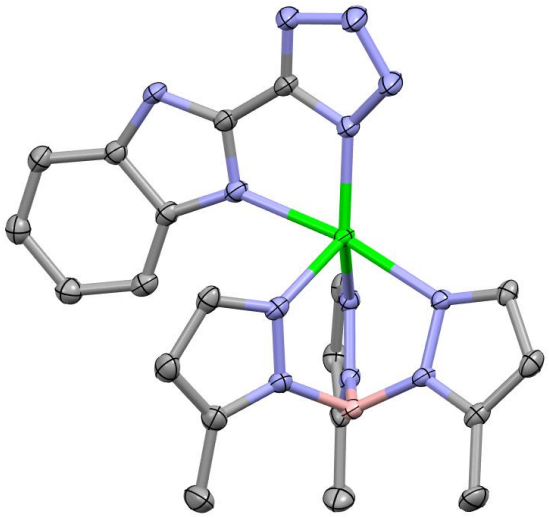

Figure 4.S17. Structure of [($Tp^{Ph,Me}$)Zn(**4.2c**)] rendered as an ORTEP with atoms at 50% thermal probability ellipsoids. Hydrogen atoms and $Tp^{Ph,Me}$ phenyl groups have been removed for clarity. The asymmetric unit consists of two complexes (one not shown) and two and a half molecules of benzene (not shown). Color scheme: carbon = gray, nitrogen = blue, boron = pink, and zinc = green.

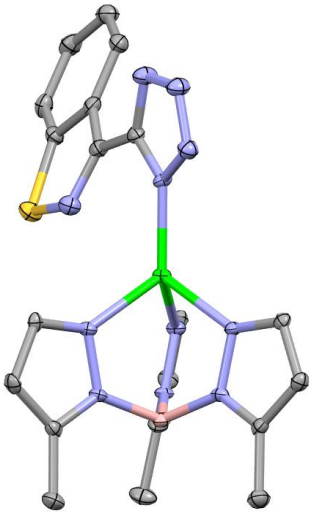

Figure 4.S18. Structure of [($Tp^{Ph,Me}$)Zn(**4.3c**)] rendered as an ORTEP with atoms at 50% thermal probability ellipsoids. Hydrogen atoms and $Tp^{Ph,Me}$ phenyl groups have been removed for clarity. The asymmetric unit consists only of the complex. Color scheme: carbon = gray, sulfur = yellow, nitrogen = blue, boron = pink, and zinc = green.

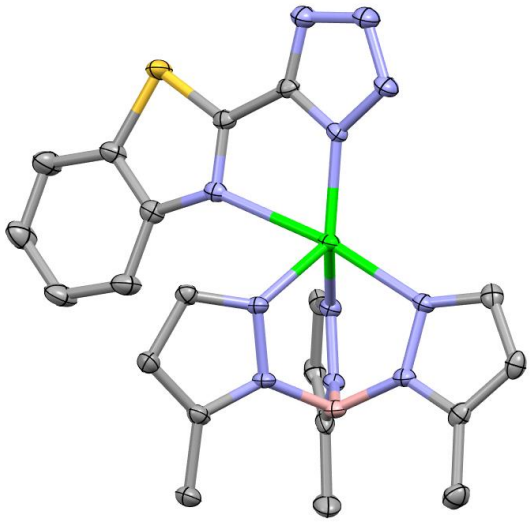

Figure 4.S19. Structure of [($Tp^{Ph,Me}$)Zn(**4.4c**)] rendered as an ORTEP with atoms at 50% thermal probability ellipsoids. Hydrogen atoms and $Tp^{Ph,Me}$ phenyl groups have been removed for clarity. The asymmetric unit consists of the complex and a molecule of benzene (not shown). Color scheme: carbon = gray, sulfur = yellow, nitrogen = blue, boron = pink, and zinc = green.

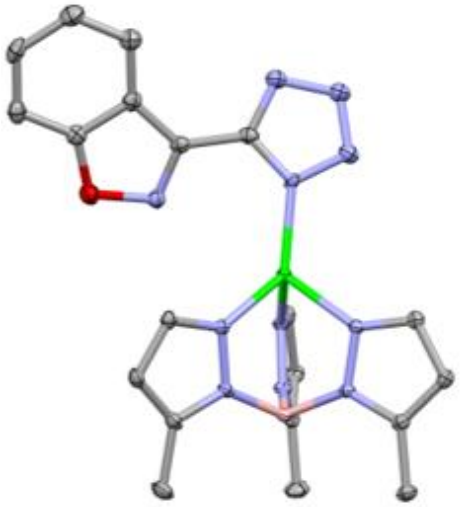

Figure 4.S20. Structure of [($Tp^{Ph,Me}$)Zn(**4.5c**)] rendered as an ORTEP with atoms at 50% thermal probability ellipsoids. Hydrogen atoms and $Tp^{Ph,Me}$ phenyl groups have been removed for clarity. The asymmetric unit consists only of the complex. Color scheme: carbon = gray, oxygen = red, nitrogen = blue, boron = pink, and zinc = green.

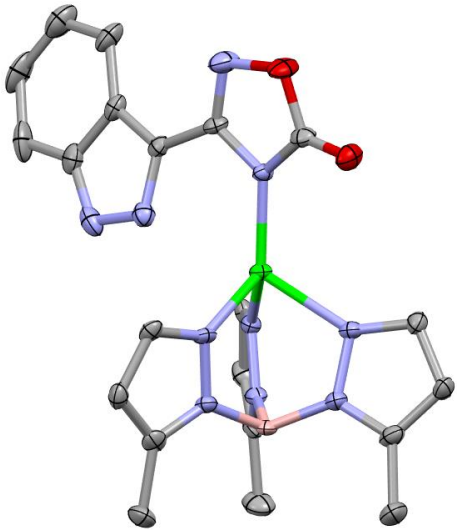

Figure 4.S21. Structure of [(Tp^{Ph,Me})Zn(**4.1d**)] rendered as an ORTEP with atoms at 50% thermal probability ellipsoids. Hydrogen atoms and Tp^{Ph,Me} phenyl groups have been removed for clarity. The asymmetric unit consists of two complexes (one not shown) and three molecules of MeOH (not shown). Color scheme: carbon = gray, oxygen = red, nitrogen = blue, boron = pink, and zinc = green.

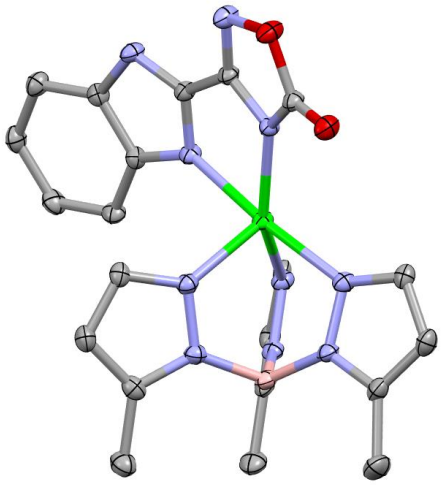

Figure 4.S22. Structure of [(Tp^{Ph,Me})Zn(**4.2d**)] rendered as an ORTEP with atoms at 50% thermal probability ellipsoids. Hydrogen atoms and Tp^{Ph,Me} phenyl groups have been removed for clarity. The asymmetric unit consists only of the complex. Color scheme: carbon = gray, oxygen = red, nitrogen = blue, boron = pink, and zinc = green.

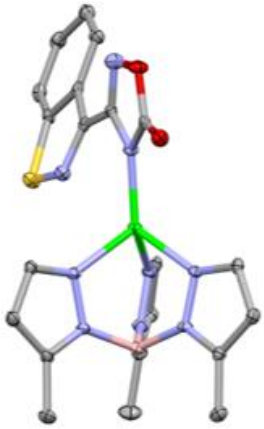

Figure 4.S23. Structure of [($Tp^{Ph,Me}$)Zn(**4.3d**)] rendered as an ORTEP with atoms at 50% thermal probability ellipsoids. Hydrogen atoms and $Tp^{Ph,Me}$ phenyl groups have been removed for clarity. The asymmetric unit consists only of the complex. Color scheme: carbon = gray, oxygen = red, sulfur = yellow, nitrogen = blue, boron = pink, and zinc = green.

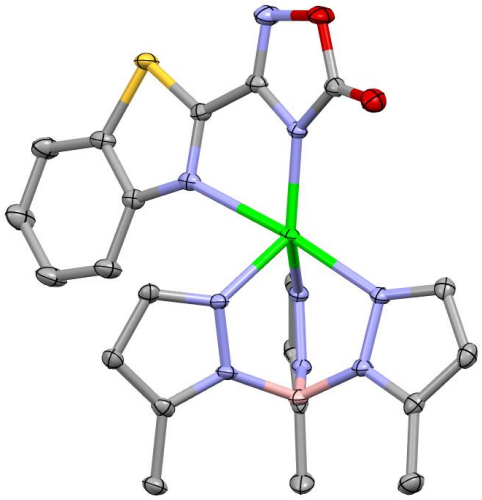

Figure 4.S24. Structure of [($Tp^{Ph,Me}$)Zn(**4.4d**)] rendered as an ORTEP with atoms at 50% thermal probability ellipsoids. Hydrogen atoms and $Tp^{Ph,Me}$ phenyl groups have been removed for clarity. The asymmetric unit consists of the complex and a molecule of benzene (not shown). Color scheme: carbon = gray, oxygen = red, sulfur = yellow, nitrogen = blue, boron = pink, and zinc = green.

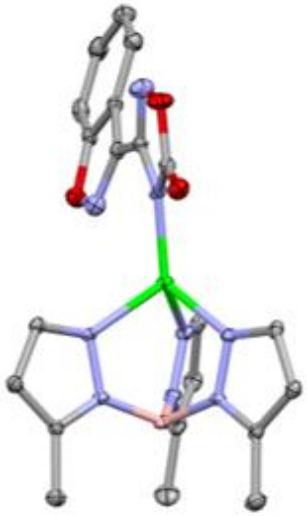

Figure 4.S25. Structure of [(Tp^{Ph,Me})Zn(**4.5d**)] rendered as an ORTEP with atoms at 50% thermal probability ellipsoids. Hydrogen atoms and Tp^{Ph,Me} phenyl groups have been removed for clarity. The asymmetric unit consists only of the complex. Color scheme: carbon = gray, oxygen = red, nitrogen = blue, boron = pink, and zinc = green.

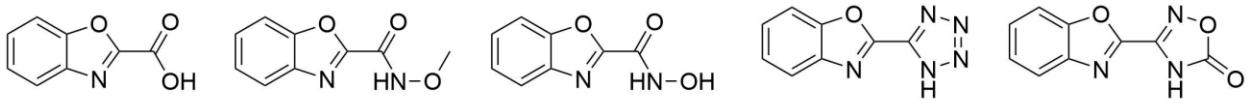

Figure 4.S26. Chemical structures of the benzoxazole derivatives examined using DFT.

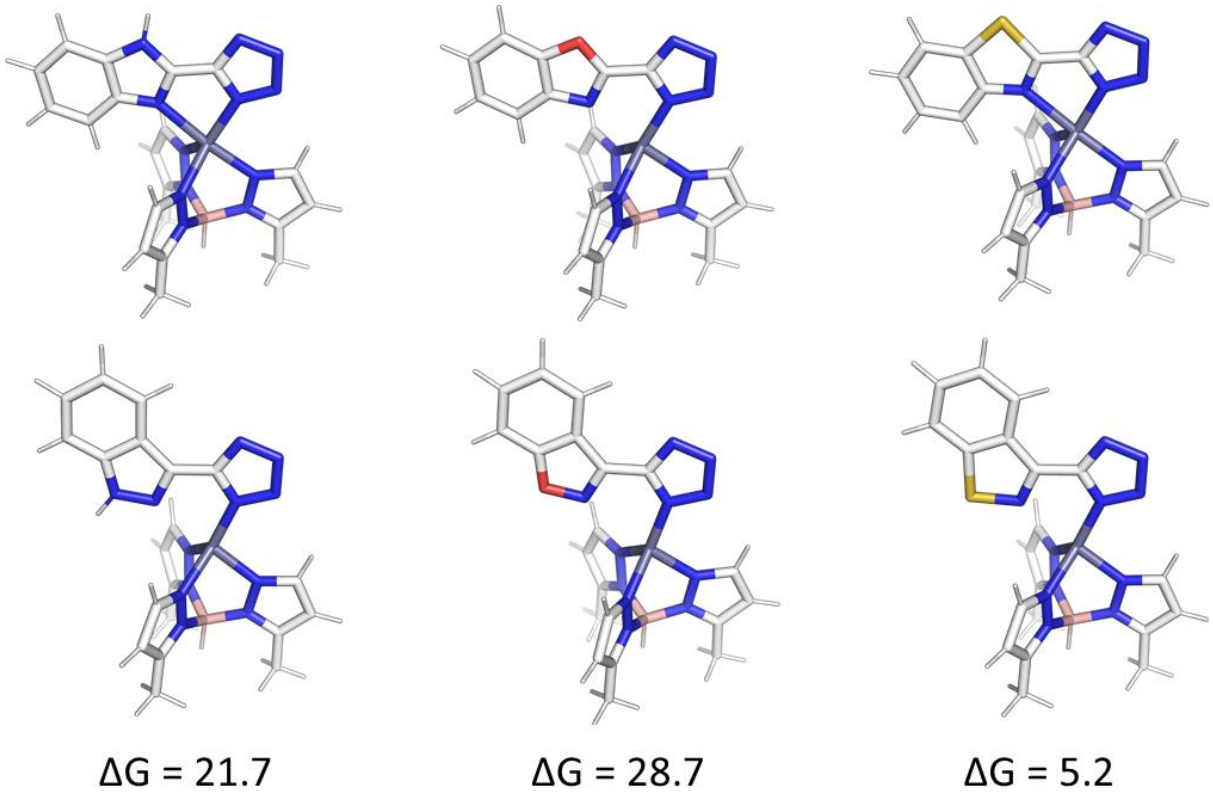

Figure 4.S27. ωB97x-D/def2-TZVPP optimized geometries of: isomeric Tp^{Me}Zn(**4.2c**) and Tp^{Me}Zn(**4.1c**) (*top and bottom left*, respectively), isomeric Tp^{Me}Zn(benzoxazole-2-tetrazole) and Tp^{Me}Zn(**4.5c**) (*top and bottom middle*, respectively), and isomeric Tp^{Me}Zn(**4.4c**) and Tp^{Me}Zn(**4.5c**) (*top and bottom right*, respectively). Energies (in kcal mol^{-1}) are electronic energies determined at the ωB97x-D/def2-TZVPP level of theory.

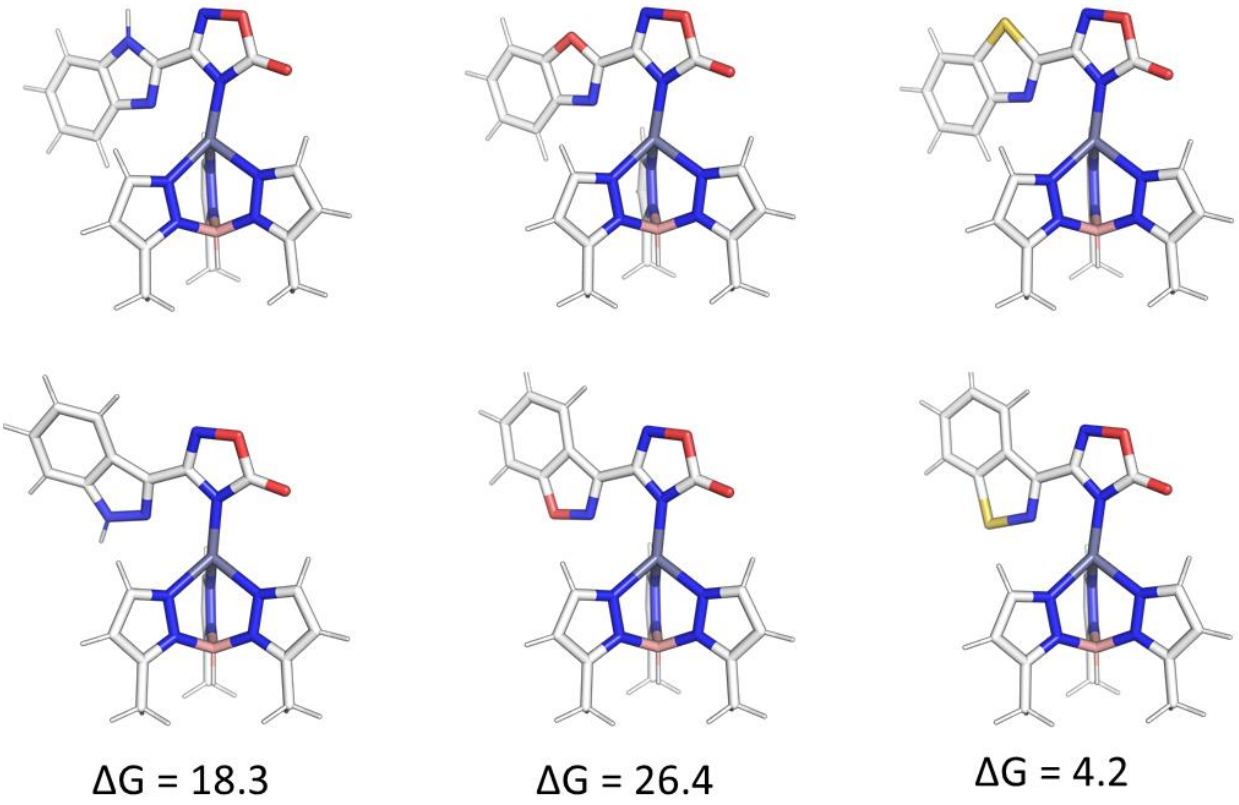

Figure 4.S28. ωB97x-D/def2-TZVPP optimized geometries of: isomeric $Tp^{Me}Zn$ (**4.2d**) and $Tp^{Me}Zn$ (**4.1d**) (*top and bottom left*, respectively), isomeric $Tp^{Me}Zn$ (benzoxazole-2-oxadiazolone) and $Tp^{Me}Zn$ (**5.5d**) (*top and bottom middle*, respectively), as well as isomeric $Tp^{Me}Zn$ (**5.4d**) and $Tp^{Me}Zn$ (**5.5d**). (*top and bottom right*, respectively). Energies (in kcal mol^{-1}) are electronic energies determined at the ωB97x-D/def2-TZVPP level of theory.

4.9 Acknowledgements

Chapter 4 is a reprint of the material published in the following publication, "Effect of Heterocycle Content on Metal-Binding Isostere Coordination" Benjamin L. Dick, Ashay Patel, and Seth M. Cohen. *Chem. Sci*., 2020, *11*, 26, 6907-6914. The dissertation author was the primary researcher and author of this paper and gratefully acknowledges the contributions of coauthors Ashay Patel and Seth M. Cohen. Reproduced with permission from the Royal Society of Chemistry, Copyright 2020.

4.10 References

1. Yang, Y.; Hu, X. Q.; Li, Q. S.; Zhang, X. X.; Ruan, B. F.; Xu, J.; Liao, C., Metalloprotein Inhibitors for the Treatment of Human Diseases. *Curr. Top. Med. Chem.* **2016,** *16* (4), 384-96.

2. Chen, A. Y.; Adamek, R. N.; Dick, B. L.; Credille, C. V.; Morrison, C. N.; Cohen, S. M., Targeting Metalloenzymes for Therapeutic Intervention. *Chem. Rev.* **2019,** *119* (2), 1323-1455.

3. Jacobsen, J. A.; Fullagar, J. L.; Miller, M. T.; Cohen, S. M., Identifying chelators for metalloprotein inhibitors using a fragment-based approach. *J. Med. Chem.* **2011,** *54* (2), 591-602.

4. Credille, C. V.; Chen, Y.; Cohen, S. M., Correction to Fragment-Based Identification of Influenza Endonuclease Inhibitors. *J. Med. Chem.* **2017,** *60* (23), 9912.

5. Credille, C. V.; Morrison, C. N.; Stokes, R. W.; Dick, B. L.; Feng, Y.; Sun, J.; Chen, Y.; Cohen, S. M., SAR Exploration of Tight-Binding Inhibitors of Influenza Virus PA Endonuclease. *J. Med. Chem.* **2019,** *62* (21), 9438-9449.

6. Chen, A. Y.; Thomas, P. W.; Stewart, A. C.; Bergstrom, A.; Cheng, Z.; Miller, C.; Bethel, C. R.; Marshall, S. H.; Credille, C. V.; Riley, C. L.; Page, R. C.; Bonomo, R. A.; Crowder, M. W.; Tierney, D. L.; Fast, W.; Cohen, S. M., Dipicolinic Acid Derivatives as Inhibitors of New Delhi Metallo-beta-lactamase-1. *J. Med. Chem.* **2017,** *60* (17), 7267-7283.

7. Perez, C.; Li, J.; Parlati, F.; Rouffet, M.; Ma, Y.; Mackinnon, A. L.; Chou, T. F.; Deshaies, R. J.; Cohen, S. M., Discovery of an Inhibitor of the Proteasome Subunit Rpn11. *J. Med. Chem.* **2017,** *60* (4), 1343-1361.

8. Patani, G. A.; LaVoie, E. J., Bioisosterism: A Rational Approach in Drug Design. *Chem. Rev.* **1996,** *96* (8), 3147-3176.

9. Friedman, H. L., Influence of Isosteric Replacements Upon Biological Activity. *Natl Acad. Sci.* **1951,** *206*, 295-362.

10. Lassila, T.; Hokkanen, J.; Aatsinki, S. M.; Mattila, S.; Turpeinen, M.; Tolonen, A., Toxicity of Carboxylic Acid-Containing Drugs: The Role of Acyl Migration and CoA Conjugation Investigated. *Chem. Res. Toxicol.* **2015,** *28* (12), 2292-303.

11. Pajouhesh, H.; Lenz, G. R., Medicinal chemical properties of successful central nervous system drugs. *NeuroRx* **2005,** *2* (4), 541-53.

12. Dick, B. L.; Cohen, S. M., Metal-Binding Isosteres as New Scaffolds for Metalloenzyme Inhibitors. *Inorg. Chem.* **2018,** *57* (15), 9538-9543.

13. Ballatore, C.; Huryn, D. M.; Smith, A. B., 3rd, Carboxylic acid (bio)isosteres in drug design. *ChemMedChem* **2013,** *8* (3), 385-95.

14. Boogaerts, I. I. F.; Nolan, S. P., Carboxylation of C-H Bonds Using N-Heterocyclic Carbene Gold(I) Complexes. *J. Am. Chem. Soc.* **2010,** *132* (26), 8858-+.

15. Hrib, N. J.; Jurcak, J. G.; Burgher, K. L.; Conway, P. G.; Hartman, H. B.; Kerman, L. L.; Roehr, J. E.; Woods, A. T., Benzisoxazole- and benzisothiazole-3-carboxamides as potential atypical antipsychotic agents. *J. Med. Chem.* **1994,** *37* (15), 2308-14.

16. Cundy, D.; Simpson, G., The Cycloaddition Reactions of Benzimidazole-2-carbonitrite Oxide With Alkenes. *Aust. J. Chem.* **1996,** *49* (2), 199-203.

17. Barba, O.; Dawson, G. J.; Krulle, T. M.; Rowley, R. J.; Smyth, D.; Thomas, G. H. Preparation of dihydroimidazothiazole derivatives as 5-HT1A agonists and noradrenaline and serotonin reuptake inhibitors for treating metabolic disorders. WO2006085118A2, 2006.

18. Gryshuk, A. L.; Perkins, J. Synthesis of 6-amino-6-deoxy-D-luciferin precursor, 2-cyano-6-aminobenzothiazole and its conjugate with amino acids useful for the preparation of carboxylate-modified luciferin amino acid and peptide probes for bioluminescent protease assays. US20110213124A1, 2011.

19. Puerta, D. T.; Cohen, S. M., Examination of Novel Zinc-Binding Groups for Use in Matrix Metalloproteinase Inhibitors. *Inorg. Chem.* **2003,** *42*, 3423-3430.

20. George, S. M.; Nam, J. H.; Lee, G. Y.; Han, J. H.; Park, B. K.; Kim, C. G.; Jeon, D. J.; Chung, T.-M., N-Alkoxy Carboxamide Stabilized Tin(II) and Germanium(II) Complexes for Thin-Film Applications. *Eur. J. Inorg. Chem.* **2016,** *2016* (36), 5539-5546.

21. Lee, J. H.; Jung, E. A.; Lee, G. Y.; Han, S. H.; Park, B. K.; Lee, S. W.; Son, S. U.; Kim, C. G.; Chung, T.-M., Synthesis of Indium Complexes for Thin Film Transistor Applications Bearing N-Alkoxy Carboxamide Ligands. *ChemistrySelect* **2018,** *3* (23), 6691-6695.

22. Heinrich, T.; Buchstaller, H. P.; Cezanne, B.; Rohdich, F.; Bomke, J.; Friese-Hamim, M.; Krier, M.; Knochel, T.; Musil, D.; Leuthner, B.; Zenke, F., Novel reversible methionine aminopeptidase-2 (MetAP-2) inhibitors based on purine and related bicyclic templates. *Bioorg. Med. Chem. Lett.* **2017,** *27* (3), 551-556.

23. Schonherr, D.; Wollatz, U.; Haznar-Garbacz, D.; Hanke, U.; Box, K. J.; Taylor, R.; Ruiz, R.; Beato, S.; Becker, D.; Weitschies, W., Characterisation of Selected Active Agents Regarding pK(a) Values, Solubility Concentrations and pH Profiles by SiriusT3. *Eur. J. Pharm. Biopharm.* **2015,** *92*, 155-170.

24. Chai, J. D.; Head-Gordon, M., Long-range corrected hybrid density functionals with damped atom-atom dispersion corrections. *Phys. Chem. Chem. Phys.* **2008,** *10* (44), 6615-20.

25. Katritzky, A. R.; Jug, K.; Oniciu, D. C., Quantitative Measures of Aromaticity for Mono-, Bi-, and Tricyclic Penta- and Hexaatomic Heteroaromatic Ring Systems and Their Interrelationships. *Chem. Rev.* **2001,** *101* (5), 1421-1450.

26. Katritzky, A. R.; Feygelman, V.; Musumarra, G.; Barczynski, P.; Szafran, M., Aromaticity as a Quantitative Concept. 3. Benzo-fused five- and six-membered heterocycles. *J. Prakt. Chem.* **1990,** *332* (6), 870-884.

27. Puerta, D. T.; Cohen, S. M., [(TpMe,Ph)2Zn2(H3O2)]ClO4: A New H3O2 Species Relevant to Zinc Proteinases. *Inorg. Chim. Acta* **2002,** *337*, 459-462.

28. Yasuda, M., Dissociation Constants of Some Carboxylic Acids in Mixed Aqueous Solvents. *Bull. Chem. Soc. Jpn.* **1959,** *32* (5), 429-432.

29. Pesce, B., *Electrolytes: Proceedings of an International Symposium Held in Trieste June, 1959*. Pergamon: 1962.

30. Slater, B.; Mccormack, A.; Avdeef, A.; Comer, J. E. A., Ph-Metric Log-P .4. Comparison of Partition-Coefficients Determined by Hplc and Potentiometric Methods to Literature Values. *J. Pharm. Sci.* **1994,** *83*, 1280-1283.

31. Frisch, M. J.; Trucks, G. W.; Schlegel, H. B.; Scuseria, G. E.; Robb, M. A.; Cheeseman, J. R.; Scalmani, G.; Barone, V.; Mennucci, B.; Petersson, G. A.; Nakatsuji, H.; Caricato, M.; Li, X.; Hratchian, H. P.; Izmaylov, A. F.; Bloino, J.; Zheng, G.; Sonnenberg, J. L.; Hada, M.; Ehara, M.; Toyota, K.; Fukuda, R.; Hasegawa, J.; Ishida, M.; Nakajima, T.; Honda, Y.; Kitao, O.; Nakai, H.; Vreven, T.; Montgomery, J. J. A.; Peralta, J. E.; Ogliaro, F.; Bearpark, M.; Heyd, J. J.; Brothers, E.; Kudin, K. N.; Staroverov, V. N.; Kobayashi, R.; Normand, J.; Raghavachari, K.; Rendell, A.; Burant, J. C.; Iyengar, S. S.; Tomasi, J.; Cossi, M.; Rega, N.; Millam, J. M.; Klene, M.; Knox, J. E.; Cross, J. B.; Bakken, V.; Adamo, C.; Jaramillo, J.; Gomperts, R.; Stratmann, R. E.; Yazyev, O.; Austin, A. J.; Cammi, R.; Pomelli, C.; Ochterski, J. W.; Martin, R. L.; Morokuma, K.; Zakrzewski, V. G.; Voth, G. A.; Salvador, P.; Dannenberg, J. J.; Dapprich, S.; Daniels, A. D.; Farkas, Ö.; Foresman, J. B.; Ortiz, J. V.; Cioslowski, J.; Fox, D. J. *Gaussian 09 Revision D.01*, Gaussian Inc: Pittsburg PA, 2009.

32. Weigend, F., Accurate Coulomb-fitting basis sets for H to Rn. *Phys. Chem. Chem. Phys.* **2006,** *8* (9), 1057-1065.

33. Weigend, F.; Ahlrichs, R., Balanced basis sets of split valence, triple zeta valence and quadruple zeta valence quality for H to Rn: Design and assessment of accuracy. *Phys. Chem. Chem. Phys.* **2005,** *7* (18), 3297-305.

34. *Avogadro: an open-source molecular builder and visualization tool. Version 1.2.0.* http://avogadro.cc.

35. Dennington, R.; Keith, T. A.; Millam, J. M. *GaussView Version 5*, 2016.

36. Hanwell, M. D.; Curtis, D. E.; Lonie, D. C.; Vandermeersch, T.; Zurek, E.; Hutchison, G. R., Avogadro: an advanced semantic chemical editor, visualization, and analysis platform. *J. Cheminf.* **2012,** *4* (1), 17.

37. *PyMOL: The PyMOL Molecular Graphics System, Version 2.2 Schrödinger, LLC*.

38. Dolomanov, O. V.; Bourhis, L. J.; Gildea, R. J.; Howard, J. A. K.; Puschmann, H., OLEX2: a complete structure solution, refinement and analysis program. *J. Appl. Crystal.* **2009,** *42* (2), 339-341.

39. Sheldrick, G., Crystal Structure Refinement with SHELXL. *Acta Crystal. Sec. C* **2015,** *71*, 3-8.

40. Sheldrick, G. M., A short history of SHELX. *Acta Crystallogr., Sect. A: Found. Adv.* **2008,** *64* (Pt 1), 112-22.

41. Spek, A. L., PLATON SQUEEZE: a tool for the calculation of the disordered solvent contribution to the calculated structure factors. *Acta Crystallogr., Sect. C: Struct. Chem.* **2015,** *71* (Pt 1), 9-18.

Chapter 5: Structure Based Analysis of Endo Inhibitor Optimization

5.1 Introduction

The influenza virus is a constant seasonal concern and results in 3 to 5 million cases of severe illness and 290,000 to 650,000 subsequent respiratory deaths annually.[1] Vaccination before the occurrence of the influenza virus is now used by most population segments around the world to prevent or lessen subsequent infection and illness.[2-3] One vaccination for influenza is not sufficient for life time immunization as the virus is constantly undergoing genetic mutation.[4] In addition, the annual vaccine covers only a prediction of what strains of the virus will be circulating that year and often fails.[5] To this end alternative methods for preventing the spread of the influenza virus have been developed and are of continued interest.

In the field of influenza antiviral therapeutics there are a variety of therapeutics that have a range of targets and efficacies.[6] Some include amantadine and rimantadine, which inhibit the M2 proton channel in the viral envelope. Unfortunately, due to emergence of widespread resistance in circulating strains of influenza, both are no longer recommended therapies.[7] Another therapeutic paradigm has been neuraminidase inhibitors such as oseltamivir (Tamiflu) and zanamivir, but they must be administered within 24 to 48 hours of presentation of symptoms to be most effective.[8-9]

An alternative target within the influenza virus that has garnered more attention recently has been the molecular machinery by which a virus combines its genetic material with the host cell's for viral replication.[10] Within each viral capsid is contained the viral RNA required for replication, bound to a heterotrimeric RNA-dependent RNA polymerase complex, made up of the PA, PB1, and PB2 subunit proteins.[11-13] While the polymerase complex performs the replication of the viral genome, it must acquire and incorporate a 5'-mRNA cap from the host into its own RNA, so called "cap-snatching", such that it can be recognized by the eukaryotic host.[14-18] This

cap-snatching mechanism begins by sequestration of host mRNA followed by cleavage via endonuclease activity with the 5'-mRNA cap then serving as a primer for viral transcription (Figure 5.1). While initially thought to be located on a different subunit, the endonuclease activity was determined to be located in the N-terminal domain of the polymerase acidic (PA) subunit.[15] Inhibition of the influenza PA subunit N-terminal endonuclease domain of the RNA-dependent RNA polymerase complex (Endo) has been an attractive target for preventing influenza viral replication since it is required for viral replication and conserved amongst circulating influenza strains.[19]

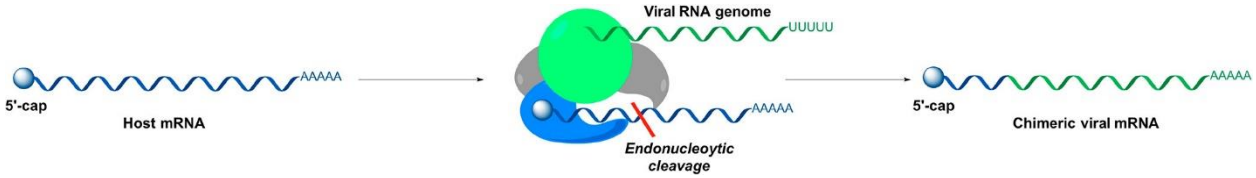

Figure 5.1. The RNA-dependent RNA polymerase complex is preloaded with viral RNA at the PB1 subunit (green). Upon sequestration of host mRNA at the PB2 subunit (blue), the host mRNA is cleaved by Endo (grey) generating a 5'-cap that is combined with the viral RNA, resulting in chimeric viral mRNA. Adapted from Chen et al.[20]

Endo is a dinuclear metalloenzyme that is speculated to be Mn^{2+} or Mg^{2+} dependent.[15, 21] The first reported crystal structure of Endo elucidated the active site showing two coordinated Mn^{2+} ions (Figure 5.2).[15] Mn_A is coordinated by His41, the backbone carbonyl of Ile120, and the carboxylates of Asp108 and Glu119, while Mn_B is coordinated by the carboxylate of Asp108 as well as the carboxylate of Glu80. The remaining open coordination sites on both metals are occupied by water molecules resulting in octahedral geometry at both metal ions. Inhibition of Endo has yielded potent inhibitors that show efficacy in vitro as well as in vivo.[22]

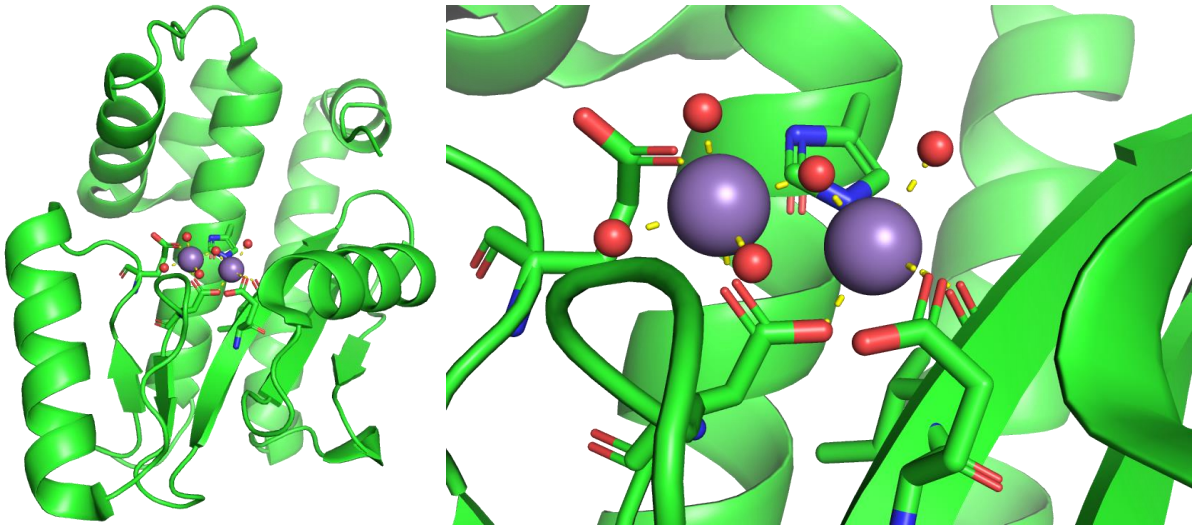

Figure 5.2. Crystal structure of PA N-terminal endonuclease domain (Endo) (PDB: 5DES) with a loop deletion (*left*). View of the dinuclear active site occupied by Mn^{2+}, with Mn_A on the right and Mn_B on the left, exhibiting octahedral coordination geometry (*right*).

One of the earliest reported inhibitors that was structurally characterized bound to the active site of Endo was the natural product epigallocatechin gallate (EGCG) (Figure 5.3).[23-24] From the crystal structure of EGCG bound to the active site of Endo it was shown that the inhibitor, which exhibits modest in vivo activity (EC_{50} values between 22-28 μM), utilizes a galloyl MBP (Figure 5.3). The MBP coordinates Mn_A in a bidentate fashion, with the second phenolic oxygen also coordinating to Mn_B as it occupies the position of a bridging water between both metals. Other polyphenolic MBP scaffolds that exhibit similar inhibitory activity against Endo include the 1,2-diphenolic MBP catechol.[22, 25] An MBP class that has been successful as inhibitors of Endo, with potent in vivo activity, has been diketo acids.[26-28] One of the most successful diketo acids reported, was the compound L-742,001 (Figure 5.3) which possesses potent in vivo activity (EC_{50} = 350 nM).[27] The crystal structure of L-742,001 coordinating to the active site of Endo exhibits the carboxylate and neighboring hydroxyl/carbonyl coordinating to Mn_A, while both carbonyls of the diketo motif are coordinating Mn_B.[24] Also the aryl/alkyl derivatization off of the diketo acid MBP

makes significant interactions with hydrophobic residues in the active site. While these class of compounds possess potent in vivo activity, they have not progressed into the clinic due to poor pharmacokinetics and toxicity profile.

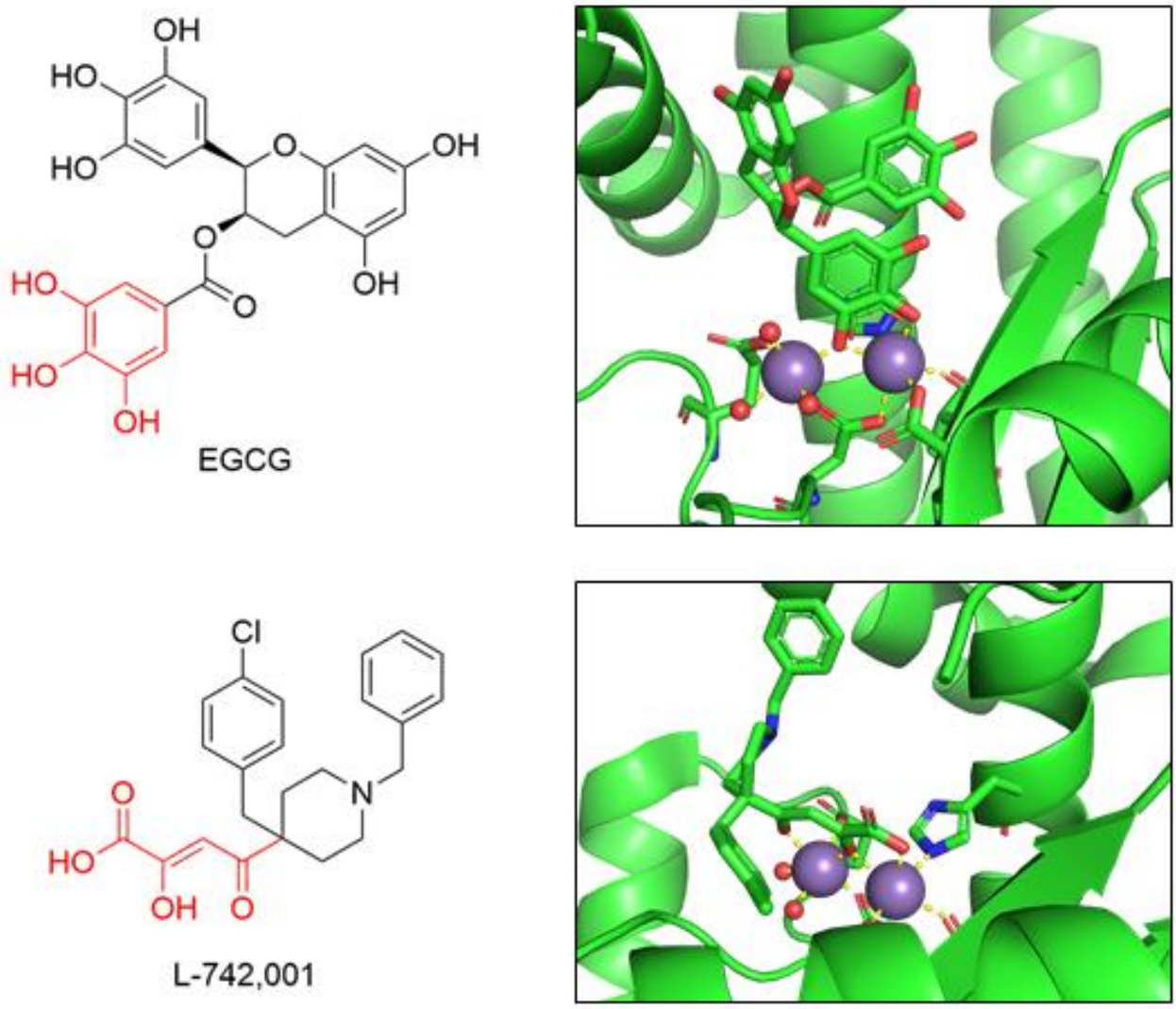

Figure 5.3. Chemical structures of EGCG (*top*) and L-742,001 (*bottom*) (with the MBPs highlighted in red). Both crystal structures of EGCG (PDB: 4AWM) and L-742,001 (PDB: 5CGV) bound to Endo coordinate the active site Mn^{2+} ions. L-742,001 engages in bidentate coordination to both metals, while EGCG only coordinates Mn_A in a bidentate fashion.

Most recently, an FDA approved therapeutic targeting Endo, Baloxavir Marboxil (shown as the active form Baloxavir acid, Figure 5.4) utilizing a ring fused 2,3-hydroxypyridinone core MBP achieved FDA approval for the treatment of the flu. The interactions that Baloxavir acid makes with the active site of Endo were elucidated by a recently solved crystal structure (Figure 5.4).[29] Based on the structure, the 2,3-hydroxypyridinone ring coordinates to Mn_A in a bidentate fashion, whereas it coordinates to Mn_B in a bidentate fashion utilizing the 2,3-hydroxypyridinone ring and the carbonyl from the neighboring ring (Figure 5.4). While Baloxavir Marboxil represents an advancement for the field, it must be administered as a prodrug and escape mutations emerge quite readily, even during the course of a treatment.[29-31] These escape mutations arise entirely from non-coordinating interactions that Baloxavir Marboxil makes with the peripheral active site, specifically with the non-MBP fused ring system (Figure 5.4).

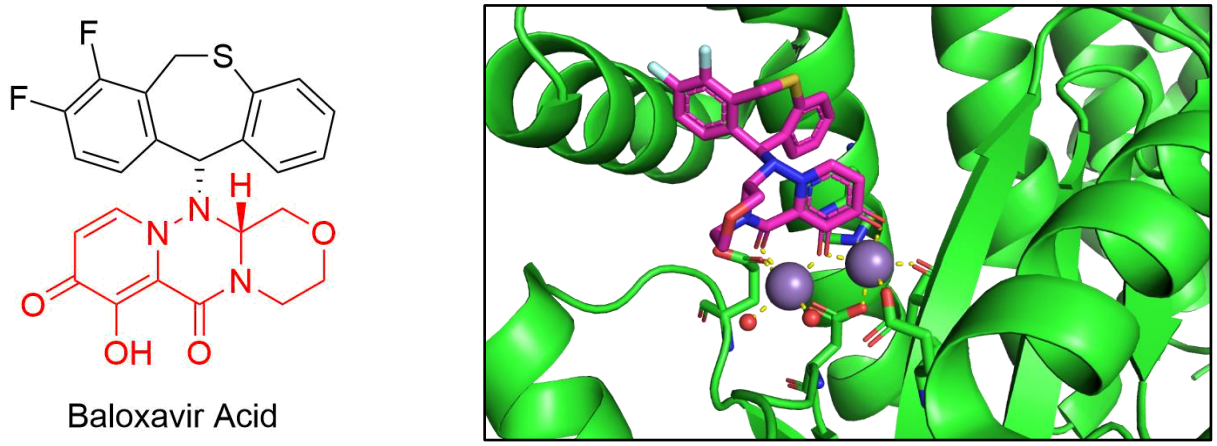

Figure 5.4. Chemical structure of Baloxavir acid, the active form of Baloxavir Marboxil (with the MBP highlighted in red) (*left*) and the crystal structure of Baloxavir acid bound to the active site of Endo (PDB: 6FS6) (*right*). Baloxavir acid coordinates both active site metals in a bidentate fashion and makes significant hydrophobic contacts with neighboring residues. The non-MBP fused ring system (shown in black) is where escape mutations interactions arise from.

In order to develop novel inhibitors of Endo that prioritize metal coordination interactions, a fragment library of MBPs was screened against Endo.[32] From this library screen the MBP allomaltol (Figure 5.5) was identified as an inhibitor with moderate inhibitory activity (IC_{50}: 17.1±1.5 μM) and through utilizing fragment growth and merging strategies even more potent inhibitory activity was developed. Unfortunately, the developed inhibitors possessed only modest in vivo activity at protecting human cells from the influenza virus, but represent only the beginning in a potential inhibitor discovery campaign.[32] While there have been significant efforts to develop novel inhibitors for targeting coordination to the active site metals in Endo, there remains an opportunity to improve novel inhibitors that may not suffer from the issues in existing inhibitors, such as requiring prodrug strategies or toxicity issues.

In order to develop novel inhibitors of Endo utilizing an MBP-FBDD approach, an understanding of an MBPs interactions with the active site was focused on. Utilizing X-ray crystallography, the binding of allomaltol derivatives to Endo was elucidated and the rationale behind the significant differences in inhibitory activity compared to others of similar structure was understood. To further modify the potency of this scaffold isostere replacement was explored preliminarily as method to modify properties and inhibitory activity. By using an approach of focusing on optimizing the coordinative interactions between Endo and metal binding inhibitors a series of extremely potent novel inhibitor were developed. This chapter describes the crystallographic characterization of a series of Endo inhibitors and discusses the observed coordination chemistry. The analysis of the coordinative interactions between the active site metals and the MBPs allowed for the development of inhibitors with increased inhibitory activity

5.2 Results and Discussion

Starting with allomaltol, the probable mode of binding was derived by determining the binding mode of derivative **5.1** with Endo (Figure 5.5). From the co-crystal structure of **5.1** bound to the active site of Endo, the MBP portion of the inhibitor was determined to coordinate to Mn_A in a bidentate fashion. This mode of binding is consistent with the body of literature that suggests binding is preferential to Mn_A over Mn_B.[24] Based on the observed coordination mode, and the presence of a proximal open coordination site on Mn_B (occupied by a water molecule), the scaffold could be derivatized further to engage in more coordinative interactions with Mn_B. Therefore, alternative MBP scaffolds with increased coordination opportunities were explored, since Endo inhibitors that possess strong inhibitory activity also coordinate the active site Mn^{2+} metal ions in a tri-coordinate fashion utilizing hard Lewis bases, such as oxygen.[20]

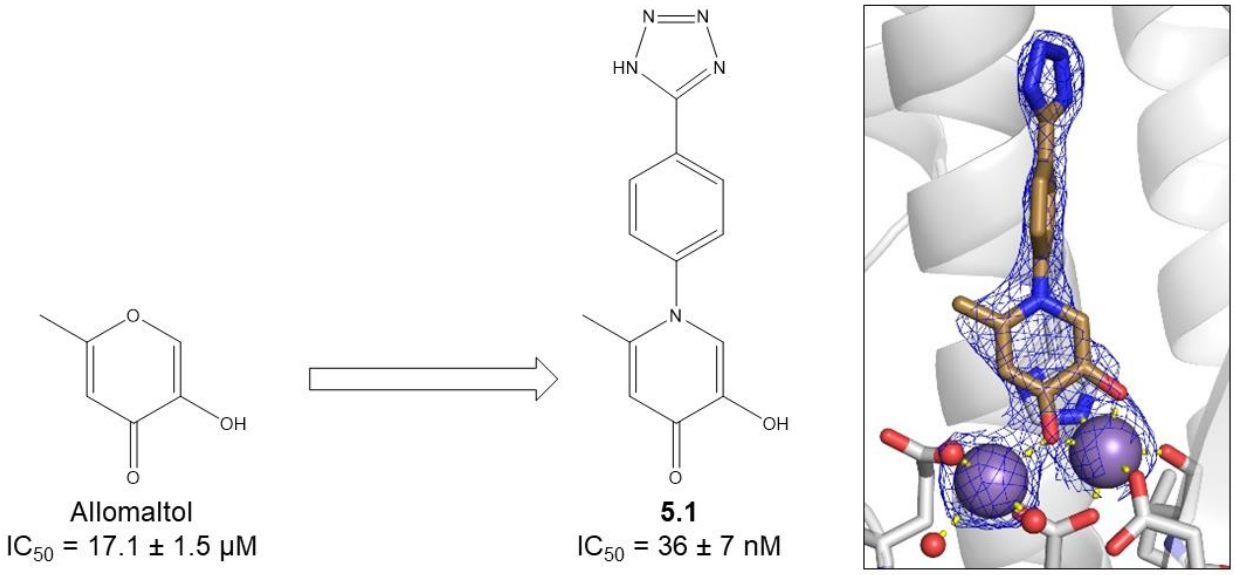

Figure 5.5. Structure and inhibitory activity of allomaltol and a derivative (**5.1**) against Endo. Compound **5.1** was found to coordinate to Mn_A in a bidentate manner and engage in a monodentate coordination interaction with Mn_B (PDB: 6E6X), which possesses additional open coordination sites (blue mesh is the $2F_0 - F_c$ map contoured to 2.0σ).

In developing MBPs for Endo that can engage in more coordinate bonds with the active site Mn^{2+} ions, open positions on the allomaltol MBP scaffold were substituted with a carboxylate. Based on the open coordination sites in the co-crystal structure of **5.1** with Endo, the position between the methyl and hydroxyl position was first tested resulting in **5.2** (Figure 5.5). While there was a modest increase in inhibitory activity (IC_{50} = 3.5 ± 0.6 μM) relative to allomaltol (IC_{50} = 17.1 ± 1.5 μM),[32] this was not as significant of an improvement as was expected. The co-crystal structure of **5.2** with Endo revealed why this compound was not more active. The coordination mode that **5.2** exhibits in Endo was almost exactly that of the derivatized allomaltol derivative **5.1**. The added carboxylate was observed to be perpendicular with the core heterocycle of the MBP and thus unable to engage in a strong coordinative interaction with Mn_B. This is likely due to the steric pressure the alpha methyl substituent has on the carboxylate. To alleviate this steric pressure the heteroatom arrangement inside the core MBP was modified resulting in **5.3** which exhibits an isosteric metal binding motif **5.2**. This modification resulted in a large increase in inhibitory activity (IC_{50} = 43 ± 9 nM), relative to allomaltol, with both active site metals bound in a bidentate fashion as expected (Figure 5.5). To confirm that the methyl substituent of **5.3** was not having a significant effect on the inhibitory activity, the derivative **5.4** was evaluated and cocrystallized with Endo. The derivative showed similar inhibitory activity (IC_{50} = 68 ± 11 nM) and an identical mode of binding to the active site metals as **5.3**. Based on the success of the aforementioned MBPs that engage in multiple coordination interactions to the active site metals other MBPs with similar potential coordination motifs were explored.

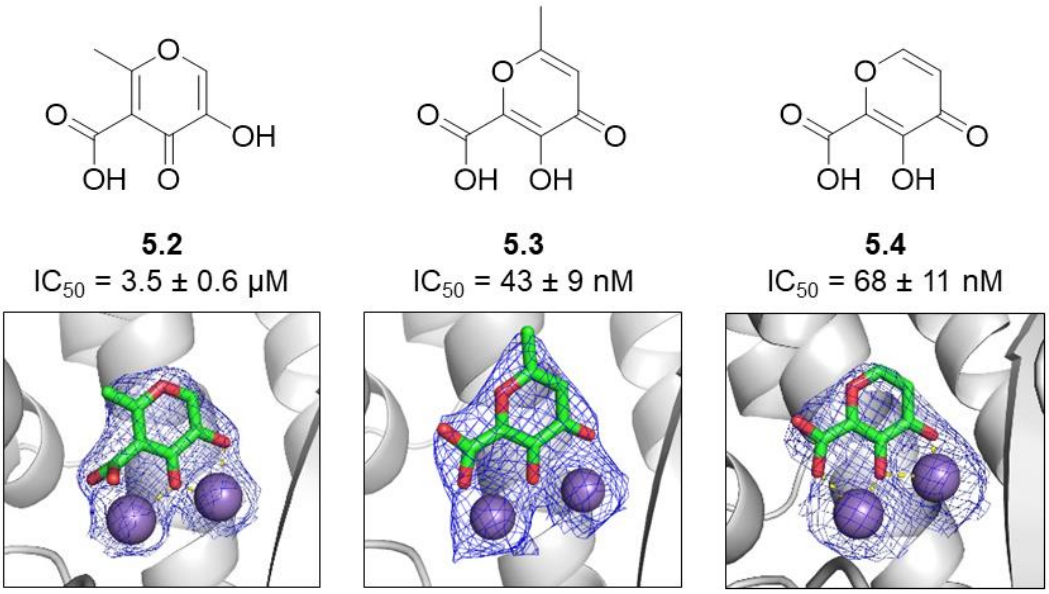

Figure 5.6. Structure and inhibitory activity of carboxylate containing MBPs **5.2**, **5.3**, and **5.4** (*top*). X-ray co-crystal structures of **5.2** (PDB: 6DCY), **5.3** (PDB: 6DZQ), and **5.4** (PDB: 6DCZ) coordinating to the active site of Endo (*bottom*). Compound **5.2** coordinates predominantly to Mn_A as the carboxylate is orthogonal to the rest of the MBP preventing optimal binding to Mn_B. For **5.3** and **5.4** the optimal bidentate binding to both Mn_A and Mn_B is observed (blue mesh is the $2F_0 - F_c$ map contoured to 2σ).

A potent MBP that was discovered from the MBP library screen was an α-hydroxy tropolone derivative **5.5** (Figure 5.7). The α-hydroxy tropolones were determined to be the most potent MBP series from the library screen with **5.5** exhibiting the greatest inhibitory activity (IC_{50} = 8.0 ± 1.1 nM). To understand the observed inhibitory activity, compound **5.5** was cocrystallized with Endo. From the crystal structure, **5.5** was found to engage in bidentate coordination interactions to both Mn_A and Mn_B. Interestingly, the MBP makes no other significant interactions with the surrounding active site residues or ordered waters. This suggests that the MBP derives its potent inhibitory activity entirely from coordination interactions with the active site metal ions. A likely reason for the significantly improved activity of **5.5** relative to **5.3** and **5.4** is that **5.5** engages in bidentate interactions utilizing only 5-membered chelate rings, while **5.3** and **5.4** utilize

a 5-membered chelate ring to coordinate to Mn_A and a perhaps less optimal 6-membered chelate ring to coordinate to Mn_B. Additionally, the difference in activity could be due to electronic differences in coordination motifs as the metal coordination motif of **5.5** is comprised of only phenolic/carbonyl donor oxygen atoms while both **5.3** and **5.4** utilize a combined carboxylic acid and phenolic/carbonyl donor motif. Unfortunately, while **5.5** was the most potent MBP inhibitor of Endo, it proved extremely difficult to derivatize and was therefore not utilized for further studies. In order to optimize the MBPs further for inhibitory activity modifications to **5.3** using isostere replacement were explored.

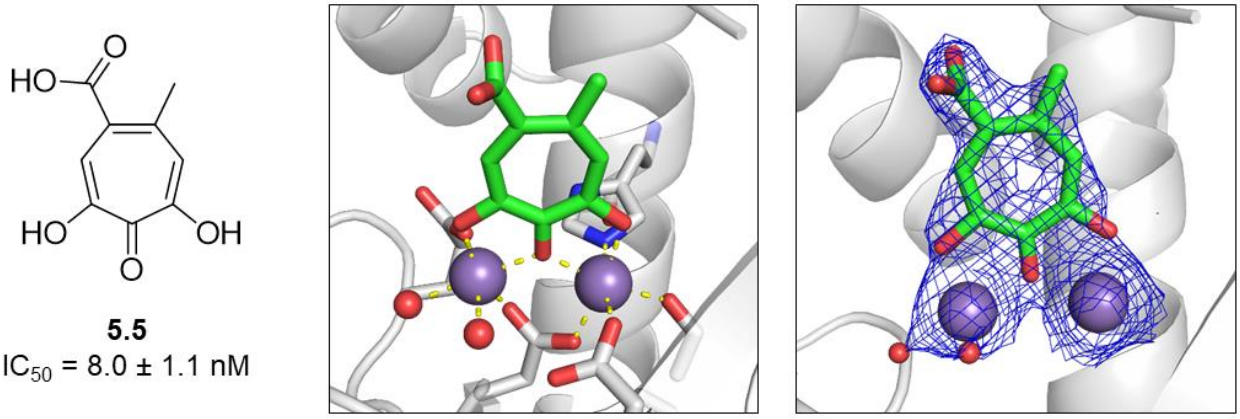

Figure 5.7. X-ray co-crystal structure of **5.5** bound to the active site metals of Endo (PDB ID: 6E0Q). Compound **5.5** was observed to bind similarly to **5.3** and **5.4**, with coordinating oxygen atoms replacing the three water molecules observed in the native structure. The carboxylate does not make any interactions with the protein active site or any ordered waters, suggesting the potent inhibitory activity is derived entirely from coordinative interactions with the active site metals (blue mesh is the $2F_0 - F_c$ map contoured to 1σ).

While **5.3** is an extremely potent inhibitor of Endo, we sought to further improve the inhibitory activity by utilizing isostere replacement. Specifically, replacements inside the MBP ring system were analyzed as the results in Chapter 4 suggest that such changes significantly

impact the donor ability of an MBP. Therefore, an oxygen to nitrogen replacement was chosen as those derivatizes had better coordination ability. The nitrogen containing MBI derivative **5.6** was developed (Figure 5.8) and screened against Endo and displayed significantly improved inhibitory activity ((IC_{50} = 17 ± 3 nM). Based on the cocrystal structure with Endo (Figure 5.8), it binds in the same manner as **5.3** and **5.4**. This suggests that the isostere replacement modulates the ligand electronics and pK_a while retaining the same binding mode. Therefore, **5.6** was chosen as the scaffold for further derivatization. One of the most potent derivatives developed was **5.7** (Figure 5.8), which reaches lower than the detection limit of the in vitro assay, and an IC_{50} = 110 ± 10 pm was extrapolated using differential scanning fluorimetry.[33-35] Unfortunately, even with its extremely potent inhibitory activity **5.7** exhibited only modest in vivo activity (EC_{50} = 21.3 ± 4.8 μM).

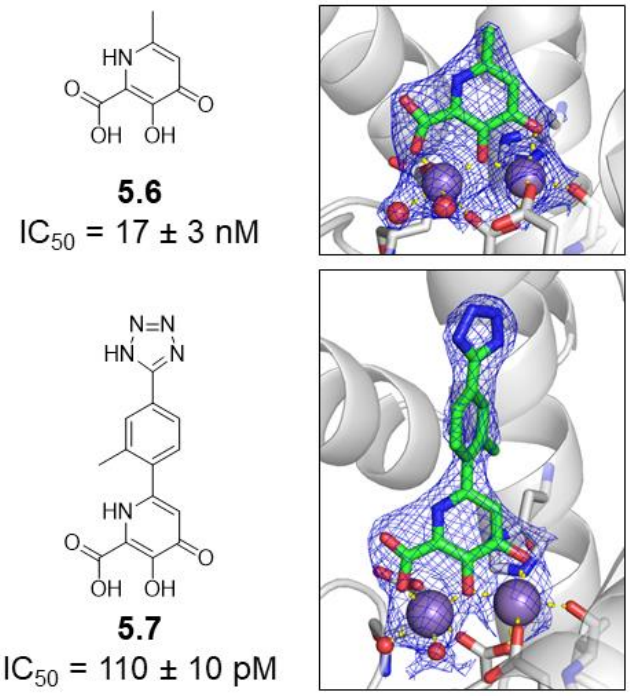

Figure 5.8. Chemical and X-ray co-crystal structure of **5.6** bound to the active site metals of Endo (PDB ID: 6E6V) (*top*). Compound **5.6** was observed to bind similarly to **5.3** and **5.4**, with coordinating oxygen atoms replacing the three water molecules observed in the native structure. Chemical and X-ray co-crystal structure of **5.7** bound to the active site metals of Endo (PDB ID: 6E6W) (*bottom*). The top portion of **5.7** makes hydrophobic interactions at the middle ring with the active site and electrostatic interactions via the top tetrazole (blue mesh is the $2F_0 - F_c$ map contoured to 1.5σ).

5.3 Conclusions

By taking a bioinorganic focused approach, a series of extremely potent inhibitors of Endo were developed. Utilizing X-ray crystallography, MBP modes of binding were observed and then tuned to increase inhibitory activity. Specifically, the addition of more coordination groups and isostere replacement aided in improving the activity of the starting MBP scaffold. Unfortunately, even after derivatization the compounds did not significantly protect human cells from the influenza virus. A likely reason for the poor in vivo activity of these inhibitors is their inability to enter human cells, as the inhibitors possess a significant number of readily ionizable functional

groups under physiological conditions. These ionized functional groups when present in sufficient number on an inhibitor can limit its ability to diffuse through the cellular phospholipid bilayer membrane. Therefore, future attempts might focus on improving the physicochemical properties of the developed scaffold through methods such as further isostere replacement. Specifically, the carboxylate moiety of the MBP would be a preliminary starting point.

5.4 Experimental

Protein Expression and Purification. Pandemic H1N1 Endo Δ52-64:Gly truncated construct was expressed from a pET-28a parent vector containing a kanamycin-resistance gene and expression inducible by the Lac 1 operon. Endo was expressed as an 8-His tagged fusion protein with a TEV protease cleavage site for tag removal. Transformation protocol was adapted from pET system manual (Novagen) using competent BL21 cells. Briefly, 1µL of 25 ng/µL recombinant plasmid was used for transformation. Cells were mixed by flicking with plasmid and were heat shocked at 42 ºC for 30 sec followed by incubation on ice for 5 min. The inoculated media was plated on LB agarose plates containing 50 µg/mL kanamycin and incubated overnight at 37 ºC. One colony was selected from the LB plate and added to 50 mL of SOC broth containing 50 µg/mL kanamycin and incubated for 5 h at 37 ºC with shaking at 125 rpm. Glycerol stocks of the culture were prepared (0.9 mL cultured media + 0.1 mL 80% glycerol) and flash frozen for future expressions. 100 mL of SOC media containing 50 µg/mL kanamycin was combined with a 1 mL frozen glycerol stock and incubated with shaking at 125 rpm overnight at 37 ºC. This culture was then equally divided into the 1L batches of expression media (Terrific Broth media with added 0.2% w/v dextrose, 0.1 mM $MnCl_2$, and 0.1 mM $MgSO_4$) containing 50 µg/mL kanamycin. Cells were grown to an OD_{600} = 0.6-0.8 at 37 ºC with shaking at 125 rpm. Expression of Endo was then

induced by the addition of IPTG to a final concentration of 0.2 mM. The media was then grown with shaking overnight at room temperature. After approximately 18 h the cells were harvested by centrifugation. The resulting paste was stored at -80 ºC prior to lysis.

For cell lysis, cell paste was thawed on ice and re-suspended in an equal volume of lysis buffer (20 mM Na_2PO_4, 500 mM NaCl, 25 mM imidazole, 1 mM $MgCl_2$, 2 mM dithiothreitol (DTT), 0.2% v/v Triton-X, pH=7.4) with EDTA free protease inhibitor tablets (Roche) (~1 tablet per 50 mL of lysis buffer) and lysed by sonication, 5×25 sec pulses with 2 min rest periods on ice. DNAse1 was added to a final concentration of 10-100 µg/mL and the lysate was shaken at 125 rpm for 15-30 min on ice until the consistency of the lysate became free-flowing. The lysate was then pelleted by centrifugation at 10000 rpm for 35-45 min at 4 ºC. The supernatant was decanted, and a HisTrap HP (GE Healthcare) column was utilized to isolate the His-tagged fusion protein. The lysate supernatant was loaded onto 5 mL cartidges (1 cartridge per 4 L of growth media collected cell paste) that had been equilibrated with binding buffer (20 mM Na_2PO_4, 500 mM NaCl, 25 mM imidazole, pH=7.4). The desired protein, Endo, was then eluted over a 45 min gradient at a flow rate of 4 mL/min, from 0-100% elution buffer (20 mM Na_2PO_4, 500 mM NaCl, 500 mM imidazole, pH=7.4), with the protein eluting typically between 40-60% elution buffer. Sodium dodecyl sulfate–polyacrylamide gel electrophoresis (SDS-PAGE) analysis showed a band corresponding to endonuclease protein running at ~23kD with several small impurities.

Fractions containing Endo were combined in a 10K MWCO dialysis bag with 1000 units of TEV protease and were dialyzed against dialysis buffer (100 mM NaCl, 1 mM DTT, 1 mM $MnCl_2$, 20 mM Tris, 5% glycerol, pH=8.0) overnight. The proteolytic cleavage of the fusion protein is slow, and greatly benefits from the addition of excess TEV protease as some Endo is lost to precipitation. To remove any precipitation the dialyzed solution was filtered through a 0.45

μm filter. The filtered protein was then passed over a 5 mL HisTrap HP cartridge that had been equilibrated with binding buffer. The flow through was collected and concentrated to 5-10 mg/mL. The concentrated protein was then purified on a gel-permeation size exclusion column (GE Superdex 75, 10/300 GL) equilibrated with buffer (150 mM NaCl, 2 Mm $MgCl_2$, 2 mM $MnCl_2$, 20 mM HEPES, pH=7.5). A large peak corresponding to the cleaved endonuclease construct eluted at approximately 12 mL elution volume. Fractions containing pure cleaved Endo were combined and concentrated.

Protein Crystallization. Crystals for soaking experiments (compound **5.4**) were obtained by utilizing a protein solution of 4-10 mg/mL in 150 mM NaCl, 20 mM HEPES pH 7.5, 2 mM $MgCl_2$, and 2 mM $MnCl_2$ and a precipitant solution of 25 % PEG 4000, 200 mM sodium acetate, and 100 mM Tris, pH=8.0. The protein and precipitant solutions were combined in a 2:1 ratio in hanging drop 24-well plates, with crystal forming within 3 days at 33-35 °C. MBPs were soaked in by incubating crystals in a 5-20 mM MBP precipitant solution. For co-crystallization experiments (compound **5.1**, **5.2**, **5.3**, **5.5**, **5.6**, and **5.7**) purified protein for crystallization was stored at 4-7 mg/mL at 4° C in buffer consisting of 150 mM NaCl, 20 mM HEPES at pH 7.5, 2 mM $MgCl_2$, and 2 mM $MnCl_2$. Co-crystallization experiments were set up in 24-well hanging drop plates with a 2:1 or 3:1 ratio of protein stock to reservoir solution. Reservoir solution consisted of 0.5 mM inhibitor, 25-40% w/v PEG 4000, 100 mM Tris pH 8.35, and 200-220 mM sodium acetate. Protein crystals grew by vapor diffusion at 33° C in hanging drops. Colorless crystals with octahedral morphology appeared within 24 h and reached full size after 3-4 days with little to moderate protein precipitation observed. Crystals were typically 50 to 150 μm in each dimension. For both soaking

and co-crystallization experiments, crystals were cryo-protected with reservoir solution supplemented with 10-20% ethylene glycol and flash frozen with liquid nitrogen.

X-ray data collection and refinement. Crystals were screened for resolution and cryo-protection conditions on an in-house X-ray generator. For these experiments and for data collection of the structure with compound **5.4** bound, diffraction data was collected on a Bruker X8 Proteum diffractometer at 100 K, using a Bruker Microfocus Rotating Anode (MicroSar FR-592) X-ray generator with a Bruker APEX II CCD detector at wavelength 1.54178 Å. The data for the structures with compounds **5.1**, **5.2**, and **5.7** bound were collected at the ALS 5.0.2 beamline using a double-crystal Si(111) monochromator set to a wavelength of 1.00 Å with a Pilatus3 6M 25 Hz detector. The data sets for the structures with compounds **5.3**, **5.5**, and **5.6** bound were collected at the ALS 5.0.1 beamline using a single-crystal, cylindrically bent, Si(220) monochromator set to a wavelength of 0.977 Å with a Pilatus 6M 25 Hz detector. All data sets were integrated, merged, and scaled within iMosflm and the CCP4 software suite.[36] For all structures phasing was determined by molecular replacement against a previously published Endo structure (PDB ID: 4AWM)[24] using PHASER. Structures were refined with REFMAC5.[37] All figures were made in PyMOL.[38] All ligands and MBP were generated via PRODRG server.[39]

Table 5.1. X-ray crystallographic data collection and refinement statistics for structures with compounds **5.1**, **5.2**, **5.3**, and **5.4** bound.

	Compound **5.1**	Compound **5.2**	Compound **5.3**	Compound **5.4**
PDB ID	6E6X	6DCY	6DZQ	6DCZ
Data Collection Statistics				
Space group	*P*$6_2$22	P$6_2$22	P$6_2$22	P$6_2$22
Cell dimensions a, b, c (Å); α, β, γ (°)	75.3, 75.3, 120.6; 90.0, 90.0, 120.0	75.54, 75.54, 120.36; 90.0, 90.0, 120.0	75.20, 75.20, 119.62; 90.0, 90.0, 120.0	75.84, 75.84, 121.30; 90.0, 90.0, 120.0
Resolution (Å)	4429-2.50 (2.60-2.50)*	37.77 – 2.08 (2.14 – 2.08)*	44.05- 2.25 (2.32 – 2.25)*	30.33 – 2.89 (3.07 – 2.89)*
R_{merge}	0.095 (0.463)*	0.083 (0.786)*	0.063 (0.523)*	0.117 (0.485)*
I/σ(I)	19.2 (5.7)*	19.1 (3.4)*	41.5 (8.5)*	12.5 (2.5)*
Completeness (%)	100.0 (100.0)*	100.0 (100.0)*	100.0 (100.0)*	95.7 (99.8)*
No. unique reflections	7520 (809)*	12849 (974)*	10089 (899)*	4826 (773)*
Redundancy	17.5 (19.4)*	16.9 (18.1)*	35.3 (35.0)*	8.8 (5.4)*
Refinement Statistics				
R_{work} / R_{free}	0.207/0.265	0.225/0.271	0.205/0.253	0.200/0.276
Average B-factor	48.7	44.595	43.616	43.918
R.m.s. bond lengths (Å)	0.016	0.01	0.009	0.008
R.m.s bond angles(°)	1.600	1.425	1.314	1.277

***** Metrics for highest resolution shell given in parentheses

Table 5.2. X-ray crystallographic data collection and refinement statistics for structures with compounds **5.5**, **5.6**, and **5.7** bound.

Compound	Compound **5.5**	Compound **5.6**	Compound **5.7**
PDB ID	6E0Q	6E6V	6E6W
Data collection statistics			
Space group	$P6_222$	$P6_222$	$P6_222$
Cell dimensions a, b, c (Å); α, β, γ (°)	75.09, 75.09, 119.67; 90.0, 90.0, 120.0	75.5, 75.5, 120.2; 90, 90, 120	74.9, 74.9, 120.0; 90, 90, 10
Resolution (Å)	44.03 – 2.35 (2.43 – 2.35)*	44.24 – 2.25 (2.32– 2.25)*	44.05 – 2.35 (2.43-2.35)*
R_{merge}	0.07 (0.517)	0.048 (0.532)*	0.089(0.439)*
I/σ(I)	40.3 (8.6)*	38.9 (6.4)*	25.3(7.3)*
Completeness (%)	100.0 (100.0)	100.0 (100.0)*	100.0 (100.0)*
No. unique reflections	8874 (846)*	10206 (901)*	8854 (831)*
Redundancy	35.1 (36.8)	19.1 (19.0)*	31.4 (31.1)*
Refinement statistics			
R_{work} / R_{free}	0.200/0.258	0.216/0.257	0.210/0.271
Average B-factor	44.568	48.64	50.0
R.m.s. bond lengths (Å)	0.009	0.010	0.015
R.m.s bond angles (°)	1.400	1.316	1.622

***** Metrics for highest resolution shell given in parentheses

Endo Enzymatic Activity Assay. Endo activity assays were carried out as previously reported.[32] Assays were performed using Black Costar 96-well plates, with each well contained a total volume of 100 μL comprised of: buffer (20 mM Tris, 150 mM NaCl, 2 mM $MnCl_2$, 10 mM β-mercaptoethanol, 0.2% Triton-X100, pH 8.0), Endo (5 or 25 nM), inhibitor (various concentrations) in buffer, and fluorescent ssDNA-oligo substrate (200 nM). A single-stranded, 17-mer DNA oligonucleotide labeled with a 5′-FAM fluorophore and a 3′-TAMRA quencher ([6-FAM]AATCGCAGGCAGCACTC[TAM], Sigma-Aldrich) was employed as the substrate. Upon addition of the substrate, the change in fluorescence was measured over 45 min at 37 °C (λ_{ex} = 485 nm; λ_{em} = 528 nm). The gain was set to 100 and the first 15 min of data were excluded from the activity calculations. Negative control wells contained no inhibitor and were set to 100% activity, while positive control wells contained the previously reported inhibitor, L-742,001 (Sigma

Aldrich, SML1010). Percent inhibition was determined by comparing the activity of wells containing inhibitors to the activity of those without. Dose-response curves were generated, fitted, and analyzed using Origin16 graphing software. For most experiments, the enzyme concentration was 25 nM, which afforded a strong change in fluorescent signal, but had an IC_{50} detection limit of ~12.5 nM. Using an enzyme concentration of 5 nM, the detection limit was observed to be ~2.5 nM; however, the change in fluorescent signal was significantly weaker than that from an enzyme concentration of 25 nM. These detection limits prompted the use of thermal shift assay to distinguish between the highly potent inhibitors reported herein.

5.5 Acknowledgements

The content and figures in this chapter are in large part adapted from "Structure-Activity Relationships in Metal-Binding Pharmacophores for Influenza Endonuclease" Cy V. Credille, Benjamin L. Dick, Christine N. Morrison, Ryjul W. Stokes, Rebecca N. Adamek, Nicholas C. Wu, Ian A. Wilson, and Seth M. Cohen. *J. Med. Chem.* 2018, *61*, 22, 10206-10217, "SAR Exploration of Tight-Binding Inhibitors of Influenza Virus PA Endonuclease" Cy V. Credille*, Christine N. Morrison*, Ryjul W. Stokes*, Benjamin L. Dick, Yifan Feng, Jiaxing Sun, Yao Chen, and Seth M. Cohen. *J. Med. Chem.* 2019, *62*, 21, 9438-9449, and "Targeting Metalloenzymes for Therapeutic Intervention" Allie Y. Chen*, Rebecca N. Adamek*, Benjamin L. Dick, Cy V. Credille, Christine N. Morrison, and Seth M. Cohen. *Chem. Rev.* 2019, *119*, 2, 1323-1455. The dissertation author was the primary researcher for the data presented and gratefully acknowledges the contributions of coauthors Cy V. Credille, Christine N. Morrison, Ryjul W. Stokes, Rebecca N. Adamek, Nicholas C. Wu, Ian A. Wilson, Yifan Feng, Jiaxing Sun, Yao Chen, Allie Y. Chen, and Seth M. Cohen. The compound synthesis and preparation details may be found in the mentioned publications and were prepared by Cy V. Credille and Ryjul W. Stokes. The

permissions to reproduce this material was granted by the American Chemical Society, Copyright 2018 and 2019.

5.6 References

1. WHO, Influenza (seasonal) fact sheet. World Health Organisation Media Centre Geneva: 2018.

2. Langmuir, A. D.; Henderson, D. A.; Serfling, R. E., The Epidemiological Basis for the Control of Influenza. *Am. J. Public Health* **1964,** *54*, 563-71.

3. Belongia, E. A.; Skowronski, D. M.; McLean, H. Q.; Chambers, C.; Sundaram, M. E.; De Serres, G., Repeated annual influenza vaccination and vaccine effectiveness: review of evidence. *Expert Rev. Vaccines* **2017,** *16* (7), 1-14.

4. Carrat, F.; Flahault, A., Influenza vaccine: the challenge of antigenic drift. *Vaccine* **2007,** *25* (39-40), 6852-62.

5. Belongia, E. A.; Kieke, B. A.; Donahue, J. G.; Greenlee, R. T.; Balish, A.; Foust, A.; Lindstrom, S.; Shay, D. K.; Marshfield Influenza Study, G., Effectiveness of inactivated influenza vaccines varied substantially with antigenic match from the 2004-2005 season to the 2006-2007 season. *J. Infect. Dis.* **2009,** *199* (2), 159-67.

6. Jefferson, T.; Demicheli, V.; Rivetti, D.; Jones, M.; Di Pietrantonj, C.; Rivetti, A., Antivirals for influenza in healthy adults: systematic review. *Lancet* **2006,** *367* (9507), 303-13.

7. Fiore, A. E.; Fry, A.; Shay, D.; Gubareva, L.; Bresee, J. S.; Uyeki, T. M.; Centers for Disease, C.; Prevention, Antiviral agents for the treatment and chemoprophylaxis of influenza --- recommendations of the Advisory Committee on Immunization Practices (ACIP). *MMWR Recomm. Rep.* **2011,** *60* (1), 1-24.

8. Antiviral drugs for treatment and prophylaxis of seasonal influenza. *Med. Lett. Drugs Ther.* **2019,** *61* (1563), 1-4.

9. Stiver, G., The treatment of influenza with antiviral drugs. *CMAJ* **2003,** *168* (1), 49-56.

10. Baloxavir marboxil (Xofluza) for treatment of influenza. *Med. Lett. Drugs Ther.* **2018,** *60* (1561), 193-196.

11. Huang, T. S.; Palese, P.; Krystal, M., Determination of influenza virus proteins required for genome replication. *J. Virol.* **1990,** *64* (11), 5669-73.

12. Fodor, E., The RNA polymerase of influenza a virus: mechanisms of viral transcription and replication. *Acta Virol.* **2013,** *57* (2), 113-22.

13. Resa-Infante, P.; Jorba, N.; Coloma, R.; Ortin, J., The influenza virus RNA synthesis machine: advances in its structure and function. *RNA Biol.* **2011,** *8* (2), 207-15.

14. Plotch, S. J.; Bouloy, M.; Ulmanen, I.; Krug, R. M., A unique cap(m7GpppXm)-dependent influenza virion endonuclease cleaves capped RNAs to generate the primers that initiate viral RNA transcription. *Cell* **1981,** *23* (3), 847-858.

15. Dias, A.; Bouvier, D.; Crepin, T.; McCarthy, A. A.; Hart, D. J.; Baudin, F.; Cusack, S.; Ruigrok, R. W., The cap-snatching endonuclease of influenza virus polymerase resides in the PA subunit. *Nature* **2009,** *458* (7240), 914-8.

16. Guilligay, D.; Tarendeau, F.; Resa-Infante, P.; Coloma, R.; Crepin, T.; Sehr, P.; Lewis, J.; Ruigrok, R. W.; Ortin, J.; Hart, D. J.; Cusack, S., The structural basis for cap binding by influenza virus polymerase subunit PB2. *Nat. Struct. Mol. Biol.* **2008,** *15* (5), 500-6.

17. Li, M. L.; Rao, P.; Krug, R. M., The active sites of the influenza cap-dependent endonuclease are on different polymerase subunits. *EMBO J.* **2001,** *20* (8), 2078-86.

18. Yuan, P.; Bartlam, M.; Lou, Z.; Chen, S.; Zhou, J.; He, X.; Lv, Z.; Ge, R.; Li, X.; Deng, T.; Fodor, E.; Rao, Z.; Liu, Y., Crystal structure of an avian influenza polymerase PA(N) reveals an endonuclease active site. *Nature* **2009,** *458* (7240), 909-13.

19. Monod, A.; Swale, C.; Tarus, B.; Tissot, A.; Delmas, B.; Ruigrok, R. W.; Crepin, T.; Slama-Schwok, A., Learning from structure-based drug design and new antivirals targeting the ribonucleoprotein complex for the treatment of influenza. *Expert Opin. Drug Discov.* **2015,** *10* (4), 345-71.

20. Chen, A. Y.; Adamek, R. N.; Dick, B. L.; Credille, C. V.; Morrison, C. N.; Cohen, S. M., Targeting Metalloenzymes for Therapeutic Intervention. *Chem. Rev.* **2019,** *119* (2), 1323-1455.

21. Doan, L.; Handa, B.; Roberts, N. A.; Klumpp, K., Metal ion catalysis of RNA cleavage by the influenza virus endonuclease. *Biochemistry* **1999,** *38* (17), 5612-9.

22. Ju, H.; Zhang, J.; Huang, B.; Kang, D.; Huang, B.; Liu, X.; Zhan, P., Inhibitors of Influenza Virus Polymerase Acidic (PA) Endonuclease: Contemporary Developments and Perspectives. *J. Med. Chem.* **2017,** *60* (9), 3533-3551.

23. Song, J. M.; Lee, K. H.; Seong, B. L., Antiviral effect of catechins in green tea on influenza virus. *Antiviral Res.* **2005,** *68* (2), 66-74.

24. Kowalinski, E.; Zubieta, C.; Wolkerstorfer, A.; Szolar, O. H.; Ruigrok, R. W.; Cusack, S., Structural analysis of specific metal chelating inhibitor binding to the endonuclease domain of influenza pH1N1 (2009) polymerase. *PLoS Pathog.* **2012,** *8* (8), e1002831.

25. Iwai, Y.; Takahashi, H.; Hatakeyama, D.; Motoshima, K.; Ishikawa, M.; Sugita, K.; Hashimoto, Y.; Harada, Y.; Itamura, S.; Odagiri, T.; Tashiro, M.; Sei, Y.; Yamaguchi, K.; Kuzuhara, T., Anti-influenza activity of phenethylphenylphthalimide analogs derived from thalidomide. *Bioorg. Med. Chem.* **2010,** *18* (14), 5379-90.

26. Tomassini, J.; Selnick, H.; Davies, M. E.; Armstrong, M. E.; Baldwin, J.; Bourgeois, M.; Hastings, J.; Hazuda, D.; Lewis, J.; McClements, W.; et al., Inhibition of cap (m7GpppXm)-dependent endonuclease of influenza virus by 4-substituted 2,4-dioxobutanoic acid compounds. *Antimicrob. Agents Chemother.* **1994,** *38* (12), 2827-37.

27. Hastings, J. C.; Selnick, H.; Wolanski, B.; Tomassini, J. E., Anti-influenza virus activities of 4-substituted 2,4-dioxobutanoic acid inhibitors. *Antimicrob. Agents Chemother.* **1996,** *40* (5), 1304-7.

28. Nakazawa, M.; Kadowaki, S. E.; Watanabe, I.; Kadowaki, Y.; Takei, M.; Fukuda, H., PA subunit of RNA polymerase as a promising target for anti-influenza virus agents. *Antiviral Res.* **2008,** *78* (3), 194-201.

29. Omoto, S.; Speranzini, V.; Hashimoto, T.; Noshi, T.; Yamaguchi, H.; Kawai, M.; Kawaguchi, K.; Uehara, T.; Shishido, T.; Naito, A.; Cusack, S., Characterization of influenza virus variants induced by treatment with the endonuclease inhibitor baloxavir marboxil. *Sci. Rep.* **2018,** *8* (1), 9633.

30. Uehara, T.; Hayden, F. G.; Kawaguchi, K.; Omoto, S.; Hurt, A. C.; De Jong, M. D.; Hirotsu, N.; Sugaya, N.; Lee, N.; Baba, K.; Shishido, T.; Tsuchiya, K.; Portsmouth, S.; Kida, H., Treatment-Emergent Influenza Variant Viruses With Reduced Baloxavir Susceptibility: Impact on

Clinical and Virologic Outcomes in Uncomplicated Influenza. *J. Infect. Dis.* **2020,** *221* (3), 346-355.

31. Kikuchi, T.; Watanabe, A., Baloxavir heralds a new era in influenza virus biology. *Respir. Investig.* **2019,** *57* (1), 1-2.

32. Credille, C. V.; Chen, Y.; Cohen, S. M., Fragment-Based Identification of Influenza Endonuclease Inhibitors. *J. Med. Chem.* **2016,** *59* (13), 6444-54.

33. Simeonov, A., Recent developments in the use of differential scanning fluorometry in protein and small molecule discovery and characterization. *Expert Opin. Drug Discov.* **2013,** *8* (9), 1071-82.

34. Matulis, D.; Kranz, J. K.; Salemme, F. R.; Todd, M. J., Thermodynamic stability of carbonic anhydrase: measurements of binding affinity and stoichiometry using ThermoFluor. *Biochemistry* **2005,** *44* (13), 5258-66.

35. Credille, C. V.; Morrison, C. N.; Stokes, R. W.; Dick, B. L.; Feng, Y.; Sun, J.; Chen, Y.; Cohen, S. M., SAR Exploration of Tight-Binding Inhibitors of Influenza Virus PA Endonuclease. *J. Med. Chem.* **2019,** *62* (21), 9438-9449.

36. The CCP4 suite: Programs for Protein Crystallography. *Acta Crystallogr. D Biol. Crystallogr.* **1994,** *50* (Pt 5), 760-3.

37. Murshudov, G. N.; Skubak, P.; Lebedev, A. A.; Pannu, N. S.; Steiner, R. A.; Nicholls, R. A.; Winn, M. D.; Long, F.; Vagin, A. A., REFMAC5 for the Refinement of Macromolecular Crystal Structures. *Acta Crystallogr. D Biol. Crystallogr.* **2011,** *67*, 355-367.

38. Schrodinger, L. *The PyMOL Molecular Graphics System*, Version 1.8; 2015.

39. Schüttelkopf, A. W.; van Aalten, D. M. F., PRODRG: a tool for high-throughput crystallography of protein-ligand complexes. *Acta Crystallogr., Sect. D: Biol. Crystallogr.* **2004,** *60*, 1355-63.